# IMPLEMENTING AERODYNAMIC PREDICTIONS FROM COMPUTATIONAL FLUID DYNAMICS IN MULTIDISCIPLINARY DESIGN OPTIMIZATION OF A HIGH-SPEED CIVIL TRANSPORT

By
Duane L. Knill

A DISSERTATION SUBMITTED TO THE FACULTY OF
VIRGINIA POLYTECHNIC INSTITUTE AND STATE UNIVERSITY
IN PARTIAL FULFILLMENT OF THE REQUIREMENTS FOR THE DEGREE OF
DOCTOR OF PHILOSOPHY
IN
AEROSPACE ENGINEERING

Bernard Grossman, Chairman

William H. Mason

Raphael T. Haftka

Layne T. Watson

Robert W. Walters

Joseph A. Schetz

December 1997
Blacksburg, Virginia

# Implementing Aerodynamic Predictions from Computational Fluid Dynamics in Multidisciplinary Design Optimization of a High-Speed Civil Transport

by
Duane L. Knill

Committee Chairman: Bernard Grossman
Aerospace and Ocean Engineering

A method to efficiently introduce supersonic drag predictions from computational fluid dynamics (CFD) calculations in a combined aerodynamic–structural optimization of a High-Speed Civil Transport (HSCT) is presented. To achieve this goal, the method must alleviate the large computational burden associated with performing CFD analyses and reduce the numerical noise present in the analyses. This is accomplished through the use of response surface (RS) methodologies, a variation of the variable-complexity modeling (VCM) technique, and coarse grained parallel computing. Variable-complexity modeling allows one to take advantage of the information gained from inexpensive lower fidelity models while maintaining the accuracy of the more expensive high fidelity methods. The utility of the method is demonstrated on HSCT design problems of five, ten, fifteen, and twenty design variables.

Motivation for including CFD predictions into the HSCT optimization comes from studies detailing the differences in supersonic aerodynamic predictions from linear theory, Euler, and parabolized Navier-Stokes (PNS) calculations for HSCT configurations. The effects of these differences in integrated forces and distributed loads on the aircraft performance and structural weight are investigated. These studies indicate that CFD drag solutions are required for accurate HSCT performance and weight estimates.

Response surface models are also used to provide useful information to the designer with minimal computational effort. Investigations into design trade-offs and sensitivities to certain design variables, available at the cost of evaluating a simple quadratic polynomial, are presented. In addition, a novel and effective approach to visualizing high dimensional, highly constrained design spaces is enabled through the use of RS models.

# Acknowledgments

There are a number of people I would like to acknowledge for their roles in my professional and personal life.

Dr. Bernard Grossman, my advisor and committee chairman, has been a continuous source of guidance and encouragement in my years as a graduate student at Virginia Tech. I appreciate all he has done to foster my academic and professional growth. Dr. William Mason has offered many insights into numerous aspects of applied aerodynamics and aircraft design. I am grateful for his assistance and advise. I must also express my gratitude to Dr. Raphael Haftka, who has remained an integral part of our research group while a faculty member at the University of Florida. I would like to thank Dr. Layne Watson for his assistance concerning mathematical and computer science related issues. Thanks also goes to Dr. Robert Walters, who first inspired me to enter the field of computational fluid dynamics, and Dr. Joseph Schetz for their input while serving as members of my committee. Special thanks goes to Dr. Schetz for taking the time to help me prepare for the preliminary exams.

I would like to acknowledge other members of our research group for their contributions. In particular, I am grateful for the help I received from Vladimir Balabanov, Tony Giunta, and Chuck Baker.

Financial support for this research was provided through the NASA Langley Research Center grants NAG1–1160 and NAG1–1562. I am thankful to the contract monitors, Mr. Peter Coen and Dr. Perry Newman, for their assistance in this work.

I am especially grateful to my friends, who have provided support, companionship, love, and lots of laughs. These acknowledgements would not be complete without the recognition of my parents, Bill and Jean Knill, for their love and support.

# Contents

# List of Tables

# List of Figures

# Nomenclature

| | |
|---|---|
| ANOVA | analysis of variance |
| $\bar{c}$ | mean aerodynamic chord |
| $c_{root}$ | wing root chord length |
| $c_{tip}$ | wing tip chord length |
| $C_D$ | drag coefficient |
| $C_{D_f}$ | friction drag coefficient |
| $C_{D_i}$ | induced drag coefficient |
| $C_{D_{OW}}$ | zero-lift wave drag coefficient |
| $C_\ell$ | section lift coefficient |
| $C_L$ | lift coefficient |
| $C_{L_\alpha}$ | lift curve slope |
| $C_m$ | pitching moment coefficient |
| $C_{m_0}$ | zero-lift pitching moment coefficient |
| $C_N$ | normal force coefficient |
| CFD | computational fluid dynamics |
| CPU | central processing unit |
| DOE | design of experiments |
| DV | design variable |
| $\mathbf{g}(\mathbf{x})$ | vector of constraint values used in the optimization |
| HSCT | high-speed civil transport |
| LE | leading edge |
| $M$ | Mach number |
| MAC | mean aerodynamic chord |
| MDO | multidisciplinary design optimization |
| MPI | message passing interface |

| | |
|---|---|
| $m$ | number of design variables |
| $n$ | number of terms in the response surface model |
| $p$ | number of designs to sample from design space |
| PNS | parabolized Navier-Stokes |
| $q$ | number of candidate designs from which to perform D-optimality search |
| $r_{fus_i}$ | fuselage radius at $i^{th}$ axial restraint |
| $R^2$ | correlation coefficient for least squares regression fit |
| $R^2_{adj}$ | adjusted correlation coefficient |
| $R_{LE}$ | leading-edge radius parameter |
| RMS | root mean square |
| RS | response surface |
| RSM | response surface methodology |
| $s_{LE_I}$ | length of inboard leading-edge wing section |
| $s_{TE_I}$ | length of inboard trailing-edge wing section |
| SQP | sequential quadratic programming |
| $(t/c)_{root}$ | airfoil thickness-to-chord ratio at wing root |
| $(t/c)_{break}$ | airfoil thickness-to-chord ratio at the wing leading-edge break |
| $(t/c)_{tip}$ | airfoil thickness-to-chord ratio at wing tip |
| $T_p$ | execution time using $p$ processors |
| $T_s$ | serial execution time |
| TE | trailing edge |
| TOGW | take-off gross weight |
| $u_*$ | friction velocity $\left(\sqrt{\tau_w/\rho}\right)$ |
| VCM | variable-complexity modeling |
| $W_{fuel}$ | fuel weight |
| $W_{wing}$ | wing weight |
| $W_{TOGW}$ | take-off gross weight |
| $W_{C-TOGW}$ | take-off gross weight corrected for range errors |
| $x_{a.c.}$ | aerodynamic center location |
| $x_{a.c._0}$ | aerodynamic center location at zero lift |
| $x_{fus_i}$ | fuselage $i^{th}$ axial restraint |
| $(x/c)_{max\text{-}t}$ | chordwise location of airfoil maximum thickness |
| $\mathbf{x}$ | vector of design variable values |
| $\mathbf{x_{min}}$ | vector of minimum values for the design variables |

| | |
|---|---|
| $\mathbf{x_{max}}$ | vector of maximum values for the design variables |
| $x_m$ | location about which the pitching moment is taken |
| $y$ | observed value of the response |
| $\hat{y}$ | predicted value of the response |
| $y^+$ | nondimensional distance from the body surface |
| $y_{nacelle}$ | spanwise location of inboard nacelle centerline |
| $\alpha$ | angle of attack |
| $\Delta y_{nacelle}$ | nacelle separation distance |
| $\Lambda_{LE_I}$ | sweep angle of the inboard wing leading edge |
| $\Lambda_{LE_O}$ | sweep angle of the outboard wing leading edge |
| $\Lambda_{TE_I}$ | sweep angle of the inboard wing trailing edge |
| $\rho$ | fluid density |
| $\tau_w$ | wall shear |
| $\nu$ | kinematic viscosity |

# Chapter 1

# Introduction

## 1.1 Motivation

With advances in computational fluid dynamics (CFD) code maturity, grid generation capabilities, and computer performance, the application of CFD in the aircraft design process[1] has received much attention. Introducing accurate CFD predictions in the early stages of design has a large potential advantage in terms of aircraft life cycle cost and time-to-market. According to Nicolai,[2] about eighty percent of the aircraft life cycle cost is set after the conceptual design stage. Using more accurate aerodynamic predictions early in the design process, when the aircraft is taking shape, can result in less time and money spent in redesign and an overall improved product.

Studies[3,4] on the use of CFD methods for supersonic High-Speed Civil Transport (HSCT) design have appeared elsewhere. For pure analysis, Hollenback and Blom[3] compared parabolized Navier-Stokes (PNS) results with experimental data, Euler, and linear theory results for a Mach 2.4 HSCT design. Pittman[4] *et al.* obtained Euler equation solutions for a Mach 3 HSCT concept, and compared the results with linear theory. Their predictions were later verified by comparison to experimental data.[5] These studies show good comparison between CFD results and experimental data. In addition, the studies revealed that linear theory overpredicted the lift, underpredicted the drag, and produced poor pitching moment results. Pittman[4] *et al.* realized that the range estimates predicted using linear theory analyses are overly optimistic; however, they concluded that linear theory is still useful in conceptual and preliminary

design. Covell[5] *et al.* concluded that higher fidelity analyses are required early in the design process for accurate stability level predictions.

There has been substantial work in multidisciplinary design optimization (MDO) of HSCT configurations, examples of which are found in Refs. 6–10. However, these studies use panel-level codes or algebraic relations for the aerodynamic predictions. Computer programs such as ACSYNT[11] and FLOPS[12] also perform aircraft MDO with lower fidelity aerodynamic and structural models.

The relatively large computational expense associated with CFD analyses can discourage its application in high dimensional MDO procedures. An individual CFD analysis can require hours on a supercomputer. It is not feasible to introduce these calculations in a traditional aircraft systems optimization procedure where, due to the multidisciplinary nature of the problem and the large number of constraints, *hundreds of thousands* of solutions may be required to arrive at an optimal design.

Aerodynamic design has been performed using CFD solutions for high dimensional problems using an adjoint formulation[13,14] of the governing equations, but this approach is not practical for MDO problems because of the large number of constraints involved. Using a collaborative optimization architecture[15,16] may allow use of efficient disciplinary optimization techniques in an MDO environment, but convergence of the procedure is not guaranteed.

CFD and FEM have been coupled in low dimensional wing design problems. Borland[17] *et al.* performed MDO of a transonic transport wing using thin-layer Navier-Stokes aerodynamics and finite element structural analysis. Due to computational expense, only three aerodynamic design variables defining the wing twist, camber, and thickness distribution were used. Baker and Giesing[18] used Euler aerodynamics and finite element structures for HSCT wing design. In this case, only two aerodynamic design variables describing the wing twist distribution were used.

In addition to the computational expense issue, CFD solutions contain *numerical noise* which manifests itself as low amplitude, high frequency variations in the computational results. For analysis purposes this noise is normally insignificant, but when used for optimization it hinders the performance of gradient-based optimizers by giving improper gradient information and creating artificial local minima throughout the design space. These variations in results are not unique to CFD solutions.

Numerical noise is present in any method with iterative procedures or discrete representations of continuous geometric shapes or physical phenomena.[7,19] Low amplitude, high frequency oscillations have been found in wave drag predictions from slender body theory[7] and in panel level drag-due-to-lift results.[20] Numerical noise can also result from sub-optimizations which are performed within the complete optimization framework. Balabanov[21] *et al.* show such noise in structural optimization and wing camber optimization procedures.

Response surface (RS) modeling techniques[25] have been used for a number of years to solve complex engineering problems. In 1964, Powers[26] used RS modeling techniques to compute minimum drag bodies of revolution. Response surface modeling methods has proven successful in eliminating problems with numerical noise,[27] but they are hindered by the *curse of dimensionality*, in that their accuracy often degrades as the number of design variables increases. To counter this behavior multipoint approximation methods[28,29] have been implemented in both structural[30] and aerodynamic[31] design problems. The multipoint approximation methods replace the optimization problem with a sequence of approximate subproblems, each of which are applicable over a subset of the entire domain. These methods can improve the accuracy of the RS model fit by "zooming in" on the optimal design.

## 1.2 Methodology

In efforts to successfully implement CFD drag predictions in high-dimensional MDO procedures, a variation of the *variable-complexity response surface modeling* approach proposed by Giunta[7] *et al.* is used. This method is tested on an existing MDO procedure developed at Virginia Tech[6,32–34] for a Mach 2.4 cruise HSCT configuration (Fig. 1.1). Accuracy of the aerodynamic predictions is especially important since the HSCT is a highly leveraged aircraft, where small errors in the drag predictions have large effects on the aircraft performance estimates. Details of the HSCT optimization problem are presented in Chapter 2.

Variable complexity modeling is a technique which uses a mixture of low, medium, and high fidelity methods to take advantage of the information gained from the inexpensive low fidelity methods and efficiently obtain the accuracy of the high fidelity analyses. In this work, low fidelity analyses are simple algebraic relationships for the

lift and drag. The medium fidelity methods include slender body theory and linear theory aerodynamics. Euler and parabolized Navier-Stokes (PNS) calculations represent the high fidelity models. The details of these methods are given in Section 2.3.

The simple conceptual-level models provide the functional form of the supersonic drag polar. By proper selection of this functional form, the dependence of the resulting *intervening functions* on certain design variables is eliminated. These intervening functions (drag polar shape parameters $C_{D_0}(\mathbf{x})$ and $K(\mathbf{x})$) also provide more descriptive and useful information to the designer. In addition, experience has shown that creating response surface models for the intervening functions gives more accurate results than creating RS models for the drag itself. Kaufman[35] *et al.* show improvements in the accuracy of RS models for structural weight gained using knowledge of the functional form of the wing weight.

*Full term* quadratic RS models are created from inexpensive linear theory methods. These RS models provide information about the terms in the RS models which play a significant role in evaluating the drag. Because the Mach 2.4 cruise is predominantly linear, the linear theory methods capture the terms that are important to the Euler calculations. Through regression analysis and analysis of variance (ANOVA) techniques, performed only on the linear theory results, terms that are not important are dropped from the RS models. With fewer coefficients to evaluate, these *reduced term* RS models are created for the CFD predictions at reduced cost. In this way, information from the conceptual-level and preliminary-level analyses are used to more efficiently create the RS models for the expensive Euler computations.

Two approaches are employed to generate the reduced term RS models. The first approach is to simply create reduced term RS models of the intervening functions for the Euler drag predictions. The other approach is to create reduced term RS models of the difference between the intervening functions for the Euler drag and the corresponding full term linear theory RS models. The total *incremental* RS models are then computed as the sum of the linear theory RS models and these *correction* RS models. Further explanation into the RS models creation is given in Chapter 7.

## 1.3 Outline

Prior to implementing CFD solutions in the optimization, extensive code verification studies are performed to assure the accuracy of the Euler and parabolized Navier-Stokes (PNS) solutions. Grid convergence and residual norm reduction studies are performed in Chapter 3 to determine the mesh sizes and computational effort required to achieve converged results. Comparisons to experimental wing loads and integrated force and moment predictions reveal the accuracy of the CFD solutions. These results also provide a comparison of the supersonic linear theory, Euler, and PNS solutions.

After establishing the level of accuracy in the CFD solutions, the integrated forces and moments for typical HSCT wings and wing-fuselage configurations are computed using the Euler and PNS equations. These results are then compared to those predicted from linear theory, and the sensitivity of the aircraft range to the predicted value of the drag is determined from analysis. The differences in distributed loads and the effects on structural analysis and optimization are also discussed. The Von Mises equivalent stresses calculated using linear theory and CFD loads are compared at supersonic cruise and off-design conditions. These loads are then used in the structural optimization to compare the wing bending material weights computed using linear theory and CFD loads. All structural analysis and optimization calculations were performed by Dr. Vladimir Balabanov. These investigations provide motivation for the need to include more accurate aerodynamic predictions in the optimization.

Chapter 6 describes the progression of simplified HSCT optimization problems from the five variable wing design through the twenty variable wing/fuselage/nacelle design. This is followed by a discussion of the RS model creation. The optimization results using the full term RS models for the linear theory and Euler drag predictions on the five, ten, and fifteen variable design cases show the typical differences in the Euler and linear theory, and establish a baseline with which to compare the results of the reduced term Euler and reduced term incremental RS models.

Parallel computing issues are discussed in Chapter 11. The chapters following detail using RS models to rapidly gain useful information on design trade-offs and sensitivities. In addition, a means to visualize high-dimensional, highly-constrained design spaces is presented. Finally, possible improvements to the current methods of including CFD results in high-dimensional MDO are discussed.

**Figure 1.1:** Typical HSCT Configuration.

# Chapter 2

# HSCT Optimization Problem

The design problem involves minimizing the take-off gross weight (TOGW) of a High-Speed Civil Transport (HSCT) with a 5500 $n.mi.$ range. The aircraft is designed to cruise at Mach 2.4 and carry 250 passengers. The idealized mission profile is composed of take-off, subsonic climb, supersonic cruise/climb, and landing segments.

Using TOGW as the objective function in the multidisciplinary design optimization provides a measure of quality with respect to a variety of important aspects. The components of the TOGW reflect the performance of the optimization with respect to each of the disciplines involved. The fuel weight is determined primarily by the aerodynamic design, and the empty weight is set mainly by the structural design. The fuel weight is also a measure of the operation cost, and the empty weight is an indicator of the acquisition cost. In this way, TOGW represents the aerodynamic performance, structural efficiency, and economic feasibility of the aircraft.

A two-level optimization formulation is employed with the aerodynamic design as the upper level and the structural design as the lower level. The structural design takes the geometric information determined from the aerodynamic design and returns the structural weight. As described by Sobieszczanski-Sobieski and Haftka,[38] this asymmetric interaction between the two disciplines offers large savings in computational cost because there is no need to compute derivatives of the aerodynamic quantities with respect to the structural variables.

## 2.1 Design Variables

The general HSCT configuration and mission is parameterized by 29 design variables. The aircraft geometry (Table 2.1) is described with 26 design variables. This provides a realistic description of the complex geometry with a relatively small number of design variables and allows the flexibility required to investigate a wide variety of aircraft configurations. Eight variables are used to describe the cranked delta planform (Fig. 2.1). These variables describe the wing root chord, tip chord, and semispan lengths, as well as the locations of the leading-edge (LE) and trailing-edge (TE) breaks and the LE of the tip chord. The airfoil sections are described using five design variables: the chordwise location of maximum thickness, leading-edge radius parameter, and thickness-to-chord ratios at three spanwise locations. An analytic description[6] provides the thickness distribution. The chordwise location of maximum thickness and leading-edge radius parameter are held constant across the span. The thickness-to-chord ratio has a piecewise linear variation between its values specified at the wing root, LE break, and wing tip.

The axi-symmetric fuselage is defined with eight design variables which provide the fuselage radii at four axial *restraint* locations. The shape of the body between these points is then determined by considering it as a minimum wave drag body of a fixed volume.[6,39] The cross-sectional area is given by

$$S(\tilde{x}) = \frac{128V}{3\pi l}\tilde{x}^{3/2}(1-\tilde{x})^{3/2} + l^2\sum_{i=1}^{4}\nu_i\left[\ln\left(\frac{z_{1i}+2z_{2i}}{z_{1i}-2z_{2i}}\right) + \frac{2z_{2i}}{9}\left(9z_{1i}-64z_{2i}^2\right)\right],$$

where $z_{1i} = \tilde{x} + k_i - 2\tilde{x}k_i$ and

$$z_{2i}^2 = \tilde{x}k_i(1-\tilde{x})(1-k_i).$$

The quantity $V$ is the fixed volume, $l$ is the fuselage length, $\tilde{x}$ is the normalized axial location $x/l$, and the $k_i$ are the normalized axial locations of the restraints. The constants $\nu_i$ are determined by solving the $4\times4$ linear system resulting from this equation applied at the four restraint locations.

The spanwise location of the nacelles is defined with two design variables. The axial location of the nacelles relative to the wing TE is fixed to obtain 25% overhang. A single design variable describes the thrust of each engine. The nacelle diameter and length are scaled relative to this value.

The horizontal and vertical tail areas are given by the final two geometric design

variables. The aspect ratio, taper ratio, and quarter chord sweep of each surface are held constant. The idealized mission is described using three design variables: the cruise climb rate, initial cruise altitude, and fuel weight.

## 2.2 Constraints

The optimization uses up to 68 inequality constraints (Table 2.2) dealing with the aircraft geometry and performance/aerodynamics. These constraints are devised to ensure feasible aircraft geometries and impose realistic performance and control capabilities. Fuel volume and wing chord-length limits are examples of geometric constraints. Aerodynamic constraints include, for example, landing angle-of-attack limits; balanced field length requirements; and wing, tail, and engine scrape prevention criteria. Emergency conditions are used to enforce the landing constraints. It is assumed that the aircraft lands on a runway $5000\,ft$ above sea level at 145 *knots*, carrying 50% of its initial fuel weight. Other aerodynamic constraints establish controllability during adverse flight conditions. For example, the aircraft must be capable of trimmed flight with both engines on one side of the aircraft inoperable. These are complicated, nonlinear constraints that require aerodynamic forces and moments, stability and control derivatives, and center of gravity and inertia estimates.

## 2.3 Analysis and Optimization Tools

### 2.3.1 Linear Theory Aerodynamic Codes

The supersonic linear theory predictions are obtained from three codes, each computing a particular component of the drag. The volumetric wave drag is computed using the Harris[40] wave drag program. Drag-due-to lift is calculated using a panel method by Carlson[41] *et al.* with attainable leading edge thrust corrections.[42] Viscous drag estimates are obtained using standard algebraic estimates[43] of the skin friction.

The optimal camber for our HSCT designs is determined using the linear theory code WINGDES.[41,44] WINGDES attempts to find the camber distribution along the wing which minimizes the drag-due-to-lift. Two runs of WINGDES per wing were

required to get the proper camber distribution. The second run serves to smooth the camber distribution and provide the maximum leading edge suction parameter closer to the design lift coefficient.

### 2.3.2 Computational Fluid Dynamics Code

Version 2.2 of the General Aerodynamic Simulation Program[45] (GASP) is used to obtain the Euler and parabolized Navier-Stokes solutions. GASP is a fully conservative CFD code which solves the Reynolds averaged Navier-Stokes equations and many of its subsets. The code uses an upwind three dimensional finite volume spatial discretization. Roe, Van Leer, Steger-Warming, and full flux functions are available in each direction. For our calculations, a third order upwind biased interpolation of the Roe fluxes is used in each of the marching planes.

The finite volume formulation of the Reynolds averaged Navier-Stokes equations may be written in terms of the vector of conserved variables, $Q$, the vector of primitive variables, $q$, the cell volume, $V$, and a residual vector, $R(q)$, as

$$\frac{\partial <Q>}{\partial q}\frac{\partial <q>}{\partial t}V + R(q) = 0.$$

The cell averaged quantity, $<Q>$, is defined as an integral over the volume of the cell

$$<Q> = \frac{1}{V}\iiint_V Q(x,y,z,t)\,dV.$$

The cell averaged quantity for the primitive variables, $<q>$, is defined in the same manner. The residual vector can be written as a function of the cell edge area averages of the inviscid fluxes, $\vec{F}$ and viscous fluxes, $\vec{F}_v$, the unit normal vectors, $\hat{n}$, to the cell faces, and the areas, $\Delta A$, of the $nf$ cell faces as

$$R(q) = \sum_{j=1}^{nf}\left(\vec{F} - \vec{F}_v\right)\cdot\hat{n}_j\,\Delta A_j.$$

The norm of this residual vector represents the convergence to the steady state solution. GASP iteratively solves the system of equations until a prescribed reduction in the residual norm is reached. Due to the large savings in computational time, space marching has been performed for all of the supersonic CFD calculations presented in this report.

### 2.3.3 Grid Generation

The grids for the space marching calculations on HSCT wings and wing-fuselage combinations are created using a 3-D grid generator originally developed by Barger.[46] The code has been modified by the author to provide better resolution of the leading edge. In addition, the code was reorganized and coding errors were eliminated, giving rise to a grid generator that is robust for large changes in the aircraft geometry. A hyperbolic tangent grid stretching, suitable for use in parabolized Navier-Stokes calculations, was also added to the original code. The grid generator receives as input the aircraft configuration stored in the Craidon[47] geometry format, extends the wing to join the fuselage, performs filleting of the wing-fuselage intersection,[48] and then creates a grid for space marching calculations. Since our HSCT optimization code creates a Craidon description file from its set of design variables, the conversion from a set of design variables to a space marching CFD grid is straightforward.

The space marching planes are created along planes of constant $x$-value. Two of these computational planes for a wing-fuselage configuration are shown in Fig. 2.2. A Mach cone analysis is used to form the outer boundary to ensure that all shocks are contained within the computational domain. The grid generator allows for flexible stretching of the grid points around and normal to the aircraft to create grids suitable for both Euler and Navier-Stokes calculations. Measures are employed to reduce grid skewness at the wing tip and wing-fuselage juncture. The grid generator is automated and robust for large planform changes, essential qualities for application in design optimization.

### 2.3.4 Structural Analysis Codes

All components of the take-off gross weight are calculated using empirically based functions obtained from the Flight Optimization System[12] (FLOPS) weight equations. Work by Huang[49] *et al.* indicated that the FLOPS wing bending material weight predictions for HSCT configurations had insufficient accuracy. Substantial work has been performed using structural optimization from the finite element code GENESIS[50] to predict the wing bending material weight.[21,34,35] In this research, GENESIS is used to compute the stresses and wing bending material weights presented in Chapter 4, but only the FLOPS weight equations are used in the HSCT optimization results.

### 2.3.5 Optimization Routine

Optimization is performed using Design Optimization Tools[51] (DOT). The constrained optimization is performed using sequential quadratic programming (SQP) and central difference gradient approximations.

**Table 2.1:** Twenty-Nine Variables in HSCT Design.

| DV | Description |
|---|---|
| 1 | wing root chord, $c_{root}$ $(ft)$ |
| 2 | LE break, x $(ft)$ |
| 3 | LE break, y $(ft)$ |
| 4 | TE break, x $(ft)$ |
| 5 | TE break, y $(ft)$ |
| 6 | LE wing tip, x $(ft)$ |
| 7 | wing tip chord, $c_{tip}$ $(ft)$ |
| 8 | wing semispan, $b/2$ $(ft)$ |
| 9 | chordwise location airfoil max. thickness, $(x/c)_{max\text{-}t}$ |
| 10 | LE radius parameter, $R_{LE}$ |
| 11 | t/c at wing root, $(t/c)_{root}$ |
| 12 | t/c at LE break, $(t/c)_{break}$ |
| 13 | t/c at wing tip, $(t/c)_{tip}$ |
| 14 | fuselage axial restraint #1, $x_{fus_1}$ $(ft)$ |
| 15 | fuselage radius at axial restraint #1, $r_{fus_1}$ $(ft)$ |
| 16 | fuselage axial restraint #2, $x_{fus_2}$ $(ft)$ |
| 17 | fuselage radius at axial restraint #2, $r_{fus_2}$ $(ft)$ |
| 18 | fuselage axial restraint #3, $x_{fus_3}$ $(ft)$ |
| 19 | fuselage radius at axial restraint #3, $r_{fus_3}$ $(ft)$ |
| 20 | fuselage axial restraint #4, $x_{fus_4}$ $(ft)$ |
| 21 | fuselage radius at axial restraint #4, $r_{fus_4}$ $(ft)$ |
| 22 | spanwise location of inboard nacelle, $y_{nacelle}$ $(ft)$ |
| 23 | spanwise location of outboard nacelle $(ft)$ |
| 24 | mission fuel weight, $W_{fuel}$ $(lb)$ |
| 25 | starting cruise altitude $(ft)$ |
| 26 | cruise climb rate $(ft/min)$ |
| 27 | vertical tail area $(ft^2)$ |
| 28 | horizontal tail area $(ft^2)$ |
| 29 | thrust per engine $(lb)$ |

**Table 2.2:** Constraints in HSCT Design.

| # | **Constraint Description** |
|---|---|
| 1 | Range $\geq 5,500\, n.mi.$ |
| 2 | Required $C_L$ at landing speed $\leq 1$ |
| 3–20 | Section $C_\ell \leq 2$ |
| 21 | Landing angle of attack $\leq 12^\circ$ |
| 22 | Fuel volume $\leq$ half of wing volume |
| 23 | Spike prevention |
| 24–41 | Wing chord $\geq 7.0\, ft$ |
| 42–43 | No engine scrape at landing $\alpha$ |
| 44–45 | No engine scrape at landing $\alpha$, with $5^\circ$ roll |
| 46 | No wing tip scrape at landing |
| 47 | Rudder deflection for crosswind landing $\leq 22.5^\circ$ |
| 48 | Bank angle for crosswind landing $\leq 5^\circ$ |
| 49 | Takeoff rotation to occur $\leq 5$ *sec* |
| 50 | Tail deflection for approach trim $\leq 22.5^\circ$ |
| 51 | Wing root T.E. $\leq$ horiz. tail L.E. |
| 52 | Balanced field length $\leq 11,000$ *ft* |
| 53 | TE break scrape at landing with $5^\circ$ roll |
| 54 | LE break $\leq$ semispan |
| 55 | TE break $\leq$ semispan |
| 56–58 | $(t/c)_{root}$, $(t/c)_{break}$, and $(t/c)_{tip} \geq 1.5\%$ |
| 59 | $x_{fus_1} \geq 5ft$ |
| 60 | $x_{fus_2} - x_{fus_1} \geq 10\, ft$ |
| 61 | $x_{fus_3} - x_{fus_2} \geq 10\, ft$ |
| 62 | $x_{fus_4} - x_{fus_3} \geq 10\, ft$ |
| 63 | $300\, ft - x_{fus_4} \geq 10\, ft$ |
| 64 | $y_{nacelle} \geq$ side-of-fuselage |
| 65 | $\Delta y_{nacelle} \geq 0$ |
| 66 | Engine-out limit with vertical tail design; otherwise $y_{nacelle} + \Delta y_{nacelle} \leq 0.5(b/2)$ |
| 67-68 | Maximum thrust required $\leq$ available thrust |

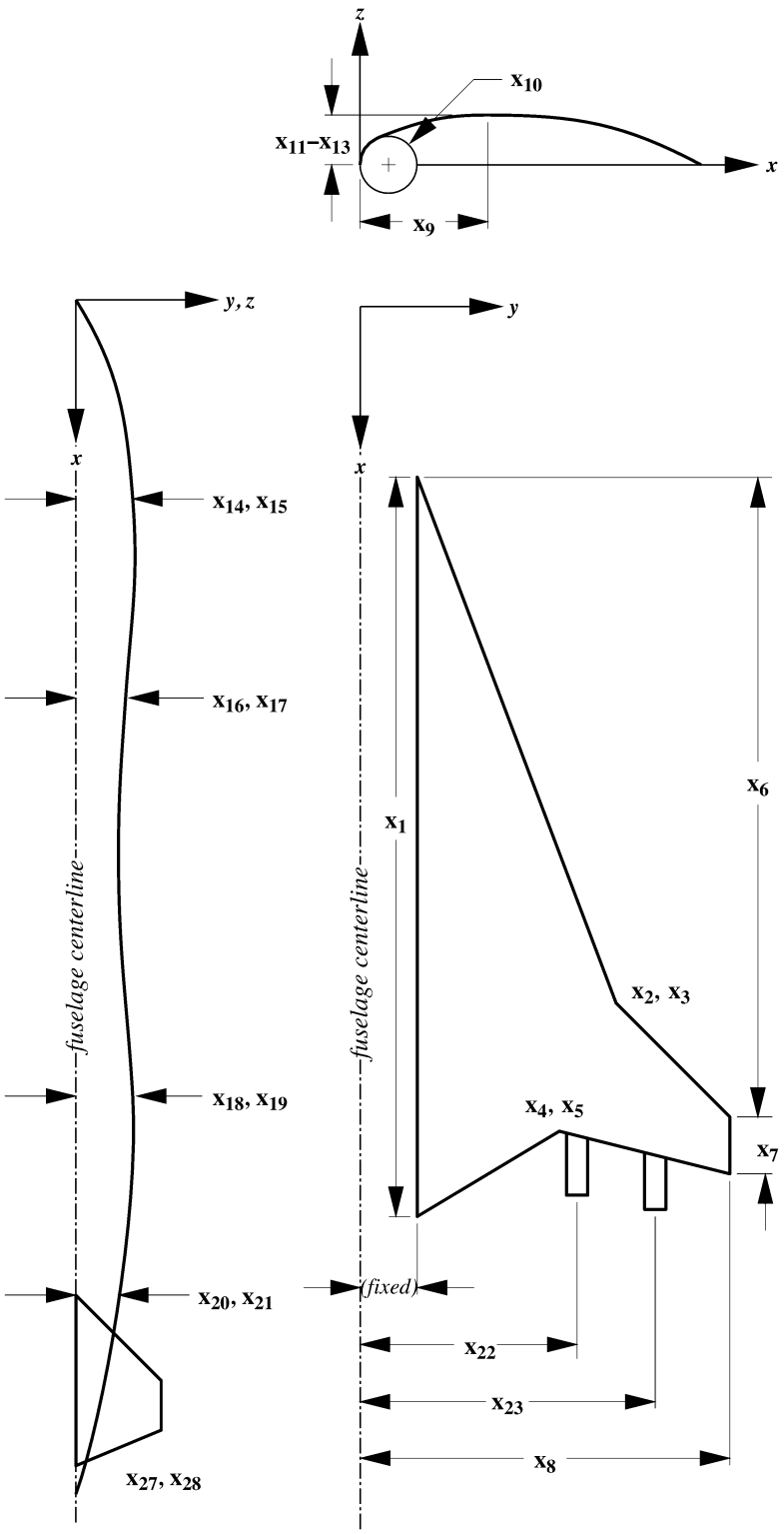


**Figure 2.1:** Geometry for 29-Variable HSCT Design Problem.

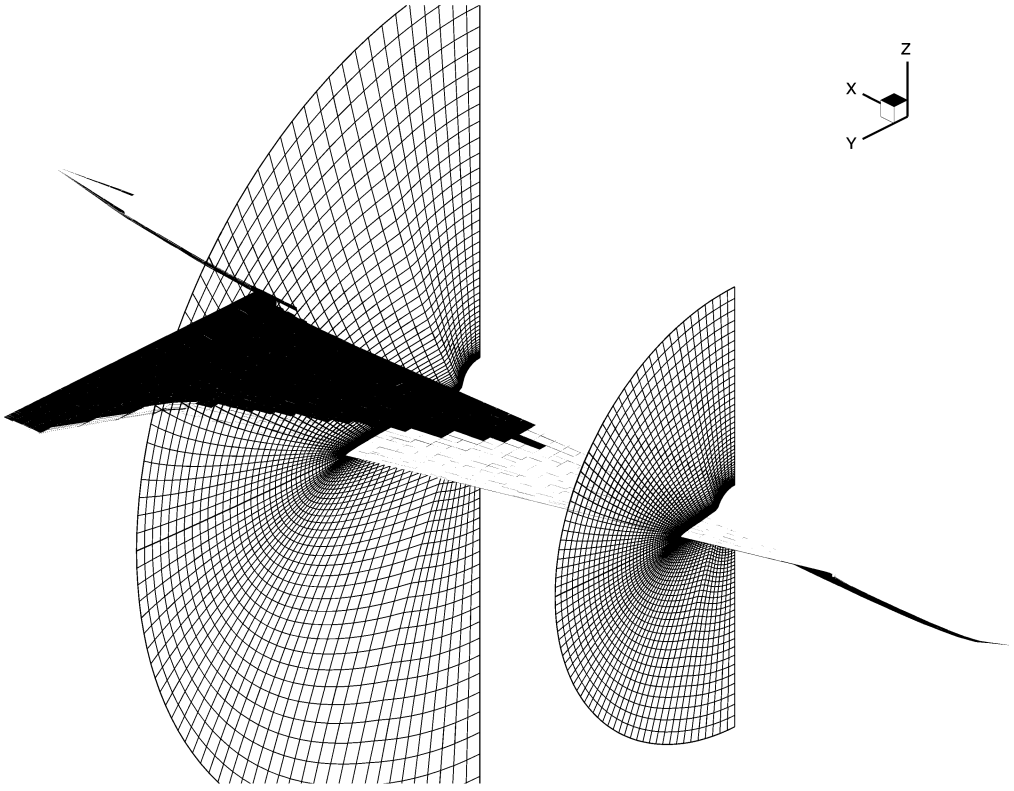


**Figure 2.2:** HSCT Wing-Fuselage with CFD Grid Planes.

# Chapter 3

# Code Verification and Preliminary Comparisons of CFD and Linear Theory

As CFD technology matured, code verification became important. In 1988, Bobbitt[52] presented a comprehensive survey of code verification issues, and AGARD held a conference[53] on the verification of CFD codes. Since then, the establishment of a rigorous basis for verifying and certifying codes has been found to be more difficult than originally envisioned. An excellent discussion has been given by Aeschliman[54] *et al.*

To assess the adequacy of our CFD results for use in multidisciplinary HSCT design optimization, the guidelines on code certification procedures outlined by NASA and the Multidisciplinary Analysis and Design Industrial Consortium (MADIC)[55–57] are followed. First in this process is the code *verification*, which establishes an acceptable level of accuracy in the calculation. The MADIC/NASA panel defines verification as "the process that demonstrates the code's ability to solve the specific set of governing equations and boundary conditions posed to the computer by the code."[56] Grid refinement studies and comparison to experimental data are key components in this process. The results of the following sections serve to verify our Euler and parabolized Navier-Stokes solutions and to provide a comparison of CFD and linear theory predictions. These results are also found in Knill[58] *et al.*

## 3.1 Haack-Adams Bodies

Our studies begin by investigating the zero-lift wave drag prediction for a series of Haack-Adams bodies.[59] Calculations have been performed using two different fineness ratios: $l/d_{max} = 7$ and $l/d_{max} = 10$. The bodies in this study have a nonzero base area, $A_{base}$, for mounting to a sting in the wing-tunnel tests. The equation for the radius, $r$, of these bodies with area ratio $A_{base}/A_{max} = 0.532$ is given as:

$$\begin{aligned}\frac{r}{r_{max}} &= \left\{0.707\left[1-\left(\frac{2x}{l}-1\right)^2\right]^{3/2}\right. \\ &+ 0.16934\left(\frac{2x}{l}-1\right)\left[1-\left(\frac{2x}{l}-1\right)^2\right]^{1/2} \\ &+ \left.0.16934\cos^{-1}\left(1-\frac{2x}{l}\right)\right\}^{1/2}.\end{aligned}$$

Investigation of the body shape (Fig. 3.1) reveals that the nose is blunt. However, following work by Mason and Lee,[60] the CFD solutions are space marched as if the nose were sharp. They found that certain classes of bodies, while having geometrically blunt noses, produce flowfields which do not exhibit classical blunt body behavior. These bodies can be treated as if they are geometrically sharp. The Haack-Adams bodies are treated in this manner.

A grid convergence study of the wave drag (Fig. 3.2) for the Euler equations is performed for the body with $l/d_{max} = 10$ at Mach 2.5. An axisymmetric grid is used for these calculations, so the total number of cells, $N$, is the number of axial cells times the number of normal cells. Meshes with uniform axial spacing and with distributions clustered at the nose are considered. For the clustered grids, two different grid aspect ratios are considered. One has an equal number of axial and normal points, while the other has twice the number of axial points as normal points. The clustered grids with a $1:1$ (*normal:axial*) grid ratio range in size from 11×11 to 71×71. The clustered grids with a $1:2$ grid ratio range in size from 11×21 to 41×81. The uniform grids with a $1:2$ grid ratio range in size from 11×21 to 81×161.

Clearly, the grids with axial points clustered near the nose outperform the grids with uniform axial spacing. Both the 36×71 and 51×51 clustered grids produce converged results, where our criteria for convergence is computed drag values within one percent of the extrapolated value as $N \to \infty$. Since the 36×71 grid has 50 fewer

grid cells than the 51×51 grid, it is chosen for use in the Euler computations. The drag for these bodies is nondimensionalized using the free stream conditions and the maximum cross sectional area, $A_{max}$, of the body.

Methods quantifying grid convergence for CFD solutions using a Grid Convergence Index (GCI) are described in Ref. 61. The GCI measures the uncertainty of the grid convergence based upon the error derived from generalized Richardson extrapolation theory. This method is applied to cases where the solutions on only a few grids are available. Since we are able to obtain solutions relatively quickly through the supersonic space marching techniques, we have the luxury of producing solutions over a large number of mesh sizes and graphically extrapolating the solution for zero mesh size. Therefore, the GCI is not used as a measure of our grid convergence. The GCI method will be applicable when this study is extended to the transonic regime where our computational costs will increase by an order of magnitude and the method used in this report for determining grid convergence will not be feasible.

Convergence of the wave drag with the prescribed residual norm reduction (Fig. 3.3) is investigated for the body in a Mach 2.5 flow using the clustered 71×71 grid. The *residual norm reduction* plotted in the graph refers to how many orders of magnitude the residual norm is required to decrease from its value at the first iteration in each marching plane. Mathematically it can be written for each marching plane as

$$\text{residual norm reduction} = \frac{||R||^{(i)}}{||R||^{(1)}},$$

where $||R||^{(i)}$ is the norm of the residual vector at the $i^{th}$ iteration. The wave drag prediction is nearly constant after the residual has been reduced by four orders of magnitude, so all other calculations on the Haack-Adams body are performed with this convergence criterion.

The Euler wave drag predictions show substantial improvement over the Harris wave drag code results (Figs. 3.4 and 3.5) for both the $l/d_{max} = 7$ and $l/d_{max} = 10$ cases. The Harris code performs poorly with increasing Mach number for this case. While the experimental data and Euler prediction of the wave drag decrease with Mach number, the Harris code wave drag prediction begins to increase with Mach number. As expected, the accuracy of the Harris wave drag results does improve for the more slender body.

The computational time required for the Euler analysis of the Haack-Adams forebody is approximately three minutes (0.07 sec/cell) for the clustered $36 \times 71$ grid on a single processor SGI R4000 workstation with a single 100 MHz IP17 Processor. By comparison, the Harris wave drag code takes less than one second to compute the drag.

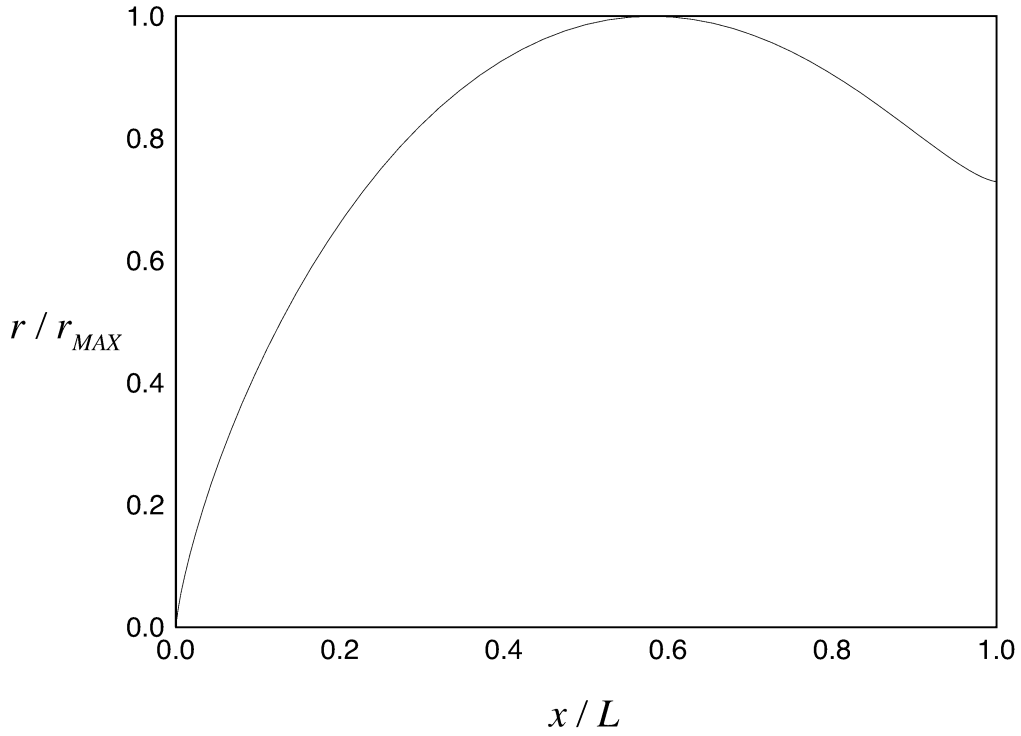


**Figure 3.1:** Haack-Adams Body Shape.

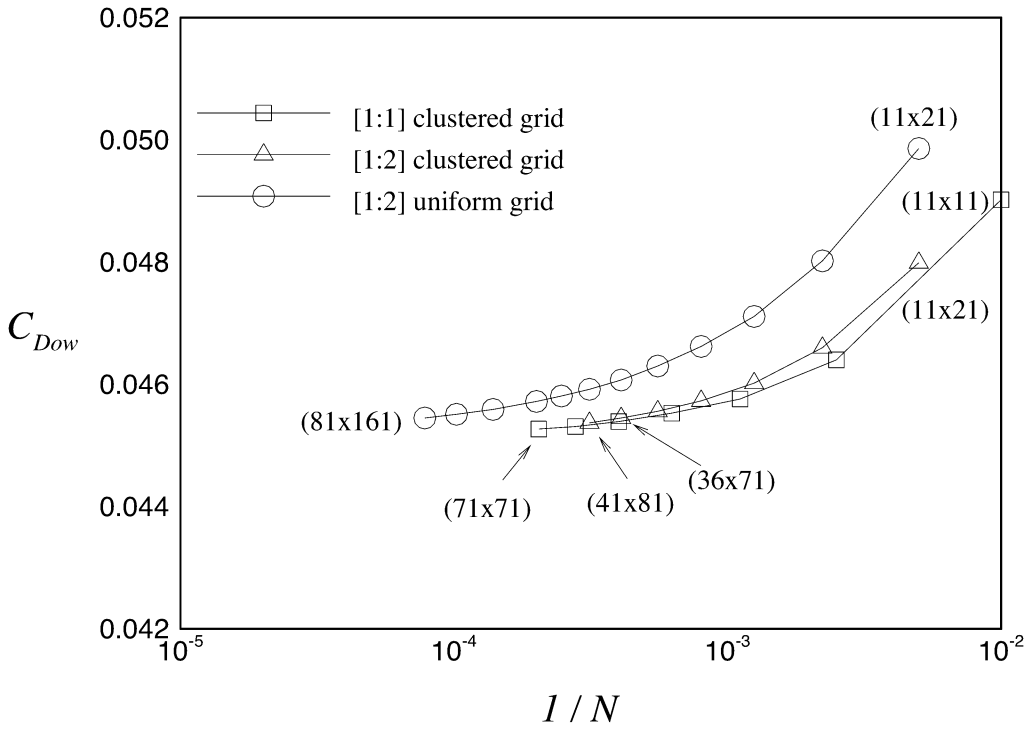


**Figure 3.2:** Haack-Adams Grid Convergence.

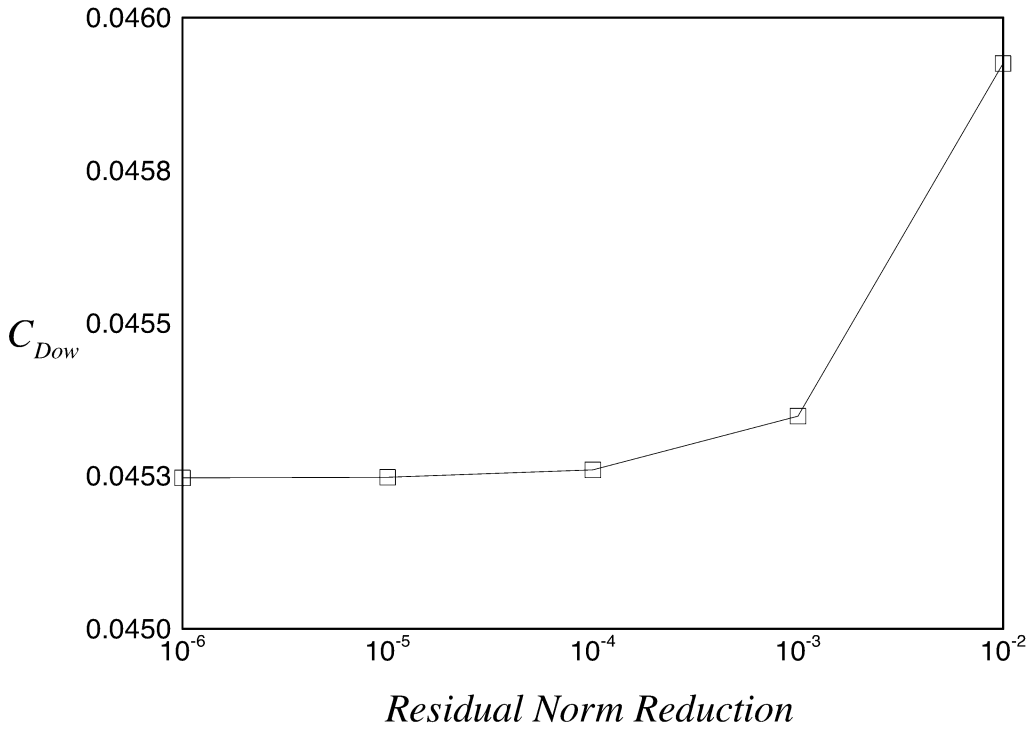


**Figure 3.3:** Haack-Adams Residual Norm Reduction.

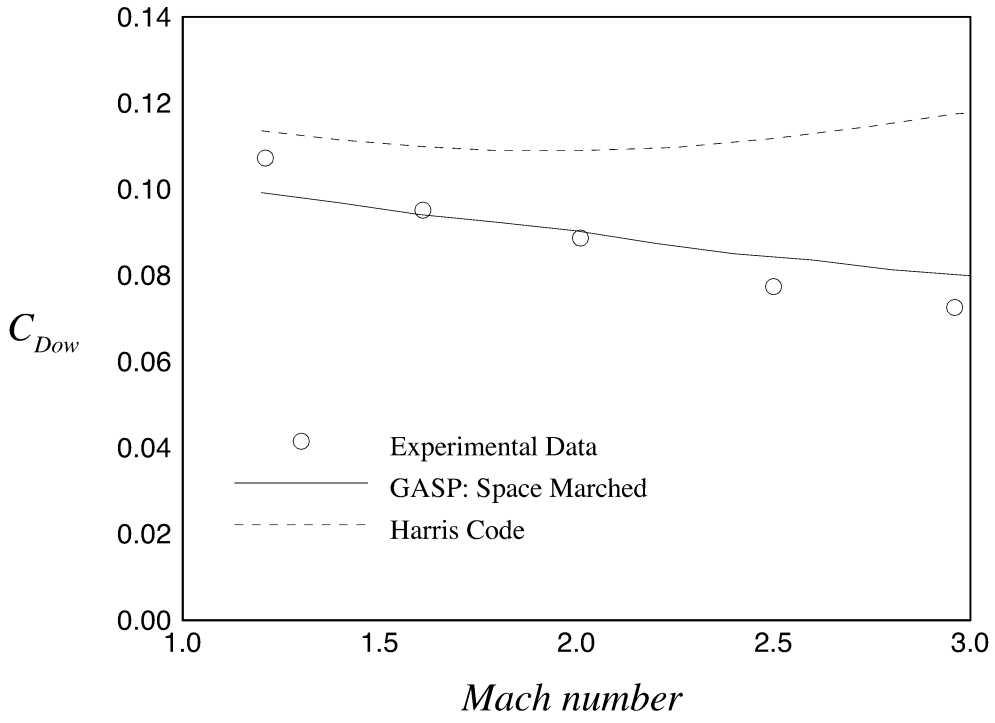


**Figure 3.4:** Haack-Adams Wave Drag ($l/d_{max} = 7$).

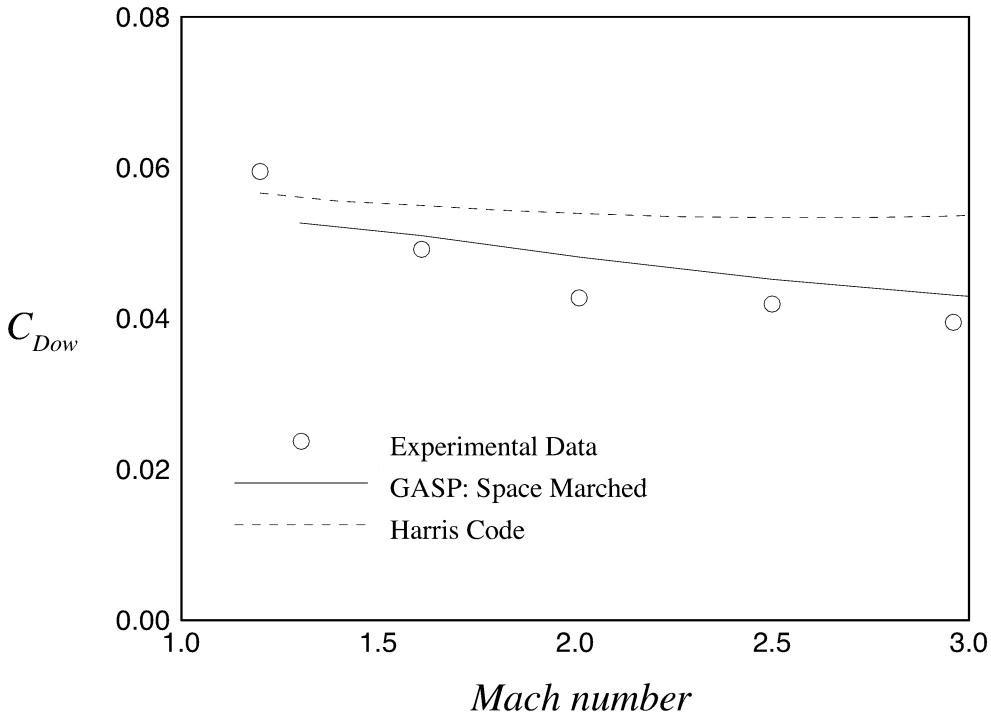


**Figure 3.5:** Haack-Adams Wave Drag ($l/d_{max} = 10$).

## 3.2 Squire Wing

We now investigate the wave drag prediction on a symmetric delta wing. The Squire wing (Fig. 3.6) is a delta wing with a biconvex centerline and elliptic cross section. The thickness of each cross section is chosen to match the cross sectional area of a 9% thick biconvex wing with a diamond shaped cross section.[62] The space marching grid is created with the grid points clustered near the wing in the same way they were for the Haack-Adams body. The wing surface grid is also clustered along the leading edge to properly define the elliptical cross section geometry.

Grid refinement studies are performed on the wing at 0° angle-of-attack and Mach 2.4. Figure 3.7 shows the relative effects of varying the number of grid points in only one direction. This is done to identify the dimension to which the wave drag is most sensitive. The drag coefficient data, based on the planform area, is given in *counts* of drag, where one count of drag is equivalent to $C_D = 0.0001$. The coarsest grid considered is 21×21×21. The number of spanwise, outward, and chordwise points are increased to 141, 81, and 101 respectively. As expected, the number of spanwise points is found to have the largest effect on the drag. Note that the scale for this graph is very small. The total change in drag from the coarsest to finest grid for the spanwise variation is slightly less than one count. With this in mind, a grid convergence study (Fig. 3.8) for a [3:2:2] aspect ratio grid [*spanwise*:*outward*:*chordwise*] is investigated. The 61×41×41 grid is chosen for our computations. The wave drag predicted from solution on this mesh is within 1/4 count of the value extrapolated as $N \to \infty$. The residual norm reduction study (Fig. 3.9) performed on the 61×41×41 grid at Mach 2.4 indicates that requiring the residual norm to decrease by two orders of magnitude is sufficient for converged wave drag results. This is a less stringent criteria than is required for converged results on the Haack-Adams bodies.

Inspection of the wave drag results (Fig. 3.10) shows good agreement between GASP and the experimental data. The Harris wave drag results show the same overprediction found in the results for the thickest Haack-Adams body. Similar comparisons of the wave drag coefficients predicted from linear theory and from a three-dimensional nonlinear full-potential code (NCOREL) are presented in Ref. 63. The Euler computation for the 61×41×41 grid took about 19 minutes (0.012 sec/cell) on the SGI R4000 workstation described in Section 3.1.

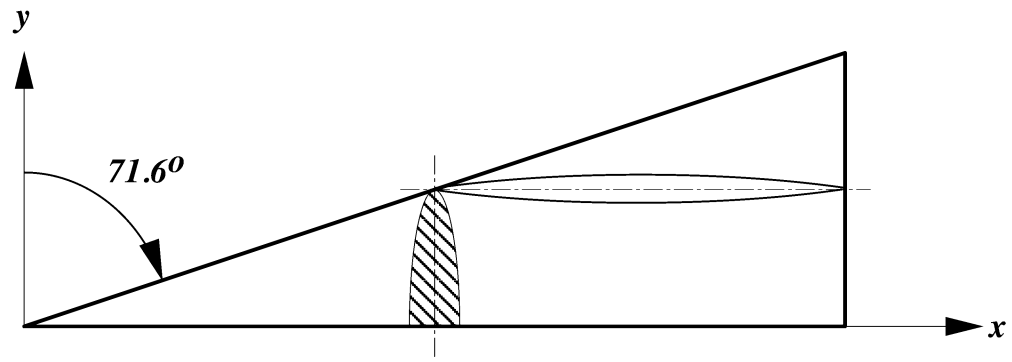


**Figure 3.6:** Squire Wing.

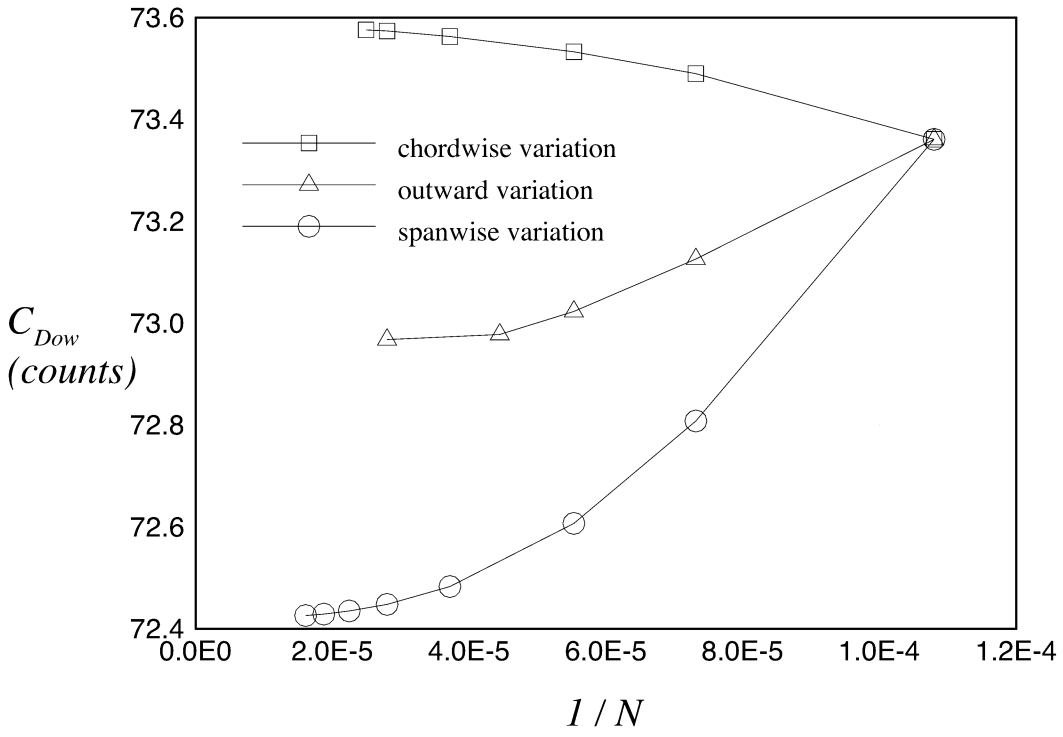


**Figure 3.7:** Squire Wing Grid Convergence.

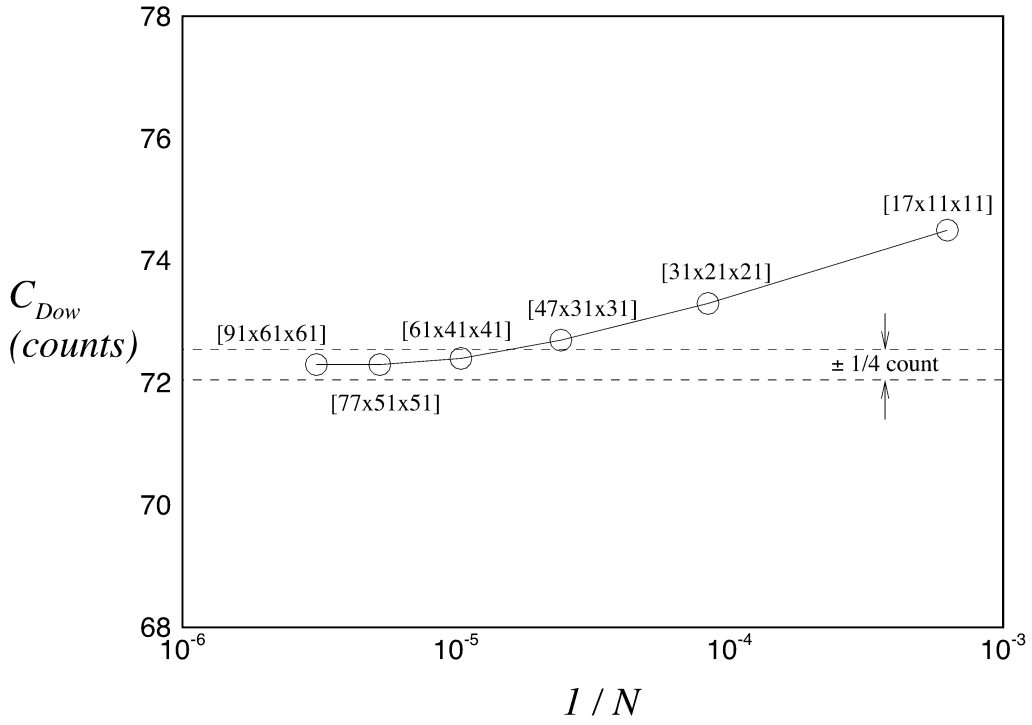


**Figure 3.8:** Squire Wing Grid Convergence.

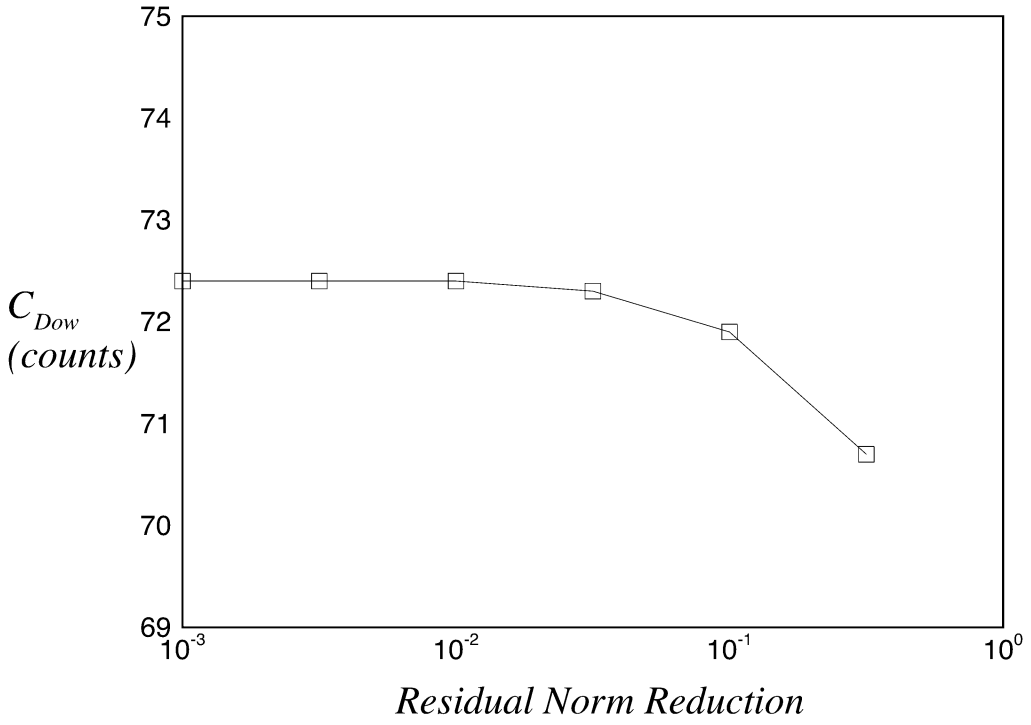


**Figure 3.9:** Squire Wing Residual Norm Reduction.

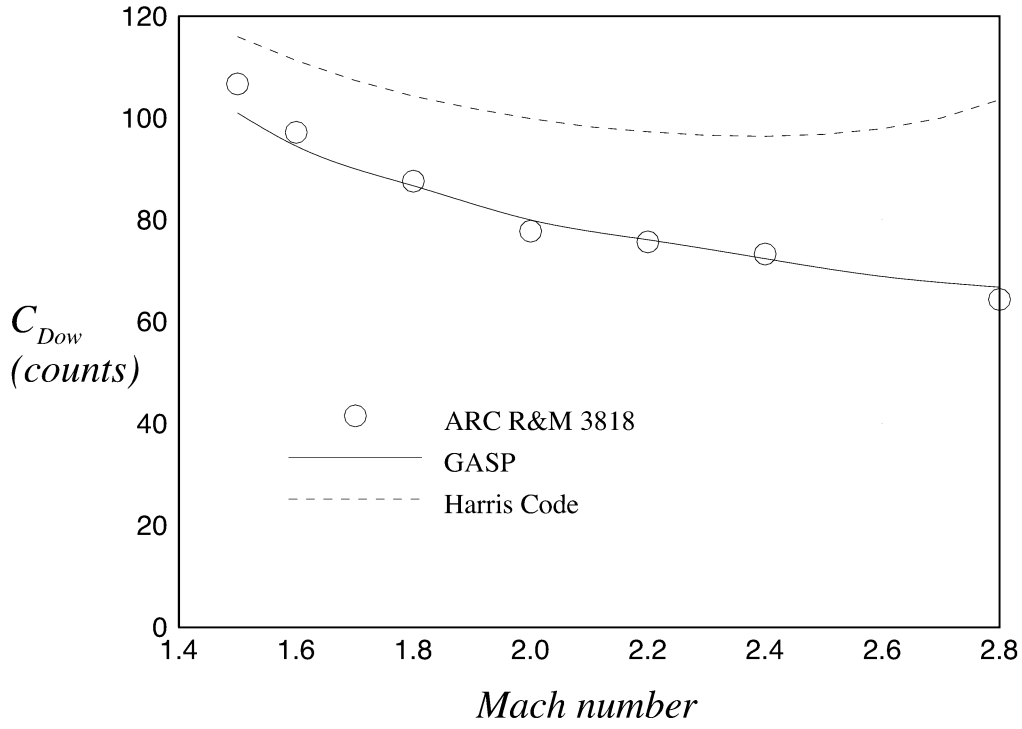


**Figure 3.10:** Squire Wing Wave Drag Coefficient.

## 3.3 High-Lift Maneuver Wing

The study will now focus on the force and moment predictions from linear supersonic theory and from GASP. A high-lift maneuver wing[64–66] with experimental force and moment data and pressure distributions is selected to assess the accuracy of the codes. The experimental pressures have previously been compared with predictions from linear theory and potential methods.[65] The high-lift wing (Fig. 3.11) is only slightly cambered in the streamwise sections, but it has pronounced spanwise cambering. Another feature of this wing is that, due to its design, inviscid flow conditions predominate on the upper surface. The wing was tested at Mach 1.62 and angles of attack, $\alpha$, ranging from 0° through 14°.

The grid convergence study (Fig. 3.12) reveals that a 77×51×77 mesh (*spanwise* ×*outward* ×*chordwise*) is sufficient for Euler computations on this wing. The solution on this mesh gave the drag coefficient within 1/2 count of the solution predicted by extrapolating to a mesh with an infinite number of cells. Calculations on this grid took about 12 minutes (0.0025 sec/cell) on an SGI *Power Challenge* R8000. A 77×91×77 grid is chosen for the PNS calculations from the grid convergence study in Figure 3.13. Computations for a single angle of attack on this grid took about 1.5 hours (0.010 sec/cell) on an SGI *Power Challenge* R8000 to converge. Using a hyperbolic tangent distribution to cluster the grid points normal to the body gives 40 cells in the boundary layer with the first cell well inside the laminar sublayer ($y^+ \approx 1.0$). Grid-converged results are therefore obtained with meshes having the same number of cells in the inviscid region for both the PNS and Euler grids.

Reducing the residual two orders of magnitude is found to be sufficient for both the parabolized Navier-Stokes and Euler computations on this wing. The calculations are started using a good solution on the initial marching plane, obtained from previous calculations on the wing. The results from the Euler and linear theory codes are adjusted to include an axial friction drag coefficient of 0.0069 to compare with the experimental data. This viscous correction was obtained by Pittman[66] *et al.* using the method in Ref. 67. This viscous term is assumed to be invariant with the angle-of-attack. Generally, the CFD results compare well with the experimental data. The PNS lift curve (Fig. 3.14) matches the experimental data nearly perfectly. The Euler results have the correct lift-curve slope, $C_{L_\alpha}$, but the zero-lift angle of attack is slightly off. There is a 7.5% overprediction in the linear theory $C_{L_\alpha}$.

The pitching moment is taken about the point $x = 16.701$, $y = 0.0$, $z = -0.275$, where the origin of the coordinate system is the wing apex. The pitching moment coefficients show the greatest discrepancy between the computational methods and experiment. While the Euler and PNS pitching moment results differ from the experimental data, they are significantly more accurate than the linear theory results. The same behaviors are seen in the pitching moment data in Ref. 66 computed using the full-potential code NCOREL.[63] The CFD and linear theory results predict a stronger nose-down tendency than does the experimental data. Some of these differences in the pitching moment can be attributed to flow separation from the trailing edge of the wing outboard of the crossflow shock at the larger values of $C_L$. Since the Euler equations are inviscid flow relations and the parabolized Navier-Stokes equations can not treat streamwise separation, these solutions give a more negative pitching moment than the experimental data. Linear theory predicts the incorrect sign for the zero-lift pitching moment coefficient as well.

The PNS drag coefficient results (Fig. 3.15) show slightly better agreement with experiment than do the Euler, but both outperform the linear theory results, especially at the larger angles of attack. PNS drag comparisons to the experimental data begin to degrade at an angle of attack around 8°. Oil flow visualizations presented in Ref. 64 reveal that this is the angle of attack at which the flow begins to separate from the tailing edge of the wing. Because linear theory overpredicts both the lift and drag coefficients at a given angle of attack for this wing, plotting the results on a drag polar (Fig. 3.16) gives better agreement with experiment. Euler and PNS results still outperform those from linear theory over most of the range of lift coefficients considered, but there is a region near $C_L = 0.35$ where the CFD and linear theory polars cross. This results in a small range of lift coefficients where the linear theory results are as accurate or more accurate than those from CFD. This phenomenon will be seen and discussed further in the studies of HSCT wings and wing-fuselage configurations.

The load distributions (Fig. 3.17) for this wing at 5.98° angle of attack show the CFD results matching well with experimental data. Euler and PNS solutions yield basically the same pressure distributions. The distributions computed from linear theory give the correct general shape, but do not capture the details as well. This is evident in the $x = 19.9$ curve where the peak and drop in $\Delta C_p$ near the leading edge are completely smoothed out. The loads (Fig. 3.18) for the wing at 12.91° angle of

attack show much more dramatic disagreement. Again both the Euler and PNS results do an excellent job predicting the load distribution. In particular, the CFD solutions capture the crossflow shock at this condition. The panel code does not capture the physics of the nonlinear flowfield, and the results are much worse than they were for the lower angle-of-attack cases. While giving good load predictions inboard of the crossflow shock location, linear theory underpredicts the load immediately outboard of this area. In addition, the leading-edge singularity produces a large peak in the leading-edge load which compares poorly to the experimental data and CFD results.

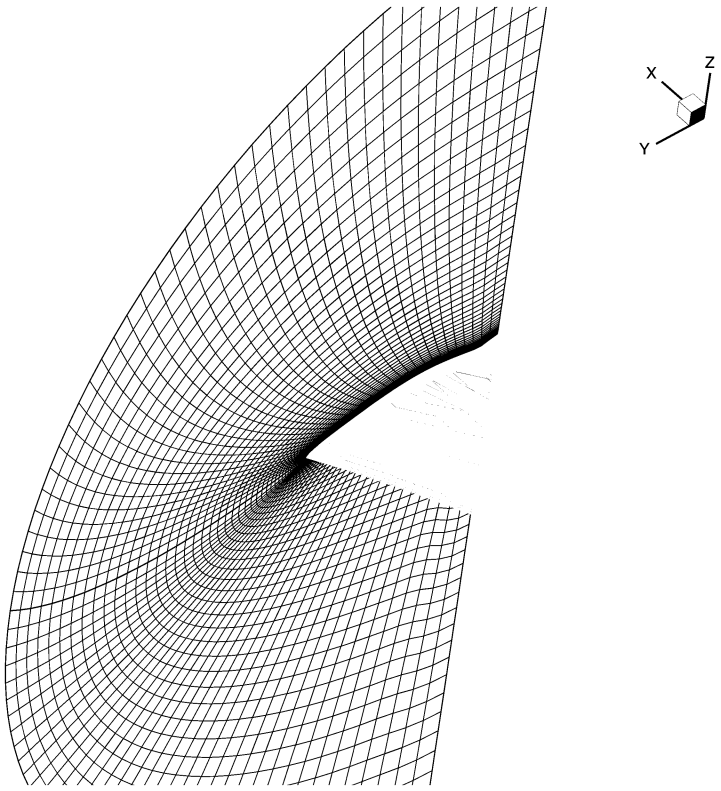


**Figure 3.11:** High-Lift Maneuver Wing with Grid Plane.

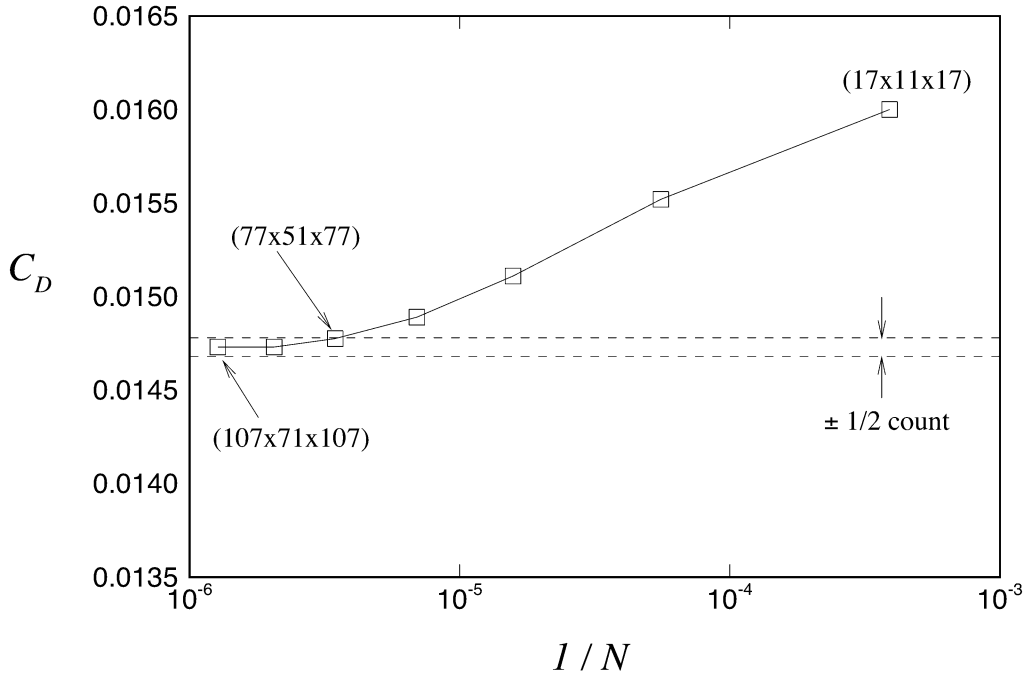


**Figure 3.12:** Euler Grid Convergence for Maneuver Wing.

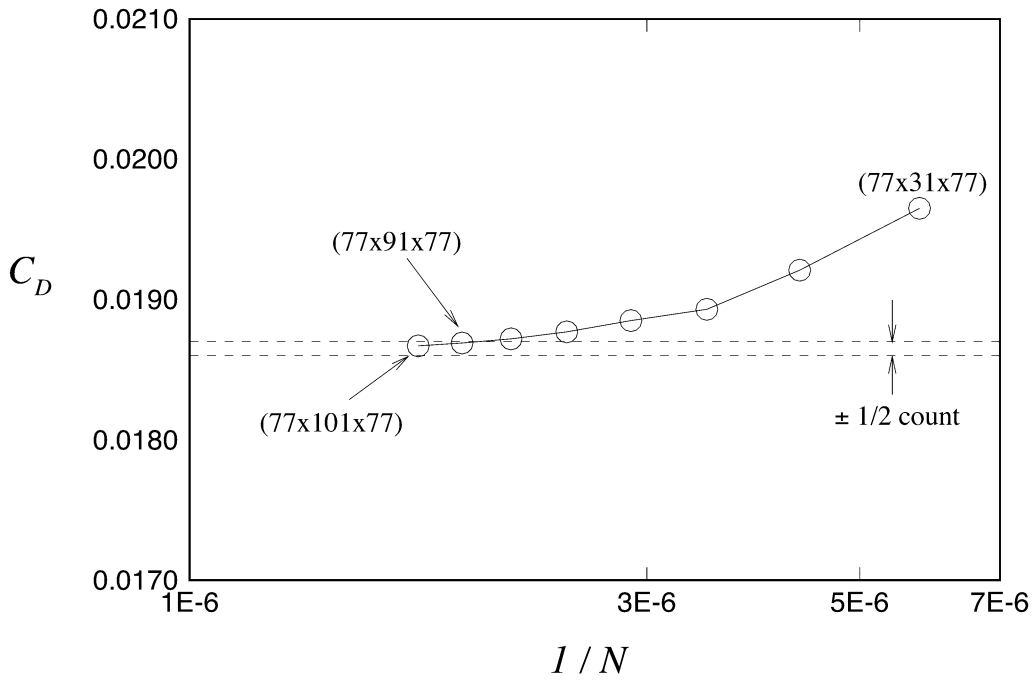


**Figure 3.13:** Parabolized Navier-Stokes Grid Convergence for Maneuver Wing.

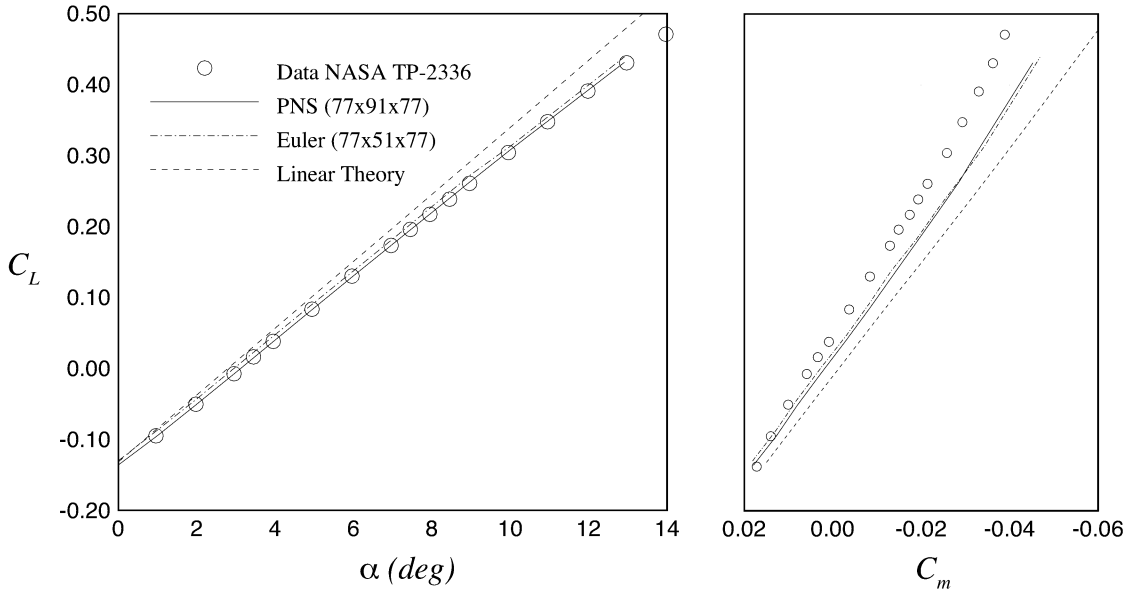


**Figure 3.14:** Maneuver Wing Lift and Pitching Moment Coefficients.

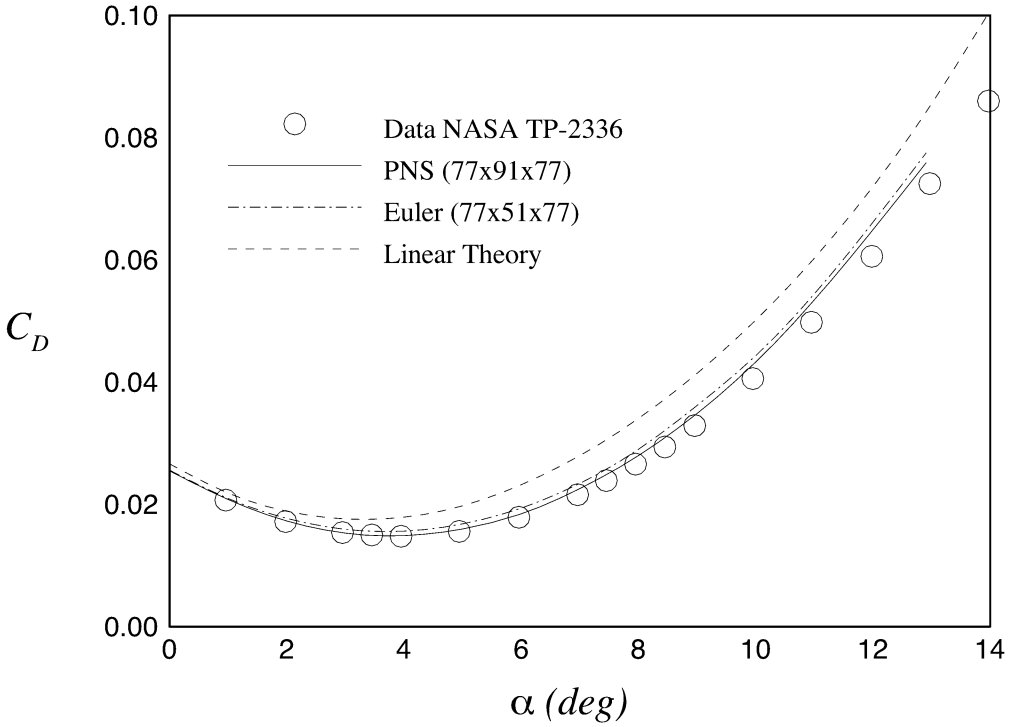


**Figure 3.15:** Maneuver Wing Drag Coefficients.

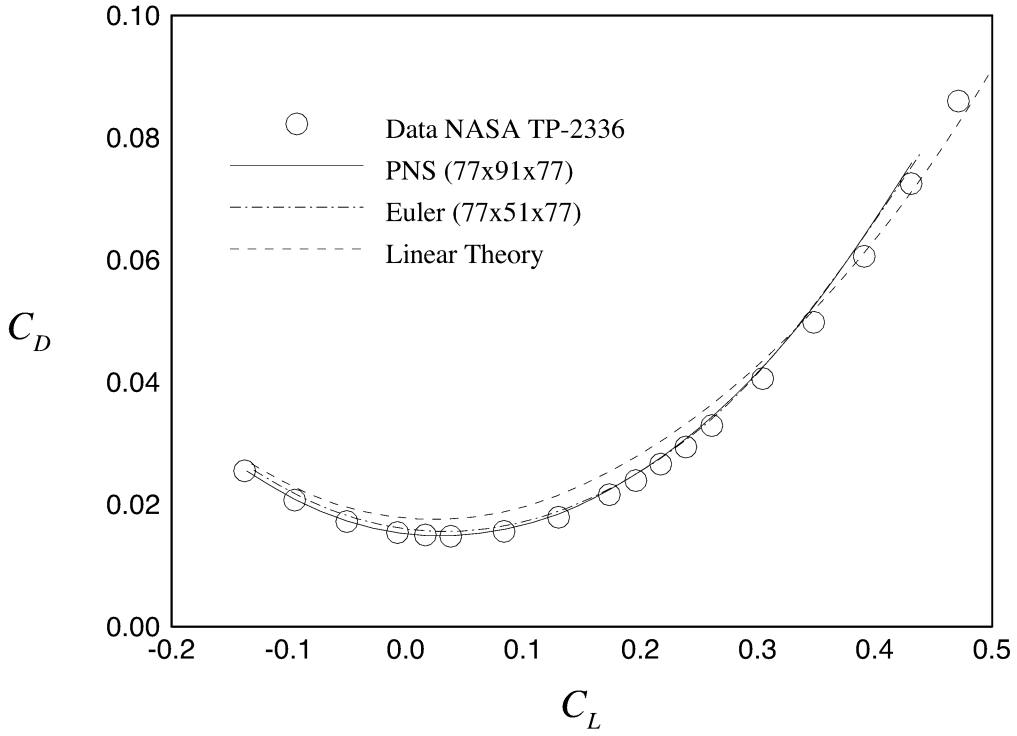


**Figure 3.16:** Maneuver Wing Drag Polar.

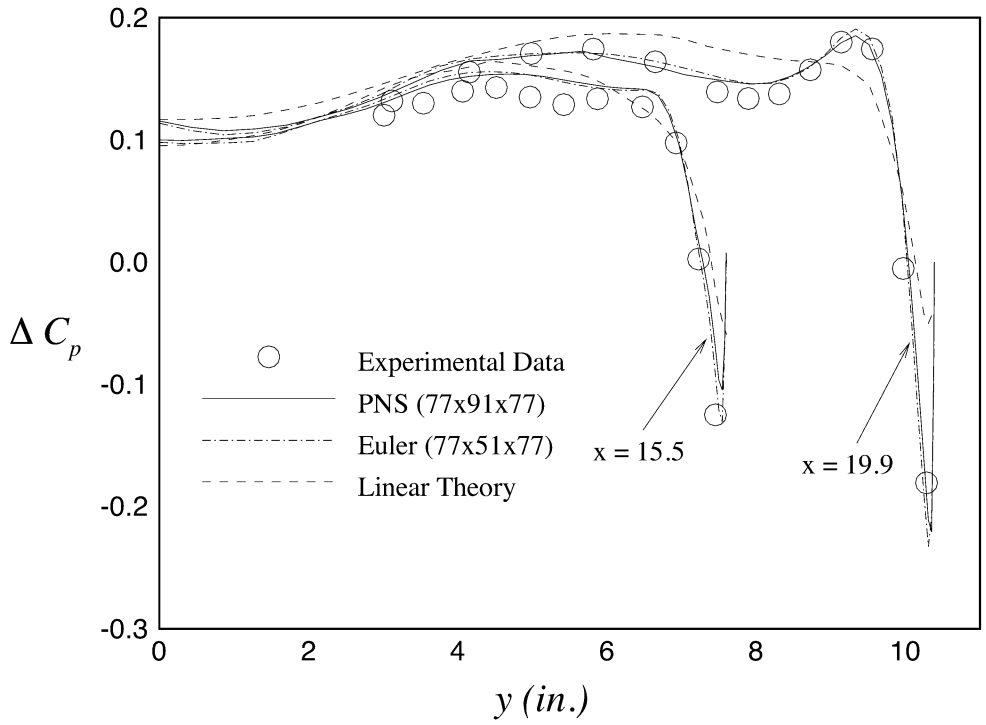


**Figure 3.17:** Maneuver Wing Load Distributions at $\alpha = 5.98°$.

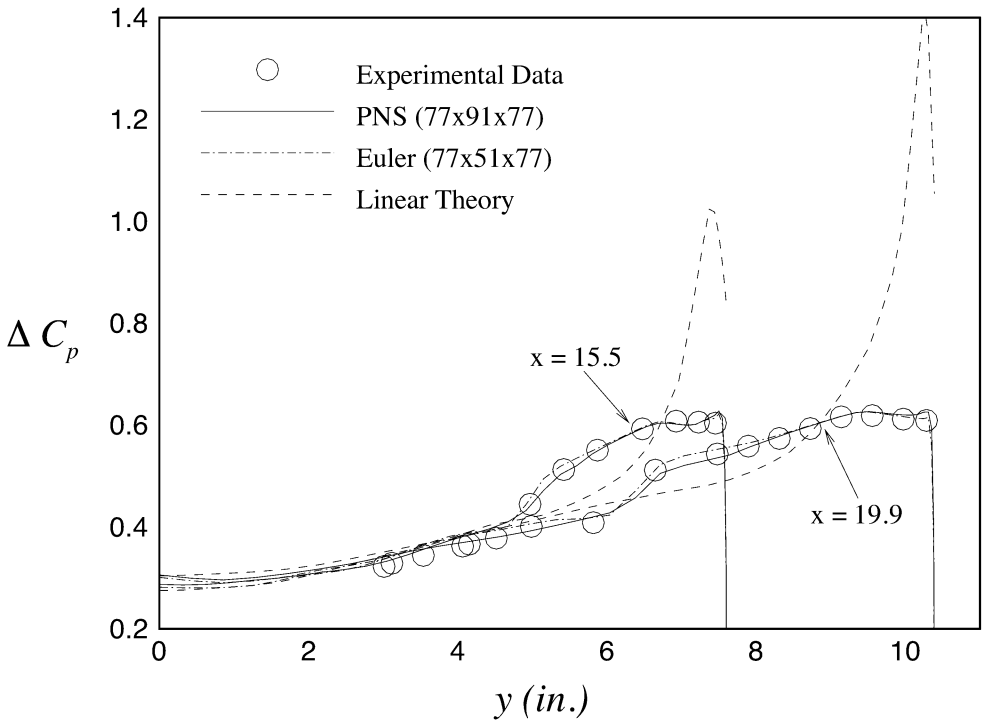


**Figure 3.18:** Maneuver Wing Load Distributions at $\alpha = 12.91°$.

# Chapter 4

# HSCT Design Studies

The previous sections indicate an opportunity to significantly improve the accuracy of our current aerodynamic predictions by supplementing linear supersonic theory results with Euler or parabolized Navier-Stokes solutions. In this chapter, differences in integrated force and moment predictions and variations in distributed loads between linear theory and CFD solutions are presented for three HSCT configurations. The sensitivity of the aircraft range to the predicted drag is determined from analysis. The effect of the loading differences on the wing bending stresses and the optimized wing bending-material weight is also presented.

## 4.1 Design Case 1

The first design considered (Fig. 4.1), which we will call Design Case 1, is a modified version of an early optimal design described in Ref. 34. The original wing planform has been altered so that there is no trailing edge sweep. This allows the grid generator to create a marching grid which models the wing trailing edge exactly. The design variables used to create this configuration are given in Table 4.1.

### Fuselage

The fuselage shape is shown in Figure 4.2. The plot shows the reduced area in the fuselage midsection, which simulates area ruling of wing-fuselage configurations.

In contrast to the Haack-Adams bodies studied earlier which have fineness ratios of 7 and 10, the HSCT fuselages are more slender with typical fineness ratios of $l/d_{max} = 25$. In addition, we have nondimensionalized the HSCT fuselage wave drag using the wing area instead of the maximum fuselage cross sectional area. These two factors result in much smaller differences between the Harris code and Euler predicted wave drag coefficients (Fig. 4.3) than were seen in the Haack-Adams study. The minimum difference between the Euler calculations on a 41×81 ($normal \times axial$) grid and Harris wave drag is approximately 0.8 counts of drag near Mach 2.0. The maximum difference in the Euler and Harris code predictions of the wave drag over the Mach number range studied is 2.0 counts.

## Uncambered Wing

We now investigate the forces and moments on the uncambered Design Case 1 wing at Mach 2.4 flight conditions. The integrated force and moment data reveal many of the same trends present in the maneuver wing results. Linear supersonic theory results show a 4.7% overprediction of the lift-curve slope (Fig. 4.4) with respect to the PNS value. The pitching moment coefficients taken about the quarter chord of the MAC show differences of about 0.006 at $C_L = 0.2$. The pitching moment curve shows significant curvature. The same behavior is seen in experimental and Euler analyses performed on the Mach 3 HSCT configuration presented in Refs. 4 and 5. The curvature in the pitching moment coefficient is related to movement in the aerodynamic center location with increasing lift. This is apparent in the basic relationship for the aerodynamic center location, $x_{a.c.}$:

$$x_{a.c.} = x_m - \bar{c}\left(\frac{\partial C_m}{\partial C_L}\right),$$

where $x_m$ is the reference point about which the pitching moment, $C_m$, is taken. Consider the following equation for the pitching moment:

$$C_m = C_{m_0} + C_N\left[\frac{x_m - x_{a.c.}}{\bar{c}}\right], \tag{4.1}$$

where $C_{m_0}$ is the zero-lift pitching moment and $C_N$ is the normal force coefficient. For an uncambered wing

$$C_{m_0} = 0 \quad \text{and} \quad C_N = \left(\frac{\partial C_N}{\partial C_L}\right)C_L.$$

Figure 4.5 shows the variation in the aerodynamic center with increasing lift coefficient. Because the wing is uncambered, the center of pressure and aerodynamic center locations are equivalent. The figure shows that the change in $x_{a.c.}$ is nearly linear. Using this assumption, an equation for the $x_{a.c.}$ in terms of $C_L$ can be written as:

$$x_{a.c.} = x_{a.c._0} + \left(\frac{\partial x_{a.c.}}{\partial C_L}\right) C_L,$$

where $x_{a.c._0}$ is the aerodynamic center location at zero lift. Substituting the relations for $C_{m_0}$, $C_N$, and $x_{a.c.}$ into Eqn. 4.1 gives the final equation for the pitching moment of an uncambered wing:

$$C_m = \left[\left(\frac{\partial C_N}{\partial C_L}\right)(x_m - x_{a.c._0})\,\frac{1}{\bar{c}}\right] C_L - \left[\left(\frac{\partial C_N}{\partial C_L}\right)\left(\frac{\partial x_{a.c.}}{\partial C_L}\right)\frac{1}{\bar{c}}\right] C_L^2. \tag{4.2}$$

The ratio of the quadratic to linear terms is

$$\frac{\textit{quadratic term}}{\textit{linear term}} = \frac{\left(\dfrac{\partial x_{a.c.}}{\partial C_L}\right)}{x_m - x_{a.c._0}}$$

For this wing, the ratio is 2.6 which explains why the pitching moment coefficient plot shows noticeable curvature. When the distance between the aerodynamic center and moment reference point is much larger than the change in the aerodynamic center location, the moment is lift-driven and behaves linearly; however, when this is not the case, the movement in the aerodynamic center produces curvature in the pitching moment curve. For this wing, the aerodynamic center travels from 53.3% of the root chord, $c_{root}$, at $C_L = 0.0$ to 52.7% at $C_L = 0.2$. The aerodynamic center locations are based on the root chord to present the results in a consistent manner with those in Ref. 68. The aerodynamic center locations for this wing are close to those presented in Ref. 68 for a similar family of diamond shaped wings. The quarter-chord of the MAC for this wing lies between the linear theory and CFD aerodynamic center locations. The Euler and PNS $x_{a.c.}$ are located about $3.5\,ft$ aft of that from linear theory, resulting in a more negative pitching moment. This is a different trend than is seen in the maneuver wing studies and in studies of other HSCT configurations by Pittman[4] *et al.* and by Hollenback and Blom.[3]

Figure 4.6 shows good agreement between the PNS drag and the Euler drag predictions with algebraic skin friction corrections. As expected, the Harris wave drag results on this nominally 2.5% thick wing show closer agreement than those for the

9.0% thick Squire wing. At Mach 2.4, the slender-body theory prediction for the zero-lift wave drag, $C_{D_{OW}}$, is 1.4 counts higher than that calculated using CFD. The algebraic skin friction estimate predicts a viscous drag coefficient of 0.00290. This is 0.9 counts higher than the PNS prediction of 0.00281 at zero angle-of-attack. For this wing, the simple skin friction estimate gives a viscous drag value within 3.2% of the PNS value. Linear supersonic theory overestimates the zero lift drag for this wing, but underestimates the induced drag. This is evident because the linear theory drag polar crosses the CFD drag polars, resulting in good comparisons at the cruise $C_L$ of 0.070. This behavior is similar to that seen in the maneuver wing drag polar (Fig. 3.16), but it is more significant since the cross-over occurs near the cruise $C_L$. The linear theory estimate is only 0.6 counts higher than the PNS result. The differences in the drag coefficient estimates become much worse at larger values of the lift coefficient.

On a single 75 MHz IP21 processor of an SGI *Power Challenge* R8000, the PNS computations take 1.5 hours (0.010 sec/cell) to converge. On the same machine, the Euler calculations approximately 12 minutes (0.0025 sec/cell), while the linear supersonic theory results take only two seconds. These times are typical for all of the wing only computations performed for this study.

## Cambered Wing

The optimal camber for our HSCT designs is determined using the linear theory code WINGDES.[44] WINGDES attempts to find the camber distribution along the wing which minimizes the drag-due-to-lift. Two runs of WINGDES per wing were required to get the proper camber distribution. The second run served to smooth the camber distribution and provide the maximum leading-edge suction parameter closer to the design lift coefficient.

The lift, pitching moment, and drag coefficient results for the Design Case 1 cambered wing configuration are given in Figures 4.7 and 4.8. Linear theory again overpredicts $C_L$ and $C_m$, and there is an additional error in these quantities at zero angle-of-attack due to the wing camber. The errors in the pitching moment are not surprising in light of the large differences in the load distributions seen in the maneuver wing of Section 3.3. The loads for the Design Case 1 configuration are presented later

in this Section. The curvature in the pitching moment due to movement in the aerodynamic center location is still present. The linear theory drag is fairly accurate at the lower lift values. The cambering of the wing did result in a reduction of the drag at cruise. From linear theory analysis, the drag coefficient for the cambered wing is 1.8 counts lower than for the uncambered wing. The improvement is not quite as good when the drag coefficient is computed using the Euler and PNS equations. PNS solutions show a 0.9 count reduction, and Euler results show a 0.6 count reduction in the cruise drag. The algebraic skin friction estimate is 0.7 counts higher than the PNS viscous drag value. For the Design Case 1 cambered wing, the difference between the linear theory and PNS predicted cruise drag coefficients is 0.3 counts. At this condition, the overestimate of the zero-lift drag is almost completely cancelled by the underestimate in the induced drag.

## Wing-Fuselage Configuration

Force and moment predictions from CFD on the cambered wing-fuselage configuration are now compared with those from linear supersonic theory. Another grid convergence study is performed to ensure a converged PNS solution. Figure 4.9 shows the convergence of the drag coefficient with mesh for the body in a Mach 2.4 flow at 4° angle of attack. A 91×91×91 (*spanwise* ×*outward* ×*chordwise*) grid gives the drag coefficient within 1/2 count of the solution extrapolated to zero mesh spacing. Boundary layer profiles (Fig. 4.10) on the wing and fuselage show that there are 3–4 cells in the laminar sublayer with the first cell center having $y^+$<1.0. The definition of this nondimensional distance from the body surface is

$$y^+ \equiv \frac{y u_*}{\nu}, \tag{4.3}$$

where $y$ is the distance to the surface of the body, $u_*$ is the friction velocity defined as $u_* = \sqrt{\tau_w/\rho}$, $\tau_w$ is the wall shear, $\rho$ is the fluid density, and $\nu$ is the kinematic viscosity.

Solutions on this mesh took approximately 2 hours (0.099 sec/cell) on the SGI *Power Challenge* R8000. Comparing this wing-fuselage grid with that required for converged wing PNS calculations, we find that additional spanwise and lengthwise points are required to properly resolve the fuselage, while the number of points normal to the body remains the same. Since the grid convergence studies for the maneuver

wing (Section 3.3) show that reducing the number of cells in the normal direction from the grid for converged PNS calculations by 40 gives a grid suitable for converged Euler results, a 91×51×91 grid is chosen for the wing-fuselage Euler calculations without an additional grid convergence investigation. Computations on this mesh required about 16 minutes (0.0024 sec/cell) of CPU time.

The linear theory drag-due-to-lift code does not handle a fuselage. The wing is simply extended to the fuselage centerline, as it is for the wing studies. For this reason, the effects of adding the fuselage will only be seen in the wave drag and skin friction components of our linear supersonic theory drag. The lift-curve slope (Fig. 4.11) for the wing-fuselage configuration shows worse agreement between linear theory and CFD than is seen in the wing studies. Our linear theory code does not predict the drop in $C_{L_\alpha}$ due to the presence of the fuselage. The pitching moment differences remain about the same as in the wing studies. The drag polar (Fig. 4.12) also shows larger discrepancies than were previously seen. At cruise, the difference between the linear supersonic theory drag coefficient and that from PNS is 1.3 counts. The algebraic skin friction estimate is only 0.4 counts higher than the PNS viscous drag. Unlike the wing studies, the zero-lift drag predicted from linear theory is lower than that from CFD. This causes the errors in the zero-lift and induced drag components to add to instead of subtract from each other at cruise.

The effect of the 1.3 count difference in drag predictions between linear theory and CFD on HSCT performance is assessed for this wing. While linear supersonic theory predicts the cruise drag within 2.0% of the PNS value, the small differences present have a large effect on the aircraft range. The increase in range resulting from a 1.3 count underprediction in the drag predicted from linear theory is 73 $n.mi.$ This corresponds to a sensitivity for this design of 56 $n.mi.$ per drag count.

## Loads and Structural Optimization

We now shift our attention from the integrated forces and moments to the distributed loads predicted from linear theory and Euler calculations. Loads from parabolized Navier-Stokes calculations are not presented since we found little difference between the pressure fields from our viscous and inviscid analyses. In the multidisciplinary design optimization, the constraints for the structural optimization are evaluated

at a number of load cases including taxi, transonic climb, low-speed cruise, high-speed cruise, and high-speed pull-up. For this study we will concentrate on three supersonic loads cases: Mach 2.4 cruise, 2.5-g pull-up at Mach 2.4, and Mach 1.2 cruise. Structural analyses performed by Dr. Vladimir Balabanov reveal the effects of differences in the loads on the Von Mises equivalent stresses at these three load conditions. He then performed structural optimizations using the supersonic loads from Euler solutions and from linear theory analyses to determine the sensitivity of the wing bending material weight to the accuracy of the predicted loads.

The loads computed from linear theory and Euler calculations on wing and wing-fuselage configurations are presented for comparison. Cruise at Mach 2.4 for Design Case 1 is achieved with a lift coefficient of 0.070. The loads at this condition (Fig. 4.13) show good agreement over most of the wing. Little variation is seen between the wing and wing-fuselage loads. There is a slight peak in the linear theory loads at the wing trailing-edge cut, but this is a difference of only about 0.02 in $\Delta C_P$.

The wing model used for the structural optimization (Figure 4.14) is described in Balabanov[21] *et al.* Figure 4.15 shows contours of the difference in wing bending stress computed from Euler and linear theory loads using the GENESIS finite-element code. The difference in stresses is negative over most of the wing, indicating that the stresses computed from Euler loads are lower. The largest magnitude difference in stress occurs on the lower wing surface in a region inboard of the leading-edge break. The value of this maximum stress difference (Table 4.2) is $-1971$ *psi*, which represents 37.0% of the nominal value. The variation in the maximum stress is lower at $-1729$ *psi* (23.6%), but is still high considering the agreement in the loads. Searching for explanations to this relatively large discrepancy led us to look at the predicted center of pressure location. The spanwise location of the center of pressure calculated from Euler analysis is $1.53\,ft$ inboard of that computed from linear theory on a wing with a semispan of $75.9\,ft$. This gives insight into why the Euler loads result in a wing with lower bending stress values. The sensitivity of the stresses to the predicted loads comes from the large amounts of fuel stored in the wings of our HSCT designs. Inertial relief from the fuel weight cancels much of the wing bending due to aerodynamic loading. This causes the wing bending stresses to become very sensitive to small changes in the loading and the spanwise location of the center of pressure.

The Mach 1.2 cruise load condition is examined next. Cruise at this Mach number

is obtained with a lift coefficient of 0.071. The Euler solution to the wing-fuselage configuration at Mach 1.2 cruise could not converge. The reason for this failure is the semivertex angle of the fuselage nose. For a free stream Mach number of 1.2, the limiting cone semivertex angle which retains supersonic flow after the shock is 14.1°. For comparison, at Mach 2.4 this maximum angle is 41.5°. This particular fuselage has a semivertex angle of 24°, which is not only larger than the maximum angle for supersonic flow after the shock, but it is also larger than the limiting deflection angle for an attached shock. This illustrates an important physical limitation of using a space marching approach to CFD solutions on our HSCT designs. The wing Euler calculations were successful, and the results (Fig. 4.16) compare well with those from linear theory. As with the Mach 2.4 cruise condition, the loads near the trailing edge show the poorest agreement.

The stress comparisons (Fig. 4.17) for the Mach 1.2 cruise condition show that, overall, the stresses computed from Euler loads are lower than those from linear theory loads. The value of the maximum stress difference (Table 4.2) is $-2710$ $psi$ which represents 17.3% of the stress value for that element, while the variation in the maximum stress is only $-641$ $psi$ (2.6%). The maximum stress occurs near the leading edge break. The spanwise center of pressure location from Euler analysis is 1.34 $ft$ inboard of that from linear theory.

The Mach 2.4 2.5-g pull-up case ($C_L = 0.154$) gives much more dramatic differences in the loading. The Euler solution (Fig. 4.18) on the wing and wing-fuselage case reveals the formation of a shock on the upper wing surface. Linear theory loads match well inboard of the shock, but underpredict the load immediately outboard of it. Linear theory also overpredicts the leading edge suction peak along the entire subsonic leading-edge. The subsonic leading edge is that portion ahead of the leading-edge break in which the component of the Mach number normal to the leading edge is subsonic. Similar behavior in the loads is evident in the high angle-of-attack loads for the maneuver wing in Section 3.3. After the wing break, the leading-edge loads predicted from linear theory match better with those from the Euler solutions; however, the peak caused by the error along the subsonic leading edge propagates and results in the peak seen at the aft-most wing station.

The effects of the differences in aerodynamic loading can be seen in the structural analysis of the aircraft. As expected, we find that the largest magnitude difference

in stresses (Table 4.2) computed from linear theory and Euler loads occurs for the Mach 2.4 2.5-g pull-up condition. The maximum difference in predicted stresses is $-8745$ *psi*, and the variation in the maximum stress is $-8543$ *psi*. The maximum stress again occurs near the wing leading edge break. As with the previous two cases, the spanwise location center of pressure is farther inboard for the Euler loads. The stresses (Fig. 4.19) from Euler loads are larger over the small outboard section of the wing; however, over the remainder of the wing they are lower than the stresses found from linear theory loads. As with the other two load cases, the maximum difference in stresses occurs near the middle of the wing. While the regions aft of the leading-edge break show large variations in the aerodynamic loading from Euler and linear theory results, they also have inertial loading from the nacelles. These inertial effects appear to explain why the maximum difference in stress does not occur farther aft on the wing.

The overall effect of these differences on the structural optimization, using the GENESIS finite-element code as described by Balabanov[21] *et al.*, is an optimal design whose wing bending-material weight is 5.6% lighter by using the Euler loads instead of the linear theory loads. The magnitude of the difference in bending-material weight is 1181 *lb*. The lower stress values from using Euler loads have resulted in a lighter wing. However, in spite of the difference in loads for the Mach 2.4 2.5-g pull-up and the relatively large variations in stresses for all load cases, the optimized wing-bending material weight only shows a small change.

**Table 4.1:** Design Variable Values (Design Case 1).

| DV | Value | Description |
|---|---|---|
| 1 | 181.00 | Wing Root Chord ($ft.$) |
| 2 | 156.00 | L.E. Break, x ($ft.$) |
| 3 | 49.20 | L.E. Break, y ($ft.$) |
| 4 | 181.00 | T.E. Break, x ($ft.$) |
| 5 | 64.00 | T.E. Break, y ($ft.$) |
| 6 | 170.00 | L.E. Wing Tip, x ($ft.$) |
| 7 | 11.00 | Wing Tip Chord ($ft.$) |
| 8 | 75.90 | Wing Semispan ($ft.$) |
| 9 | 0.4019 | x-Loc. Airfoil Max. t/c ($x/c$) |
| 10 | 3.6921 | L.E. Radius Parameter |
| 11 | 2.5789 | t/c at Wing Root ($\%c$) |
| 12 | 2.1594 | t/c at L.E. Break ($\%c$) |
| 13 | 1.8039 | t/c at Wing Tip ($\%c$) |
| 14 | 2.196 | Fuselage X-Restraint #1 |
| 15 | 1.0610 | Fuselage R-Restraint #1 |
| 16 | 12.200 | Fuselage X-Restraint #2 |
| 17 | 3.4961 | Fuselage R-Restraint #2 |
| 18 | 132.463 | Fuselage X-Restraint #3 |
| 19 | 5.3410 | Fuselage R-Restraint #3 |
| 20 | 248.668 | Fuselage X-Restraint #4 |
| 21 | 4.6661 | Fuselage R-Restraint #4 |

**Table 4.2:** Structural Analysis and Optimization Results (Design Case 1).

| Load Case | $(\Delta\sigma)_{\max}$ | | $\Delta(\sigma_{\max})$ | | $\Delta y_{\text{c.p.}}$ | $\frac{W_{\text{S/O-Euler}}}{W_{\text{S/O-LT}}}$ |
|---|---|---|---|---|---|---|
| | *psi* | % | *psi* | % | *ft* | |
| M=2.4 n=1.0 | −1971 | (37.0%) | −1729 | (23.6%) | −1.528 | |
| M=1.2 n=1.0 | −2710 | (17.3%) | −641 | (2.6%) | −1.342 | 0.944 |
| M=2.4 n=2.5 | −4696 | (25.5%) | −4341 | (16.7%) | −1.218 | |

(Results courtesy of Dr. Vladimir Balabanov)

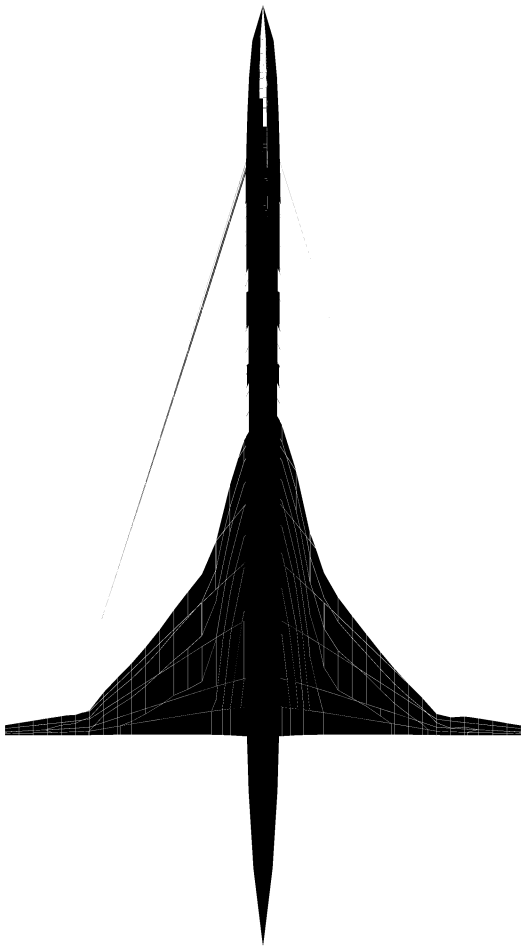

**Figure 4.1:** Configuration Planform View (Design Case 1).

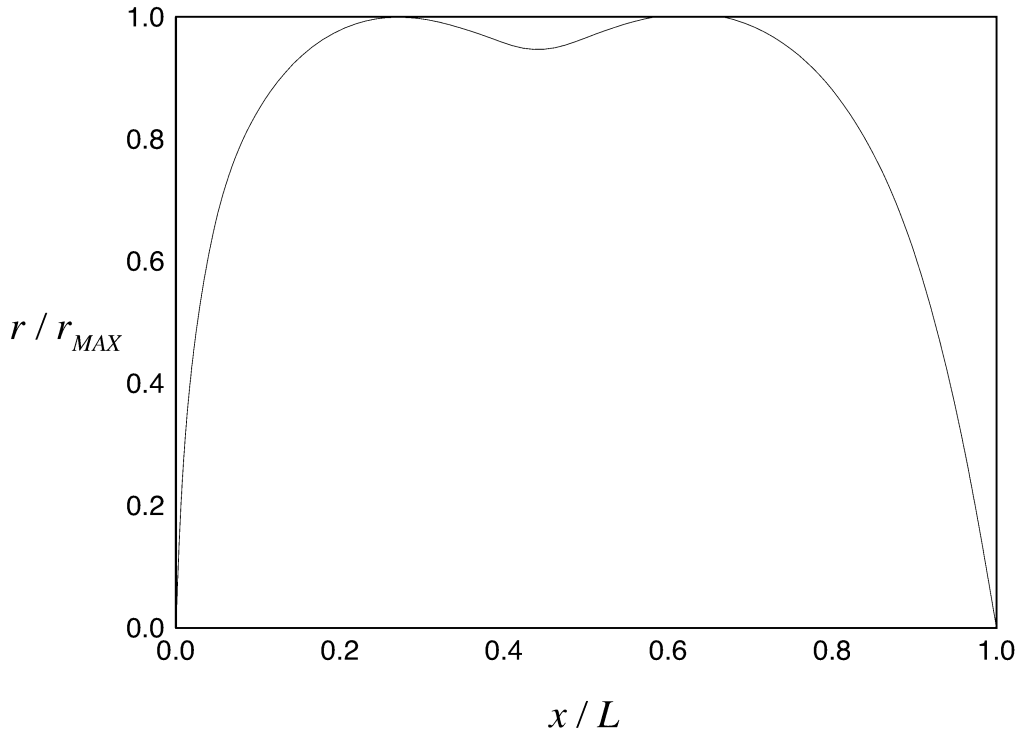


**Figure 4.2:** Fuselage Description (Design Case 1).

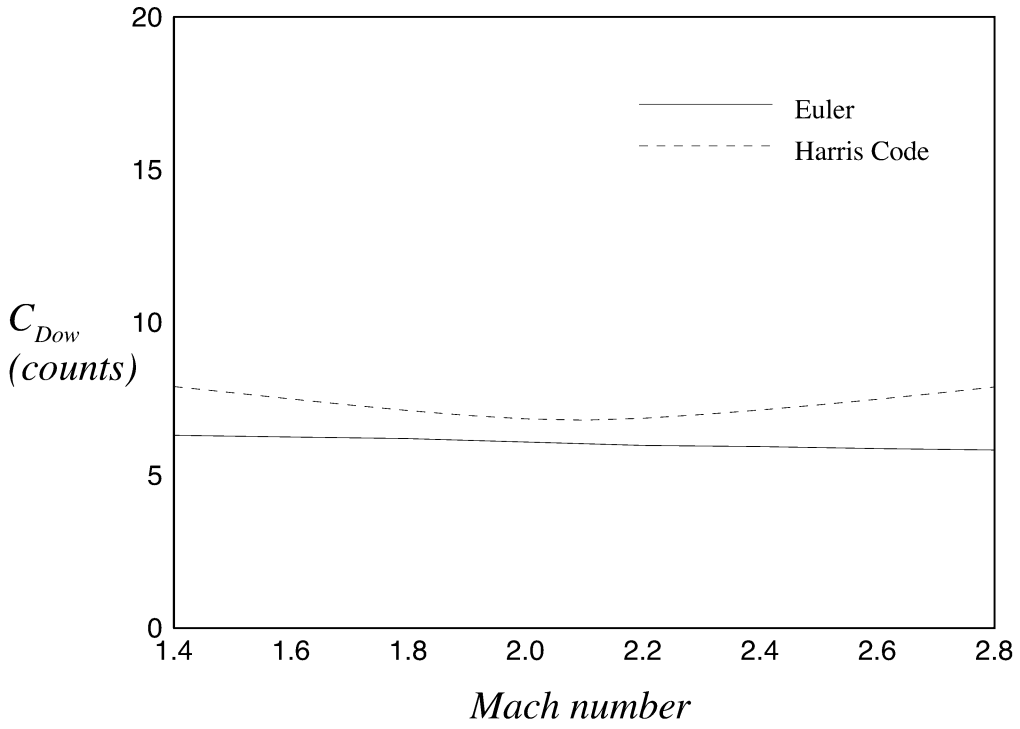


**Figure 4.3:** Fuselage Wave Drag Coefficient (Design Case 1).

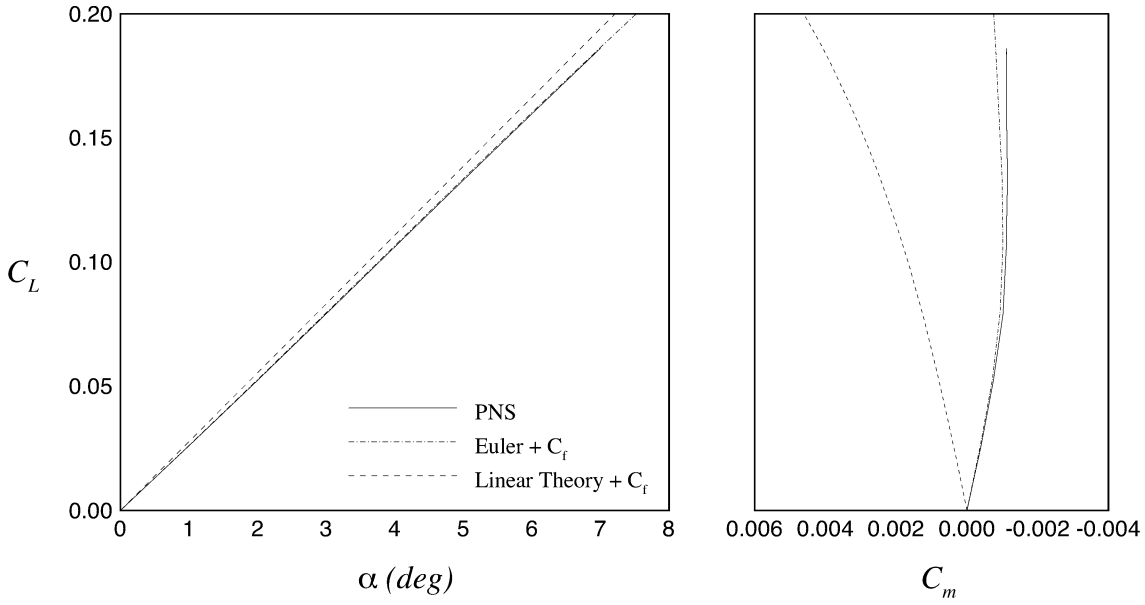


**Figure 4.4:** Lift and Pitching Moment Coefficients for Uncambered Wing (Design Case 1).

[Moments are taken about the quarter chord of the MAC.]

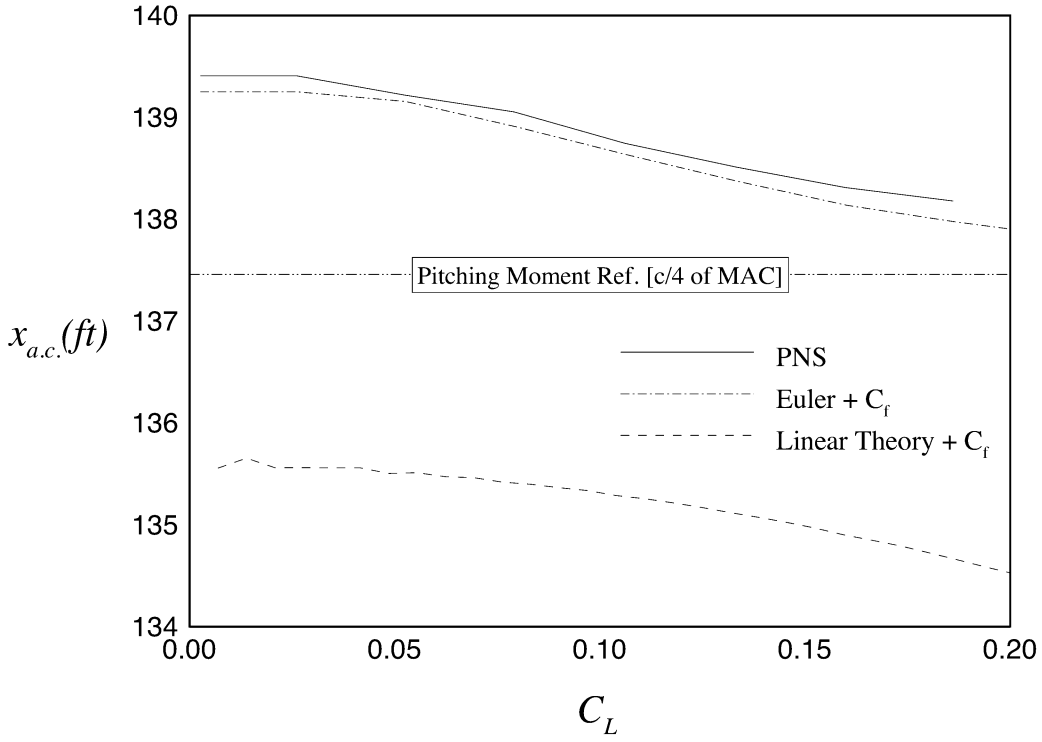


**Figure 4.5:** Change in Center of Pressure Location with Lift Coefficient.

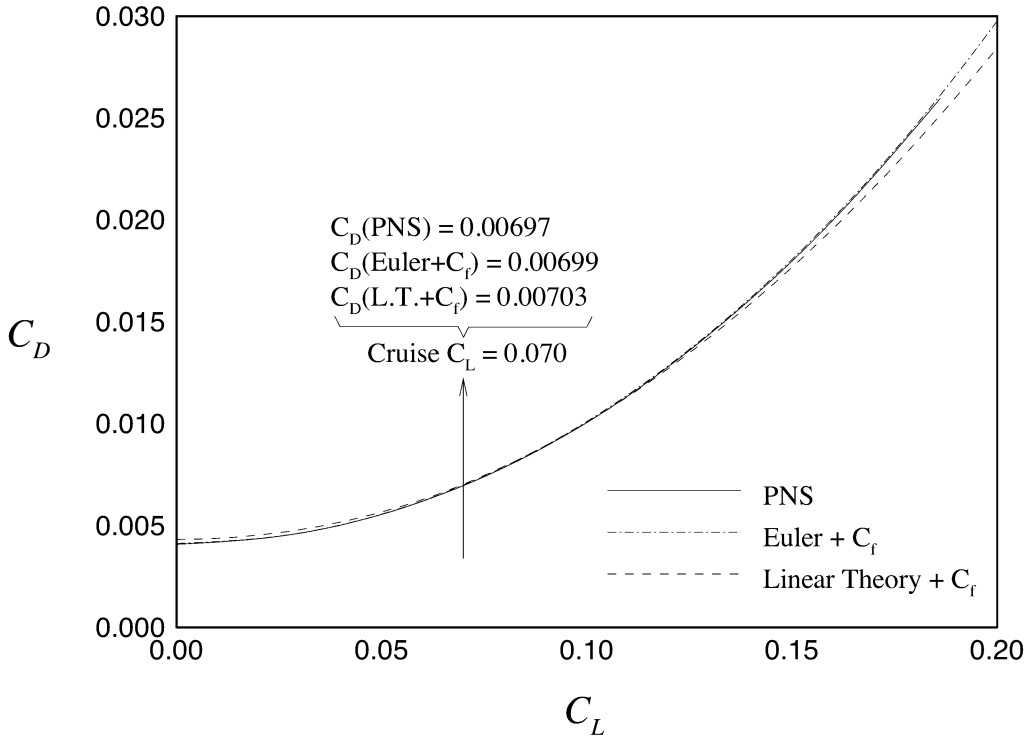


**Figure 4.6:** Drag Polar for Uncambered Wing (Design Case 1).

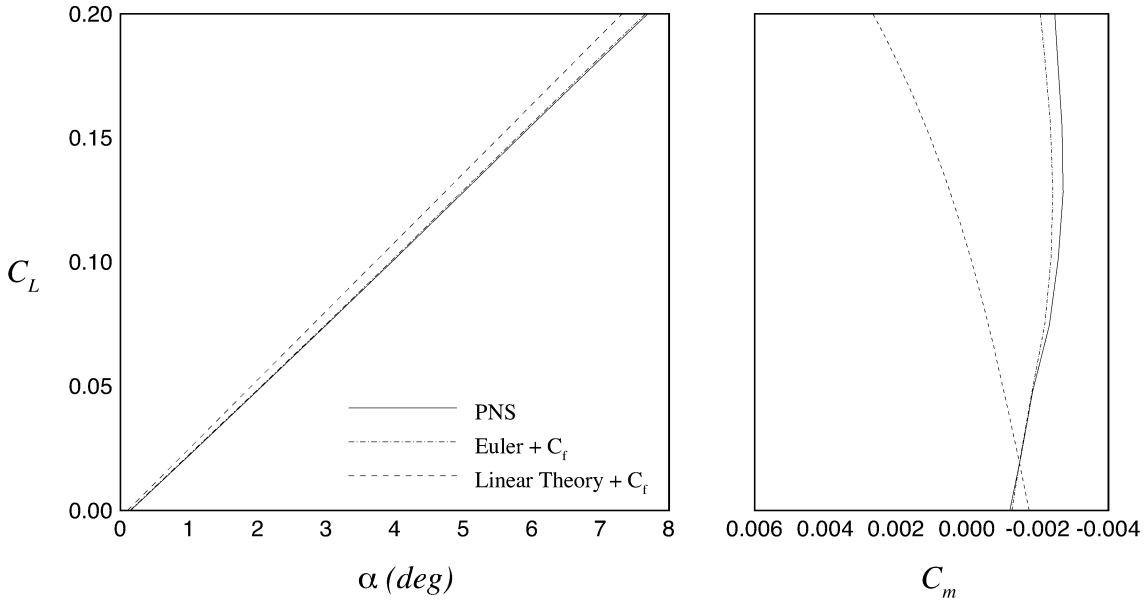


**Figure 4.7:** Lift and Pitching Moment Coefficients for Cambered Wing (Design Case 1).

[Moments are taken about the quarter chord of the MAC.]

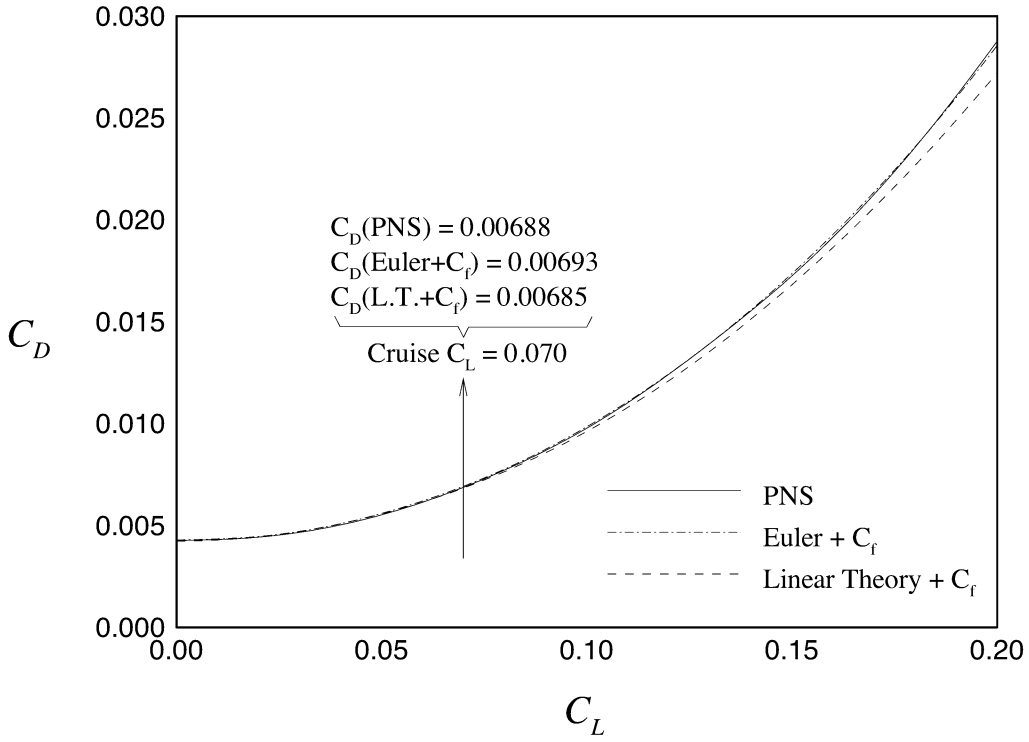


**Figure 4.8:** Drag Polar for Cambered Wing (Design Case 1).

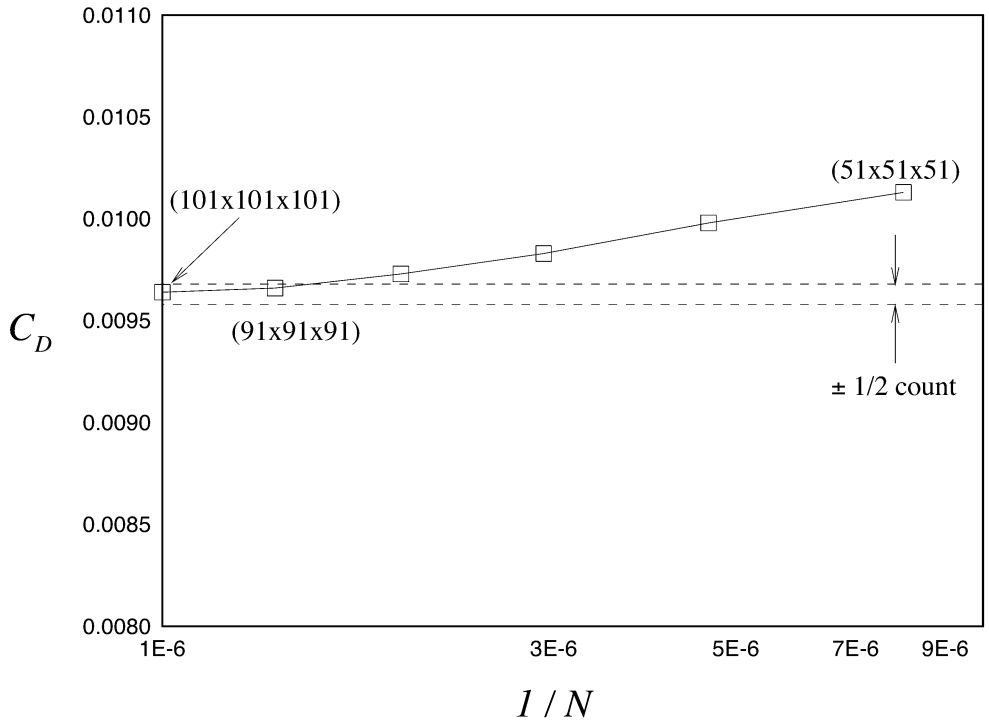


**Figure 4.9:** Parabolized Navier-Stokes Grid Convergence for Wing-Fuselage Configuration.

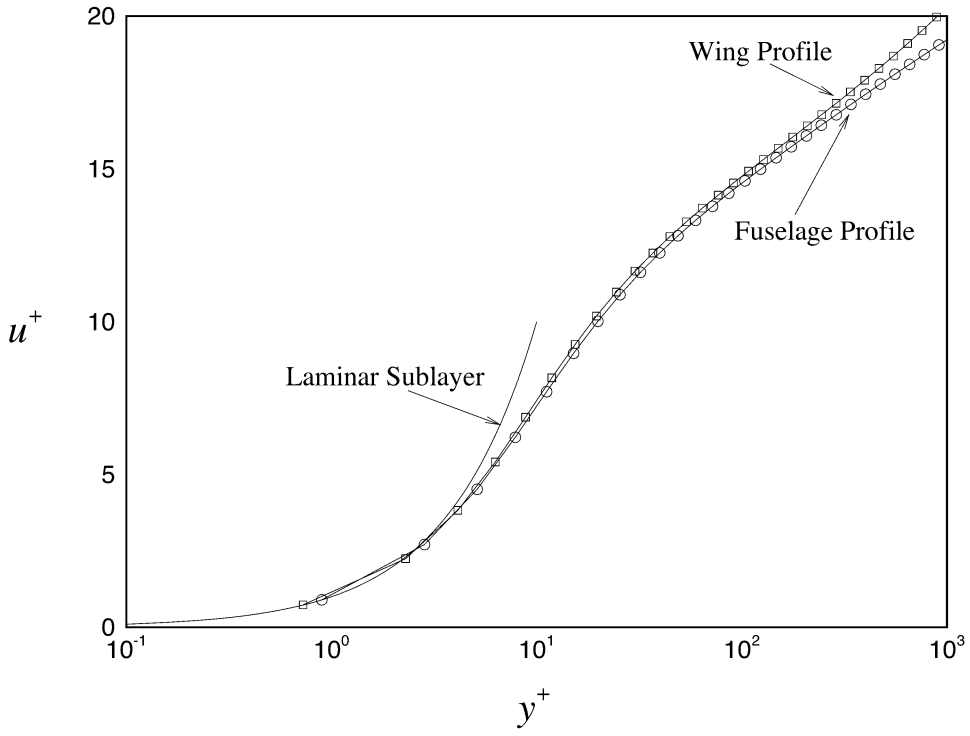


**Figure 4.10:** Boundary Layer Profiles.

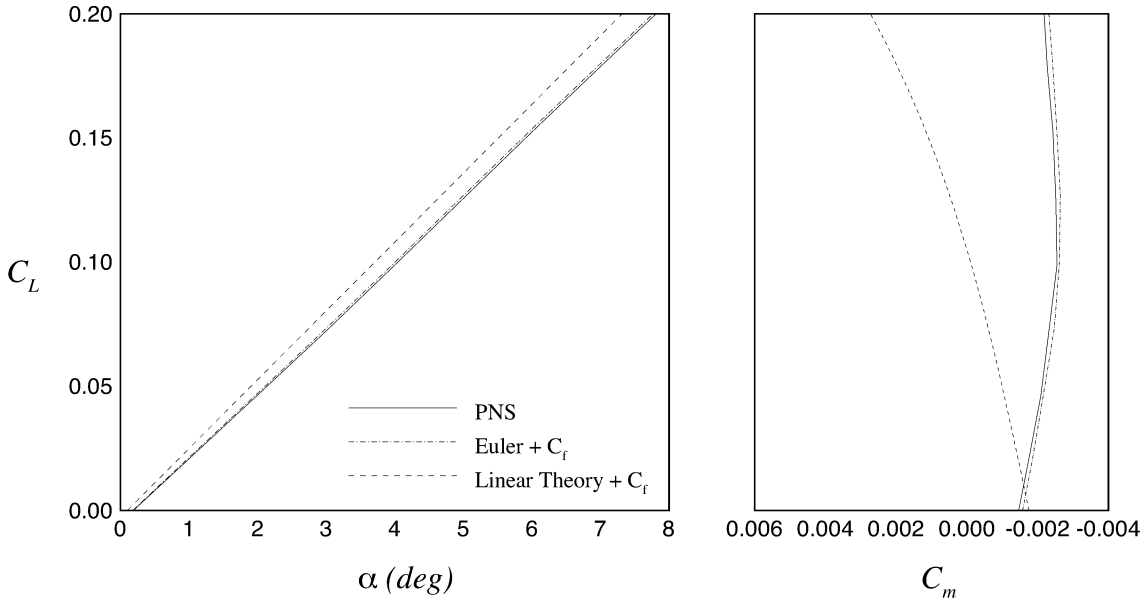


**Figure 4.11:** Lift and Pitching Moment Coefficients for Wing-Fuselage Configuration (Design Case 1).

[Moments are taken about the quarter chord of the MAC.]

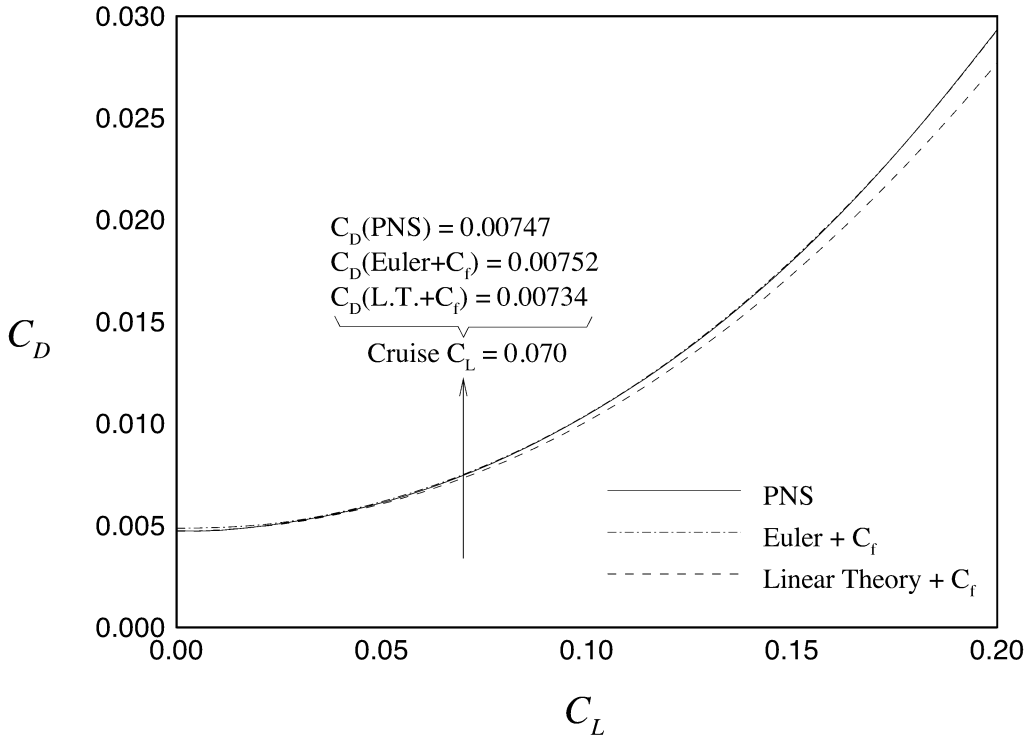


**Figure 4.12:** Drag Polar for Wing-Fuselage Configuration (Design Case 1).

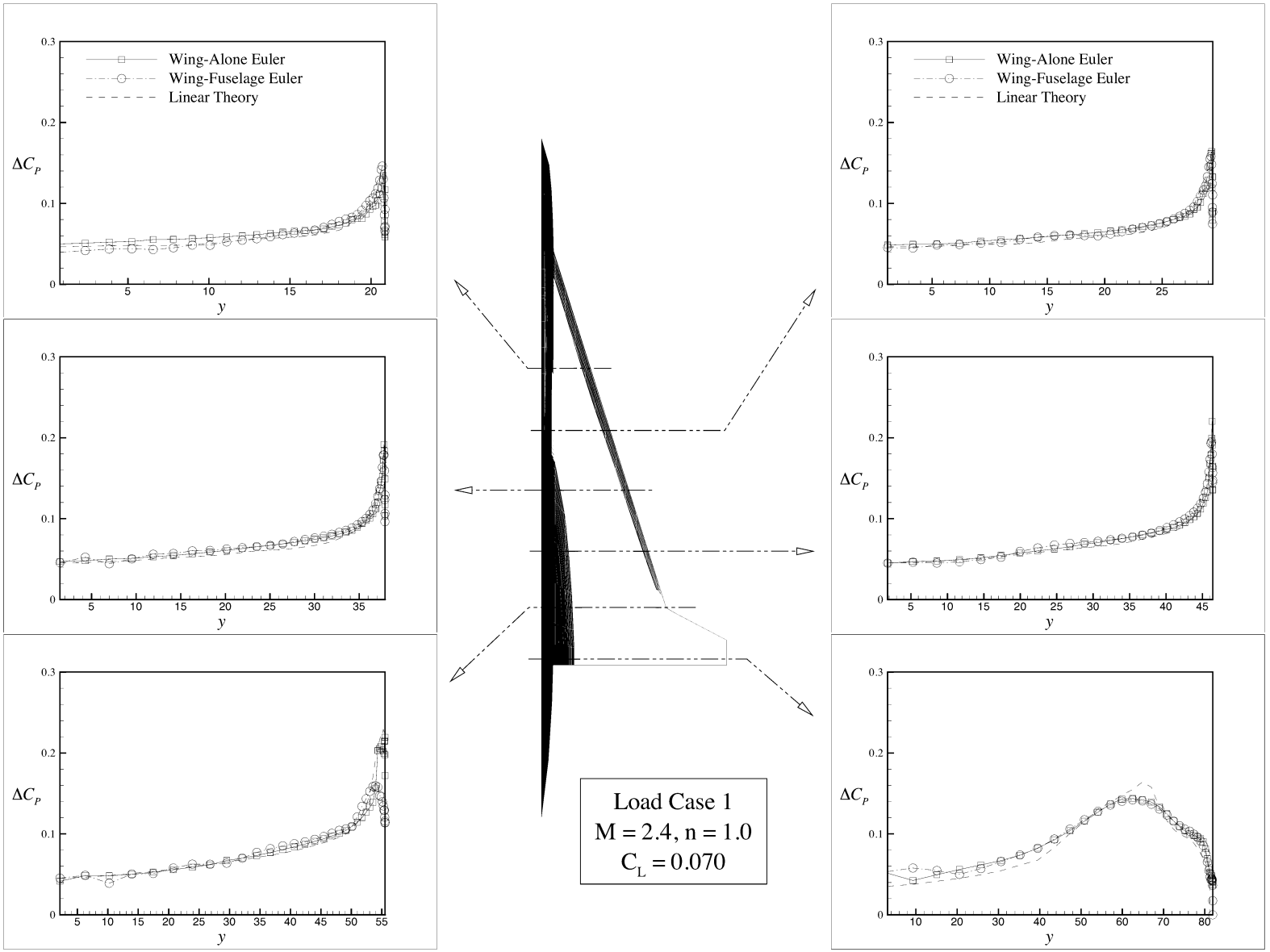


**Figure 4.13:** Aerodynamic Loads at Mach 2.4 Cruise (Design Case 1).

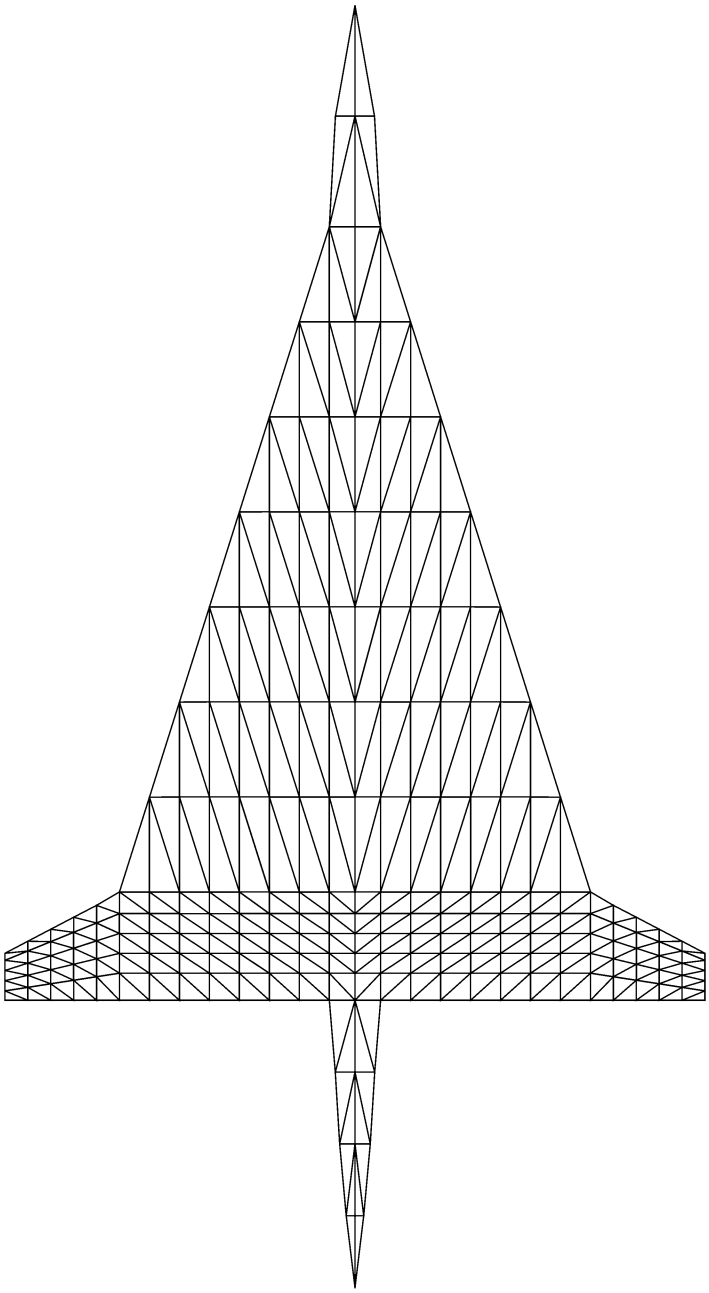

**Figure 4.14:** Structural Mesh for Design Case 1.
(Courtesy of Dr. Vladimir Balabanov)

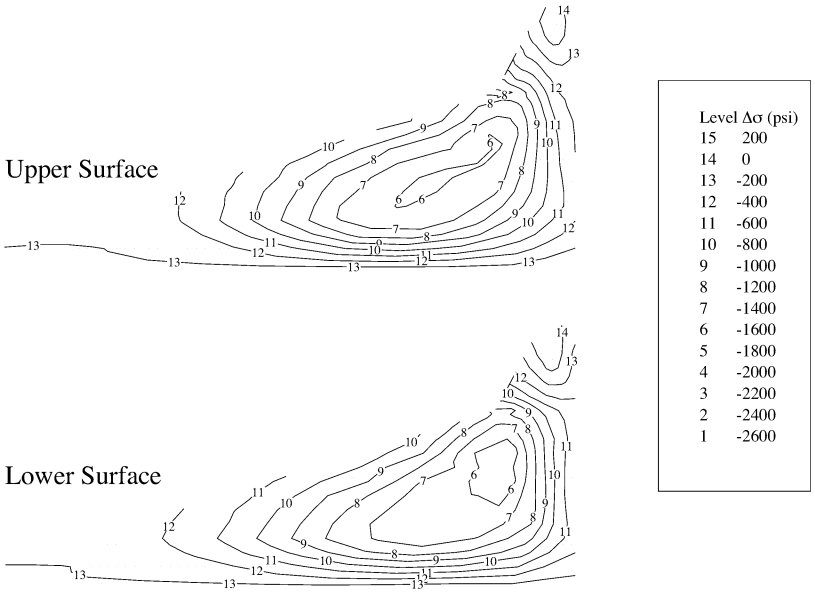


**Figure 4.15:** Stress Differences at Mach 2.4 Cruise (Design Case 1). (Results courtesy of Dr. Vladimir Balabanov)

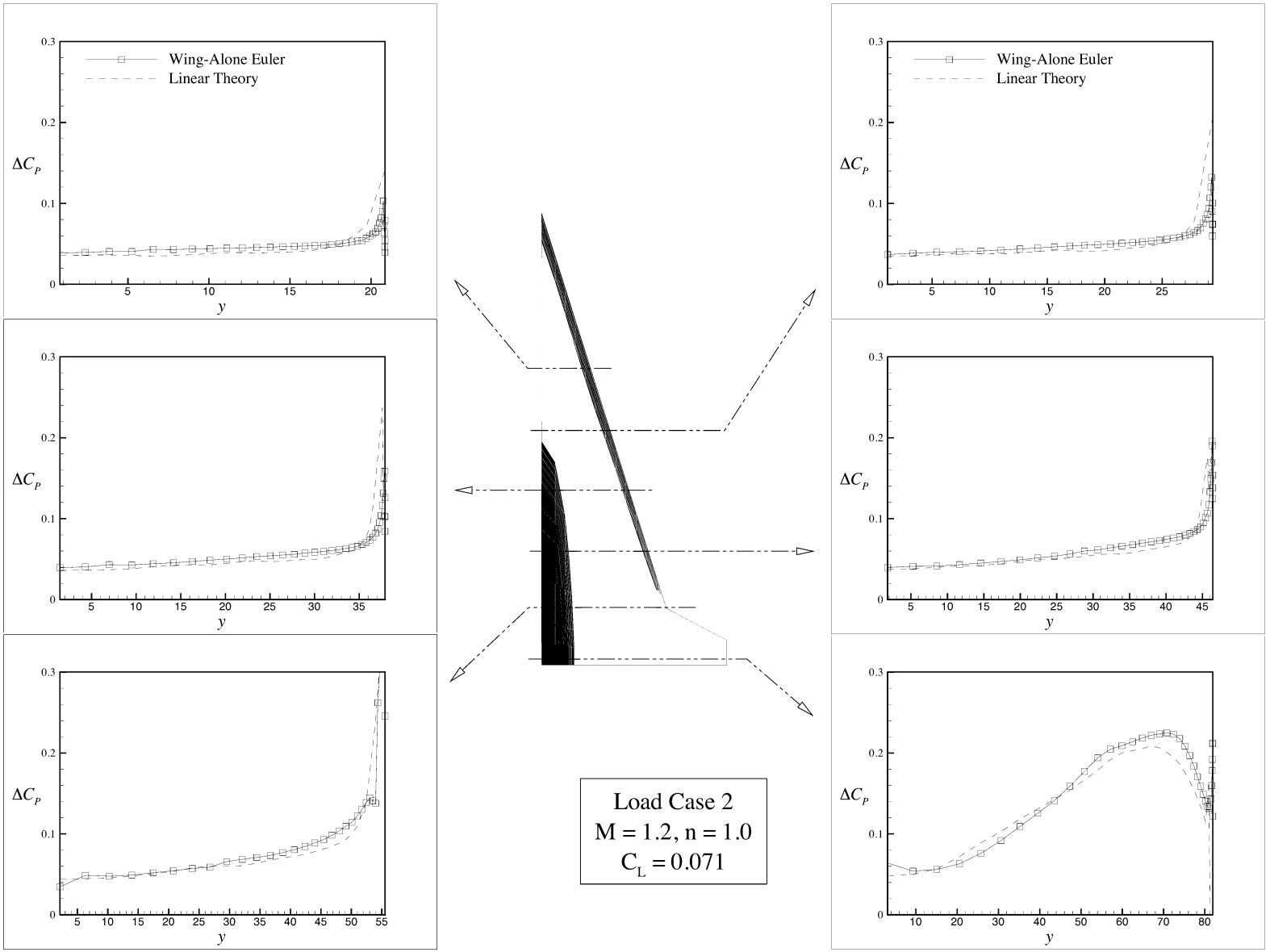


**Figure 4.16:** Aerodynamic Loads at Mach 1.2 cruise (Design Case 1).

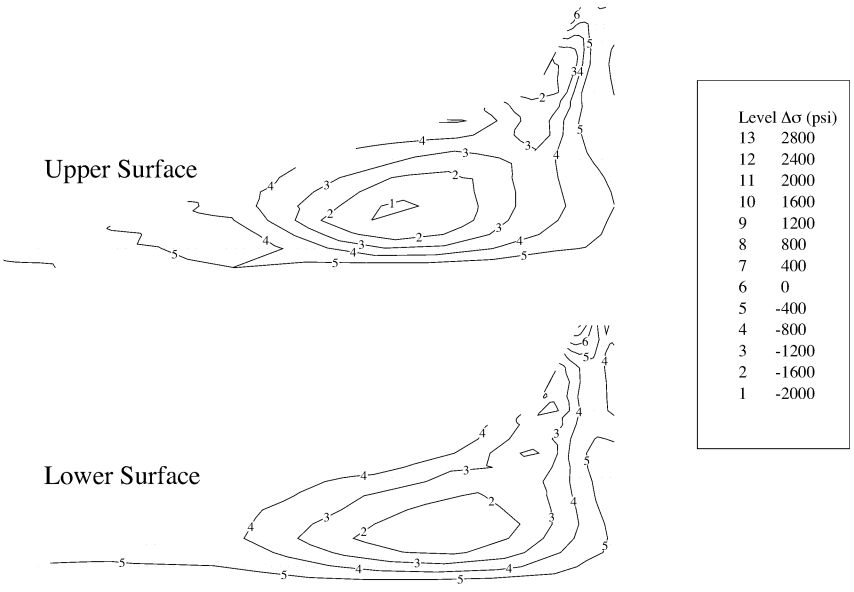


**Figure 4.17:** Stress Differences at Mach 1.2 Cruise (Design Case 1). (Results courtesy of Dr. Vladimir Balabanov)

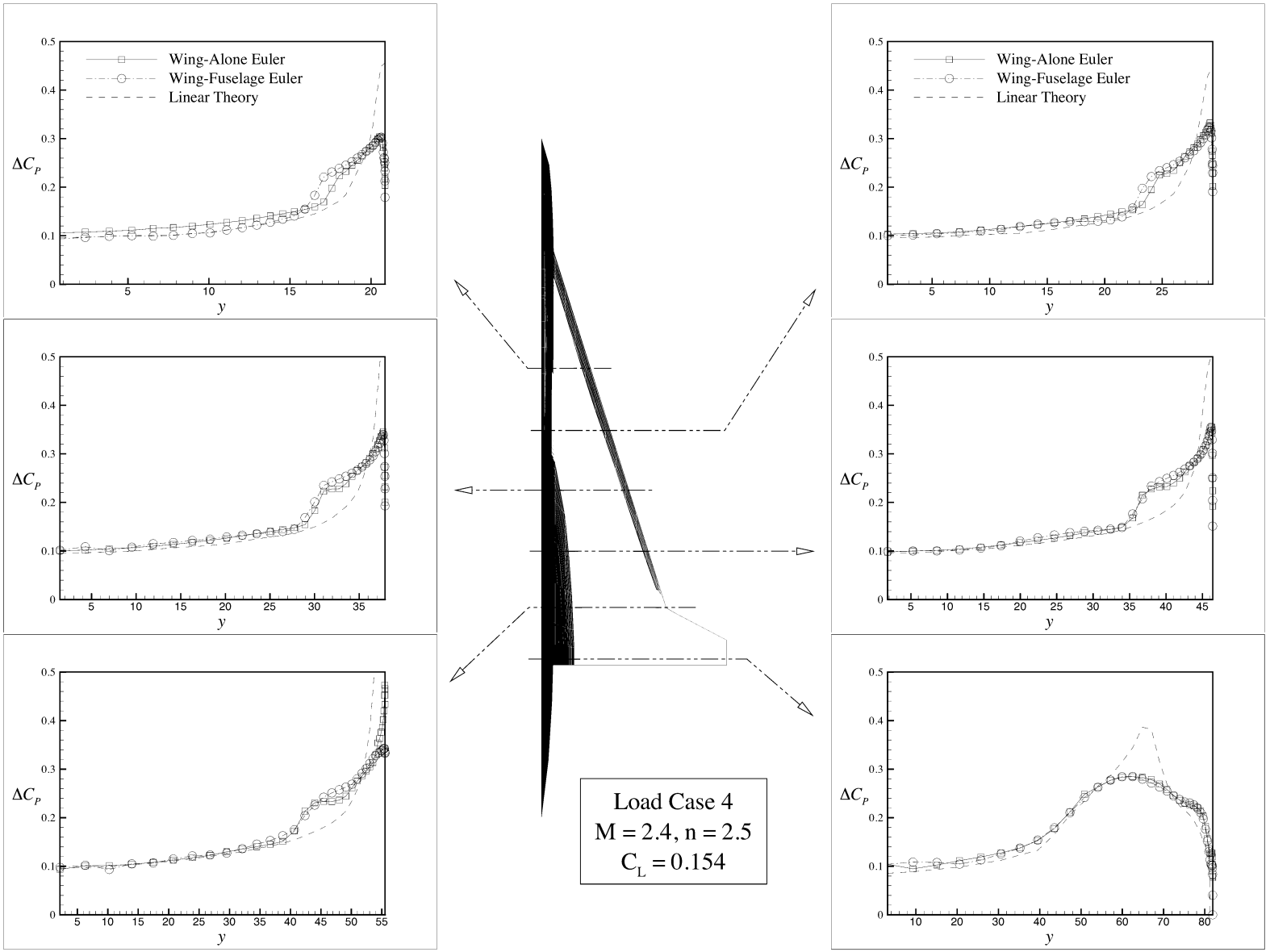


**Figure 4.18:** Aerodynamic Loads at Mach 2.4 2.5-g pull-up (Design Case 1).

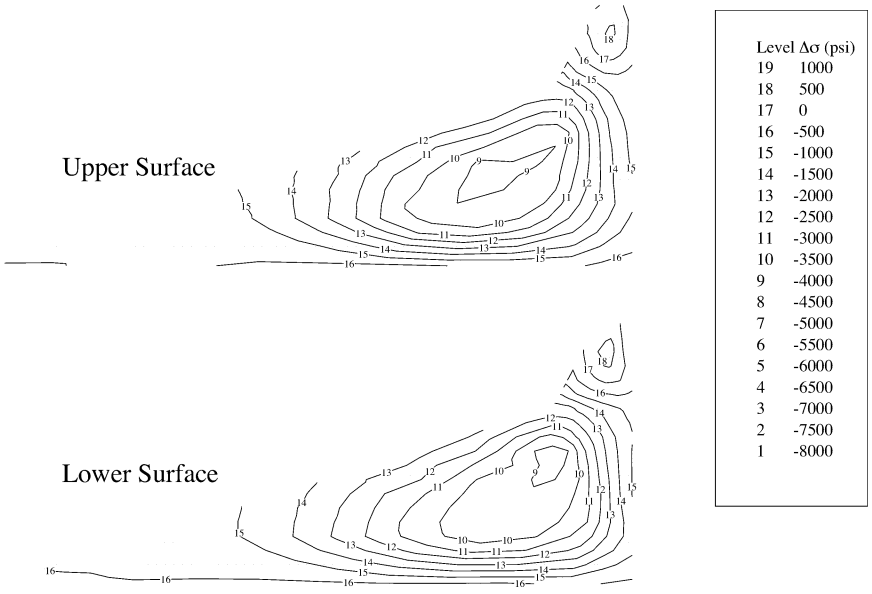


**Figure 4.19:** Stress Differences at Mach 2.4 2.5-g pull-up (Design Case 1). (Results courtesy of Dr. Vladimir Balabanov)

## 4.2 Design Case 2

The next HSCT design (Fig. 4.20) presented is an optimal design with an unusual planform. A full description of the optimization is given in Ref. 69. This type of planform with a forward-swept trailing edge has been encountered in other HSCT optimizations.[33,69] Table 4.3 contains the design variables which describe the wing and fuselage geometry.

### Uncambered Wing

For the uncambered wing, linear theory gives an overprediction in the lift and pitching moment coefficient taken about the quarter chord of the MAC (Fig. 4.21) compared to CFD solutions. Unlike the previous design, the pitching moment curves behave linearly. Taking the ratio of the quadratic and linear terms of the pitching moment relation (Eqn. 4.2), as is done in Section 4.1, gives $(\textit{quadratic term}/\textit{linear term}) = 0.27$. The linear term is therefore overshadowing the quadratic term in the pitching moment equation. Another way to look at this is that the effect of the moment arm for the normal force is much larger than the effect due to the movement in the aerodynamic center location. This is illustrated in Fig. 4.22. The aerodynamic center travels from 33.1% of $c_{root}$ at $C_L = 0.0$ to 32.7% of $c_{root}$ at $C_L = 0.2$. The forward sweep of the trailing edge has resulted in a more forward position of the aerodynamic center compared to Design Case 1. This trend is consistent with the diamond wing studies presented in Ref. 68. The aerodynamic center location predicted from CFD is $4.0ft$ aft of that from linear theory.

The drag polar (Fig. 4.23) shows linear theory underestimating the PNS drag coefficient by 1.4 counts at the cruise $C_L$ of 0.082. This comes mostly from the 1.2 count underprediction in the linear theory induced drag. The skin friction estimate is 0.9 counts higher than the viscous drag predicted from the PNS solution.

### Cambered Wing

Cambering the wing again results in a reduced cruise drag coefficient. Linear theory predicts a 1.5 count improvement, Euler analysis gives a 1.3 count reduction, and PNS

calculations show a 0.9 count improvement in the cruise drag due to wing cambering. The agreement between the linear theory and CFD lift coefficient values (Fig. 4.24) is slightly worse for the cambered wing. The linear theory zero-lift pitching moment coefficient is more negative, but the slope of the curve is more positive than that from Euler and PNS. The drag coefficients (Fig. 4.25) also show worse agreement between CFD and linear theory than for the uncambered wing. Linear theory calculations give a drag coefficient which is 2.1 counts lower than that from PNS. This is a 2.7% error relative to the PNS prediction of the cruise drag. The viscous drag estimate compares well to the PNS values for this wing.

The sensitivity of the range to the computed drag coefficient is 60 $n.mi.$/count for this design. This indicates that linear supersonic theory is overestimating the range by 126 $n.mi.$ This is a significant error in an aircraft with a required 5500 $n.mi.$ range constraint. Linear theory estimates of the cruise drag, while having relatively small errors, are not sufficient for accurate aircraft range calculations.

## Wing-Fuselage Configuration

Comparison of the force and moment data for the wing-fuselage configurations show the same basic trends as seen in the previous cases. The largest difference between linear theory and CFD lift and pitching moment coefficients (Fig. 4.26) occurs for this configuration. The PNS computed drag coefficient (Fig. 4.27) is 0.7 counts higher than the linear supersonic theory value. Surprisingly, this is less than the difference seen in the wing studies. The reason is the larger overprediction in the zero-lift drag value which tends to cancel the induced drag errors.

## Loads and Structural Optimization

The distributed loads on Design Case 2 computed from linear theory and Euler analyses reveal similar comparisons to those from Design Case 1. The loads (Fig. 4.28) on the body at Mach 2.4 cruise compare well. The wing-fuselage loads show a drop in $\Delta C_P$ due to the shock formed at the wing-fuselage juncture impinging on the fuselage. Over the remainder of the wing, the wing and wing-fuselage loads do not differ significantly.

The mesh used for the Design Case 2 structural analysis is shown in Figure 4.29. Figure 4.30 reveals that the location of the maximum variation is inboard of the subsonic leading edge. Using Euler loads results in lower wing bending stresses over the inboard wing and larger ones over a region of the outboard section. The maximum stress difference (Table 4.4) for the Mach 2.4 cruise condition is $-706$ *psi*, which is 25.2% of the stress value from Euler loads over that element. The difference in the maximum stress predicted from the Euler and linear theory loads is $-265$ *psi*. This is a smaller stress difference than for Design Case 1, and it is accompanied by a reduction in the difference between the predicted spanwise center of pressure locations.

Euler calculations on the wing-fuselage configuration at Mach 1.2 cruise did converge for this design. The fuselage nose half angle is 13.9°, which is lower than the maximum deflection angle for supersonic flow after the shock. The Mach 1.2 cruise loads (Fig. 4.31) from Euler and linear theory agree well at the chordwise locations examined.

The differences in predicted stresses for the Mach 1.2 cruise case are shown in Figure 4.32. Although the stresses from the Euler loads are lower than those from linear theory over most of the wing, there is a large region over the rear of the wing where the stresses from Euler are larger. The maximum difference between the stresses is $-2049$ *psi*. Again, we see an improvement in the agreement in stresses and the predicted center of pressure location (Table 4.4) compared to the Design Case 1 wing. The value of the nominal stress is small over the element where the maximum difference in stress of $-2049$ *psi* occurs. This results in the large 49.0% relative error based on the stress from Euler loads. The error in the maximum stress is smaller at $-1496$ *psi*.

As expected, the loads for the Mach 2.4 2.5-g pull-up (Fig. 4.33) show the largest variation. Linear theory loads agree well inboard of the crossflow shock location, except for the area where the shock is impinging on the fuselage. For this design, a double shock is present in the wing-fuselage case. As is seen in the maneuver wing and Design Case 1 loads, linear theory underpredicts the load near the crossflow shock and then overpredicts the load at the leading edge. This peak in the leading edge load propagates down past the leading-edge break.

The largest difference in predicted stresses also occurs for the Mach 2.4 2.5-g pull-up load case. The maximum difference is stress is $-2088$ *psi*. Contours of the

difference in predicted stresses (Fig. 4.34) shows the same behavior as seen in the previous cases, where the Euler loads give lower stress values over most of the inboard section, with the maximum difference occurring near the center of the wing. Over the outboard wing section, the stresses from Euler analysis are typically higher than from linear theory. The difference in maximum stress is $-1043$ $psi$ which represents only 6.3% of the value from Euler loads. The maximum stress is location near the leading edge break for all three load cases. As with the other load cases, the spanwise center of pressure location (Table 4.4) and wing bending stresses computed from Euler and linear theory loads show better agreement for Design Case 2 than for the Design Case 1.

The wing bending material weights from the structural optimization show the effect of the improved agreement in stresses. The ratio of the wing bending material weight predicted from Euler loads to that from linear theory loads is 0.971. A lighter design is obtained using the more accurate loads, but the overall difference is extremely small ($325\,lb$).

**Table 4.3:** Design Variable Values (Design Case 2).

| DV | Value | Description |
|---|---|---|
| 1 | 167.31 | Wing Root Chord ($ft.$) |
| 2 | 103.52 | L.E. Break, x ($ft.$) |
| 3 | 32.06 | L.E. Break, y ($ft.$) |
| 4 | 138.09 | T.E. Break, x ($ft.$) |
| 5 | 31.15 | T.E. Break, y ($ft.$) |
| 6 | 122.45 | L.E. Wing Tip, x ($ft.$) |
| 7 | 10.55 | Wing Tip Chord ($ft.$) |
| 8 | 56.14 | Wing Semispan ($ft.$) |
| 9 | 0.4182 | x-Loc. Airfoil Max. t/c ($x/c$) |
| 10 | 2.8193 | L.E. Radius Parameter |
| 11 | 2.2646 | t/c at Wing Root ($\%c$) |
| 12 | 1.5632 | t/c at L.E. Break ($\%c$) |
| 13 | 1.5334 | t/c at Wing Tip ($\%c$) |
| 14 | 27.437 | Fuselage X-Restraint #1 |
| 15 | 4.0653 | Fuselage R-Restraint #1 |
| 16 | 129.866 | Fuselage X-Restraint #2 |
| 17 | 5.0904 | Fuselage R-Restraint #2 |
| 18 | 143.983 | Fuselage X-Restraint #3 |
| 19 | 4.8947 | Fuselage R-Restraint #3 |
| 20 | 244.050 | Fuselage X-Restraint #4 |
| 21 | 5.0596 | Fuselage R-Restraint #4 |

**Table 4.4:** Structural Analysis and Optimization Results (Design Case 2).

| Load Case | $(\Delta\sigma)_{\max}$ | | $\Delta(\sigma_{\max})$ | | $\Delta y_{\text{c.p.}}$ | $\frac{W_{\text{S/O-Euler}}}{W_{\text{S/O-LT}}}$ |
|---|---|---|---|---|---|---|
| | *psi* | % | *psi* | % | *ft* | |
| M=2.4 n=1.0 | −706 | (25.2%) | −265 | (5.0%) | −0.532 | |
| M=1.2 n=1.0 | −2049 | (49.0%) | −1496 | (15.5%) | −0.197 | 0.971 |
| M=2.4 n=2.5 | −2088 | (55.4%) | −1043 | (6.3%) | −0.811 | |

(Results courtesy of Dr. Vladimir Balabanov)

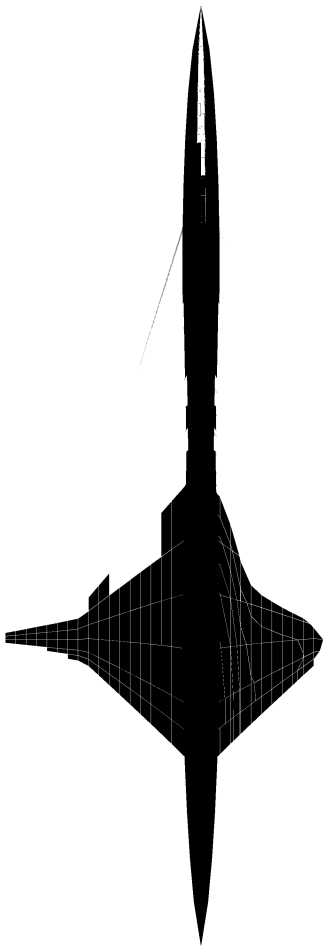

**Figure 4.20:** Configuration Planform View (Design Case 2).

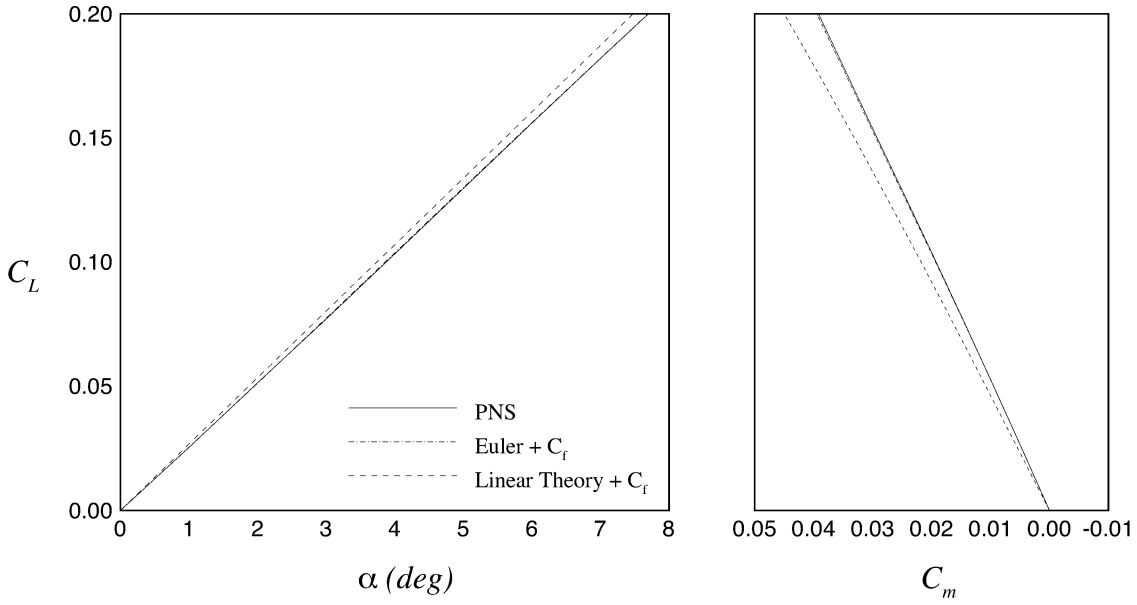


**Figure 4.21:** Lift and Pitching Moment Coefficients for Uncambered Wing (Design Case 2).

[Moments are taken about the quarter chord of the MAC.]

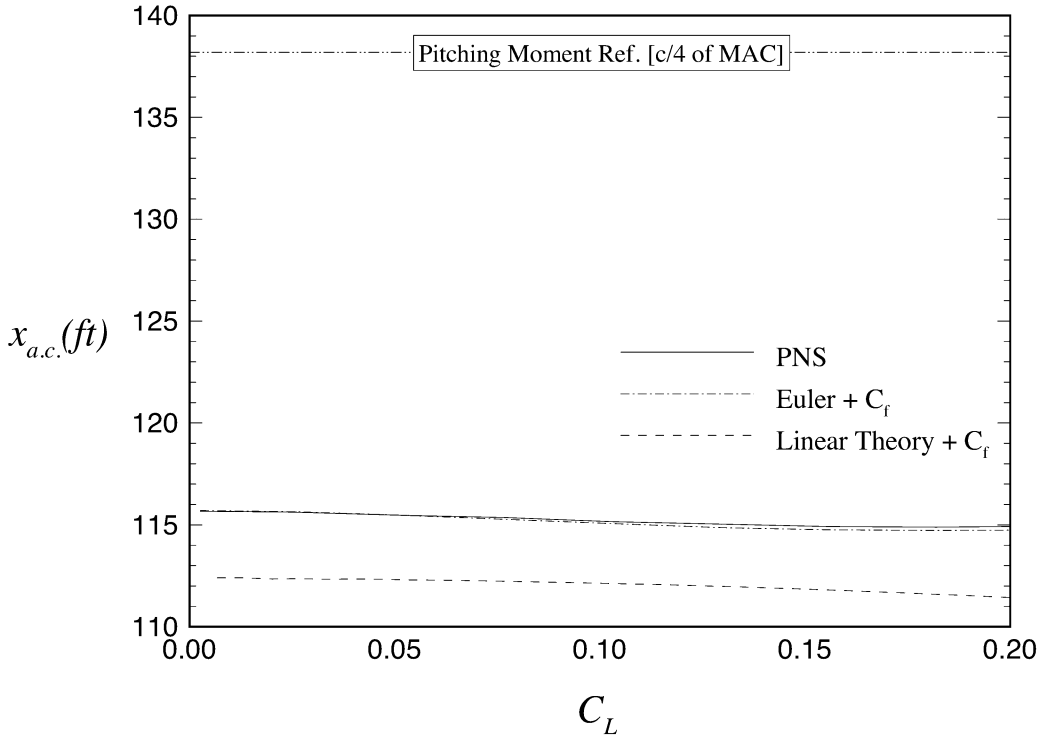


**Figure 4.22:** Change in Center of Pressure Location with Lift Coefficient.

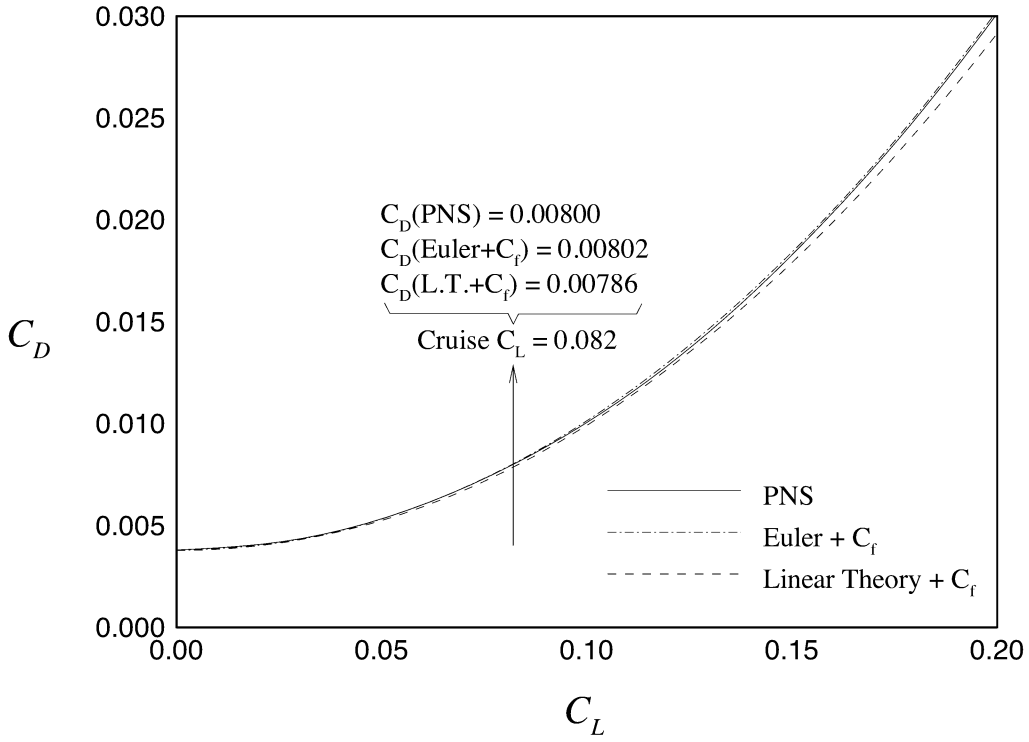


**Figure 4.23:** Drag Polar for Uncambered Wing (Design Case 2).

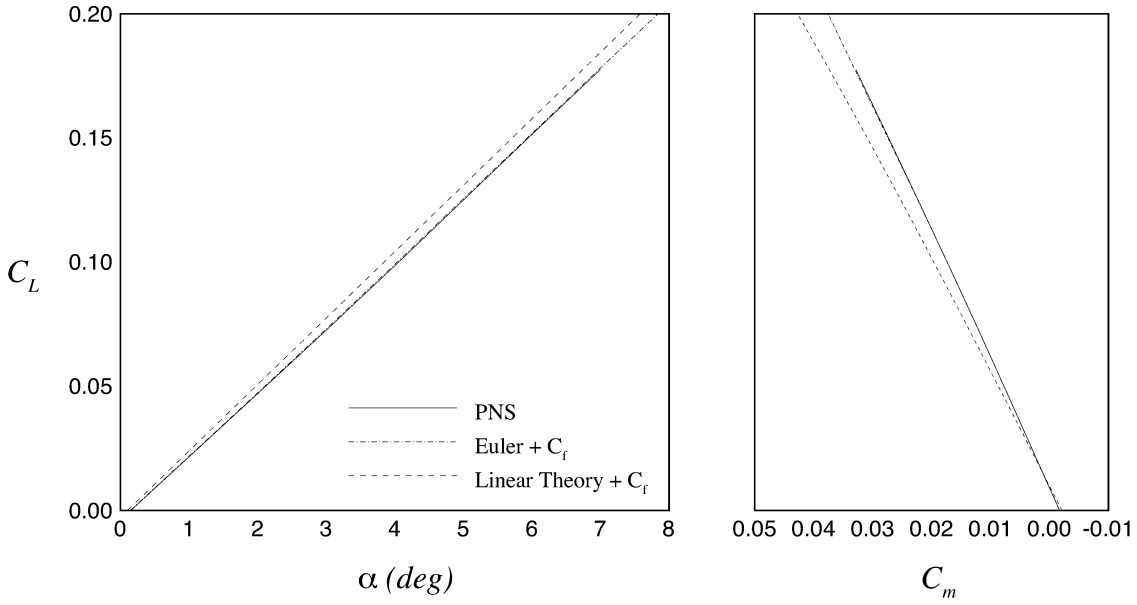


**Figure 4.24:** Lift and Pitching Moment Coefficients for Cambered Wing (Design Case 2).

[Moments are taken about the quarter chord of the MAC.]

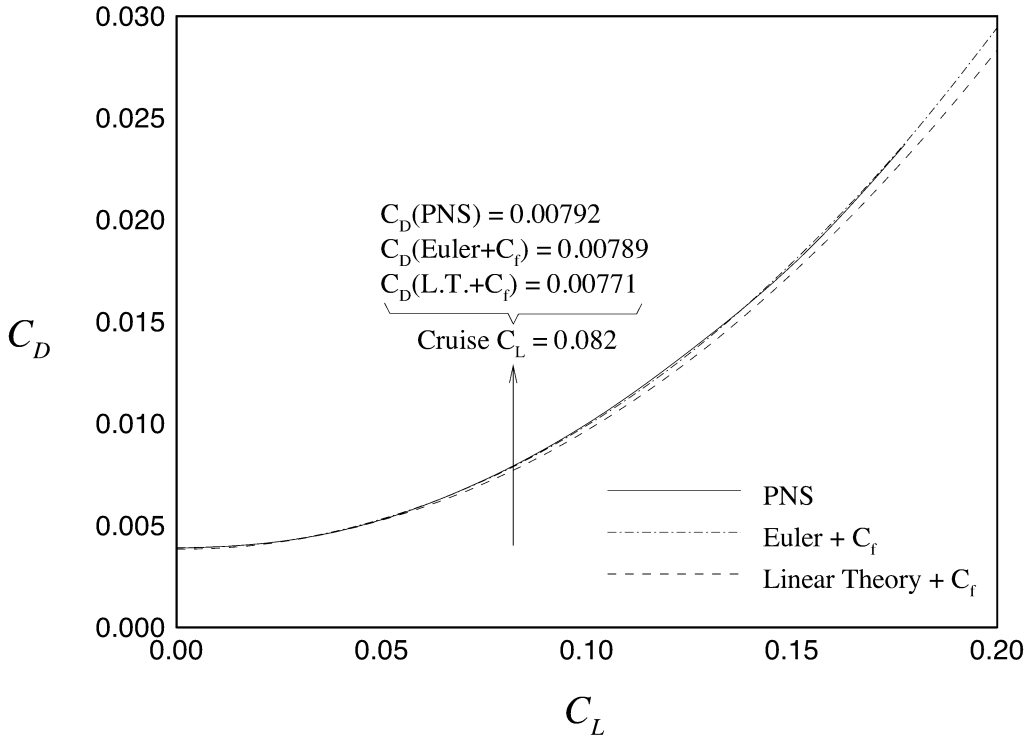


**Figure 4.25:** Drag Polar for Cambered Wing (Design Case 2).

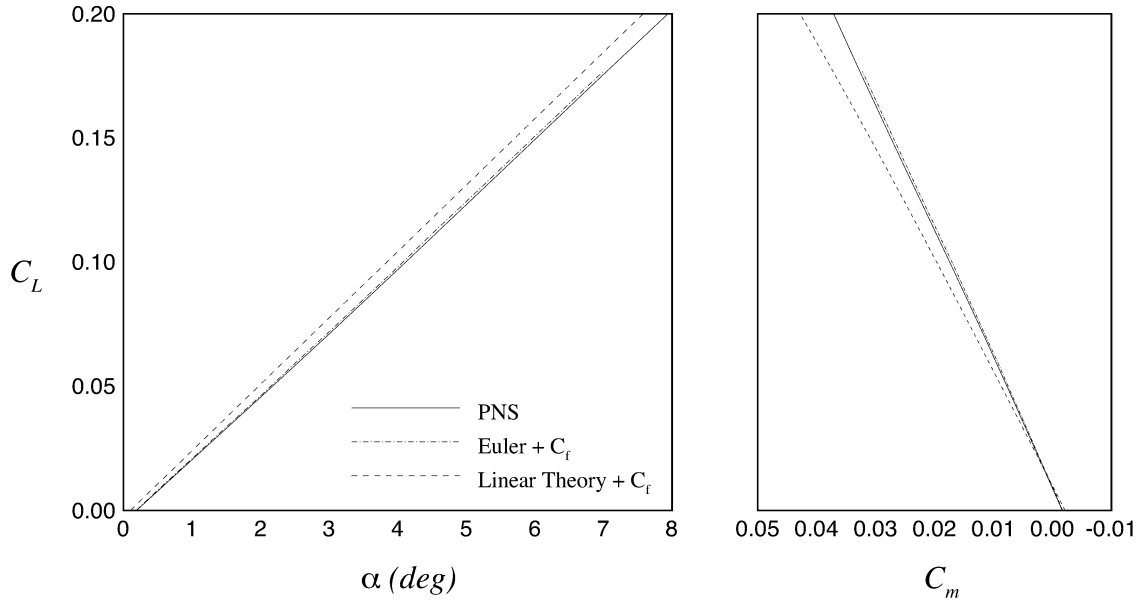


**Figure 4.26:** Lift and Pitching Moment Coefficients for Wing-Fuselage Configuration (Design Case 2).

[Moments are taken about the quarter chord of the MAC.]

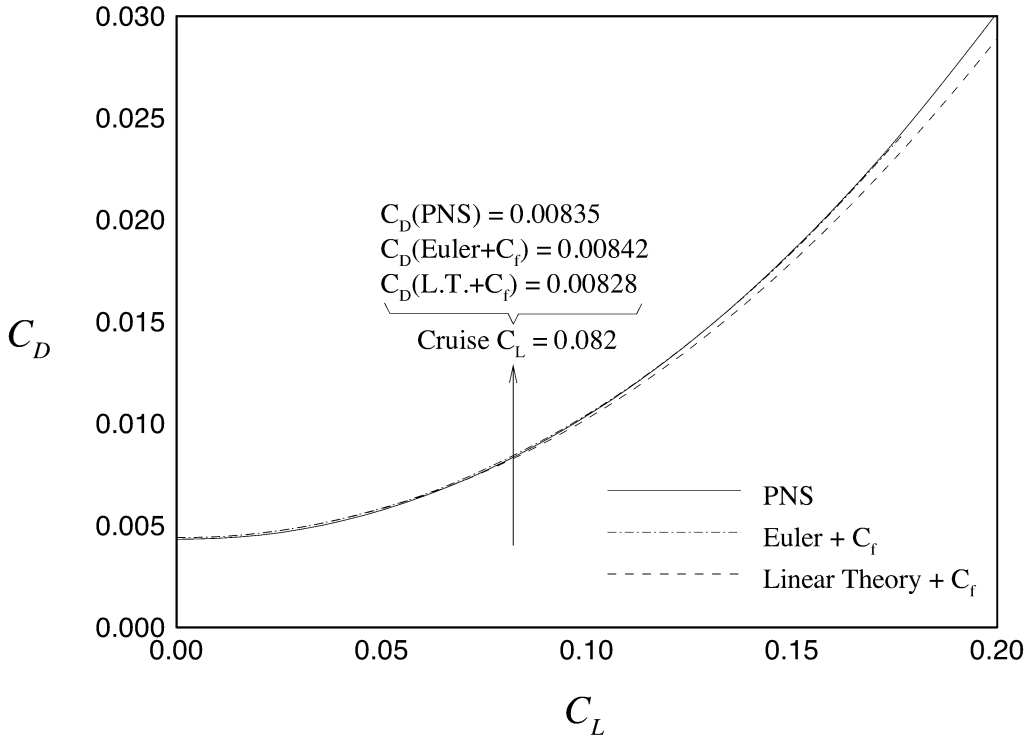


**Figure 4.27:** Drag Polar for Wing-Fuselage Configuration (Design Case 2).

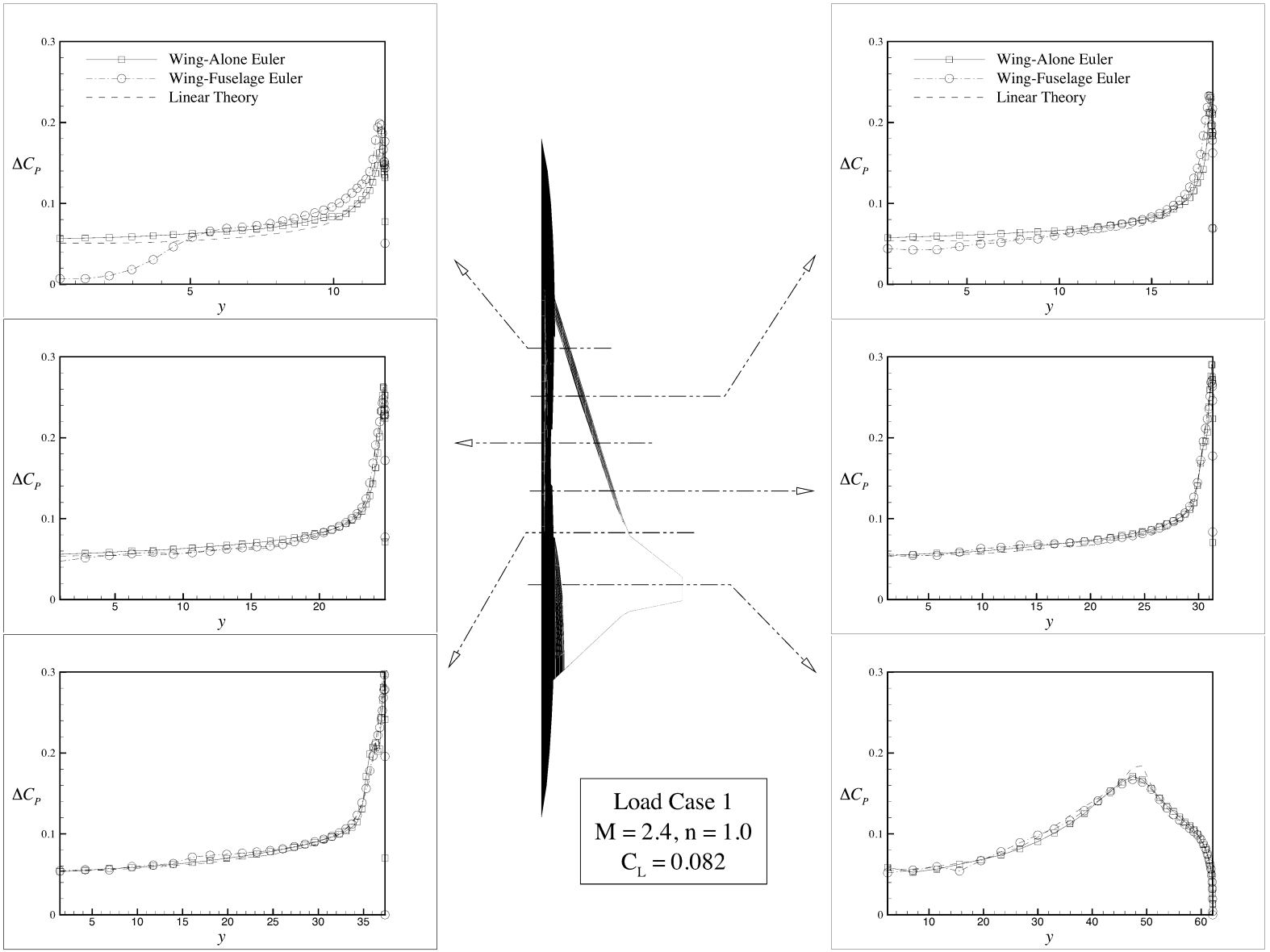


**Figure 4.28:** Aerodynamic Loads at Mach 2.4 Cruise (Design Case 2).

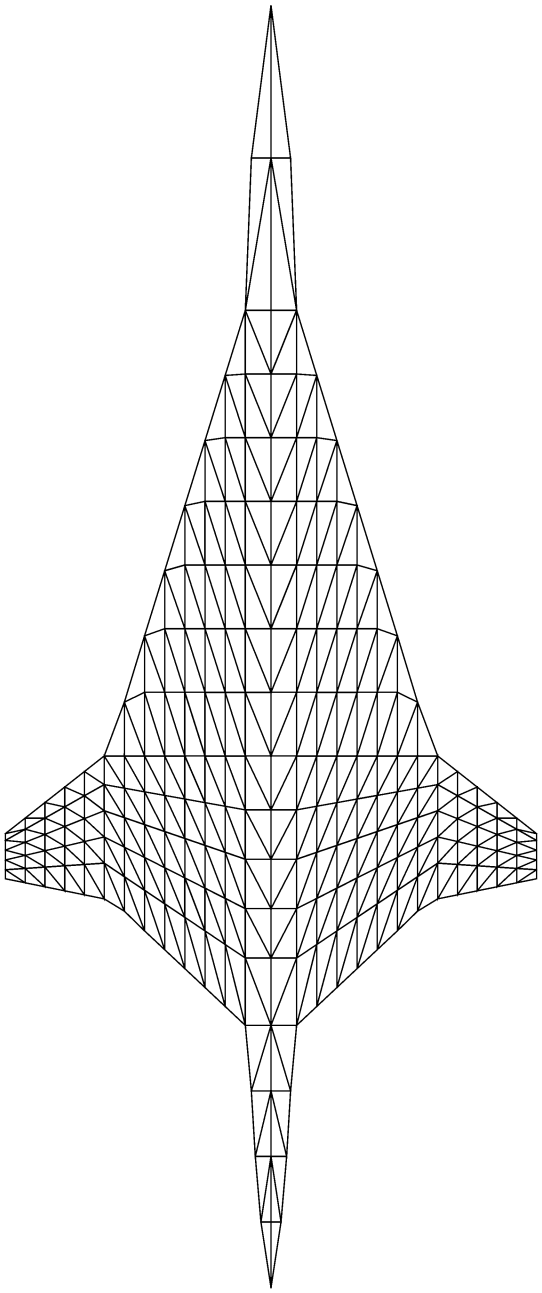

**Figure 4.29:** Structural Mesh for Design Case 2.
(Courtesy of Dr. Vladimir Balabanov)

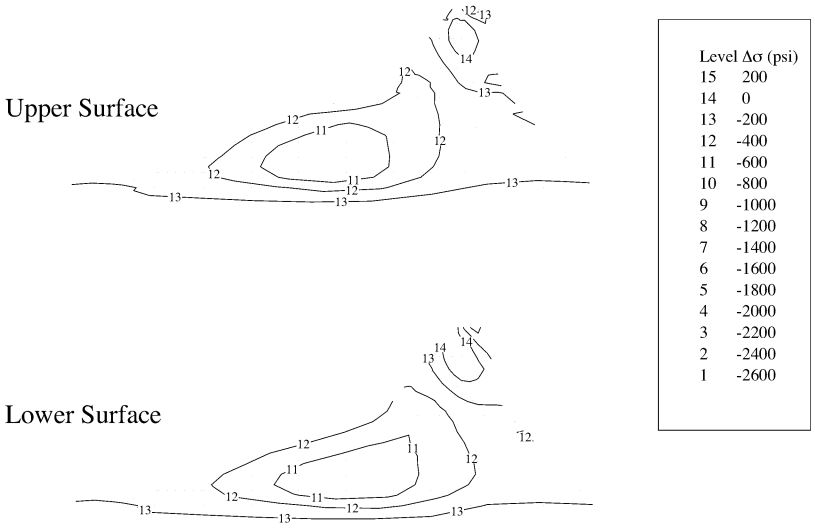


**Figure 4.30:** Stress Differences at Mach 2.4 Cruise (Design Case 2). (Results courtesy of Dr. Vladimir Balabanov)

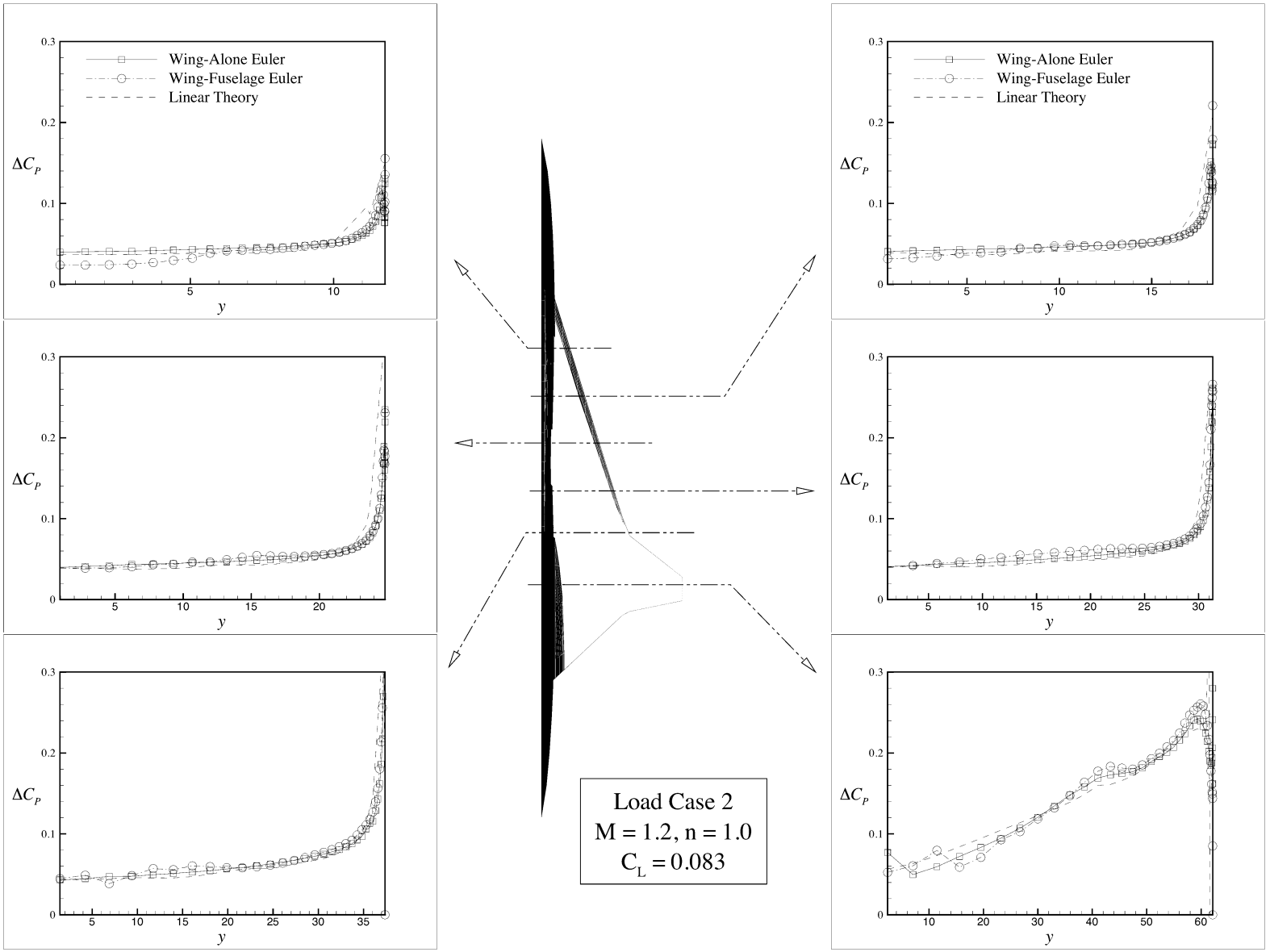


**Figure 4.31:** Aerodynamic Loads at Mach 1.2 Cruise (Design Case 2).

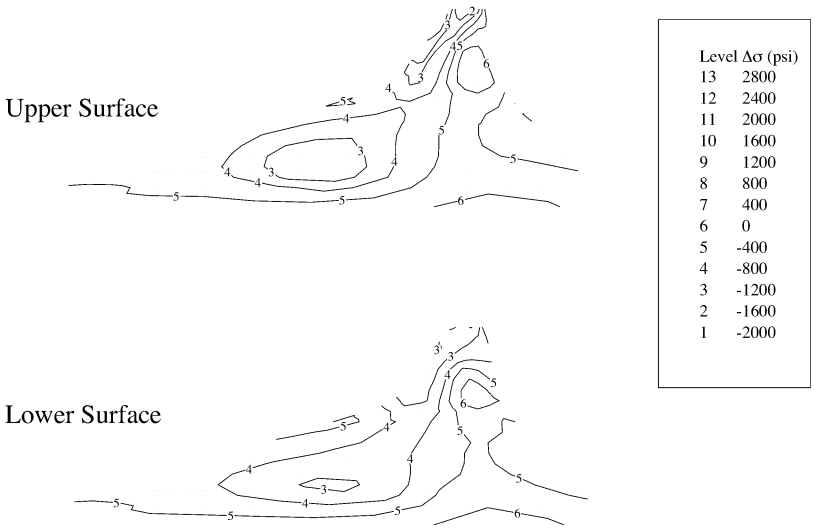


**Figure 4.32:** Stress Differences at Mach 1.2 Cruise (Design Case 2). (Results courtesy of Dr. Vladimir Balabanov)

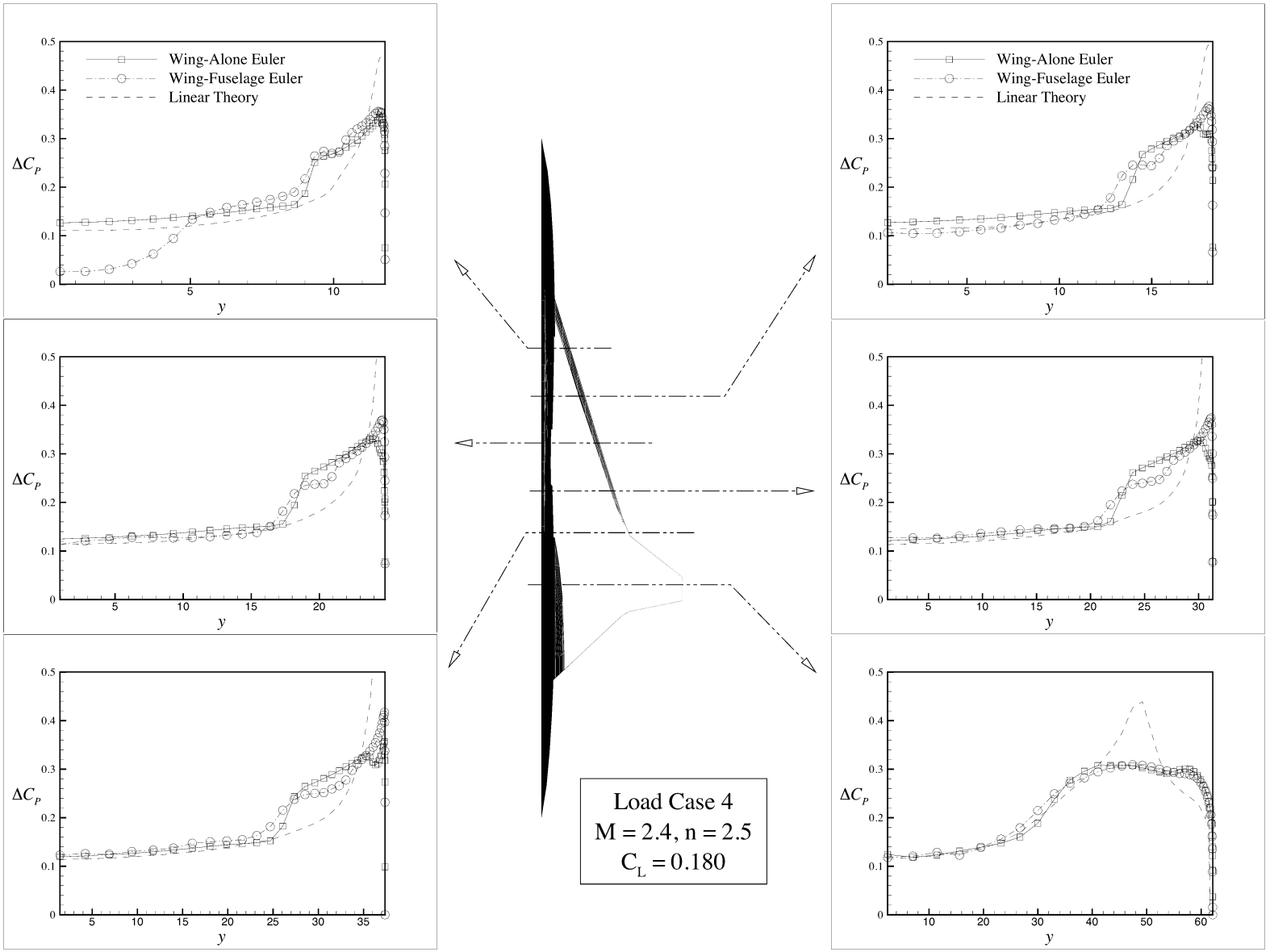


**Figure 4.33:** Aerodynamic Loads at Mach 2.4 2.5-g pull-up (Design Case 2).

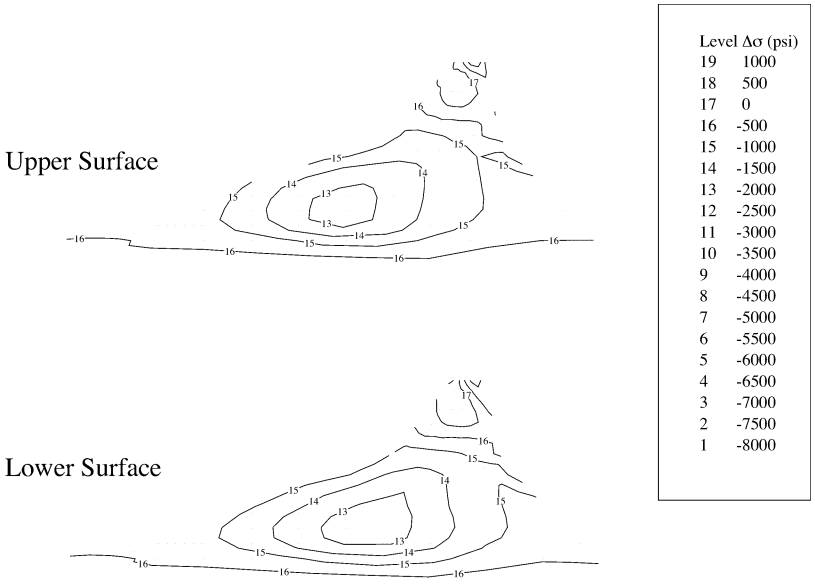


**Figure 4.34:** Stress Differences at Mach 2.4 2.5-g pull-up (Design Case 2). (Results courtesy of Dr. Vladimir Balabanov)

## 4.3 Design Case 3

The third planform considered (Fig. 4.35) is a starting point design used in our optimization. This wing has a highly swept leading edge both inboard and outboard of the leading-edge break, and the wing trailing edge is aft-swept. The design variables used to create Design Case 3 are given in Table 4.5.

### Uncambered Wing

The lift and pitching moment coefficient data for the Design Case 3 uncambered wing are plotted in Figure 4.36. As for all the HSCT pitching moment data, is taken about the quarter chord of the MAC. These plots show many of the same trends in force predictions seen throughout this study. Linear theory overestimates the lift-curve slope and predicts a more positive $C_m$ compared to CFD. The ratio of the quadratic to linear pitching moment terms from Eqn. 4.2 is 1.7 for this configuration. This ratio is lower than that for Design Case 1, and the curvature, while still apparent in the pitching moment plot, is correspondingly less. Figure 4.37 shows the movement in the aerodynamic center along with the location of the quarter-chord of the MAC. The aerodynamic center travels from 63.3% of $c_{root}$ at $C_L = 0.0$ to 61.2% of $c_{root}$ at $C_L = 0.2$. These locations are farther aft than those of Design Case 1 due to the aft-swept trailing edge. This trend and the nominal values of $x_{a.c.}$ are again in agreement with the diamond wing results presented in Ref. 68. As is true for the previous two designs, the aerodynamic center location from Euler and PNS calculations is farther aft than that from linear theory, resulting in a stronger nose-down tendency. The difference in $x_{a.c.}$ is $5.5\,ft$ for this design.

The drag polar is given in Figure 4.38. For this design, cruise at Mach 2.4 is achieved with a lift coefficient of 0.077. PNS calculations give a cruise drag coefficient which is 1.0 count higher than that from linear theory. The skin friction estimate is only 0.4 counts larger than the PNS viscous drag. The wave drag computed from the Harris code is 0.7 count lower than that from PNS and 0.4 count lower than that from Euler. The errors in friction and wave drag cancel each other, giving a good value for the linear supersonic theory zero-lift drag. As with the other cases, the drag-due-to-lift error results in poor drag prediction at larger values of $C_L$.

## Cambered Wing

Figures 4.39 and 4.40 show the lift curve and drag polar for the cambered wing. Cambering the wing resulted in a 2.9 count reduction in the cruise drag predicted from linear theory and a 2.4 count reduction in the cruise drag predicted from PNS. This is the largest drag reduction due to wing camber seen our studies.

The agreement between linear theory and CFD for the cambered wing is worse than it is for the uncambered wing. The friction drag estimate remains 0.6 counts higher than the PNS viscous drag prediction, but the total variation in the cruise drag for the cambered wing is 1.5 counts. Analysis shows that the sensitivity of the range to changes in the drag for this design is 61.5 $n.mi.$/count. This means that the range computed from linear supersonic theory is 92 $n.mi.$ greater than if we used PNS aerodynamics. Again, we see that seemingly small differences in the drag coefficient result in large variations in the predicted range.

## Wing-Fuselage Design

The wing-fuselage lift, moment, and drag coefficient data are plotted in Figures 4.41 and 4.42. The linear theory cruise drag is 0.7 counts lower than the PNS cruise drag. The skin friction estimate is 0.4 counts higher than the PNS prediction for the viscous drag. For all three designs studied, the skin friction estimate overpredicts the viscous drag, but the errors have been within one count.

## Loads and Structural Optimization

The loads for the wing and wing-fuselage configurations at Mach 2.4 cruise (Fig. 4.43) show good agreement much like the previous two designs. The structural model used for the finite-element analysis is shown in Figure 4.44. The stress distributions for this load case (Fig. 4.45) indicate that the largest difference in predicted stresses occurs near the middle of the wing. In addition, this difference is negative meaning that the stresses from Euler loads are lower than those from linear theory loads. This is in agreement with the results from the previous two designs. The magnitude of the differences in stress and spanwise center of pressure location (Table 4.6) are larger than those of Design Cases 1 and 2. The maximum difference in predicted stresses

$-2764$ *psi* (23.4%), and the difference in maximum stress is $-2520$ *psi* (18.9%). As seen in the previous wings, the wing bending stresses are very sensitive to small variations in the wing loading.

The Mach 1.2 cruise loads show good agreement over most of the wing. There is some variation in loads aft of the leading-edge break. The wing-fuselage configuration shows the largest differences at the last wing cut. The stresses (Fig. 4.47) from the Euler loads are lower than those from linear theory loads over the middle of the inboard wing section. However, there is a large region where the Euler stresses are larger. In fact, as seen in Table 4.6, the maximum difference between the stresses from Euler and linear theory loads is $+4600$ *psi* (21.2%). The maximum stress from Euler loads is also 4594 *psi* larger than that from linear theory loads. While, the Design Case 2 stresses for this load case did show a fairly large region of positive stress difference, this is the first case seen where the maximum difference in stresses and difference in maximum stress are positive.

The 2.5-g pull-up at Mach 2.4 (Fig. 4.48) again gives the largest disagreement in loads. Linear theory fails to properly predict the loads outboard of the crossflow shock. The stress differences (Fig. 4.49) for this case are also large. The maximum difference in stress is $-8745$ *psi*, which is 22.8% of the stress value at that element. The difference in maximum stress is 8543 *psi*. As is the case for Design Cases 1 and 2, the maximum stress on the wing occurs near the leading edge break. The stresses from the Euler loads are lower over the majority of the wing. This stress disagreement is larger than in the other load cases, as is the error in the predicted spanwise location of the center of pressure.

The structural optimization shows the effects of the larger Euler stresses in the Mach 1.2 cruise condition. In contrast to the previous two designs, structural optimization produced a heavier wing when using the Euler loads than when using linear theory loads. The ratio of wing bending material weights is 1.051. This amounts to only a 1761 *lb* difference in weight. For all designs studied, we have seen that significant differences in the wing bending stresses do not translate into large differences in wing weight from structural optimization. It appears that while significant gains can be achieved using CFD for the HSCT performance predictions, linear theory loads may be adequate for use in our HSCT wing bending material weight calculations.

**Table 4.5:** Design Variable Values (Design Case 3).

| DV | Value | Description |
|---|---|---|
| 1 | 169.47 | Wing Root Chord ($ft.$) |
| 2 | 143.34 | L.E. Break, x ($ft.$) |
| 3 | 37.73 | L.E. Break, y ($ft.$) |
| 4 | 176.05 | T.E. Break, x ($ft.$) |
| 5 | 30.39 | T.E. Break, y ($ft.$) |
| 6 | 189.83 | L.E. Wing Tip, x ($ft.$) |
| 7 | 7.02 | Wing Tip Chord ($ft.$) |
| 8 | 74.33 | Wing Semispan ($ft.$) |
| 9 | 0.4800 | x-Loc. Airfoil Max. t/c ($x/c$) |
| 10 | 3.2000 | L.E. Radius Parameter |
| 11 | 2.1400 | t/c at Wing Root ($\%c$) |
| 12 | 1.7300 | t/c at L.E. Break ($\%c$) |
| 13 | 1.5100 | t/c at Wing Tip ($\%c$) |
| 14 | 70.000 | Fuselage X-Restraint #1 |
| 15 | 6.0000 | Fuselage R-Restraint #1 |
| 16 | 135.000 | Fuselage X-Restraint #2 |
| 17 | 5.8000 | Fuselage R-Restraint #2 |
| 18 | 170.000 | Fuselage X-Restraint #3 |
| 19 | 5.8000 | Fuselage R-Restraint #3 |
| 20 | 215.000 | Fuselage X-Restraint #4 |
| 21 | 6.0000 | Fuselage R-Restraint #4 |

**Table 4.6:** Structural Analysis and Optimization Results (Design Case 3).

| Load Case | $(\Delta\sigma)_{\max}$ | | $\Delta(\sigma_{\max})$ | | $\Delta y_{\text{c.p.}}$ | $\frac{W_{\text{S/O-Euler}}}{W_{\text{S/O-LT}}}$ |
|---|---|---|---|---|---|---|
| | *psi* | % | *psi* | % | *ft* | |
| M=2.4 n=1.0 | −2764 | (23.4%) | −2520 | (18.9%) | −1.713 | |
| M=1.2 n=1.0 | +4601 | (21.2%) | +4594 | (12.7%) | −0.056 | 1.051 |
| M=2.4 n=2.5 | −8745 | (22.8%) | −8543 | (21.1%) | −1.952 | |

(Results courtesy of Dr. Vladimir Balabanov)

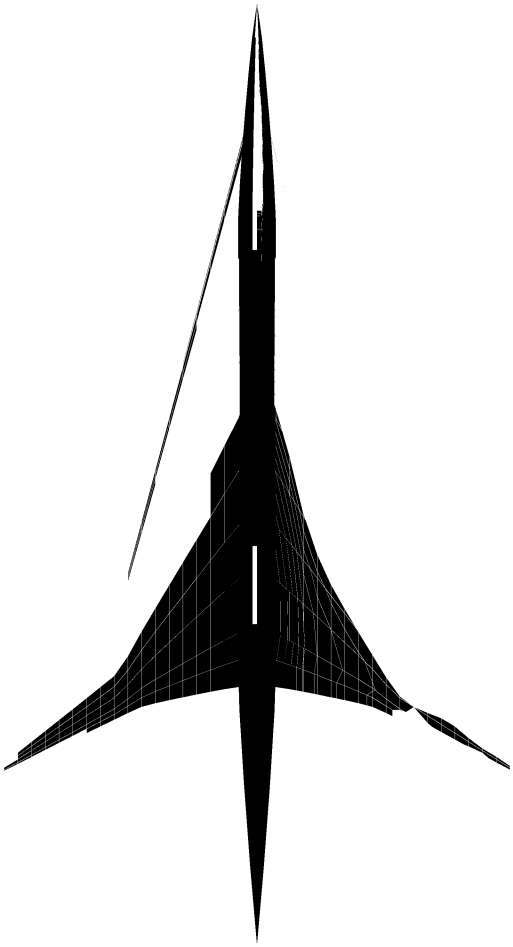

**Figure 4.35:** Configuration Planform View (Design Case 3).

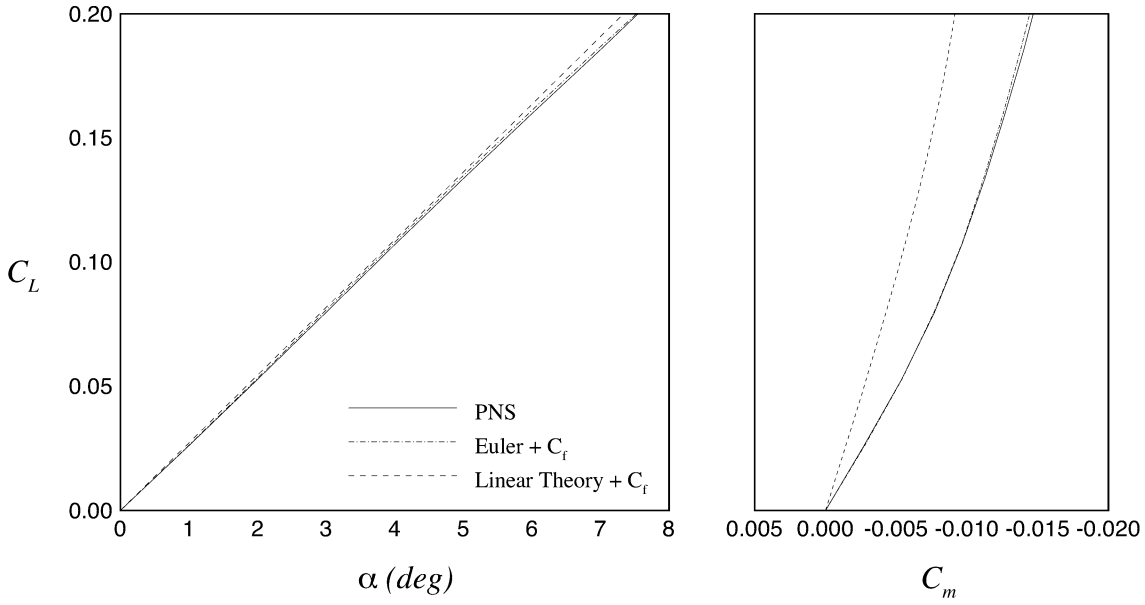


**Figure 4.36:** Lift and Pitching Moment Coefficients for Uncambered Wing (Design Case 3).

[Moments are taken about the quarter chord of the MAC.]

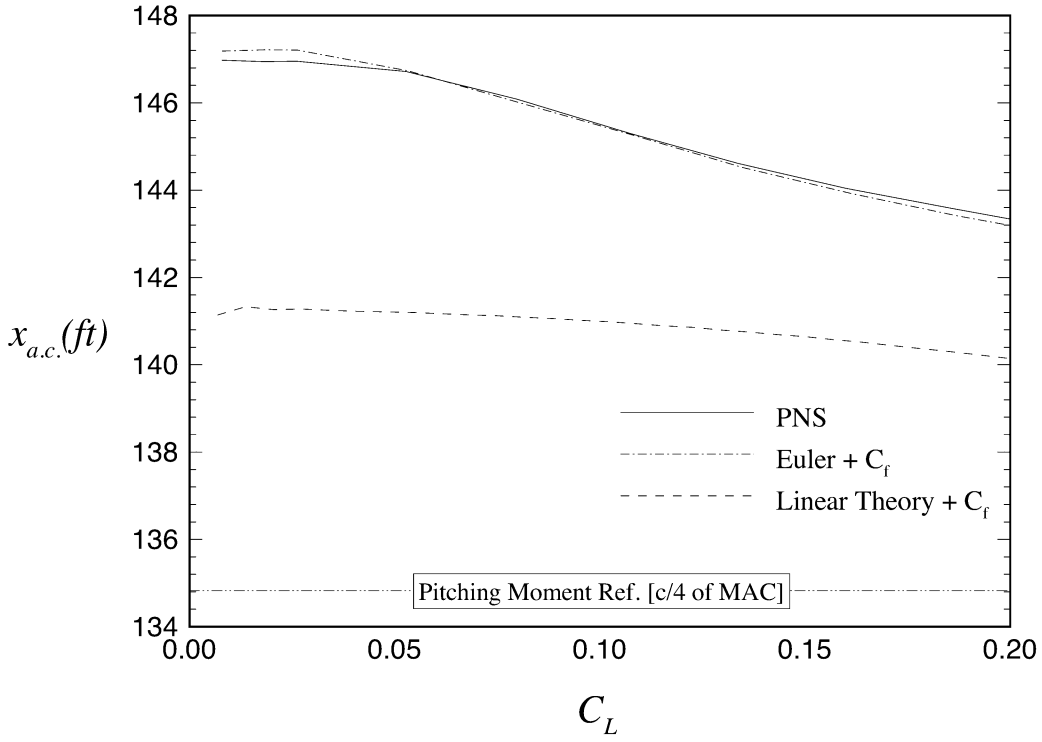


**Figure 4.37:** Change in Center of Pressure Location with Lift Coefficient.

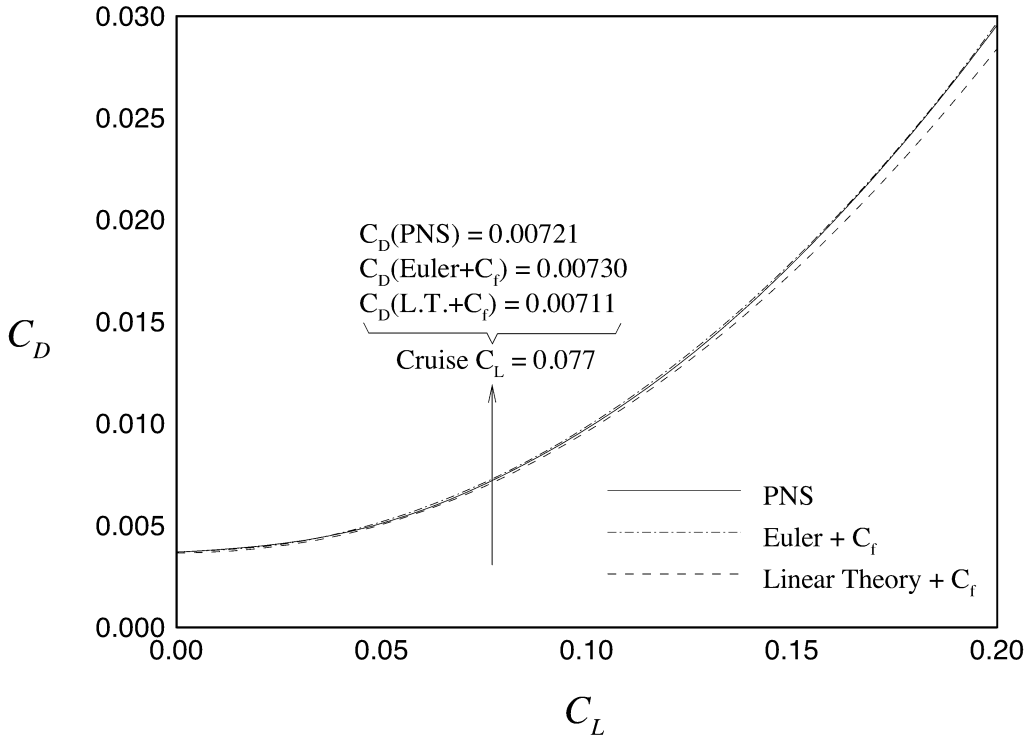


**Figure 4.38:** Drag Polar for Uncambered Wing (Design Case 3).

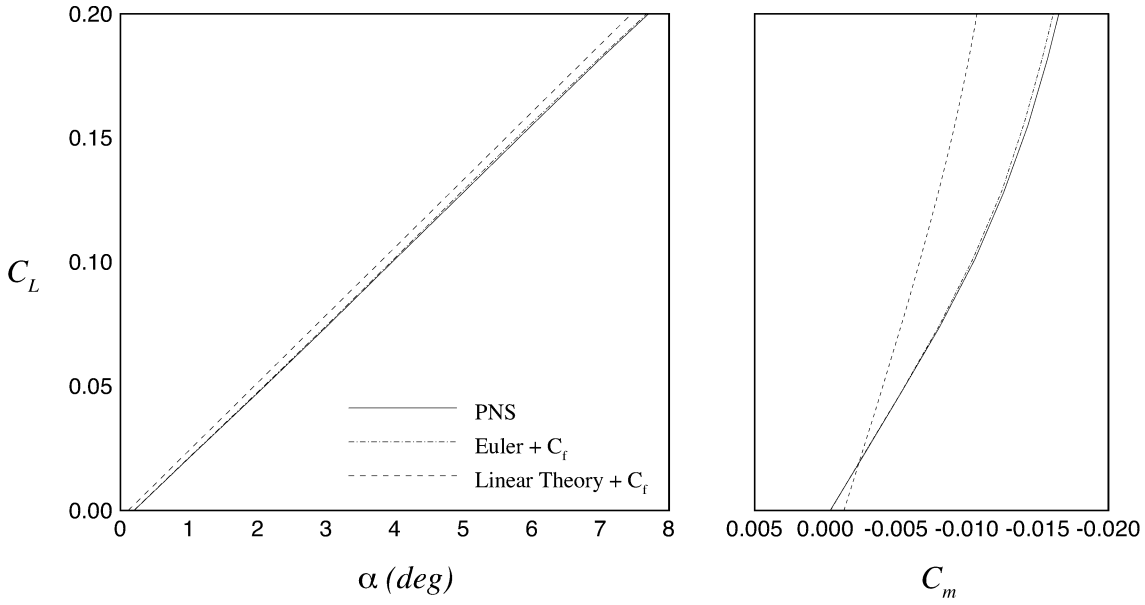


**Figure 4.39:** Lift and Pitching Moment Coefficients for Cambered Wing (Design Case 3).

[Moments are taken about the quarter chord of the MAC.]

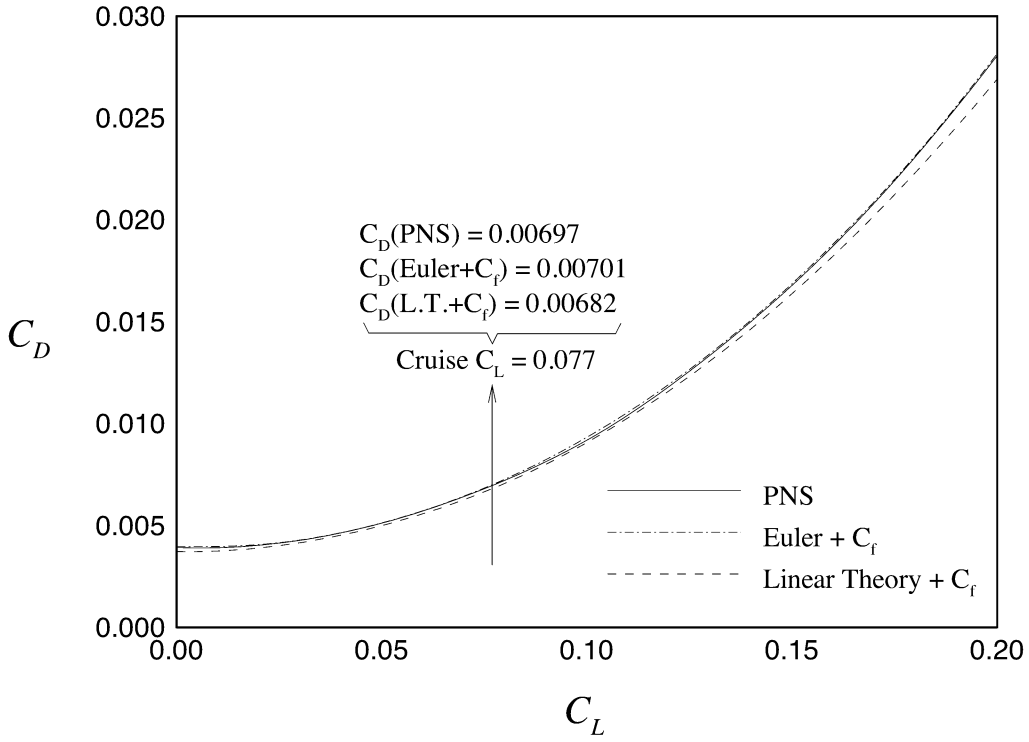


**Figure 4.40:** Drag Polar for Cambered Wing (Design Case 3).

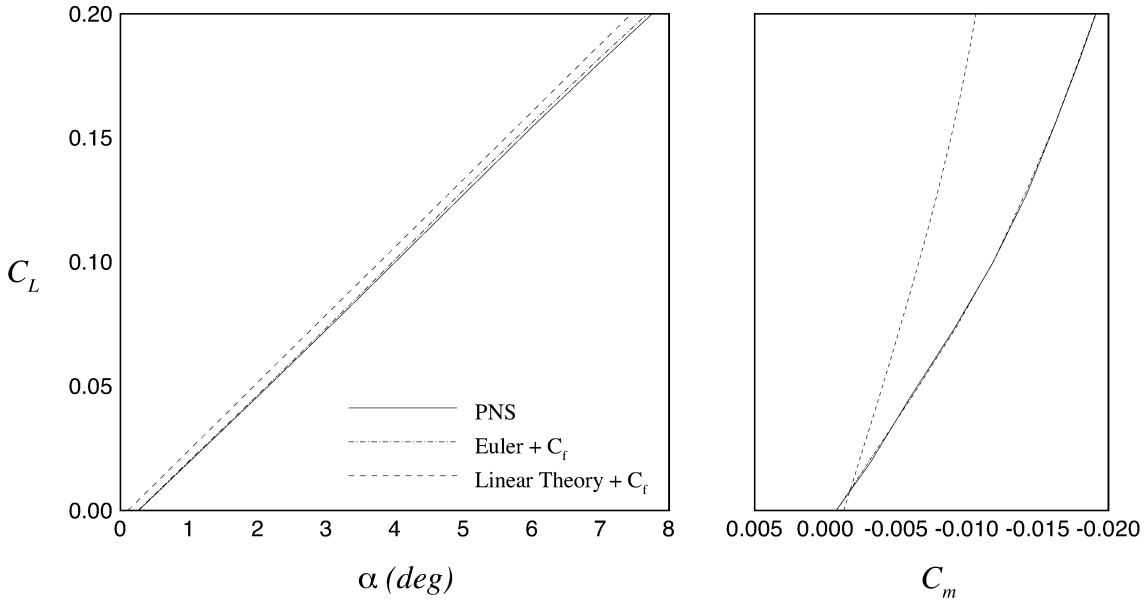


**Figure 4.41:** Lift and Pitching Moment Coefficients for Wing-Fuselage Configuration (Design Case 3).

[Moments are taken about the quarter chord of the MAC.]

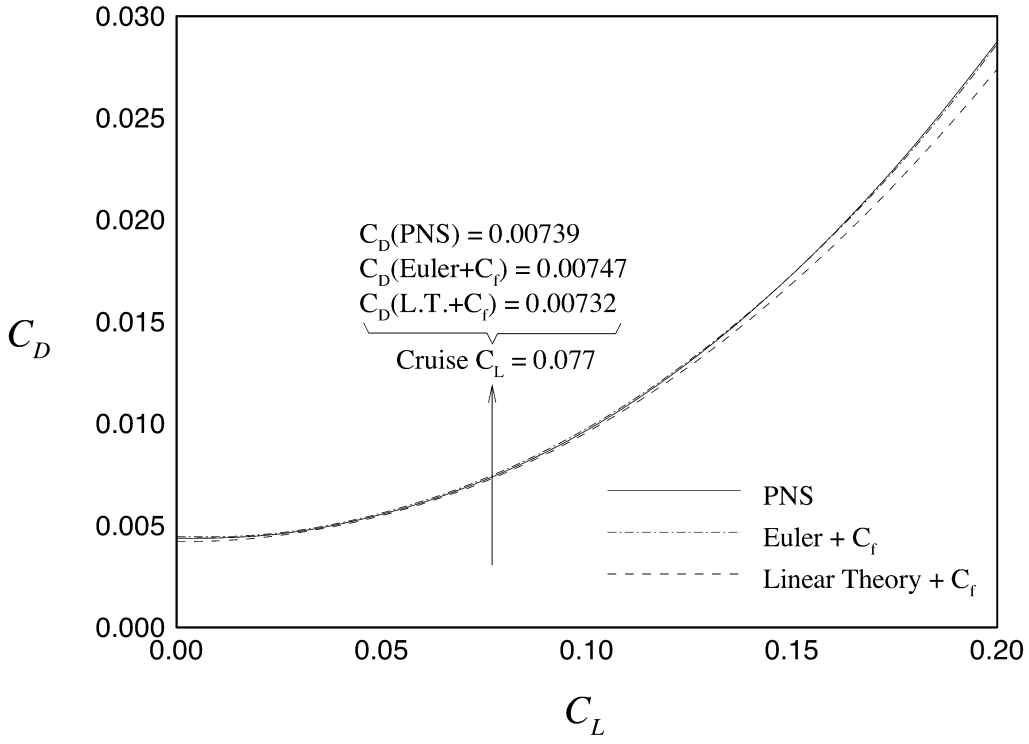


**Figure 4.42:** Drag Polar for Wing-Fuselage Configuration (Design Case 3).

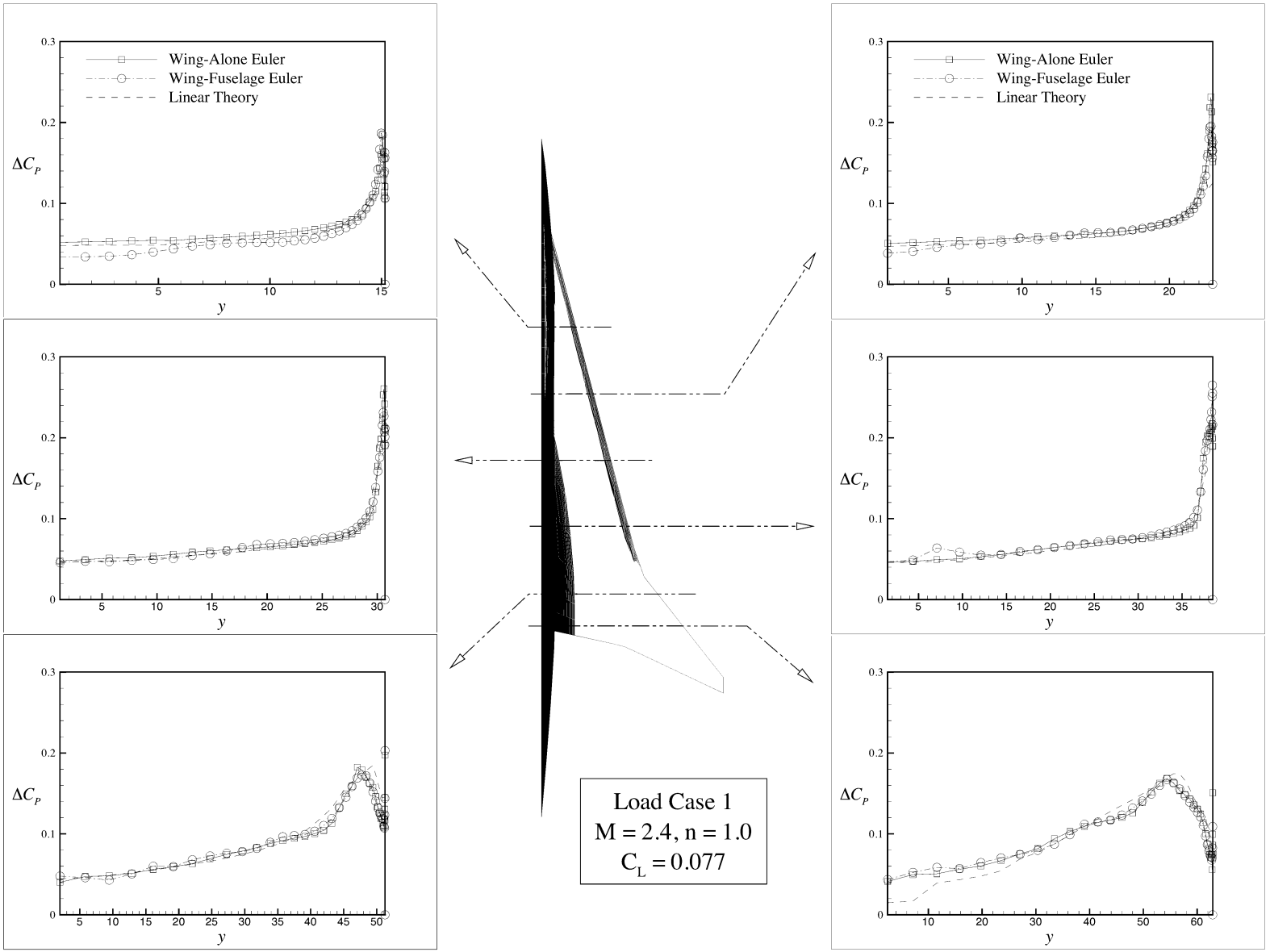


**Figure 4.43:** Aerodynamic Loads at Mach 2.4 Cruise (Design Case 3).

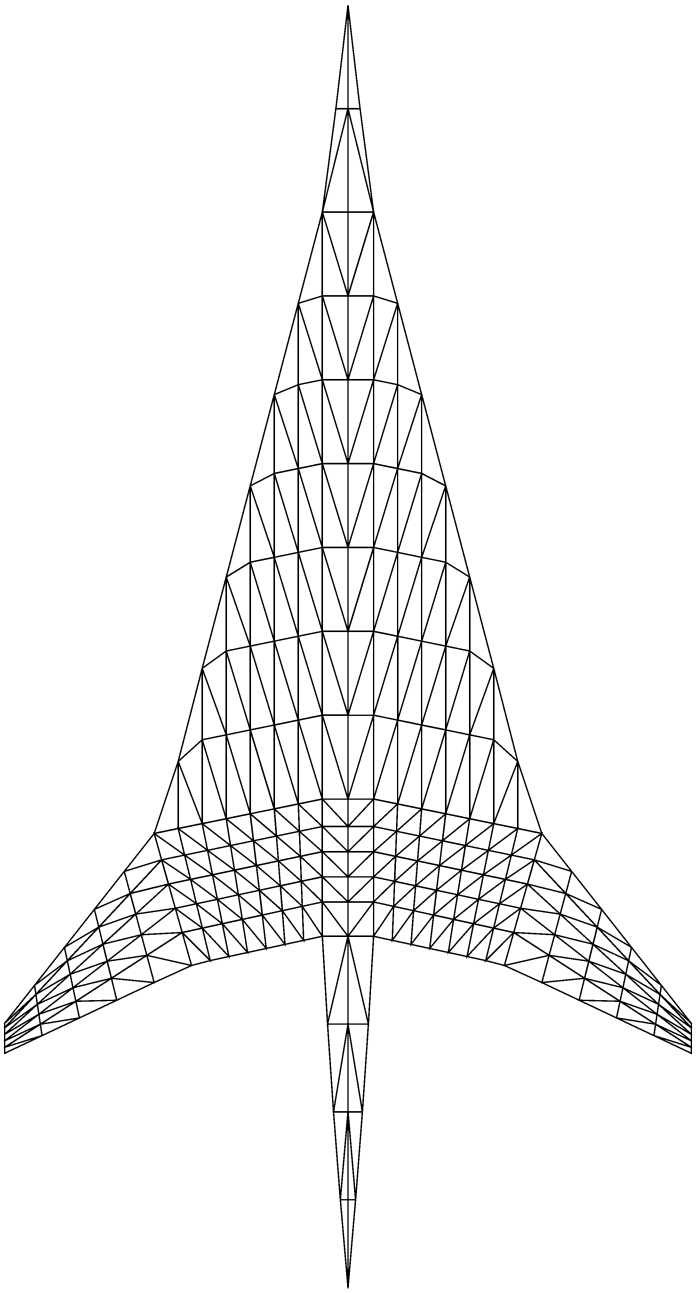

**Figure 4.44:** Structural Mesh for Design Case 3.
(Courtesy of Dr. Vladimir Balabanov)

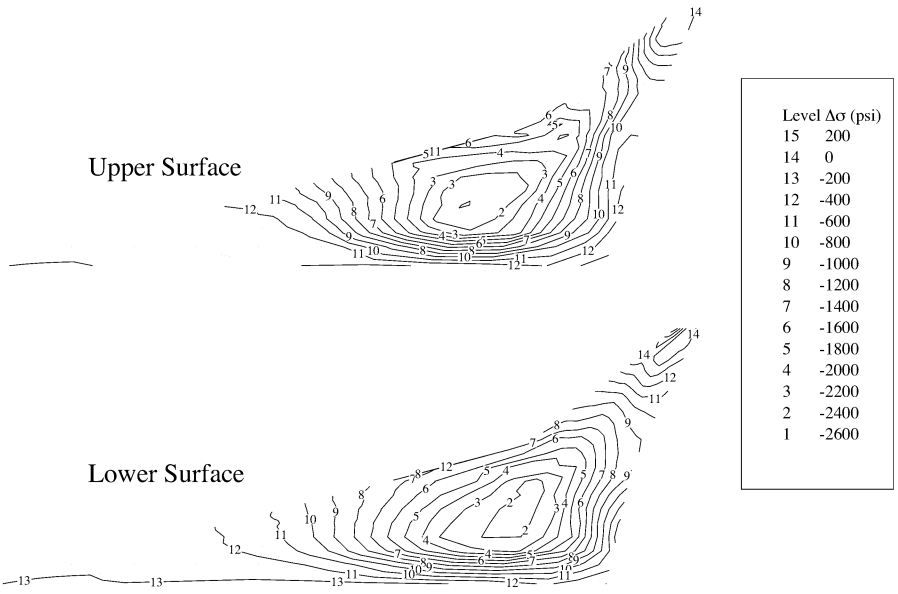


**Figure 4.45:** Stress Differences at Mach 2.4 Cruise (Design Case 3).
(Results courtesy of Dr. Vladimir Balabanov)

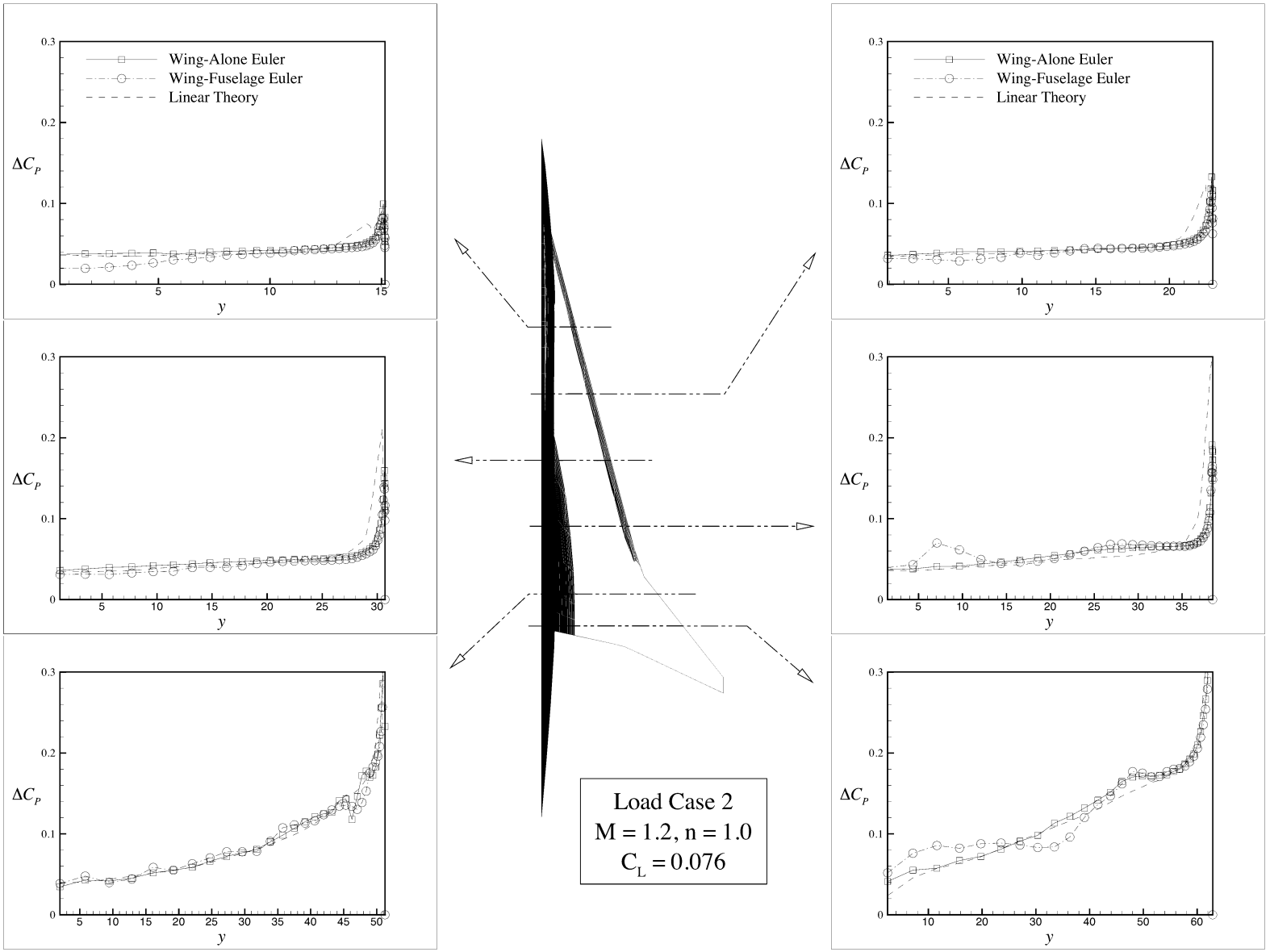


**Figure 4.46:** Aerodynamic Loads at Mach 1.2 Cruise (Design Case 3).

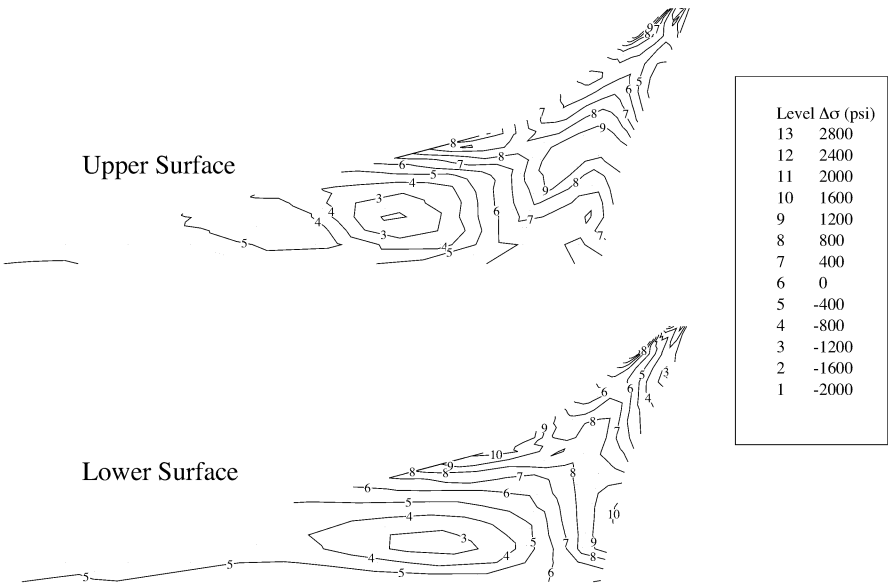


**Figure 4.47:** Stress Differences at Mach 1.2 Cruise (Design Case 3).
(Results courtesy of Dr. Vladimir Balabanov)

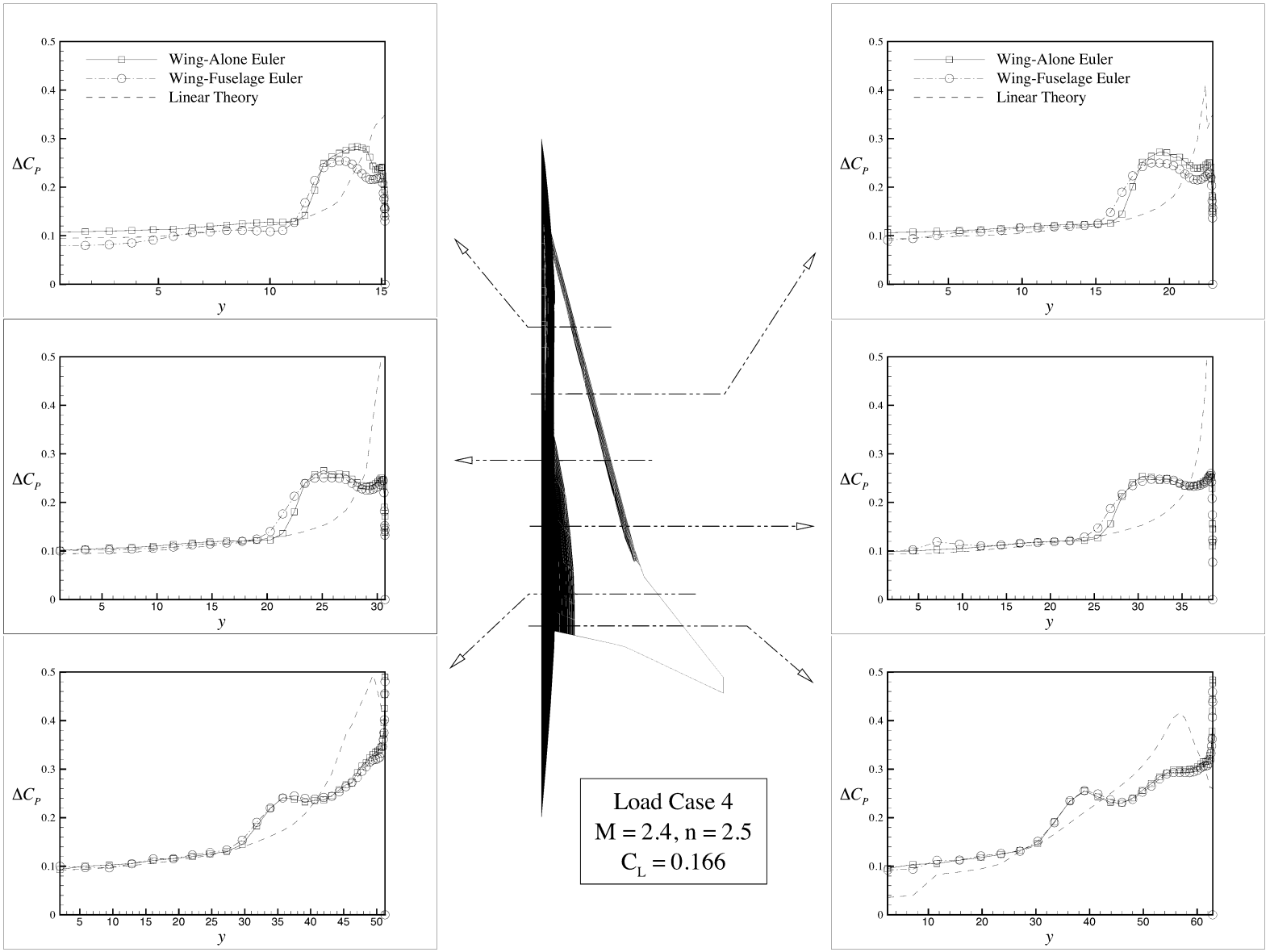


**Figure 4.48:** Aerodynamic Loads at Mach 2.4 2.5-g pull-up (Design Case 3).

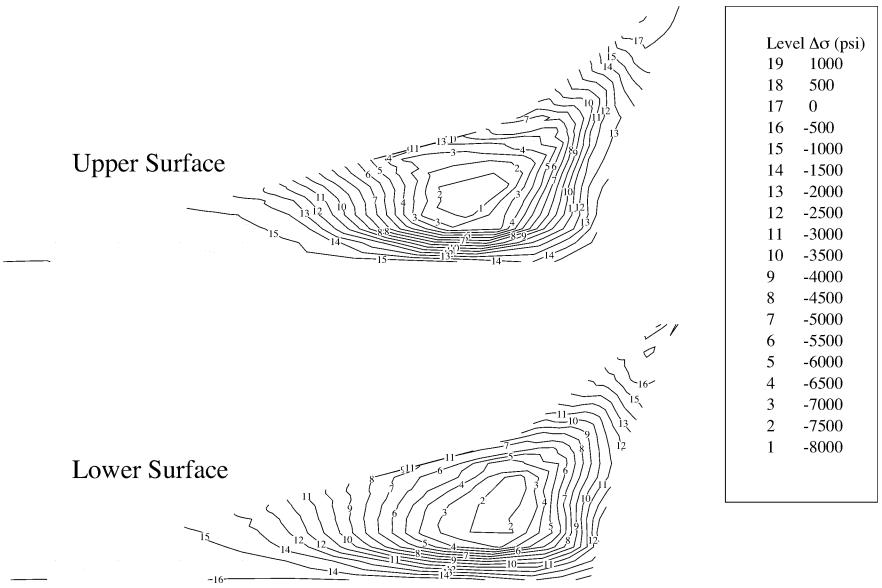


**Figure 4.49:** Stress Differences at Mach 2.4 2.5-g pull-up (Design Case 3). (Results courtesy of Dr. Vladimir Balabanov)

# Chapter 5

# Summary of Preliminary Studies

Euler and PNS solutions for the supersonic performance and loads of HSCT wing and wing-fuselage designs are compared with those from linear theory. Grid convergence studies showed that, for wing-alone configurations, a 77×51×77 grid is sufficient to resolve the drag within 1/2 count of the solution extrapolated to zero mesh size. The same resolution was obtained using a 77×91×77 grid for PNS calculations. Reducing the residual 2 orders of magnitude is required for converged solutions in the supersonic flow conditions considered. The computational costs of the wing-alone Euler and PNS calculations are 12 minutes and 1.5 hours, respectively, on an SGI *Power Challenge* R8000 machine.

The configurations examined show linear theory consistently overpredicting the lift. Linear theory pitching moments for the HSCT designs considered show a stronger nose-up tendency than those from CFD because the aerodynamic center is located farther forward. Studies of other configurations have indicated the opposite trend.[3,4] Curvature in the pitching moment results occur due to forward movement of the aerodynamic center location with increasing lift. While this movement is small (0.5%–1.5% of $c_{root}$), it is significant when the moment reference point is near the aerodynamic center. Analysis of the three designs at Mach 2.4 flight conditions shows that the nominal aerodynamic center location moves aft (Fig. 5.1) as the trailing edge of the wing becomes more aft-swept. This agrees with studies of diamond shaped planforms presented in Jones and Cohen.[68]

For the uncambered wing-alone configurations, the difference in the Harris code

and CFD predictions for the zero-lift wave drag range from $-1.4$ counts to $+0.7$ count. (Negative values indicating that CFD results are lower.) The skin friction estimates are as much as 0.9 count higher than the PNS values. Linear theory is found to underpredict the induced drag for these configurations. When the linear theory zero-lift drag is larger than that from CFD, these errors tend to cancel each other at cruise. However, when the linear theory zero-lift drag is lower, the errors add. The largest discrepancy in the linear theory and PNS cruise drag for the uncambered wings is 1.4 counts.

Using WINGDES to find the optimal camber distribution results in a reduction of the cruise drag by up to 2.9 counts from the original uncambered wing using linear theory analysis. PNS predictions are not quite as optimistic. The best reduction in cruise drag through cambering is 2.4 counts when using PNS results. The algebraic skin friction estimates are again larger than the PNS viscous drag values, but they are within 1.0 count. The differences in cruise drag coefficient range from $+0.3$ to $+2.1$ counts. The 0.3 count difference occurs when the linear theory zero-lift drag and induced drag errors cancel, and the 2.1 count difference occurs when they add.

Wing-fuselage solutions require a larger number of spanwise and lengthwise points for drag results within 1/2 count of the extrapolated zero mesh value. A $91\times91\times91$ grid is sufficient for PNS calculations and, following the pattern seen in the wing-alone grid sizes, a $91\times51\times91$ grid is chosen for the wing-fuselage Euler computations. The computational cost for the Euler and PNS solutions on an SGI *Power Challenge* R8000 are 16 minutes and 2 hours respectively. The algebraic skin friction estimates are still within 1.0 count of those from PNS. Linear theory underpredicts the cruise drag for all three designs by 0.7 to 1.3 counts.

The PNS and Euler loads match closely at the flight conditions examined. At supersonic cruise, linear theory also compares well with CFD. The same is not true for high-lift conditions where crossflow shocks appear on the wings. In these cases, linear theory predicts the loads well inboard of the shock, underestimates the loads immediately outboard of the shock, and overestimates the loads at the subsonic leading edge. Despite the good agreement in loads at cruise, differences of 21%–49% are seen in the Von Mises stresses. The differences in maximum stress are lower, but still reach 23.6%. The magnitude of the differences in stresses is reflected in the differences in the spanwise center of pressure locations. Using Euler loads in the structural

analysis results in a more inboard center of pressure and lower stresses over most of the wing. The Mach 1.2 cruise conditions show the largest regions on the wing where the stresses from Euler loads are bigger than those from linear theory loads. For Design Cases 1 and 2, the wing bending-material weights computed using Euler loads are lower than those from linear theory loads. However in Design Case 3, the larger stresses in the Mach 1.2 load case result in a heavier design using Euler loads. The bending material weights are not as sensitive as the wing stresses to the differences in loads. The difference in bending material weights is not greater than 5.6% for the three designs.

The aircraft range is sensitive to the relatively small differences in the cruise drag predictions from linear theory and Euler analyses. For the Design Case 2 cambered wing, the drag coefficient predictions from PNS, Euler, and linear theory are 79.2 counts, 78.9 counts, and 77.1 counts, respectively. While these differences are relatively small, the resulting range from linear theory is $126\,n.mi.$ larger than that predicted from PNS aerodynamics. Golovidov[69] investigated the effect of *ad hoc* changes in the drag coefficient to a baseline optimized design. Two counts were added to and subtracted from the drag coefficient, and then the design was optimized again. He found that the aircraft TOGW is also very sensitive to drag variations of this magnitude. Compensating for the linear theory cruise drag underestimate by adding 2.0 counts to the drag coefficient in the optimization procedure results in an aircraft that is $56,000\,lb$ heavier than the original design. The majority of this added weight comes from the extra fuel required to meet the range constraint.

These studies suggest that significant improvements in aircraft performance prediction are available by replacing linear theory predictions with those from CFD. For the configurations and flight conditions studied, Euler predictions are comparable to those from PNS calculations, but require significantly less computational time to perform. For this reason, it is deemed most advantageous to investigate the effects of including Euler analyses into multidisciplinary HSCT design. The computational expense of the Euler analyses prohibits its implementation in a traditional aircraft systems optimization procedure where, due to the multidisciplinary nature of the problem and the large number of constraints, *hundreds of thousands* of solutions may be required to arrive at an optimal design. For this reason, response surface models

for the Euler drag predictions are used. The following chapters present the set of simplified HSCT optimization problems that serve as testbeds for including aerodynamic predictions from Euler analyses, followed by the response surface modeling technique implemented in this study.

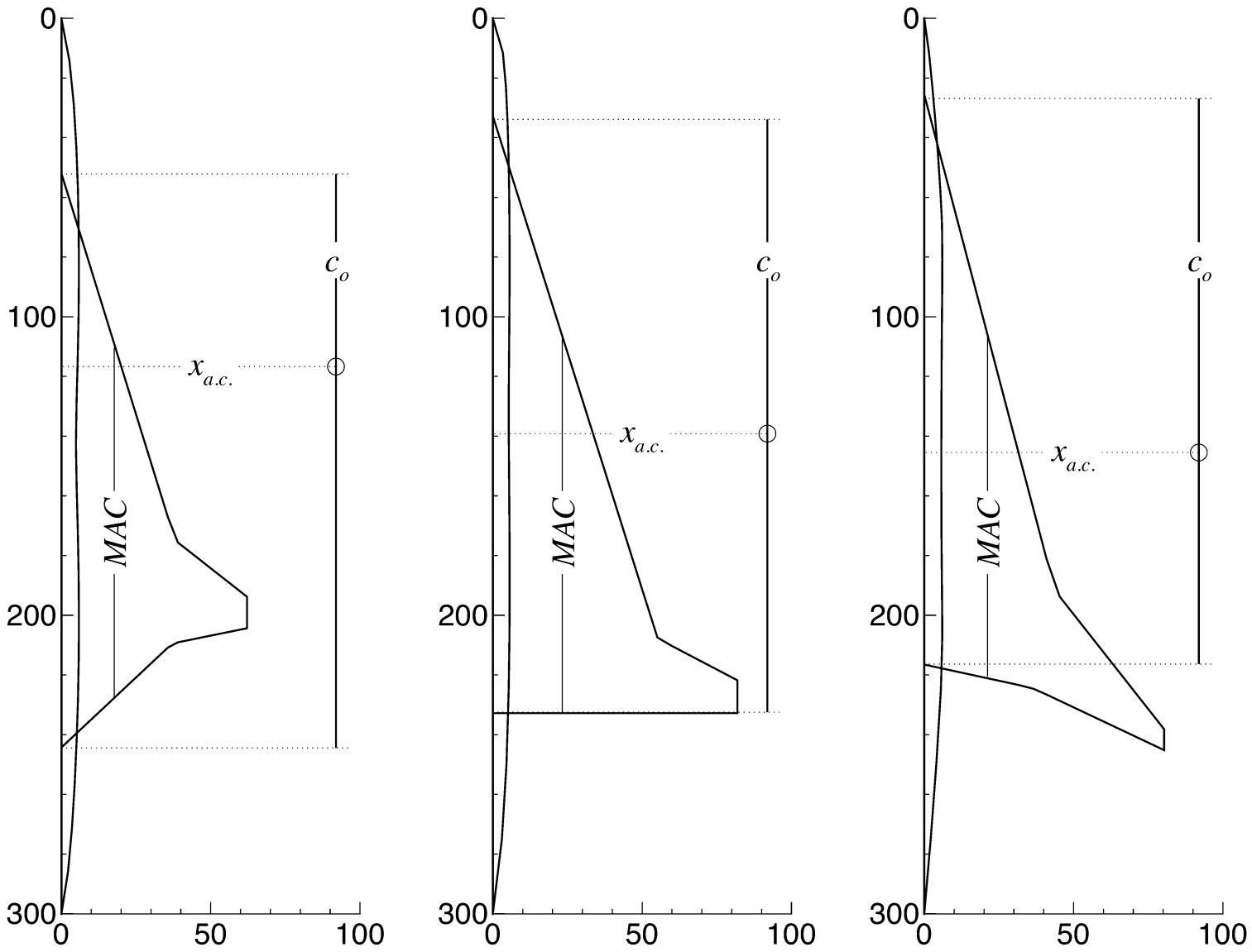


**Figure 5.1:** Aerodynamic Center Location Shift with Trailing-Edge Sweep ($M = 2.4$)

# Chapter 6

# Simplified HSCT Design Problems

A series of simplified optimization problems serve to evaluate the methods of including Euler analyses in multidisciplinary HSCT design. The design variables (Table 6.1) used to define the geometry and mission are subsets of those used in the full 29 variable design, although some appear in a different form. For example, instead of specifying the $x$ and $y$ locations of the leading edge (LE) and trailing edge (TE) break points, the simplified problems use more meaningful variables specifying the wing sweep angles and the inboard surface lengths. In the same way, the variable specifying the $x$-location of the wing tip LE is replaced with a variable stipulating the outboard LE sweep angle. The upper and lower limits of the active design variables (Table 6.2) remain the same throughout the series of optimization problems.

The simplified designs are also subject to a reduced set of constraints (Table 6.3). There are three basic reasons why certain constraints are eliminated:

1. The design variable(s) on which the constraints depend are not active.
2. Explicit limits on the design variables prevent geometric constraints from becoming active.
3. Simplifications to the mission eliminate related constraints.

Vertical tail sizing is not active for the simplified designs, therefore constraints number 47 and 48 do not appear. Unlike the 29 variable design, these configurations have no

horizontal tail. This eliminates constraints 49, 50, and 51. The engine thrust also remains constant, removing constraints 52, 67, and 68 from the active list.

A simplified five variable wing design is considered first. The ten variable design problem is an extension of the five variable problem, enabling more general planform and airfoil geometries, and allowing variation in the spanwise location of the nacelles. Fuselage shaping is enabled with the fifteen variable design. Finally, the twenty variable design provides a complete description of the wing, airfoil, fuselage, and nacelles.

## 6.1 Five Variable HSCT Design

The geometry for the five variable wing design (Fig. 6.1) is created with four design variables specifying the root chord, $c_{root}$; tip chord, $c_{tip}$; inboard leading-edge (LE) sweep angle, $\Lambda_{LE_I}$; and the thickness-to-chord ratio, $t/c$. The fifth design variable gives the fuel weight, $W_{fuel}$. The allowable ranges of values for the variables are shown in Table 6.2. These ranges are chosen using results from previous optimization studies in an attempt to bracket the optimal designs within the bounds of the design variables. To uniquely describe the aircraft, a number of geometric parameters are specified. The fuselage and vertical tail shapes remain constant. The trailing edge (TE) for these configurations is straight with no TE break. The length of the LE from the wing apex to the LE break is constant ($s_{LE_I} = 132\,ft$), as is the sweep angle of the outboard LE ($\Lambda_{LE_O} = 25°$) and the wing semispan ($b/2 = 74\,ft$). Two airfoil parameters are held fixed: the leading-edge radius parameter ($R_{LE} = 2.5$) and the chordwise location of the maximum thickness ($(x/c)_{max\text{-}t} = 40\%$). The engine thrust, spanwise nacelle positions, relative position of the wing to the fuselage, and the cruise altitude are also invariant.

The optimization problem is the minimization of the take-off gross weight (TOGW) subject to 42 constraints (Table 6.3) related to both the geometry and the mission. Side constraints limit the values of the design variables. The optimization problem can be written as

$$\begin{aligned} &\min_{\mathbf{x}\in\Re^5} TOGW\,(\mathbf{x})\,, \\ &\qquad \text{subject to:} \quad \mathbf{g}(\mathbf{x}) \leq 0, \end{aligned} \tag{6.1}$$

$$\mathbf{x_{min}} \leq \mathbf{x} \leq \mathbf{x_{max}}$$

where $\mathbf{x}$ is the five dimensional vector of design variables, and $\mathbf{g}(\mathbf{x})$ is the 42 dimensional vector of nonlinear inequality constraints. The minimum and maximum values of the design variables are given by $\mathbf{x_{min}}$ and $\mathbf{x_{max}}$.

## 6.2 Ten Variable HSCT Design

The wing planform for the ten variable design (Fig. 6.2) is created with five design variables specifying the root chord, $c_{root}$; tip chord, $c_{tip}$; semispan, $b/2$; inboard LE sweep angle, $\Lambda_{LE_I}$; and outboard LE sweep angle, $\Lambda_{LE_O}$. The airfoil sections are described using three design variables: the leading-edge radius parameter, $R_{LE}$; location of maximum thickness, $(x/c)_{max\text{-}t}$; and thickness-to-chord ratio, $t/c$. The final two variables specify the inboard nacelle placement, $y_{nacelle}$, and the mission fuel weight, $W_{fuel}$. The allowable ranges of values for these variables are shown in Table 6.2. For these configurations, the fuselage and vertical tail shapes are fixed. The length of the leading edge from the wing apex to the leading-edge break is constant ($s_{LE_I} = 132\,ft$), and the trailing edge is straight. The engine thrust, spanwise distance between nacelles, relative position of the wing to the fuselage, and the cruise altitude are also fixed.

The optimization problem is to minimize the TOGW subject to 49 constraints (Table 6.3). This can be written as

$$\begin{aligned} &\min_{\mathbf{x}\in\Re^{10}} TOGW\,(\mathbf{x})\,, \\ &\text{subject to:} \quad \mathbf{g}(\mathbf{x}) \leq 0, \\ &\qquad\qquad \mathbf{x_{min}} \leq \mathbf{x} \leq \mathbf{x_{max}} \end{aligned} \tag{6.2}$$

where $\mathbf{x}$ is the ten dimensional vector of design variables, and $\mathbf{g}(\mathbf{x})$ is the 49 dimensional vector of nonlinear inequality constraints.

## 6.3 Fifteen Variable HSCT Design

The wing planform for the fifteen variable design (Fig. 6.3) is created with six design variables specifying the root chord, $c_{root}$; tip chord, $c_{tip}$; semispan, $b/2$; inboard LE

length, $s_{LE_I}$; inboard LE sweep angle, $\Lambda_{LE_I}$; and outboard LE sweep angle, $\Lambda_{LE_O}$. The airfoil sections are described using three design variables: the leading-edge radius parameter, $R_{LE}$; location of maximum thickness, $(x/c)_{max\text{-}t}$; and thickness-to-chord ratio, $t/c$. The fuselage radii, $r_{fus_i}$, are specified at four axial locations. The final variables specify the inboard nacelle placement, $y_{nacelle}$, and fuel weight, $W_{fuel}$. The allowable ranges of values for these variables are shown in Table 6.2. For these configurations, the wing TE is straight. The vertical tail shape, engine thrust, distance between nacelles, relative position of the wing to the fuselage, and the cruise altitude are constant.

The optimization problem is the minimization of the take-off gross weight (TOGW) subject to 49 constraints (Table 6.3) related to both the geometry and the mission. Side constraints limit the values of the design variables. The optimization problem can be written as

$$\begin{aligned} \min_{\mathbf{x}\in\Re^{15}} \; & TOGW\,(\mathbf{x})\,, \\ \text{subject to:} \quad & \mathbf{g}(\mathbf{x}) \leq 0, \\ & \mathbf{x_{min}} \leq \mathbf{x} \leq \mathbf{x_{max}} \end{aligned} \tag{6.3}$$

where $\mathbf{x}$ is the fifteen dimensional vector of design variables, and $\mathbf{g}(\mathbf{x})$ is the 49 dimensional vector of nonlinear inequality constraints.

## 6.4 Twenty Variable HSCT Design

The wing planform for the twenty variable design (Fig. 6.4) is created with eight design variables specifying the root chord, $c_{root}$; tip chord, $c_{tip}$; semispan, $b/2$; inboard LE length, $s_{LE_I}$; inboard LE sweep angle, $\Lambda_{LE_I}$; outboard LE sweep angle, $\Lambda_{LE_O}$; the inboard TE length, $s_{TE_I}$; and the inboard TE sweep angle, $\Lambda_{TE_I}$. The airfoil sections are described using five design variables: the leading-edge radius parameter, $R_{LE}$; location of maximum thickness, $(x/c)_{max\text{-}t}$; and the thickness-to-chord ratios at the wing root, $(t/c)_{root}$, LE break, $(t/c)_{break}$, and wing tip, $(t/c)_{tip}$. The thickness-to-chord ratio is varied linearly between these three spanwise locations. The fuselage radii, $r_{fus_i}$, are specified at four axial locations. The final variables specify the inboard nacelle placement, $y_{nacelle}$, the separation between the inboard and outboard nacelles, $\Delta y_{nacelle}$, and fuel weight, $W_{fuel}$. The allowable ranges of values for these variables

are shown in Table 6.2. The vertical tail shape, engine thrust, relative position of the wing to the fuselage, and the cruise altitude are fixed.

The optimization problem is the minimization of the take-off gross weight (TOGW) subject to 50 constraints (Table 6.3) related to both the geometry and the mission. Side constraints limit the values of the design variables. The optimization problem can be written as

$$\begin{aligned} &\min_{\mathbf{x}\in\Re^{20}} TOGW\left(\mathbf{x}\right), \\ &\qquad \text{subject to:} \quad \mathbf{g}(\mathbf{x}) \leq 0, \\ &\qquad\qquad\qquad\quad \mathbf{x_{min}} \leq \mathbf{x} \leq \mathbf{x_{max}} \end{aligned} \tag{6.4}$$

where $\mathbf{x}$ is the twenty dimensional vector of design variables, and $\mathbf{g}(\mathbf{x})$ is the 50 dimensional vector of nonlinear inequality constraints.

**Table 6.1:** Active Design Variables in the Simplified Optimization Problems.

| | Wing Designs | | Wing/Fuselage Designs | |
|---|---|---|---|---|
| **Design Variable** | **5 Variable** | **10 Variable** | **15 Variable** | **20 Variable** |
| ***Planform Variables*** | | | | |
| $c_{root}$ | X | X | X | X |
| $c_{tip}$ | X | X | X | X |
| $b/2$ | | X | X | X |
| $s_{LE_I}$ | | | X | X |
| $\Lambda_{LE_I}$ | X | X | X | X |
| $\Lambda_{LE_O}$ | | X | X | X |
| $s_{TE_I}$ | | (straight trailing edge) | | X |
| $\Lambda_{TE_I}$ | | (straight trailing edge) | | X |
| ***Airfoil Variables*** | | | | |
| $(x/c)_{max\text{-}t}$ | | X | X | X |
| $R_{LE}$ | | X | X | X |
| $(t/c)_{root}$ | X | X | X | X |
| $(t/c)_{break}$ | | ($t/c$ constant across span) | | X |
| $(t/c)_{tip}$ | | ($t/c$ constant across span) | | X |
| ***Fuselage Variables*** | | | | |
| $x_{fus_1}$ | | | | |
| $r_{fus_1}$ | | | X | X |
| $x_{fus_2}$ | | | | |
| $r_{fus_2}$ | | | X | X |
| $x_{fus_3}$ | | | | |
| $r_{fus_3}$ | | | X | X |
| $x_{fus_4}$ | | | | |
| $r_{fus_4}$ | | | X | X |
| ***Nacelle, Mission, and Empennage Variables*** | | | | |
| $y_{nacelle}$ | | X | X | X |
| $\Delta y_{nacelle}$ | | | | X |
| $W_{fuel}$ | X | X | X | X |
| Starting Cruise Alt. | | | | |
| Cruise Climb Rate | | | | |
| Vertical Tail Area | | | | |
| Horizontal Tail Area | | (No horizontal tail) | | |
| Engine Thrust | | | | |

**Table 6.2:** Design Variable Limits in the Simplified Optimization Problems.

| Design Variable | Wing Designs | | Wing/Fuselage Designs | |
|---|---|---|---|---|
| | **5 Variable** | **10 Variable** | **15 Variable** | **20 Variable** |
| ***Planform Variables*** | | | | |
| $c_{root}$ | $150\,ft - 190\,ft$ | | | |
| $c_{tip}$ | $7\,ft - 13\,ft$ | | | |
| $b/2$ | $[74\,ft]$ | $58\,ft - 78\,ft$ | | |
| $s_{LE_I}$ | $[132\,ft]$ | | $105\,ft - 135\,ft$ | |
| $\Lambda_{LE_I}$ | $67° - 76°$ | | | |
| $\Lambda_{LE_O}$ | $[25°]$ | $12° - 32°$ | | |
| $s_{TE_I}$ | (straight trailing edge) | | | $10\,ft - 30\,ft$ |
| $\Lambda_{TE_I}$ | (straight trailing edge) | | | -55° − 16° |
| ***Airfoil Variables*** | | | | |
| $(x/c)_{max\text{-}t}$ | $[40\%]$ | $38\% - 52\%$ | | |
| $R_{LE}$ | $[2.5]$ | $2.1 - 4.1$ | | |
| $(t/c)_{root}$ | $1.5\% - 2.7\%$ | | | |
| $(t/c)_{break}$ | ($t/c$ constant across span) | | | $1.5\% - 2.7\%$ |
| $(t/c)_{tip}$ | ($t/c$ constant across span) | | | $1.5\% - 2.7\%$ |
| ***Fuselage Variables*** | | | | |
| $x_{fus_1}$ | $[50\,ft]$ | | | |
| $r_{fus_1}$ | $[5.2\,ft]$ | | $4.5\,ft - 6.0\,ft$ | |
| $x_{fus_2}$ | $[100\,ft]$ | | | |
| $r_{fus_2}$ | $[5.7\,ft]$ | | $4.5\,ft - 6.0\,ft$ | |
| $x_{fus_3}$ | $[200\,ft]$ | | | |
| $r_{fus_3}$ | $[5.9\,ft]$ | | $4.5\,ft - 6.0\,ft$ | |
| $x_{fus_4}$ | $[250\,ft]$ | | | |
| $r_{fus_4}$ | $[5.5\,ft]$ | | $4.5\,ft - 6.0\,ft$ | |
| ***Nacelle, Mission, and Empennage Variables*** | | | | |
| $y_{nacelle}$ | $[20\,ft]$ | $10\,ft - 35\,ft$ | | |
| $\Delta y_{nacelle}$ | $[6\,ft]$ | | | $6\,ft - 18\,ft$ |
| $W_{fuel}$ | No Limits | | | |
| Starting Cruise Alt. | $[65,000\,ft]$ | | | |
| Cruise Climb Rate | $[100\,ft/min]$ | | | |
| Vertical Tail Area | $[548\,ft^2]$ | | | |
| Horizontal Tail Area | (No horizontal tail) | | | |
| Engine Thrust | $[39,000\,lb]$ | | | |

$[\,\cdot\,]$ indicates value of a variable when it is not active in the design

**Table 6.3:** Active Constraints in the Simplified Optimization Problems.

| # | Constraint Description | Number of Variable | | | |
|---|---|---|---|---|---|
| | | **5** | **10** | **15** | **20** |
| 1 | Range $\geq 5,500\, n.mi.$ | X | X | X | X |
| 2 | Required $C_L$ at landing speed $\leq 1$ | X | X | X | X |
| 3–20 | Section $C_\ell \leq 2$ | X | X | X | X |
| 21 | Landing angle of attack $\leq 12°$ | | X | X | X |
| 22 | Fuel volume $\leq$ half of wing volume | X | X | X | X |
| 23 | Spike prevention | X | X | X | X |
| 24–41 | Wing chord $\geq 7.0\, ft$ | X | X | X | X |
| 42–43 | No engine scrape at landing $\alpha$ | | X | X | X |
| 44–45 | No engine scrape at landing $\alpha$, with 5° roll | | X | X | X |
| 46 | No wing tip scrape at landing | | X | X | X |
| 47 | Rudder deflection for crosswind landing $\leq 22.5°$ | | | | |
| 48 | Bank angle for crosswind landing $\leq 5°$ | | | | |
| 49 | Takeoff rotation to occur $\leq 5$ *sec* | | | | |
| 50 | Tail deflection for approach trim $\leq 22.5°$ | | | | |
| 51 | Wing root T.E. $\leq$ horiz. tail L.E. | | | | |
| 52 | Balanced field length $\leq 11,000$ *ft* | | | | |
| 53 | TE break scrape at landing with 5° roll | | X | X | X |
| 54 | LE break $\leq$ semispan | X | X | X | X |
| 55 | TE break $\leq$ semispan | | | | X |
| 56–58 | $(t/c)_{root}$, $(t/c)_{break}$, and $(t/c)_{tip} \geq 1.5\%$ | | | | |
| 59 | $x_{fus_1} \geq 5ft$ | | | | |
| 60 | $x_{fus_2} - x_{fus_1} \geq 10\, ft$ | | | | |
| 61 | $x_{fus_3} - x_{fus_2} \geq 10\, ft$ | | | | |
| 62 | $x_{fus_4} - x_{fus_3} \geq 10\, ft$ | | | | |
| 63 | $300\, ft - x_{fus_4} \geq 10\, ft$ | | | | |
| 64 | $y_{nacelle} \geq$ side-of-fuselage | | | | |
| 65 | $\Delta y_{nacelle} \geq 0$ | | | | |
| 66 | Engine-out limit with vertical tail design; otherwise $y_{nacelle} + \Delta y_{nacelle} \leq 0.5(b/2)$ | X | X | X | X |
| 67-68 | Maximum thrust required $\leq$ available thrust | | | | |
| | **Total Active Constraints** | **42** | **49** | **49** | **50** |

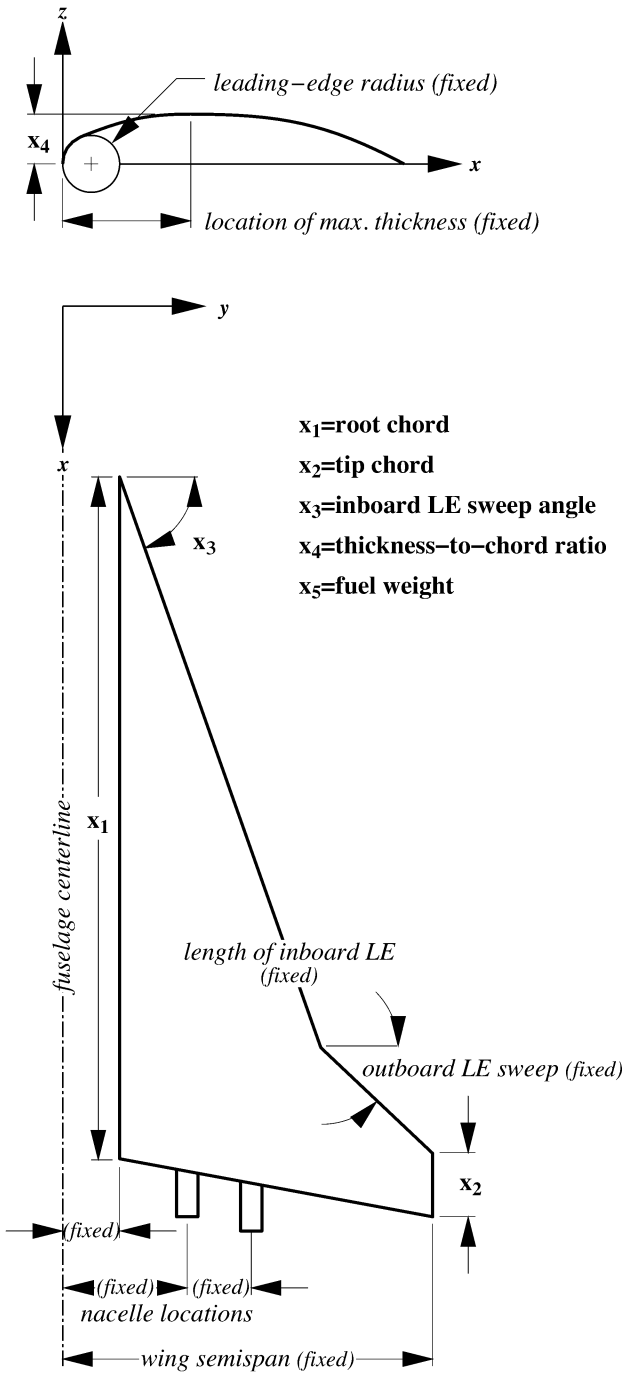


**Figure 6.1:** Geometry for Five Variable Design Problem.

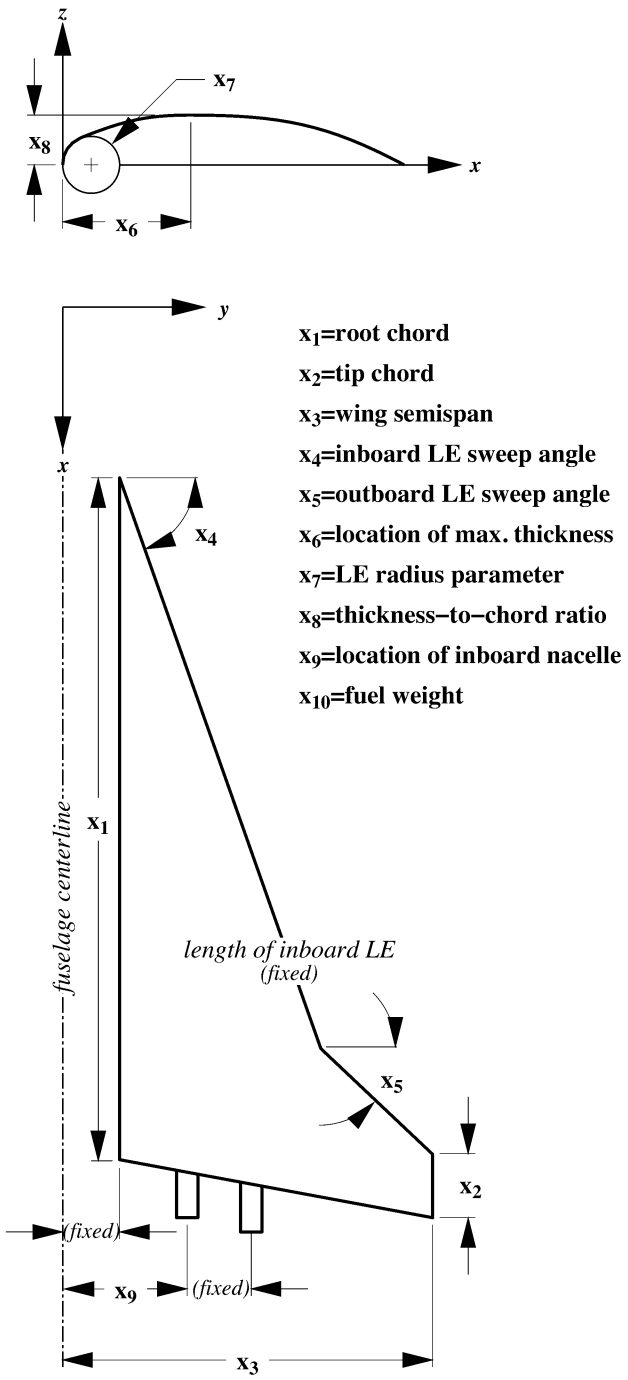


**Figure 6.2:** Geometry for Ten Variable Design Problem.

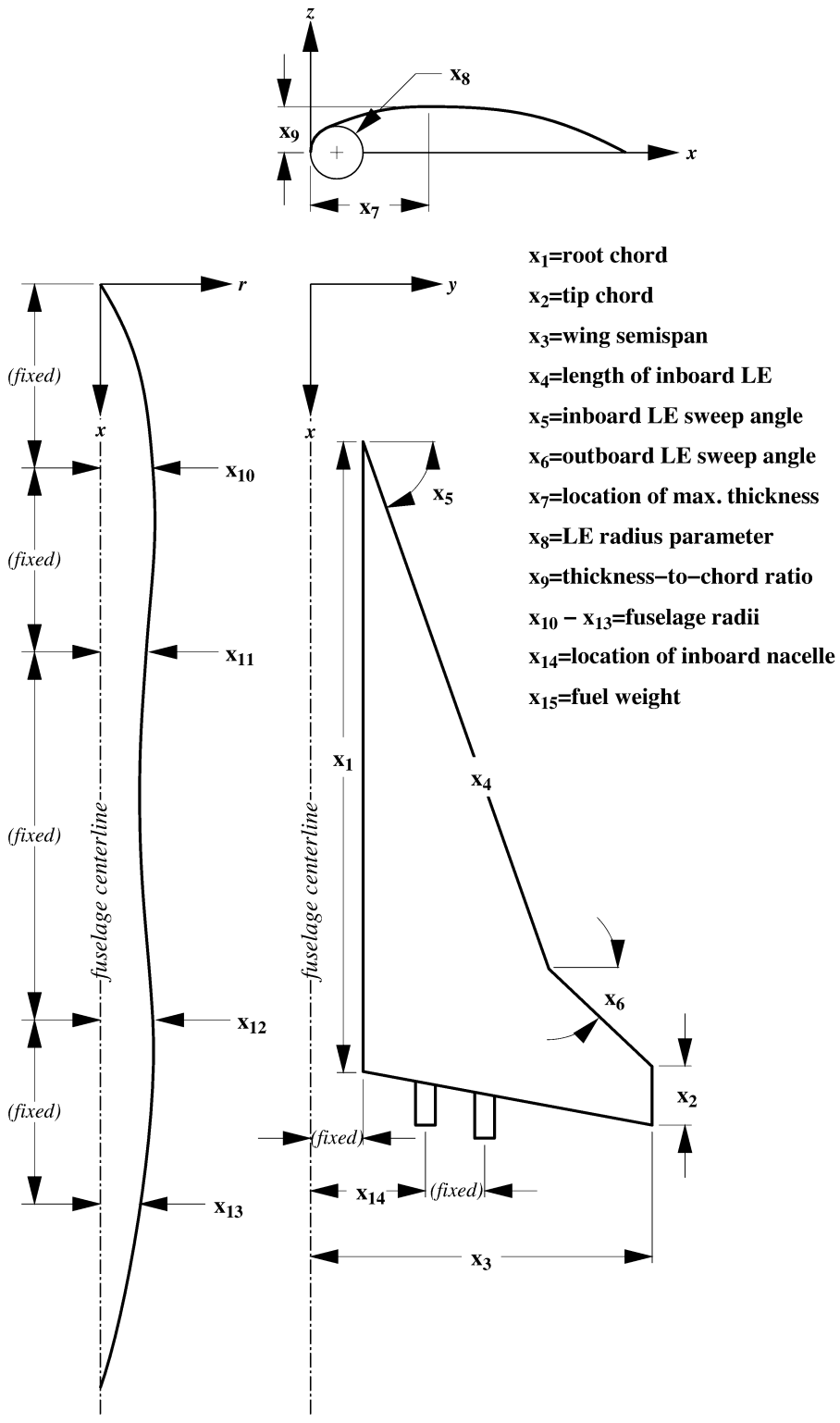


**Figure 6.3:** Geometry for Fifteen Variable Design Problem.

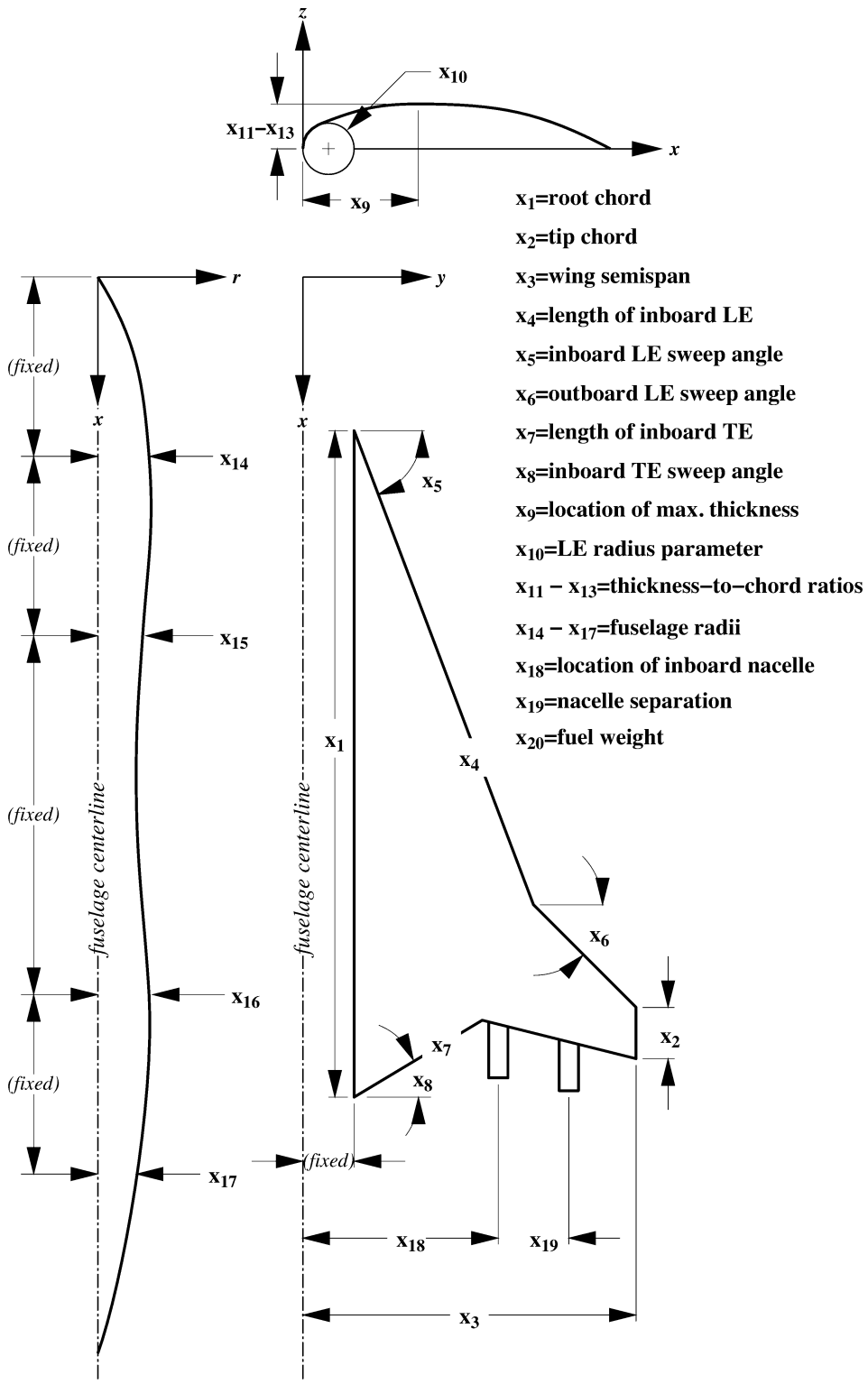


**Figure 6.4:** Geometry for Twenty Variable Design Problem.

# Chapter 7

# Response Surface Modeling

To use relatively expensive Euler solutions for the large number of constraint evaluations required in our multidisciplinary optimization, RS models of the supersonic aerodynamics are created. Response surface modeling techniques for aerodynamic and structural design improve the performance of highly constrained gradient based optimizations.[7,21,70,71] Using RS models offers a number of benefits. First, the RS models smooth out numerical noise present in the analyses. This noise can distort gradient information and lead to artificial local minima in the design space. Second, the analysis codes are separated from the optimization routines. This eliminates problems associated with integrating large, production level grid generators, analysis codes, and post processing utilities. It also allows analyses to be performed by experts in the specific discipline on parallel architecture machines. Results from parallel computing efforts are described in Chapter 11. Finally, by replacing complex analysis codes with simple quadratic polynomials, one can readily obtain information on design trade-offs, sensitivities to certain variables, and insight into the highly constrained, nonconvex design spaces. These aspects are presented in Chapters 12 and 13.

## 7.1 Design of Experiments

Design of experiments (DOE) theory provides a systematic means of selecting the set of points (called an *experimental design*) within the design space at which to perform

computational analyses. The $2^m$ vertices formed by the upper and lower bounds on the design variables define the *design bounding box* or *hypercube* within which the experimental design is created. The range of each design variable is scaled to span $[-1, 1]$ for both numerical stability and ease of notation.[25] To create the experimental design, the ranges of the design variables are discretized at evenly spaced intervals. For example, a $2^m$ full factorial design is created by specifying each design variable at two levels: the lower bound $(-1)$ and the upper bound (1). Therefore, this experimental design consists of every vertex in the design bounding box. The type of experimental design created is defined by the number of intervals and the distribution of the points on those intervals. The choice of experimental design depends on the dimension of the problem, the computational resources available, and the type of function to which one wishes to fit the data. Four types of experimental designs are used in this research: $3^m$ *full factorial experimental designs*,[72] *face centered central-composite designs*,[25,72] *small-composite designs*,[25] and *D-optimal experimental designs*.[73]

A $3^m$ full factorial design[72] is created by specifying the design variables at three levels $(-1,0,1)$ corresponding to the lower bound, midpoint, and upper bound of the design variables. A $3^3$ experimental design is presented in Fig. 7.2. This experimental design provides sufficient information to construct quadratic polynomial RS models. However, as the number of design variables increases, the number of computational experiments required becomes prohibitively large. For example, a $3^m$ full factorial design in twenty dimensional space requires $3^{20} \approx 3.5\times10^9$ computational experiments.

A face centered central-composite design[25,72] (CCD) enables resolution of quadratic terms in the RS models with fewer computational experiments. It is created by taking a $2^m$ full factorial design and adding $2m$ "star" points on the faces of the hypercube and another point in the middle of the design hypercube. The "star" points correspond to a set of design variables in which all variables are held at their midpoint value except for a single variable which is specified at either its upper or lower bound. Figure 7.3 shows a face centered CCD in three dimensions. As the number of design variables is further increased, these experimental designs also become prohibitively large. Creating a face centered CCD in a twenty dimensional space requires $2^{20} + 2 \cdot 20 + 1 \approx 1.0\times10^6$ computational experiments.

The small-composite experimental design[25] allows even fewer computational experiments with which to evaluate quadratic RS models. This experimental design is constructed in a manner similar to that for the central-composite design except that a *fractional factorial*[25] experimental design is used in place of the $2^m$ full factorial design. The fractional factorial design includes only $2^{m-\beta}$ vertices of the $m$ dimensional bounding box ($\beta$ is an integer number smaller than $m$). There is some freedom in the value of $\beta$, however it can not be too large or there will be insufficient data to properly resolve all terms in the quadratic polynomial. Certain vertices of the design space will not have any associated data when using this experimental design. While this is not an ideal situation, it is inevitable since the number of vertices grows exponentially with the number of design variables.

The final experimental design used in this study is the D-optimal experimental design.[73] D-optimal designs allow great flexibility in the number of computational experiments that is not allowed in the previously discussed experimental designs. D-optimal designs are also well suited for irregularly shaped design spaces, while the classical designs are geared toward rectangular design spaces. D-optimal designs minimize the uncertainty in the polynomial coefficient estimates and in the predicted value of the response. To create a D-optimal experimental design, one selects $p$ design points out of $q$ candidate points. In this research, the candidate points are derived from one of the three classical experimental designs described above. An iterative optimization method is then used to find the $p$ D-optimal points.

For the five and ten variable cases, the JMP[74] statistical software package is used to provide the D-optimal designs. The approach implemented in JMP uses sets of randomly selected seed candidate points, and the best points in terms of the prediction variance are kept throughout the iterative procedure. Because the design points are selected in a quasi-random manner, it is unlikely that the experimental design chosen from JMP is truly a D-optimal set. Limitations in JMP prevent its use for the larger design problems. A routine employing Mitchell's "k-exchange" method,[75] developed by Dr. Dan Haim, is used for the fifteen and twenty variable cases.

## 7.2 Functional Form of the Response

Conceptual level aerodynamic models provide useful information into basic relationships between the lift and drag coefficients. One of the simplest relationships is the uncambered form of the drag polar, which is written as

$$\begin{aligned} C_D &= C_{D_0} + K\, {C_L}^2, \\ \text{where} \quad C_{D_0} &= C_{D_0}(\mathbf{x}) \quad \text{and} \\ K &= K(\mathbf{x}) \end{aligned} \tag{7.1}$$

Knowledge of the functional form of the aircraft drag suggests using RS models for the intervening functions, $C_{D_0}$ and $K$, instead of a single RS model for the drag itself. There are a number of reasons why this approach is beneficial:

1. $C_{D_0}$ and $K$ are a function of only the geometric variables, thereby reducing the dimension of the RS model by eliminating mission related variables such as the fuel weight. The fuel weight is represented completely by $C_L$.

2. From a design standpoint, more insight is obtained from the intervening functions than from individual drag values.

3. Using knowledge of the simple aerodynamic theory enables the selection of an accurate functional form for the response without relying on the RS models to capture the correct form.

4. Experience has indicated that more accurate results are obtained by building the function from quadratic RS models for its components, instead of using a single RS model for $C_D$.

The HSCT wings have little camber since they are optimized for cruise at Mach 2.4; therefore, this form of the drag polar for uncambered wings is still fairly accurate. The error in fitting the Euler drag polars to this form is less than 0.5 count over $0.05 \leq C_L \leq 0.12$. These values of $C_L$ cover the range of cruise lift coefficients found for our HSCT designs.

## 7.3 Creating Quadratic RS Models

The procedure for creating the RS models for $C_{D_0}$ and $K$ is illustrated in Fig. 7.1. The first step is to perform an initial screening using a full factorial, central-composite, or small-composite experimental design. After creating the experimental design, geometric constraints are applied to eliminate infeasible designs. With only geometrically feasible designs from which to choose, the D-optimality criterion is used to further reduce the size of the experimental design to an acceptable size.

WINGDES is used to provide a camber distribution for each of the D-optimal design points. The lift and drag are then computed from both linear theory and Euler analysis. Since the Euler calculations are only for wing–fuselage configurations, wave drag predictions for the vertical tail and nacelles from linear theory analysis are added to the Euler drag data. The values of $C_{D_0}$ and $K$ are computed using data from two points on the drag polar. Response surface models for $C_{D_0}$ and $K$ are found from the set of computational experiments using JMP.

A quadratic response surface model in $m$ variables has the form

$$y = c_0 + \sum_{1 \le j \le m} c_j \, x_j + \sum_{1 \le j \le k \le m} c_{jk} \, x_j \, x_k, \tag{7.2}$$

where $y$ is the response, the $x_j$ are the design variables, and $c_0$, $c_j$, and $c_{jk}$ are the polynomial coefficients. There are $(m+1)(m+2)/2$ coefficients for a quadratic response surface model in $m$ variables, requiring a minimum of $(m+1)(m+2)/2$ design calculations to evaluate them. Studies by Giunta[76] *et al.* reveal that using approximately twice the minimum number of required points is sufficient to accurately compute the value of the coefficients for problems with five variables. However, as the dimension of the problem increases, the ratio of the number of points to the number of terms $p/m$ in the response surface also increases. A systematic increase from $p/m = 2.0$ in the five variable case to $p/m = 3.5$ in the twenty variable case is used to provide adequate information for accurate RS modeling. This translates to 60, 276, 720, and 1470 CFD evaluations per RS model for the 5, 10, 15, and 20 variable problems, respectively. To compute the coefficients for the quadratic RS models of both $C_{D_0}$ and $K$ for a 30 variable problem would require 4184 CFD evaluations. On a single processor of the SGI *Power Challenge* R8000, this would require over 46 days of computation! Clearly, a method must be developed which enables accurate response surface estimates with a reduced number of required CFD analyses.

## 7.4 Reduced Term RS Models

Linear theory RS models can be readily created for moderately high dimensional spaces because the evaluations are so computationally inexpensive. Regression analysis, performed to obtain the coefficients of the polynomial models, also provides a means of systematically removing terms[25] from the RS models that have little or no impact on the response through a process called *stepwise regression analysis*. Terms are eliminated using a measure of the significance level of the term called the $p$-value. This represents the probability that the coefficient of a particular term is actually zero, not the value computed. Typically, a $p$-value of 0.05 or less indicates that the term is significant in predicting the variation in the response. As the prescribed value of the $p$-value is reduced, more terms are eliminated from the RS model. At some point in the stepwise regression process, the error in the RS model fit increases noticeably, indicating that too many terms have been eliminated in order to satisfy the $p$-value limit. For this research, the statistical package JMP[74] is used to perform the stepwise regression analysis.

The root mean square (RMS) error estimate is used to indicate the error in the RS model fit. The RMS error is calculated as

$$\text{RMS error} = \sqrt{\frac{\sum_{i=1}^{N} (y_i - \hat{y}_i)^2}{N}}, \tag{7.3}$$

where $y_i$ is the observed value of the response and $\hat{y}_i$ is the predicted value of the response at the $N$ sample points. The $N$ sample points are a randomly selected subset of the points used in the initial screening experimental design not including the design points used in the creation of the RS models.

The stepwise regression technique is applied to the RS models for the linear theory aerodynamics to create *reduced term* RS models. Since the Mach 2.4 cruise regime is predominantly linear, performing regression analysis on the RS models for the linear theory aerodynamics should give a polynomial with nearly the same terms as the reduced term RS models for the Euler aerodynamics. Instead of creating quadratic RS models for the Euler results, one needs only to create the reduced term models found using linear theory analyses. Computational time is therefore not wasted evaluating coefficients which do not have a significant effect on the response.

Two approaches to implementing the reduced term models are investigated. The

first approach creates reduced term RS models for the Euler values for $C_{D_0}$ and $K$. These results are presented in Chapter 9. The second approach creates reduced term RS models for the difference between Euler and the linear theory RS models, $\Delta C_{D_0}$ and $\Delta K$. To obtain the Euler values of the response, these *correction* RS models are added to the full term quadratic linear theory RS models. The sum of the linear theory and correction RS models will be referred to as the *incremental* RS models (*i.e.* $n$ term incremental RS model = full term linear theory RS model + $n$ term correction RS models). These results are presented in Chapter 10.

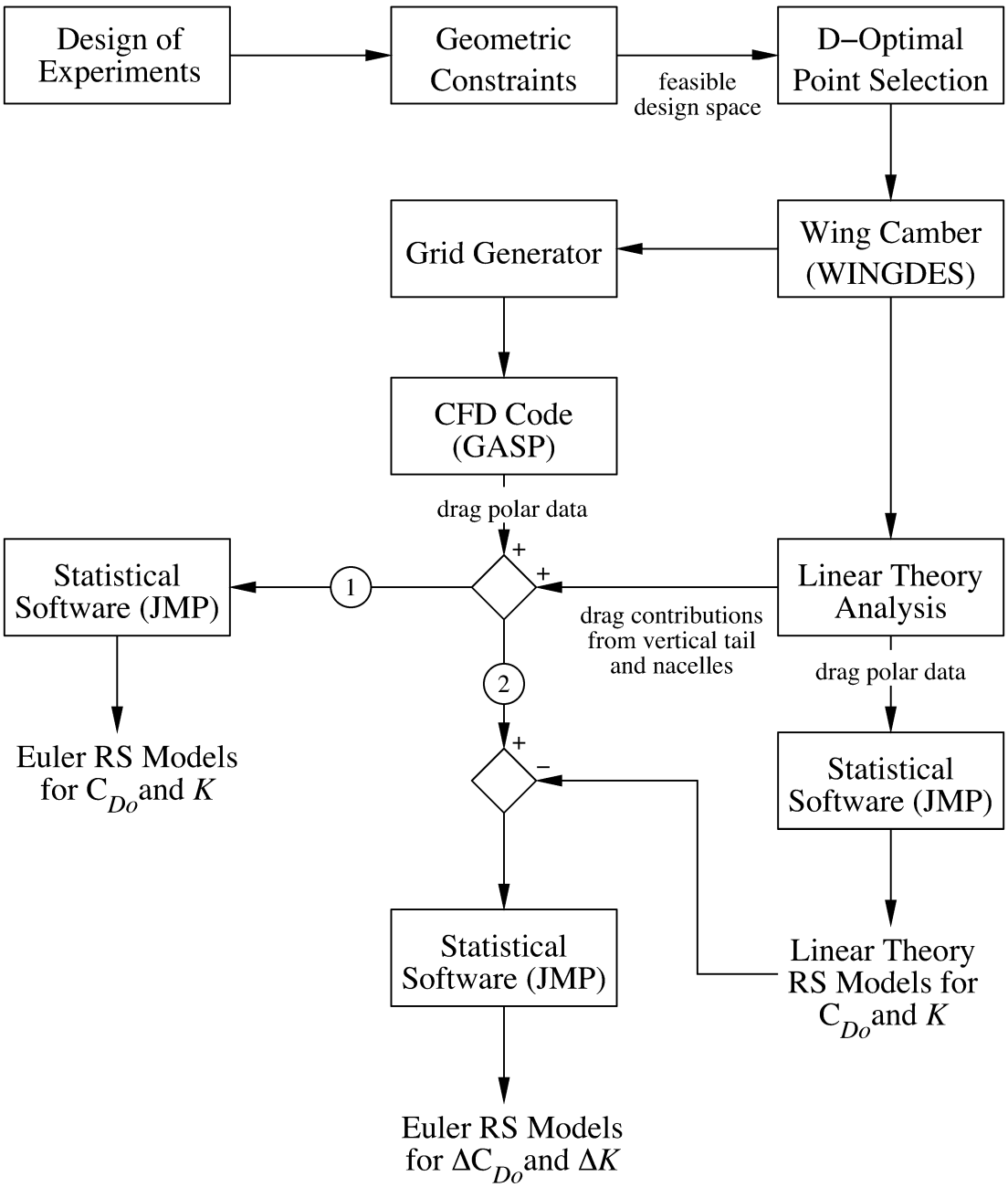


**Figure 7.1:** Flowchart for Creating RS Models.

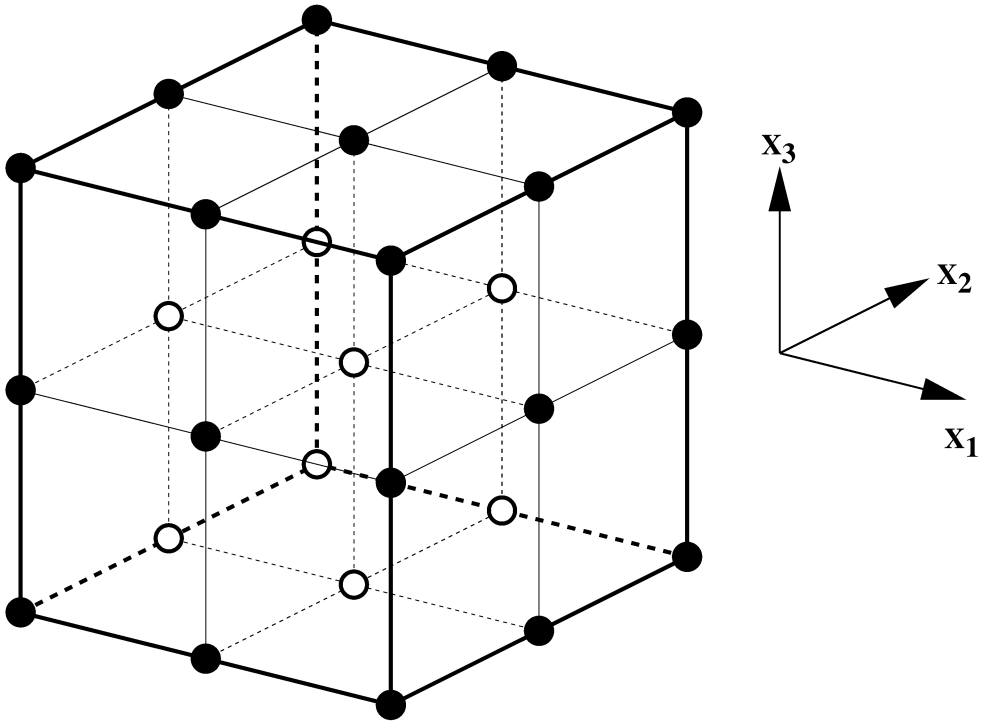


**Figure 7.2:** $3^3$ Full Factorial Experimental Design.

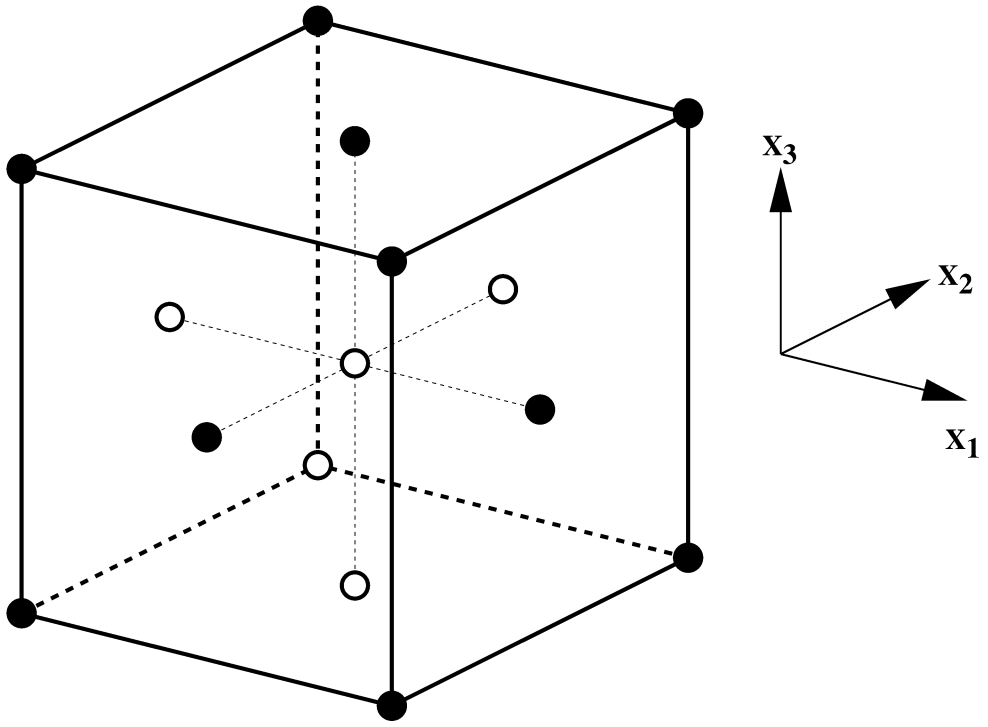


**Figure 7.3:** Face Centered Central Composite Experimental Design in Three Dimensions.

# Chapter 8

# Optimization: Full Term RS Models

In this chapter, quadratic RS models are created for the supersonic drag shape parameters from both linear theory and Euler aerodynamics. Differences in the optimal designs from linear theory and Euler RS models are directly attributed to the differences in the aerodynamic predictions. We are able to create the quadratic Euler RS models for the low-dimensional problems; however, due to the increasing computational expense, this is not practical for the twenty variable problem. Optimization results from the linear theory RS models are presented for the twenty variable design case. Optimization results from Euler RS models are presented for the five variable, ten variable, and fifteen variable problems. The Euler optima serve as baselines for evaluating the reduced term RS models in Chapters 9 and 10.

## 8.1 Five Variable HSCT Design

As discussed in Section 7.2, using knowledge of the functional form of the drag polar eliminates the fuel weight dependency of the response. Therefore, response surface models for $C_{D_0}$ and $K$ are created using only four of the five design variables. The quadratic RS models therefore have $\frac{1}{2}(4+1)(4+2) = 15$ terms instead of $\frac{1}{2}(5+1)(5+2) = 21$ terms. A $3^{m-1}$ full factorial experimental design[72] is used for the initial screening of the four variable design space, giving a total of $3^4 = 81$

design points. None of these designs are geometrically infeasible, so the D-optimality criterion is used to select the $2.0 \times n = 30$ design points to provide the computational experiments.

The accuracy of the RS models is computed using a set of 30 randomly selected designs. As described in Section 7.4, these points are selected from the set of full factorial experimental design points that are not used in the RS model creation. For the linear theory models, the RMS error in the RS value for the cruise drag coefficient is 0.59 count. This is an error relative to linear theory predictions, not Euler predictions. The RS models from Euler aerodynamics result in a similar RMS cruise drag error of 0.60 count.

Optimization is performed using six starting point designs. The design variables used to create the starting point designs (Fig. 8.1) span the prescribed ranges of the geometric variables. The choice of starting points did not effect the results of the final optimum. This indicates that the RS models are successful at removing the artificial local minima caused by numerical noise. Figure 8.2 is a graphical representation of the optimal design variable values within the allowable ranges. Each symbol represents the design variable for an optimal design which is obtained by started from one of the six starting points. There are slight variations in the design variable values do to convergence criteria.

The optimal designs found from the linear theory and Euler RS models are compared in Fig. 8.3. The corresponding design variables are given in Table 8.1. The higher drag predictions from Euler analysis result in an optimal design with a smaller thickness-to-chord ratio, $t/c$, and larger wing and fuel weights. In addition, the Euler optimum has less sweep for the inboard LE of the wing. The correlation to the increase in drag coefficient may not be intuitively obvious as first. One must realize that higher wing sweep, while reducing the supersonic drag on the inboard portion of the wing, has a concomitant increase in the size of the outboard section which has poorer supersonic characteristics. These same trends are seen in the ten variable and fifteen variable results. Chapter 12 outlines studies that make use of the RS models to investigate and understand the design trade-offs that influence these variables.

At the Euler optimum, the RS model value for the Euler drag is 0.67 count higher than the value from Euler analysis. At the linear theory optimum, the RS model value for the linear theory drag is 0.23 count higher than that from linear theory

analysis and 0.40 count lower than that from Euler analysis. The underprediction in the linear theory drag results in an optimal TOGW that is 6200 $lb$ less than that of the optimum from Euler RS models. When the drag of the linear theory optimum is adjusted to match the Euler prediction, the range drops to 5474 $n.mi.$ To correct for this deficiency, fuel weight is added until the range constraint is satisfied. When the drag predictions for both optimal designs are corrected to match the those from Euler analysis, the linear theory design turns out to be 1000 $lb$ heavier than the Euler optimum. Analyzing the linear theory optimum with an Euler analysis should result in a heavier design assuming that the global optimum from the Euler RS models has been found and that the Euler RS models are reasonably accurate at the optimal designs. In addition, the linear theory design no longer satisfies all of the constraints. Adding the fuel weight has resulted in certain section lift coefficients exceeding the maximum allowable limit.

The higher fidelity aerodynamic predictions are accompanied by an increase in the computational cost of the evaluations. An individual linear theory evaluation takes only a couple of seconds on an SGI *Power Challenge* R8000 machine, while a supersonic, space-marched Euler solution takes approximately 16 minutes. The computational time required to evaluate $C_{D_o}$ and $K$ for the 30 D-optimal designs is only 2 minutes when using linear theory analysis, but that time increases to 16 hours when using Euler analysis. This disparity in computational expense becomes worse as the dimension of the problem increases.

## 8.2 Ten Variable HSCT Design

Because of the lack of dependence on the fuel weight, the RS models for $C_{D_0}$ and $K$ are created using only nine of the ten design variables. The quadratic RS models therefore have $\frac{1}{2}(9+1)(9+2) = 55$ terms. A face centered central-composite experimental design[72] is used for the initial screening of the nine dimensional design space, giving a total of $2^9 + 2\times 9 + 1 = 531$ design points. None of these designs are geometrically infeasible, so the D-optimality criterion is used to select the $2.5\times n = 138$ design points to provide the computational experiments.

A set of 138 randomly selected points is used to evaluate the accuracy of the RS models. For the linear theory models, the RMS error in the RS value for the cruise

drag coefficient is 0.89 count. The error in the Euler RS models has increased to 1.14 counts. This indicates that the drag from Euler predictions has a more nonquadratic variation through the design space than the linear theory results.

Optimization is performed using six starting point designs. As in the five variable problem, the design variables (Fig. 8.4) used to create the starting point designs span the ranges of the variables. Depending on the starting point used in the optimization, one of two optima are reached using the Euler RS models. The design variables for these two local optima are shown in Fig. 8.5. Three of the six starting point designs led to the lightest local optima (denoted as 'A' in Fig. 8.5) and the other three led to a local optima that is 3900 $lb$ heavier (denoted as 'B' in Fig. 8.5). These local optima are a consequence of the nonconvex feasible design space resulting from the complex constraint boundaries. Chapter 13 shows an example of the types of design space and constraint boundary shapes that result in local optima. In this section, results are presented for the optimal design with the lowest TOGW.

The optimal designs found from the linear theory and Euler RS models are compared in Fig. 8.6, and the corresponding design variables are given in Table 8.2. Again we find that the higher drag predictions from Euler analysis result in an optimal design with a smaller $t/c$, larger wing and fuel weights, and less inboard LE wing sweep. Another trend appears with the inclusion of the outboard LE sweep angle as a design variable. Since Euler analysis predicts a larger drag penalty for the outboard section, the optimal design has more sweep than that from linear theory.

At the Euler optimum, the RS model value for the drag is 0.22 count lower than that from Euler analysis. At the linear theory optimum, the RS model value for the linear theory drag is 0.84 count higher than that from linear theory analysis and 0.72 count lower than that from Euler analysis. Because linear theory underpredicts the drag, the TOGW for the linear theory optimum is 2000 $lb$ lower than that of the Euler optimum. However, when both designs are evaluated using Euler analysis and fuel weight is added to correct for differences in the range predictions, the linear theory design turns out to be 1200 $lb$ heavier than the Euler optimum. In this case both methods underpredict the drag, and adding fuel weight to meet the range constraint results in other constraint violations. The computational time required to evaluate $C_{D_o}$ and $K$ for the 138 D-optimal designs is only 9 minutes when using linear theory analysis, but that time increases to 73.4 hours when using Euler analysis.

## 8.3 Fifteen Variable HSCT Design

For the fifteen-variable design, a central-composite experimental design[72] is used for the initial screening of the design space, giving a total of $2^{14}+2\times14+1=16,413$ design points. The fuselage shaping results in 400 infeasible designs. For these designs, the fuselage radii and wing thickness are such that the wing root does not intersect the fuselage. The D-optimality criterion is used to select the $3.0\times n = 360$ out of the remaining $16,013$ design points to provide the computational experiments.

A set of 360 randomly selected points is used to evaluate the accuracy of the RS models. For the linear theory models, the RMS error in the RS value for the cruise drag coefficient is 1.05 counts, and the error in the Euler RS models is 1.35 counts. The enlarged design space has hurt the accuracy of both sets of RS models.

Another set of six starting point designs whose design variables span the allowable ranges (Fig. 8.7) are used to start the optimization. In addition, the optimal designs from the 10 variable problem are used as starting points. In this case, all starting points gave rise to different local optima. The best design from the linear theory RS models came from using the 10 variable linear theory optimum as the starting point design. Similarly, the best design from the Euler RS models came from using the 10 variable Euler optimum as the starting point design. The optimal designs found from the linear theory and Euler RS models are compared in Fig. 8.8, and the corresponding design variables are given in Table 8.3. Again we find that the higher drag predictions from Euler analysis result in an optimal design with a smaller wing thickness, larger wing and fuel weights. The inboard and outboard LE wing sweep angles also show the usual trends.

At the Euler optimum, the RS model value for the Euler drag is 0.08 count higher than the value from Euler analysis. At the linear theory optimum, the RS model value for the linear theory drag is 0.38 count higher than that from linear theory analysis and 0.66 count lower than that from Euler analysis. The TOGW for the linear theory optimum is $2300\,lb$ lighter than that of the Euler optimum. However, when both designs are evaluated using Euler analysis and the results are corrected for differences in the range predictions, the linear theory design turns out to be $2800\,lb$ heavier than the Euler optimum. In addition, adding fuel weight to the linear theory optimum results in violation of other constraints. The fuel volume constraint becomes

violated, indicating that the aircraft can not hold the extra fuel required to meet the range constraint. The RS prediction for the cruise drag of the Euler optimum is within 1/10 count of the actual Euler value, resulting in a range difference of only $5\,n.mi.$. On the SGI *Power Challenge*, the computational time required to evaluate $C_{D_o}$ and $K$ for the 360 D-optimal designs is only 24 minutes when using linear theory analysis. That time expands to 192 hours when using Euler analysis. The Euler solutions were actually computed in parallel on the 119 node Intel *Paragon* XP/S at Virginia Tech. The details of this are given in Chapter 11.

## 8.4 Twenty Variable HSCT Design

A small-composite experimental design[72] is used for the initial screening of the twenty variable design space, giving a total of $2^{14} + 2\times19 + 1 = 16,423$ design points. From this set of configurations, 688 infeasible configurations are present. For some of these designs the fuselage radii and wing thickness are such that the wing root does not intersect the fuselage. Other infeasible designs (Fig. 8.9) had very small chord lengths near the wing LE break and negative taper ratios. The D-optimality criterion is used to select the $3.5\times n = 735$ out of the remaining $15,735$ design points to provide the computational experiments.

Increasing the dimension of the problem has again resulted in reduced accuracy of the response surface models. The RMS error in the linear theory RS models has increased from 1.05 counts in the 15 variable problem to 1.26 counts. The optimal design from the linear theory RS models is shown in Fig. 8.10. The cruise drag estimate from the linear theory RS models is 0.69 count higher than that from linear theory analysis and 1.9 counts lower than that from an actual Euler analysis. This reduces the aircraft range from $5500\,n.mi.$ to $5380\,n.mi.$ A large amount of additional fuel $(10,490\,lb)$ is required to compensate for this error. This gives rise to a number of constraint violations. The fuel volume constraint is violated, indicating that the aircraft is not even capable of carrying the extra fuel. The landing angle of attack and engine scrape prevention at landing angle of attack constraints also become violated with the additional fuel.

Due to computational expense, the 210 term Euler RS models were not created. To evaluate $C_{D_0}$ and $K$ for the 735 D-optimal designs would require over 16 days on

the SGI *Power Challenge* machine. The following chapters outline methods that will enable the Euler RS models to be created for problems of twenty or more variables.

**Table 8.1:** Optimal Design Variables (5 Variable HSCT Optimization).

| | **21 Term L.T. RS** | **21 Term Euler RS** |
|---|---|---|
| $c_{root}$ | $177.7\,ft$ | $174.2\,ft$ |
| $c_{tip}$ | $7.5\,ft$ | $7.8\,ft$ |
| $\Lambda_{LE_I}$ | $71.9°$ | $70.6°$ |
| $t/c$ | $1.89\%$ | $1.81\%$ |
| $W_{fuel}$ | $309,100\,lb$ | $313,200\,lb$ |
| $W_{wing}$ | $102,100\,lb$ | $103,900\,lb$ |
| $W_{TOGW}$ | $620,100\,lb$ | $626,300\,lb$ |
| Range: (Euler) | $5474\,n.mi.$ | $5544\,n.mi.$ |
| $\Delta W_{fuel}$ | $2380\,lb$ | $-4010\,lb$ |
| $W_{C-TOGW}$ | $\star 622,800\,lb$ | $621,800\,lb$ |

$\star$ Adding fuel results in constraint violation

**Table 8.2:** Optimal Design Variables (10 Variable HSCT Optimization).

| | **55 Term L.T. RS** | **55 Term Euler RS** |
|---|---|---|
| $c_{root}$ | $169.6\,ft$ | $174.3\,ft$ |
| $c_{tip}$ | $10.5\,ft$ | $7.5\,ft$ |
| $b/2$ | $71.7°$ | $72.3°$ |
| $\Lambda_{LE_I}$ | $70.6°$ | $70.1°$ |
| $\Lambda_{LE_O}$ | $12.2°$ | $26.5°$ |
| $(x/c)_{max\text{-}t}$ | 49.4% | 50.1% |
| $R_{LE}$ | 3.1 | 2.1 |
| $t/c$ | 1.93% | 1.82% |
| $y_{nacelle}$ | $29.9\,ft$ | $30.2\,ft$ |
| $W_{fuel}$ | $304,674\,lb$ | $301,000\,lb$ |
| $W_{wing}$ | $94,200\,lb$ | $99,200\,lb$ |
| $W_{TOGW}$ | $606,900\,lb$ | $608,900\,lb$ |
| Range: (Euler) | $5455\,n.mi.$ | $5485\,n.mi.$ |
| $\Delta W_{fuel}$ | $4100\,lb$ | $1300\,lb$ |
| $W_{C-TOGW}$ | $\star 611,500\,lb$ | $\star 610,300\,lb$ |

$\star$ Adding fuel results in constraint violation

**Table 8.3:** Optimal Design Variables (15 Variable HSCT Optimization).

| | **120 Term L.T. RS** | **120 Term Euler RS** |
|---|---|---|
| $c_{root}$ | $172.1\,ft$ | $166.2\,ft$ |
| $c_{tip}$ | $7.9\,ft$ | $7.7\,ft$ |
| $b/2$ | $68.3\,ft$ | $68.2\,ft$ |
| $s_{LE_I}$ | $119.2\,ft$ | $120.3\,ft$ |
| $\Lambda_{LE_I}$ | $70.9°$ | $69.4°$ |
| $\Lambda_{LE_O}$ | $16.2°$ | $23.8°$ |
| $(x/c)_{max\text{-}t}$ | 49.4% | 49.7% |
| $R_{LE}$ | 3.1 | 2.1 |
| $t/c$ | 1.95% | 1.99% |
| $r_{fus_1}$ | $5.2\,ft$ | $5.1\,ft$ |
| $r_{fus_2}$ | $5.6\,ft$ | $5.6\,ft$ |
| $r_{fus_3}$ | $5.6\,ft$ | $5.6\,ft$ |
| $r_{fus_4}$ | $5.1\,ft$ | $5.2\,ft$ |
| $y_{nacelle}$ | $28.1\,ft$ | $28.0\,ft$ |
| $W_{fuel}$ | $298,700\,lb$ | $300,100\,lb$ |
| $W_{wing}$ | $87,500\,lb$ | $87,900\,lb$ |
| $W_{TOGW}$ | $589,800\,lb$ | $591,500\,lb$ |
| Range: (Euler) | $5460\,n.mi.$ | $5505\,n.mi.$ |
| $\Delta W_{fuel}$ | $3600\,lb$ | $-440\,lb$ |
| $W_{C-TOGW}$ | $\star 593,800\,lb$ | $591,000\,lb$ |

$\star$ Adding fuel results in constraint violation

**Table 8.4:** Optimal Design Variables (20 Variable HSCT Optimization).

| | **210 Term L.T. RS** |
|---|---|
| $c_{root}$ | $167.1\,ft$ |
| $c_{tip}$ | $8.5\,ft$ |
| $b/2$ | $68.1\,ft$ |
| $s_{LE_I}$ | $125.8\,ft$ |
| $\Lambda_{LE_I}$ | $70.9°$ |
| $\Lambda_{LE_O}$ | $29.1°$ |
| $s_{TE_I}$ | $16.3\,ft$ |
| $\Lambda_{TE_I}$ | $-24.8°$ |
| $(x/c)_{max\text{-}t}$ | $50.6\%$ |
| $R_{LE}$ | $3.3$ |
| $(t/c)_{root}$ | $2.01\%$ |
| $(t/c)_{break}$ | $1.59\%$ |
| $(t/c)_{tip}$ | $1.79\%$ |
| $r_{fus_1}$ | $5.0\,ft$ |
| $r_{fus_2}$ | $5.8\,ft$ |
| $r_{fus_3}$ | $5.8\,ft$ |
| $r_{fus_4}$ | $4.7\,ft$ |
| $y_{nacelle}$ | $18.6\,ft$ |
| $W_{fuel}$ | $289,200\,lb$ |
| $W_{wing}$ | $89,700\,lb$ |
| $W_{TOGW}$ | $584,900\,lb$ |
| Range: (Euler) | $5380\,n.mi.$ |
| $\Delta W_{fuel}$ | $10,490\,lb$ |
| $W_{C-TOGW}$ | $\star 596,500\,lb$ |

$\star$ Adding fuel results in constraint violation

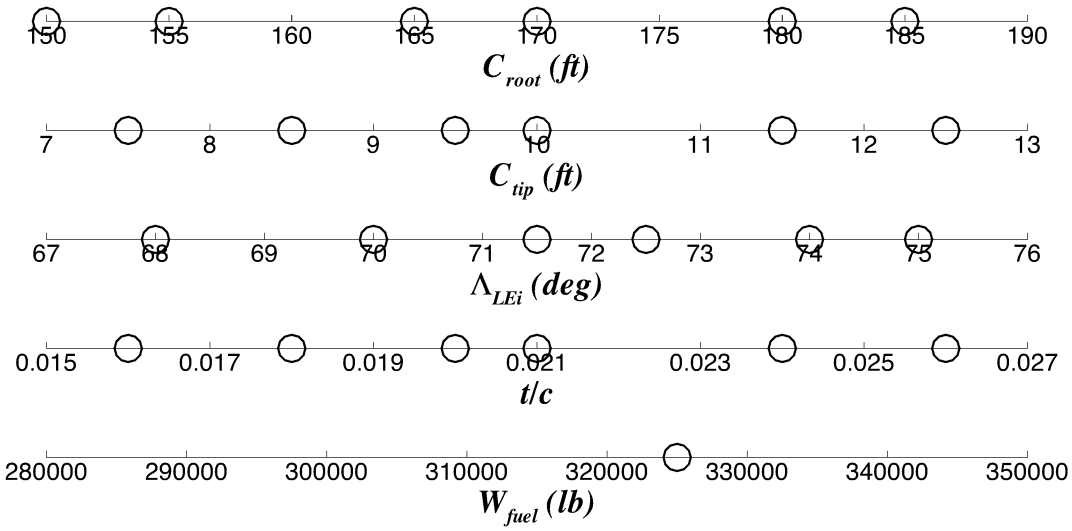


**Figure 8.1:** Starting Point Designs Variables (5 Variable HSCT Design).

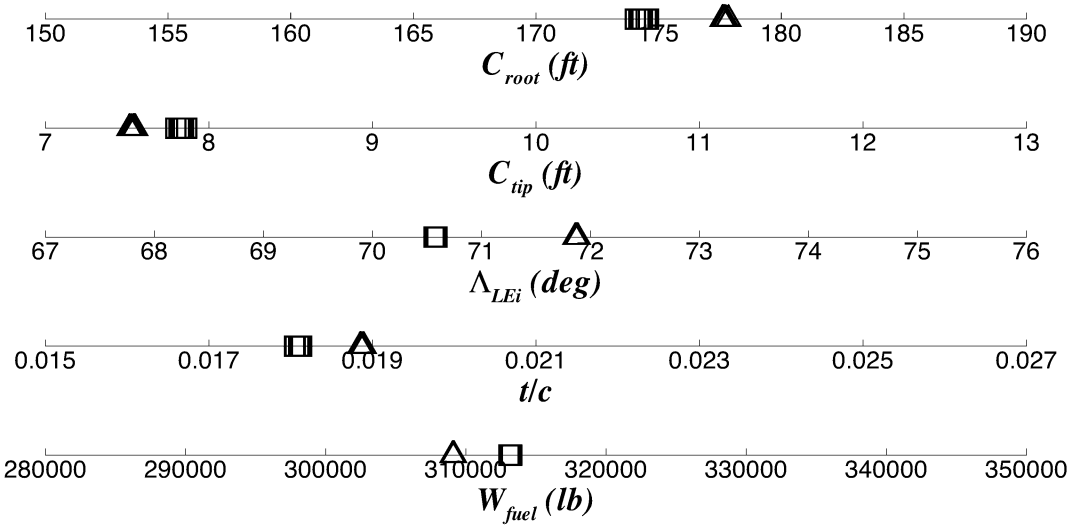


□ Optimal Design Variables (Euler RS Models)
△ Optimal Design Variables (Linear Theory RS Models)

**Figure 8.2:** Optimal Designs Variables (5 Variable HSCT Design).

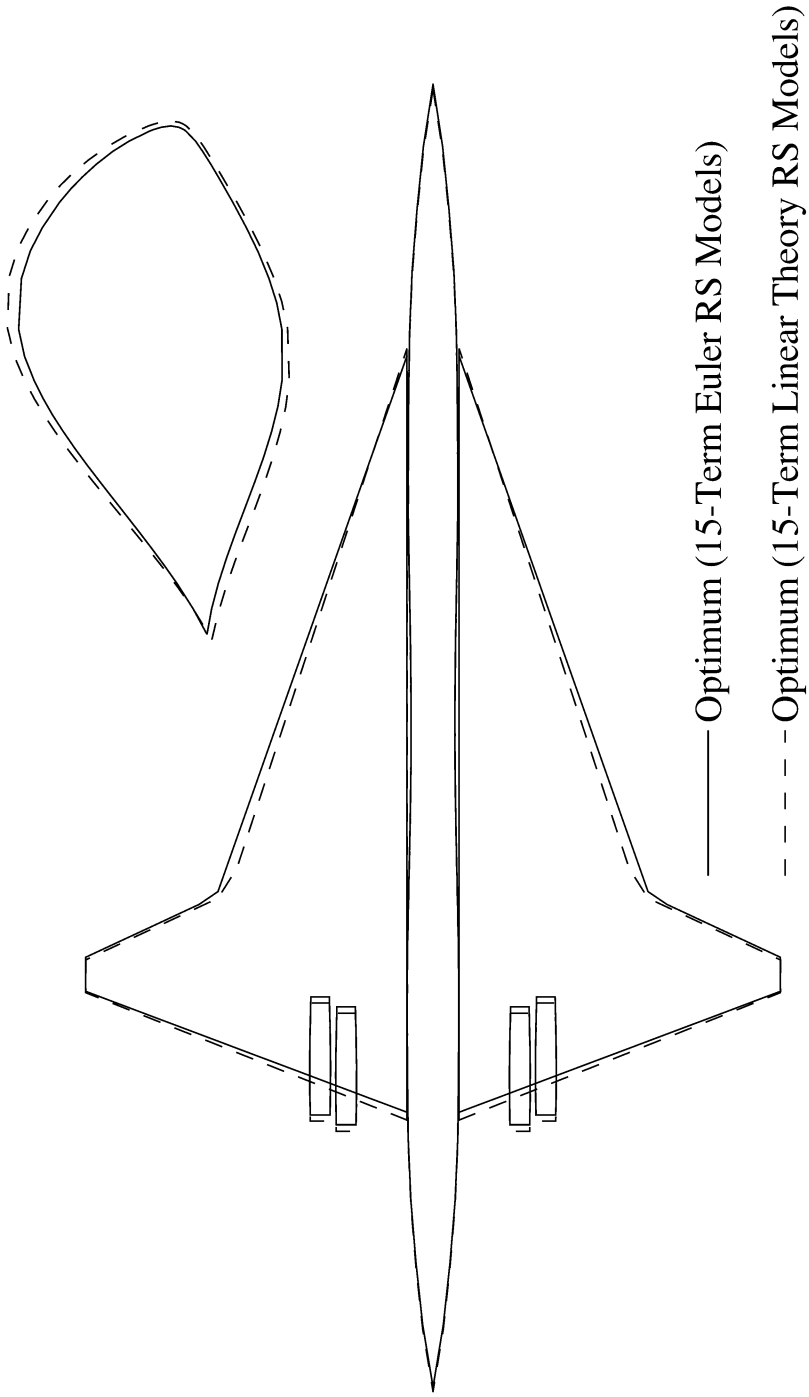


**Figure 8.3:** Optimal Designs from Linear Theory and Euler RS Models.

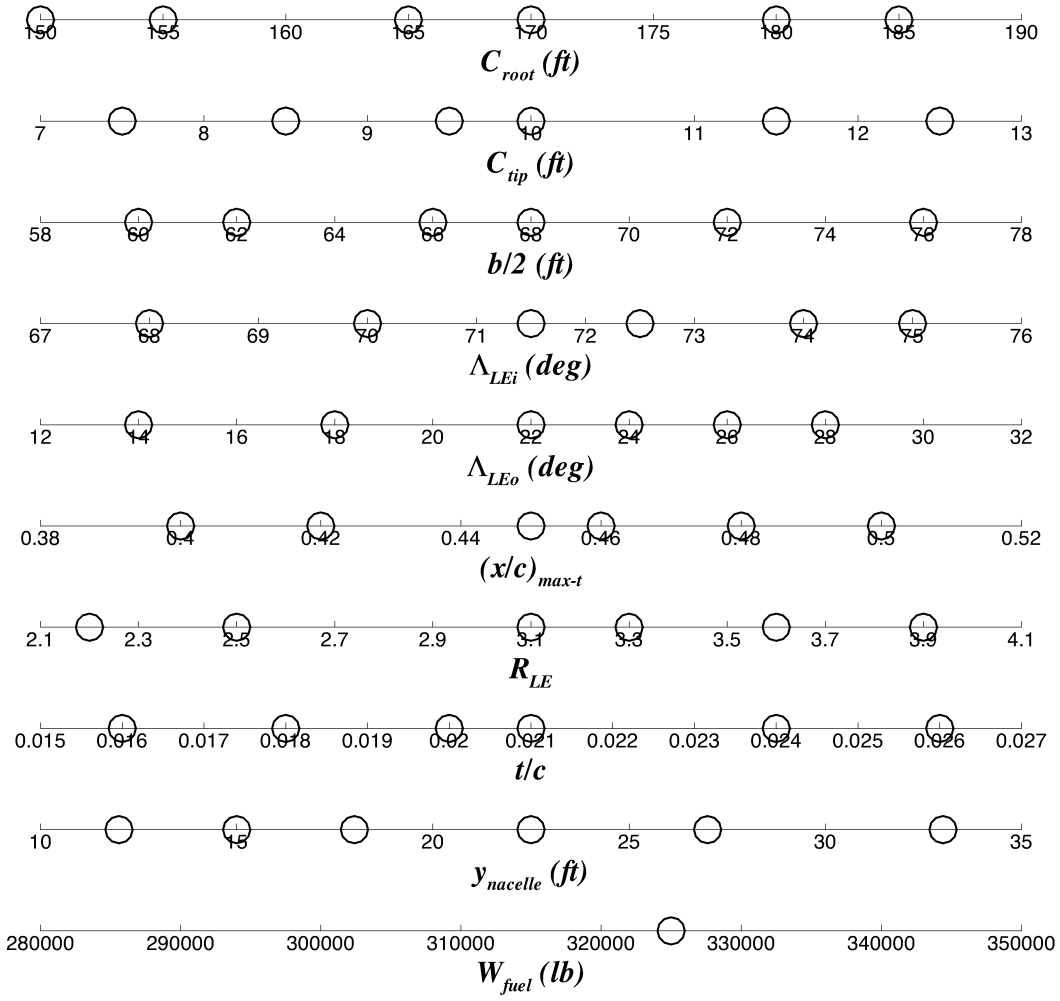


**Figure 8.4:** Starting Point Designs Variables (10 Variable HSCT Design).

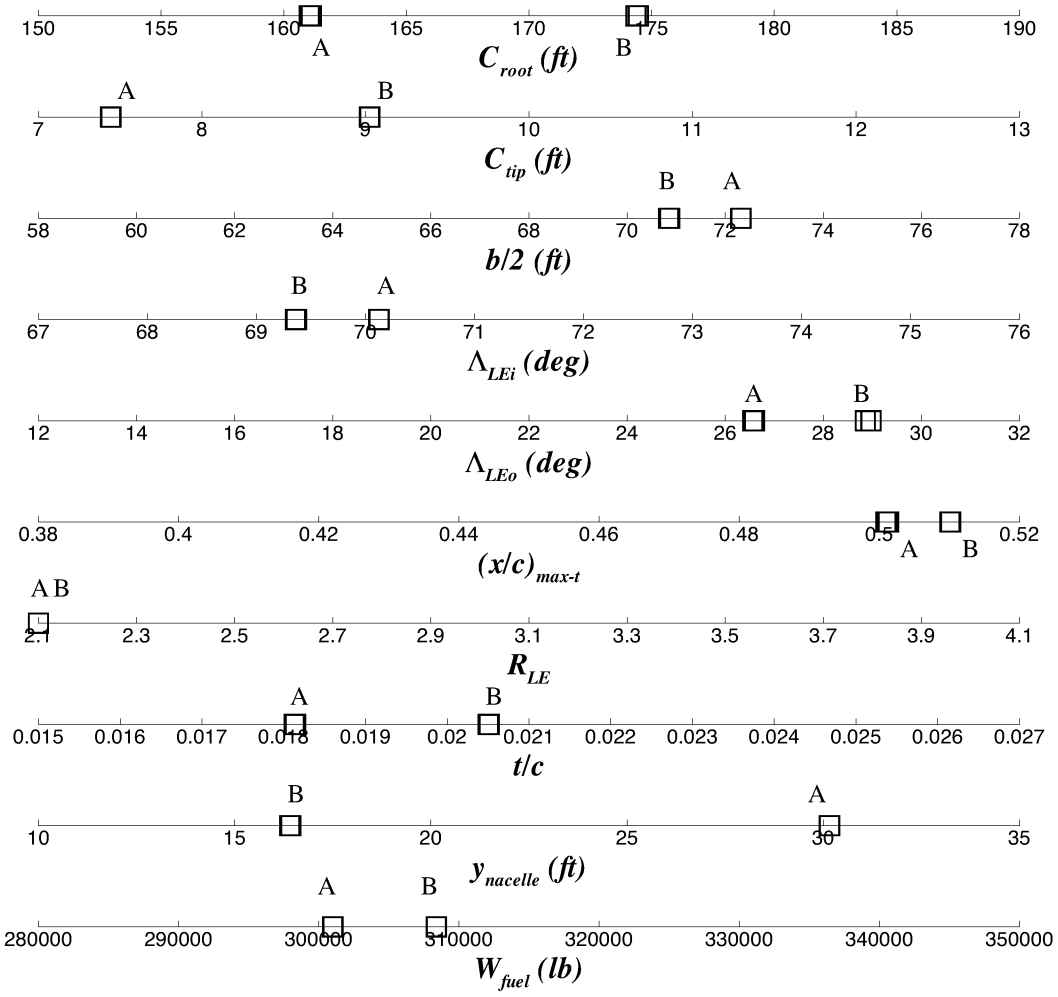


**Figure 8.5:** Optimal Designs Variables (10 Variable HSCT Design).

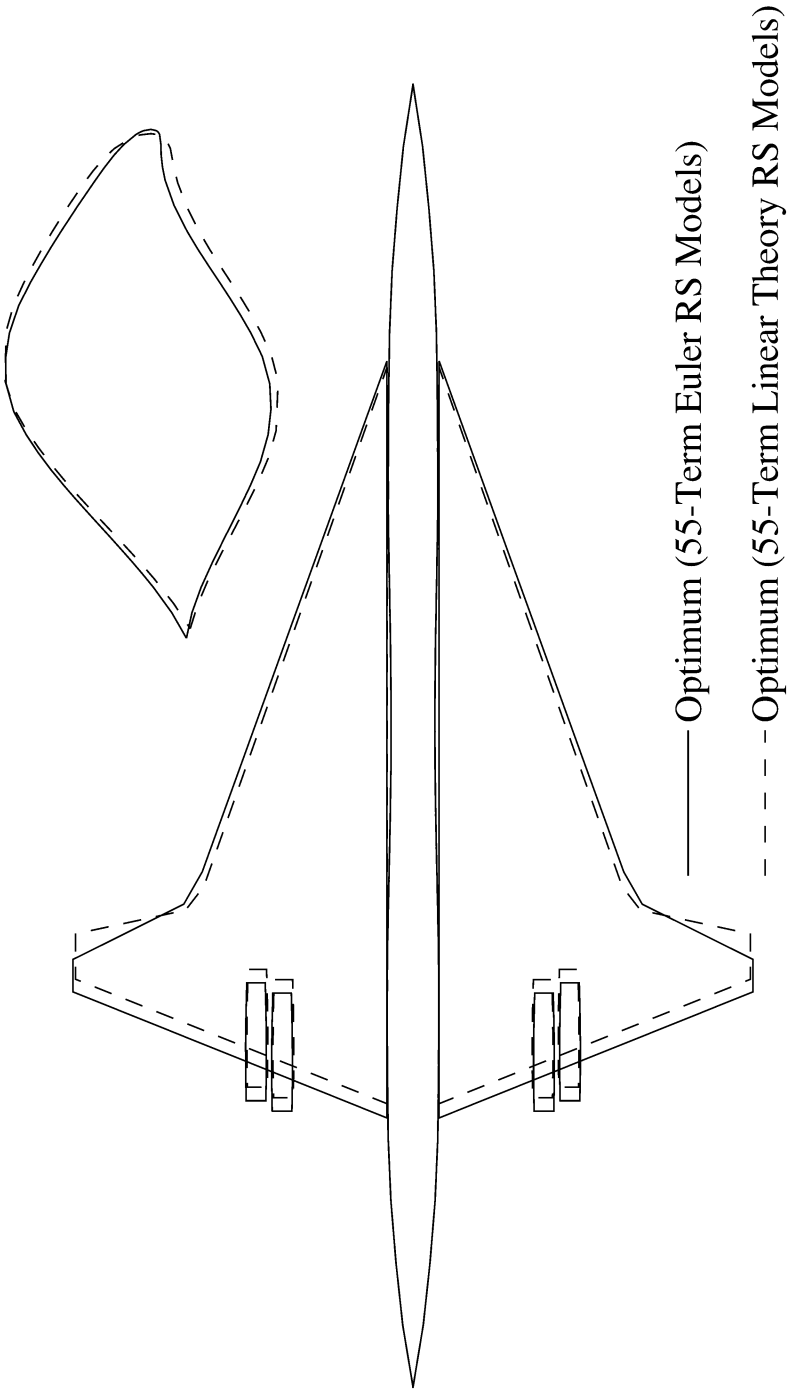


**Figure 8.6:** Optimal Designs from Linear Theory and Euler RS Models.

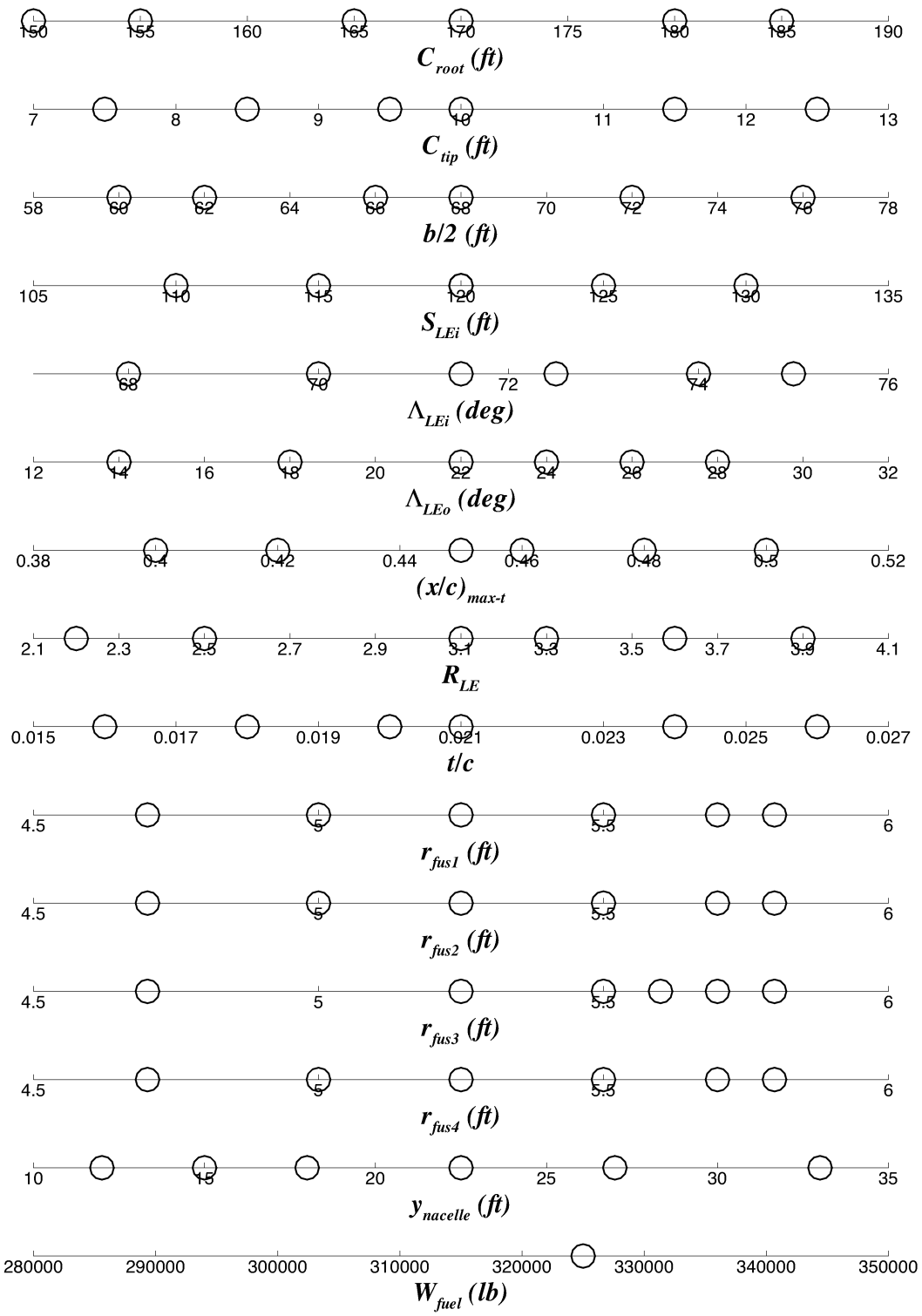


**Figure 8.7:** Starting Point Designs Variables (15 Variable HSCT Design).

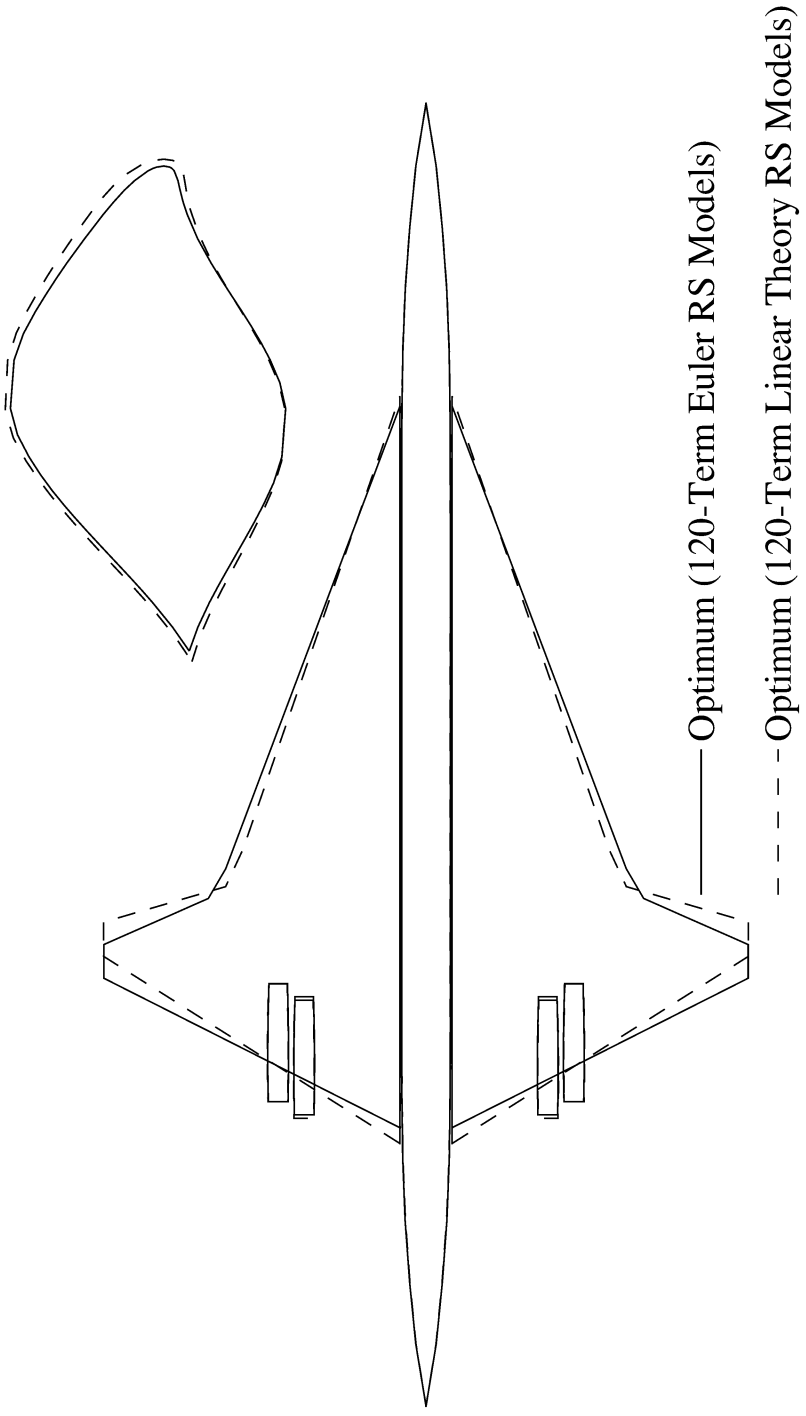


**Figure 8.8:** Optimal Designs from Linear Theory and Euler RS Models.

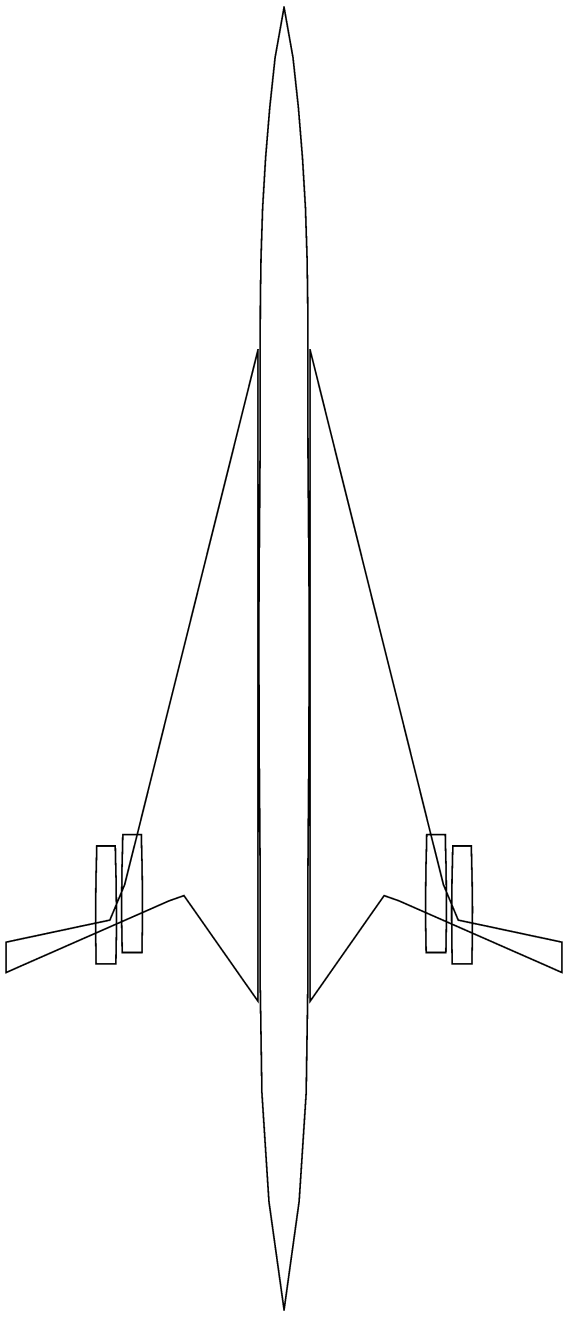

**Figure 8.9:** Infeasible Geometry from Screening Experimental Design

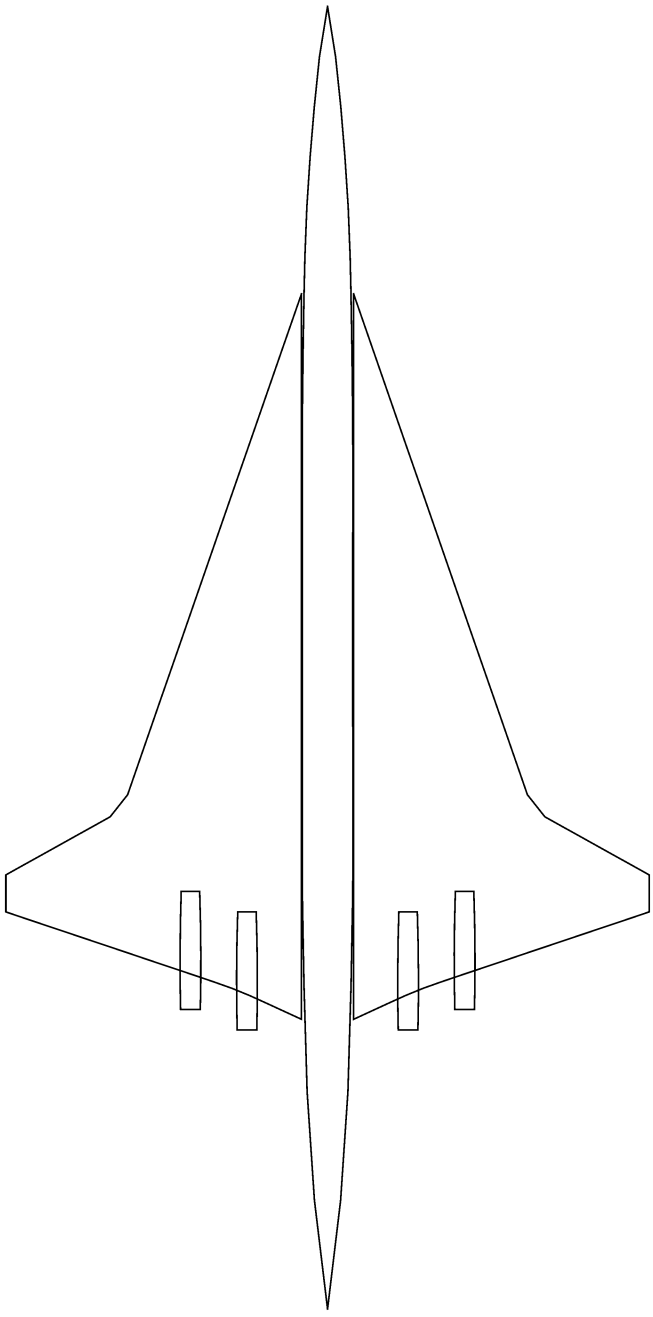

**Figure 8.10:** Optimal Design from Linear Theory RS Models.

# Chapter 9

# Optimization: Reduced Term Euler RS Models

Creating *reduced term* RS models for the Euler drag shape parameters is the first attempt made to enable implementation of CFD analyses in high-dimensional MDO problems. The technique takes advantage of knowledge of the flow physics and results from lower fidelity methods to more efficiently create RS models for the Euler aerodynamics.

## 9.1 Five Variable HSCT Design

Results from stepwise regression analysis for the five variable design are shown in Fig. 9.1. This figure shows the RMS errors in the response surface prediction of the cruise drag coefficient computed at the same randomly selected points used in evaluating the errors of the models in Section 8.1. The two lines on the plot graph the RMS errors in the linear theory RS models with respect to the linear theory values and the RMS errors in the Euler RS models with respect to the actual Euler predictions. The results are plotted in terms of drag *counts*, where a change of one drag count is equal to a change in $C_D$ of $1\times10^{-4}$. Terms are removed from the RS models using information from the stepwise regression analysis on the *linear theory data*. These models are then applied to Euler data without performing another stepwise regression analysis on the *Euler data*. This is done because, as the dimension of the problem

becomes large, it will not be possible to compute the full term Euler RS models. Such is true for the 20 variable problem.

The stepwise regression plot demonstrates two aspects that are vital to the success of the reduced term model approach. First, the stepwise regression technique is successful in eliminating unimportant terms from the response surface models. A large number of terms can be removed with little or no effect on the error. The second important aspect is that the curves from linear theory and Euler models have similar behavior. Most importantly, the errors in the linear theory and Euler RS models begin to grow near the same point as far as the number of terms in the polynomial. This indicates that linear theory analysis does reveal the terms that are important to the Euler analyses.

Accurate results can be obtained using only seven of the original fifteen terms in the response surface model. Table 9.4 contains a complete listing of the seven terms that remain and those that are removed. The terms that remain are the intercept, $c_{root}$, $\Lambda_{LE_I}$, $t/c$, $\Lambda_{LE_I} \cdot \Lambda_{LE_I}$, $t/c \cdot \Lambda_{LE_I}$, and $t/c \cdot t/c$. From an aerodynamic standpoint the choice of these terms (predicted by purely statistical means) is sound. The thickness-to-chord ratio and the LE sweep angle should have the largest effect on the supersonic drag predictions. In addition, the tip chord length should have the smallest effect.

Fig. 9.2 shows good comparison between the optima from the 15 term and 7 term models. The design variables are presented in Table 9.1. The cruise drag prediction from the 7 term RS model is 0.7 counts higher than that from Euler analysis. When $W_{TOGW}$ is corrected for the difference in the range prediction, $W_{C-TOGW}$ is only $400\,lb$ different than that from the 15 term RS models.

## 9.2 Ten Variable HSCT Design

As in the five variable case, using results from linear theory stepwise regression is successful in eliminating unimportant terms from the Euler response surface models. Errors in the RS model prediction of the cruise drag coefficient from stepwise regression analysis are shown in Fig. 9.3. A 24 term model is chosen using the for the reduced term RS models. Table 9.4 contains a complete listing of the terms that are

retained and those that are removed. Fig. 9.4 shows good comparison between the optima from the 55 term and 24 term models. The design variables are presented in Table 9.2. The cruise drag prediction from the 24 Term RS model is equal to that from Euler analysis, so no corrections to the TOGW are required.

## 9.3 Fifteen Variable HSCT Design

Regression analysis for the 15 variable design problem shows little change in the RMS error in cruise drag prediction down to about 58 terms. Table 9.4 contains a complete listing of the terms that are retained and those that are removed. The optimal designs from the 58 term and 120 term RS models are compared in Table 9.3 and Fig. 9.6. Although the optimal design from the 58 term RS models is geometrically similar to that from the full term RS model, there is large error in the cruise drag prediction. The RS model prediction for the cruise drag is 2.1 counts lower than that from an actual Euler analysis. The actual range of the aircraft is 5367 $n.mi.$ instead of 5500 $n.mi.$ When fuel weight is added to correct for the range, the TOGW is 2700 $lb$ larger than that from the full term RS models. These large errors in the drag prediction are not acceptable. A more accurate method is needed to provide Euler predictions at reasonable computational cost. The incremental RS models discussed in the next chapter show promise in this endeavor.

**Table 9.1:** Optimal Design Variables (5 Variable HSCT Optimization).

| | **7 Term Euler RS** | **15 Term Euler RS** |
|---|---|---|
| $c_{root}$ | $173.6\,ft$ | $174.2\,ft$ |
| $c_{tip}$ | $7.9\,ft$ | $7.8\,ft$ |
| $\Lambda_{LE_I}$ | $70.5°$ | $70.6°$ |
| $t/c$ | $1.83\%$ | $1.81\%$ |
| $W_{fuel}$ | $314,200\,lb$ | $313,200\,lb$ |
| $W_{wing}$ | $103,600\,lb$ | $103,900\,lb$ |
| $W_{TOGW}$ | $626,900\,lb$ | $626,300\,lb$ |
| Range: (Euler) | $5554\,n.mi.$ | $5544\,n.mi.$ |
| $\Delta W_{fuel}$ | $-4960\,lb$ | $-4010\,lb$ |
| $W_{C-TOGW}$ | $621,400\,lb$ | $621,800\,lb$ |

**Table 9.2:** Optimal Design Variables (10 Variable HSCT Optimization).

| | **24 Term Euler RS** | **55 Term Euler RS** |
|---|---|---|
| $c_{root}$ | $173.3\,ft$ | $174.3\,ft$ |
| $c_{tip}$ | $7.8\,ft$ | $7.5\,ft$ |
| $b/2$ | $72.4\,ft$ | $72.3\,ft$ |
| $\Lambda_{LE_I}$ | $70.0°$ | $70.1°$ |
| $\Lambda_{LE_O}$ | $24.6°$ | $26.5°$ |
| $(x/c)_{max\text{-}t}$ | $52.0\%$ | $50.1\%$ |
| $R_{LE}$ | $2.1$ | $2.1$ |
| $t/c$ | $1.88\%$ | $1.82\%$ |
| $y_{nacelle}$ | $30.2\,ft$ | $30.2\,ft$ |
| $W_{fuel}$ | $304,600\,lb$ | $301,000\,lb$ |
| $W_{wing}$ | $98,300\,lb$ | $99,200\,lb$ |
| $W_{TOGW}$ | $611,500\,lb$ | $608,900\,lb$ |
| Range: (Euler) | $5500\,n.mi.$ | $5485\,n.mi.$ |
| $\Delta W_{fuel}$ | $0\,lb$ | $1300\,lb$ |
| $W_{C-TOGW}$ | $611,500\,lb$ | $610,300\,lb$ |

**Table 9.3:** Optimal Design Variables (15 Variable HSCT Optimization).

| | **58 Term Euler RS** | **120 Term Euler RS** |
|---|---|---|
| $c_{root}$ | $168.4\,ft$ | $166.2\,ft$ |
| $c_{tip}$ | $7.5\,ft$ | $7.7\,ft$ |
| $b/2$ | $67.9°$ | $68.2°$ |
| $s_{LE_I}$ | $121.5\,ft$ | $120.3\,ft$ |
| $\Lambda_{LE_I}$ | $70.3°$ | $69.4°$ |
| $\Lambda_{LE_O}$ | $24.3°$ | $23.8°$ |
| $(x/c)_{max\text{-}t}$ | 51.5% | 49.7% |
| $R_{LE}$ | 2.10 | 2.10 |
| $t/c$ | 1.98% | 1.99% |
| $r_{fus_1}$ | $5.2\,ft$ | $5.1\,ft$ |
| $r_{fus_2}$ | $5.5\,ft$ | $5.6\,ft$ |
| $r_{fus_3}$ | $5.5\,ft$ | $5.6\,ft$ |
| $r_{fus_4}$ | $5.2\,ft$ | $5.2\,ft$ |
| $y_{nacelle}$ | $27.6\,ft$ | $28.0\,ft$ |
| $W_{fuel}$ | $291,100\,lb$ | $300,100\,lb$ |
| $W_{wing}$ | $87,100\,lb$ | $87,900\,lb$ |
| $W_{TOGW}$ | $581,000\,lb$ | $591,500\,lb$ |
| Range: (Euler) | $5367\,n.mi.$ | $5505\,n.mi.$ |
| $\Delta W_{fuel}$ | $11,650\,lb$ | $-440\,lb$ |
| $W_{C-TOGW}$ | $\star 593,700\,lb$ | $591,000\,lb$ |

$\star$ Adding fuel results in constraint violation

**Table 9.4:** Significant Terms in the RS Models.

| Term | # DV 5 | 10 | 15 | 20 |
|---|---|---|---|---|
| *intercept* | X | X | X | X |
| $c_{root}$ | X | X | X | X |
| $c_{tip}$ | | X | X | X |
| $b/2$ | ▬ | X | X | X |
| $s_{LE_I}$ | ▬ | ▬ | X | X |
| $\Lambda_{LE_I}$ | X | X | X | X |
| $\Lambda_{LE_O}$ | ▬ | X | X | X |
| $s_{TE_I}$ | ▬ | ▬ | ▬ | X |
| $\Lambda_{TE_I}$ | ▬ | ▬ | ▬ | X |
| $(x/c)_{max\text{-}t}$ | ▬ | X | X | X |
| $R_{LE}$ | ▬ | X | X | X |
| $(t/c)_{root}$ | X | X | X | X |
| $(t/c)_{tip}$ | ▬ | ▬ | ▬ | X |
| $(t/c)_{break}$ | ▬ | ▬ | ▬ | X |
| $r_{fus_1}$ | ▬ | ▬ | X | X |
| $r_{fus_2}$ | ▬ | ▬ | X | X |
| $r_{fus_3}$ | ▬ | ▬ | X | X |
| $r_{fus_4}$ | ▬ | ▬ | X | X |
| $y_{nacelle}$ | ▬ | | X | |
| $\Delta y_{nacelle}$ | ▬ | ▬ | ▬ | |
| $c_{root} \cdot c_{root}$ | | | | |
| $c_{tip} \cdot c_{root}$ | | | X | |
| $c_{tip} \cdot c_{tip}$ | | | | |
| $b/2 \cdot c_{root}$ | ▬ | X | X | X |
| $b/2 \cdot c_{tip}$ | ▬ | | | X |
| $b/2 \cdot b/2$ | ▬ | | | |
| $s_{LE_I} \cdot c_{root}$ | ▬ | ▬ | X | X |
| $s_{LE_I} \cdot c_{tip}$ | ▬ | ▬ | | X |
| $s_{LE_I} \cdot b/2$ | ▬ | ▬ | X | X |
| $s_{LE_I} \cdot s_{LE_I}$ | ▬ | ▬ | | |
| $\Lambda_{LE_I} \cdot c_{root}$ | | X | X | X |
| $\Lambda_{LE_I} \cdot c_{tip}$ | | X | X | |
| $\Lambda_{LE_I} \cdot b/2$ | ▬ | | X | X |
| $\Lambda_{LE_I} \cdot s_{LE_I}$ | ▬ | ▬ | X | X |
| $\Lambda_{LE_I} \cdot \Lambda_{LE_I}$ | X | X | X | X |

| Term | # DV 5 | 10 | 15 | 20 |
|---|---|---|---|---|
| $\Lambda_{LE_O} \cdot c_{root}$ | ▬ | X | X | X |
| $\Lambda_{LE_O} \cdot c_{tip}$ | ▬ | X | | |
| $\Lambda_{LE_O} \cdot b/2$ | ▬ | X | X | X |
| $\Lambda_{LE_O} \cdot s_{LE_I}$ | ▬ | ▬ | X | |
| $\Lambda_{LE_O} \cdot \Lambda_{LE_I}$ | ▬ | X | X | X |
| $\Lambda_{LE_O} \cdot \Lambda_{LE_O}$ | ▬ | | | |
| $s_{TE_I} \cdot c_{root}$ | ▬ | ▬ | ▬ | X |
| $s_{TE_I} \cdot c_{tip}$ | ▬ | ▬ | ▬ | |
| $s_{TE_I} \cdot b/2$ | ▬ | ▬ | ▬ | |
| $s_{TE_I} \cdot s_{LE_I}$ | ▬ | ▬ | ▬ | |
| $s_{TE_I} \cdot \Lambda_{LE_I}$ | ▬ | ▬ | ▬ | |
| $s_{TE_I} \cdot \Lambda_{LE_O}$ | ▬ | ▬ | ▬ | |
| $s_{TE_I} \cdot s_{TE_I}$ | ▬ | ▬ | ▬ | |
| $\Lambda_{TE_I} \cdot c_{root}$ | ▬ | ▬ | ▬ | X |
| $\Lambda_{TE_I} \cdot c_{tip}$ | ▬ | ▬ | ▬ | |
| $\Lambda_{TE_I} \cdot b/2$ | ▬ | ▬ | ▬ | X |
| $\Lambda_{TE_I} \cdot s_{LE_I}$ | ▬ | ▬ | ▬ | |
| $\Lambda_{TE_I} \cdot \Lambda_{LE_I}$ | ▬ | ▬ | ▬ | X |
| $\Lambda_{TE_I} \cdot \Lambda_{LE_O}$ | ▬ | ▬ | ▬ | X |
| $\Lambda_{TE_I} \cdot s_{TE_I}$ | ▬ | ▬ | ▬ | X |
| $\Lambda_{TE_I} \cdot \Lambda_{TE_I}$ | ▬ | ▬ | ▬ | |
| $(x/c)_{max\text{-}t} \cdot c_{root}$ | ▬ | | | X |
| $(x/c)_{max\text{-}t} \cdot c_{tip}$ | ▬ | | | |
| $(x/c)_{max\text{-}t} \cdot b/2$ | ▬ | | | |
| $(x/c)_{max\text{-}t} \cdot s_{LE_I}$ | ▬ | ▬ | | |
| $(x/c)_{max\text{-}t} \cdot \Lambda_{LE_I}$ | ▬ | X | X | X |
| $(x/c)_{max\text{-}t} \cdot \Lambda_{LE_O}$ | ▬ | | | |
| $(x/c)_{max\text{-}t} \cdot s_{TE_I}$ | ▬ | ▬ | ▬ | |
| $(x/c)_{max\text{-}t} \cdot \Lambda_{TE_I}$ | ▬ | ▬ | ▬ | |
| $(x/c)_{max\text{-}t} \cdot (x/c)_{max\text{-}t}$ | ▬ | | | |
| $R_{LE} \cdot c_{root}$ | ▬ | | | |
| $R_{LE} \cdot c_{tip}$ | ▬ | | | |
| $R_{LE} \cdot b/2$ | ▬ | | | |
| $R_{LE} \cdot s_{LE_I}$ | ▬ | ▬ | | X |
| $R_{LE} \cdot \Lambda_{LE_I}$ | ▬ | X | X | X |

X Terms that are significant to the drag prediction
▬ Terms containing variables that are not active

**Table 9.4** (cont.)

| Term | # DV | | | |
|---|---|---|---|---|
| | 5 | 10 | 15 | 20 |
| $R_{LE} \cdot \Lambda_{LE_O}$ | ▬ | | | |
| $R_{LE} \cdot s_{TE_I}$ | ▬ | ▬ | ▬ | |
| $R_{LE} \cdot \Lambda_{TE_I}$ | ▬ | ▬ | ▬ | |
| $R_{LE} \cdot (x/c)_{max\text{-}t}$ | ▬ | | | |
| $R_{LE} \cdot R_{LE}$ | ▬ | | | |
| $(t/c)_{root} \cdot c_{root}$ | | X | | X |
| $(t/c)_{root} \cdot c_{tip}$ | | | | |
| $(t/c)_{root} \cdot b/2$ | ▬ | | X | X |
| $(t/c)_{root} \cdot s_{LE_I}$ | ▬ | ▬ | X | X |
| $(t/c)_{root} \cdot \Lambda_{LE_I}$ | X | X | X | X |
| $(t/c)_{root} \cdot \Lambda_{LE_O}$ | ▬ | | | |
| $(t/c)_{root} \cdot s_{TE_I}$ | ▬ | ▬ | ▬ | |
| $(t/c)_{root} \cdot \Lambda_{TE_I}$ | ▬ | ▬ | ▬ | X |
| $(t/c)_{root} \cdot (x/c)_{max\text{-}t}$ | ▬ | X | X | X |
| $(t/c)_{root} \cdot R_{LE}$ | ▬ | X | X | |
| $(t/c)_{root} \cdot (t/c)_{root}$ | X | X | | |
| $(t/c)_{break} \cdot c_{root}$ | ▬ | ▬ | ▬ | X |
| $(t/c)_{break} \cdot c_{tip}$ | ▬ | ▬ | ▬ | |
| $(t/c)_{break} \cdot b/2$ | ▬ | ▬ | ▬ | X |
| $(t/c)_{break} \cdot s_{LE_I}$ | ▬ | ▬ | ▬ | X |
| $(t/c)_{break} \cdot \Lambda_{LE_I}$ | ▬ | ▬ | ▬ | X |
| $(t/c)_{break} \cdot \Lambda_{LE_O}$ | ▬ | ▬ | ▬ | |
| $(t/c)_{break} \cdot s_{TE_I}$ | ▬ | ▬ | ▬ | |
| $(t/c)_{break} \cdot \Lambda_{TE_I}$ | ▬ | ▬ | ▬ | X |
| $(t/c)_{break} \cdot (x/c)_{max\text{-}t}$ | ▬ | ▬ | ▬ | X |
| $(t/c)_{break} \cdot R_{LE}$ | ▬ | ▬ | ▬ | |
| $(t/c)_{break} \cdot (t/c)_{root}$ | ▬ | ▬ | ▬ | X |
| $(t/c)_{break} \cdot (t/c)_{break}$ | ▬ | ▬ | ▬ | |
| $(t/c)_{tip} \cdot c_{root}$ | ▬ | ▬ | ▬ | |
| $(t/c)_{tip} \cdot c_{tip}$ | ▬ | ▬ | ▬ | |
| $(t/c)_{tip} \cdot b/2$ | ▬ | ▬ | ▬ | |
| $(t/c)_{tip} \cdot s_{LE_I}$ | ▬ | ▬ | ▬ | |
| $(t/c)_{tip} \cdot \Lambda_{LE_I}$ | ▬ | ▬ | ▬ | |
| $(t/c)_{tip} \cdot \Lambda_{LE_O}$ | ▬ | ▬ | ▬ | |
| $(t/c)_{tip} \cdot s_{TE_I}$ | ▬ | ▬ | ▬ | |

| Term | # DV | | | |
|---|---|---|---|---|
| | 5 | 10 | 15 | 20 |
| $(t/c)_{tip} \cdot \Lambda_{TE_I}$ | ▬ | ▬ | ▬ | |
| $(t/c)_{tip} \cdot (x/c)_{max\text{-}t}$ | ▬ | ▬ | ▬ | |
| $(t/c)_{tip} \cdot R_{LE}$ | ▬ | ▬ | ▬ | |
| $(t/c)_{tip} \cdot (t/c)_{root}$ | ▬ | ▬ | ▬ | |
| $(t/c)_{tip} \cdot (t/c)_{break}$ | ▬ | ▬ | ▬ | |
| $(t/c)_{tip} \cdot (t/c)_{tip}$ | ▬ | ▬ | ▬ | |
| $r_{fus_1} \cdot c_{root}$ | ▬ | ▬ | | |
| $r_{fus_1} \cdot c_{tip}$ | ▬ | ▬ | | |
| $r_{fus_1} \cdot b/2$ | ▬ | ▬ | | |
| $r_{fus_1} \cdot s_{LE_I}$ | ▬ | ▬ | | |
| $r_{fus_1} \cdot \Lambda_{LE_I}$ | ▬ | ▬ | | |
| $r_{fus_1} \cdot \Lambda_{LE_O}$ | ▬ | ▬ | | |
| $r_{fus_1} \cdot s_{TE_I}$ | ▬ | ▬ | ▬ | |
| $r_{fus_1} \cdot \Lambda_{TE_I}$ | ▬ | ▬ | ▬ | |
| $r_{fus_1} \cdot (x/c)_{max\text{-}t}$ | ▬ | ▬ | X | X |
| $r_{fus_1} \cdot R_{LE}$ | ▬ | ▬ | | |
| $r_{fus_1} \cdot (t/c)_{root}$ | ▬ | ▬ | X | X |
| $r_{fus_1} \cdot (t/c)_{break}$ | ▬ | ▬ | ▬ | |
| $r_{fus_1} \cdot (t/c)_{tip}$ | ▬ | ▬ | ▬ | |
| $r_{fus_1} \cdot r_{fus_1}$ | ▬ | ▬ | | |
| $r_{fus_2} \cdot c_{root}$ | ▬ | ▬ | X | X |
| $r_{fus_2} \cdot c_{tip}$ | ▬ | ▬ | | |
| $r_{fus_2} \cdot b/2$ | ▬ | ▬ | X | X |
| $r_{fus_2} \cdot s_{LE_I}$ | ▬ | ▬ | | |
| $r_{fus_2} \cdot \Lambda_{LE_I}$ | ▬ | ▬ | X | X |
| $r_{fus_2} \cdot \Lambda_{LE_O}$ | ▬ | ▬ | X | X |
| $r_{fus_2} \cdot s_{TE_I}$ | ▬ | ▬ | ▬ | |
| $r_{fus_2} \cdot \Lambda_{TE_I}$ | ▬ | ▬ | ▬ | X |
| $r_{fus_2} \cdot (x/c)_{max\text{-}t}$ | ▬ | ▬ | X | X |
| $r_{fus_2} \cdot R_{LE}$ | ▬ | ▬ | X | |
| $r_{fus_2} \cdot (t/c)_{root}$ | ▬ | ▬ | | |
| $r_{fus_2} \cdot (t/c)_{break}$ | ▬ | ▬ | ▬ | |
| $r_{fus_2} \cdot (t/c)_{tip}$ | ▬ | ▬ | ▬ | |
| $r_{fus_2} \cdot r_{fus_1}$ | ▬ | ▬ | X | X |
| $r_{fus_2} \cdot r_{fus_2}$ | ▬ | ▬ | X | X |

X Terms that are significant to the drag prediction
▬ Terms containing variables that are not active

**Table 9.4** (concl.)

| Term | # DV 5 | 10 | 15 | 20 |
|---|---|---|---|---|
| $r_{fus_3} \cdot c_{root}$ | ▬ | ▬ | X | X |
| $r_{fus_3} \cdot c_{tip}$ | ▬ | ▬ | | |
| $r_{fus_3} \cdot b/2$ | ▬ | ▬ | | |
| $r_{fus_3} \cdot s_{LE_I}$ | ▬ | ▬ | | |
| $r_{fus_3} \cdot \Lambda_{LE_I}$ | ▬ | ▬ | X | X |
| $r_{fus_3} \cdot \Lambda_{LE_O}$ | ▬ | ▬ | | |
| $r_{fus_3} \cdot s_{TE_I}$ | ▬ | ▬ | ▬ | |
| $r_{fus_3} \cdot \Lambda_{TE_I}$ | ▬ | ▬ | ▬ | |
| $r_{fus_3} \cdot (x/c)_{max\text{-}t}$ | ▬ | ▬ | | |
| $r_{fus_3} \cdot R_{LE}$ | ▬ | ▬ | | |
| $r_{fus_3} \cdot (t/c)_{root}$ | ▬ | ▬ | | |
| $r_{fus_3} \cdot (t/c)_{break}$ | ▬ | ▬ | ▬ | |
| $r_{fus_3} \cdot (t/c)_{tip}$ | ▬ | ▬ | ▬ | |
| $r_{fus_3} \cdot r_{fus_1}$ | ▬ | ▬ | X | X |
| $r_{fus_3} \cdot r_{fus_2}$ | ▬ | ▬ | X | X |
| $r_{fus_3} \cdot r_{fus_3}$ | ▬ | ▬ | X | |
| $r_{fus_4} \cdot c_{root}$ | ▬ | ▬ | | X |
| $r_{fus_4} \cdot c_{tip}$ | ▬ | ▬ | | |
| $r_{fus_4} \cdot b/2$ | ▬ | ▬ | | |
| $r_{fus_4} \cdot s_{LE_I}$ | ▬ | ▬ | | |
| $r_{fus_4} \cdot \Lambda_{LE_I}$ | ▬ | ▬ | | |
| $r_{fus_4} \cdot \Lambda_{LE_O}$ | ▬ | ▬ | | |
| $r_{fus_4} \cdot s_{TE_I}$ | ▬ | ▬ | ▬ | |
| $r_{fus_4} \cdot \Lambda_{TE_I}$ | ▬ | ▬ | ▬ | |
| $r_{fus_4} \cdot (x/c)_{max\text{-}t}$ | ▬ | ▬ | X | X |
| $r_{fus_4} \cdot R_{LE}$ | ▬ | ▬ | | |
| $r_{fus_4} \cdot (t/c)_{root}$ | ▬ | ▬ | X | X |
| $r_{fus_4} \cdot (t/c)_{break}$ | ▬ | ▬ | ▬ | |
| $r_{fus_4} \cdot (t/c)_{tip}$ | ▬ | ▬ | ▬ | |
| $r_{fus_4} \cdot r_{fus_1}$ | ▬ | ▬ | X | X |
| $r_{fus_4} \cdot r_{fus_2}$ | ▬ | ▬ | X | X |
| $r_{fus_4} \cdot r_{fus_3}$ | ▬ | ▬ | X | X |
| $r_{fus_4} \cdot r_{fus_4}$ | ▬ | ▬ | | |
| $y_{nacelle} \cdot c_{root}$ | ▬ | | X | |
| $y_{nacelle} \cdot c_{tip}$ | ▬ | | | |

| Term | # DV 5 | 10 | 15 | 20 |
|---|---|---|---|---|
| $y_{nacelle} \cdot b/2$ | ▬ | | | |
| $y_{nacelle} \cdot s_{LE_I}$ | ▬ | ▬ | | |
| $y_{nacelle} \cdot \Lambda_{LE_I}$ | ▬ | | X | |
| $y_{nacelle} \cdot \Lambda_{LE_O}$ | ▬ | | | |
| $y_{nacelle} \cdot s_{TE_I}$ | ▬ | ▬ | ▬ | |
| $y_{nacelle} \cdot \Lambda_{TE_I}$ | ▬ | ▬ | ▬ | |
| $y_{nacelle} \cdot (x/c)_{max\text{-}t}$ | ▬ | | | |
| $y_{nacelle} \cdot R_{LE}$ | ▬ | | | |
| $y_{nacelle} \cdot (t/c)_{root}$ | ▬ | | | |
| $y_{nacelle} \cdot (t/c)_{break}$ | ▬ | ▬ | ▬ | |
| $y_{nacelle} \cdot (t/c)_{tip}$ | ▬ | ▬ | ▬ | |
| $y_{nacelle} \cdot r_{fus_1}$ | ▬ | ▬ | | |
| $y_{nacelle} \cdot r_{fus_2}$ | ▬ | ▬ | | |
| $y_{nacelle} \cdot r_{fus_3}$ | ▬ | ▬ | | |
| $y_{nacelle} \cdot r_{fus_4}$ | ▬ | ▬ | X | |
| $y_{nacelle} \cdot y_{nacelle}$ | ▬ | | | |
| $\Delta y_{nacelle} \cdot c_{root}$ | ▬ | ▬ | ▬ | |
| $\Delta y_{nacelle} \cdot c_{tip}$ | ▬ | ▬ | ▬ | |
| $\Delta y_{nacelle} \cdot b/2$ | ▬ | ▬ | ▬ | |
| $\Delta y_{nacelle} \cdot s_{LE_I}$ | ▬ | ▬ | ▬ | |
| $\Delta y_{nacelle} \cdot \Lambda_{LE_I}$ | ▬ | ▬ | ▬ | |
| $\Delta y_{nacelle} \cdot \Lambda_{LE_O}$ | ▬ | ▬ | ▬ | |
| $\Delta y_{nacelle} \cdot s_{TE_I}$ | ▬ | ▬ | ▬ | |
| $\Delta y_{nacelle} \cdot \Lambda_{TE_I}$ | ▬ | ▬ | ▬ | |
| $\Delta y_{nacelle} \cdot (x/c)_{max\text{-}t}$ | ▬ | ▬ | ▬ | |
| $\Delta y_{nacelle} \cdot R_{LE}$ | ▬ | ▬ | ▬ | |
| $\Delta y_{nacelle} \cdot (t/c)_{root}$ | ▬ | ▬ | ▬ | |
| $\Delta y_{nacelle} \cdot (t/c)_{break}$ | ▬ | ▬ | ▬ | |
| $\Delta y_{nacelle} \cdot (t/c)_{tip}$ | ▬ | ▬ | ▬ | |
| $\Delta y_{nacelle} \cdot r_{fus_1}$ | ▬ | ▬ | ▬ | |
| $\Delta y_{nacelle} \cdot r_{fus_2}$ | ▬ | ▬ | ▬ | |
| $\Delta y_{nacelle} \cdot r_{fus_3}$ | ▬ | ▬ | ▬ | |
| $\Delta y_{nacelle} \cdot r_{fus_4}$ | ▬ | ▬ | ▬ | |
| $\Delta y_{nacelle} \cdot y_{nacelle}$ | ▬ | ▬ | ▬ | |
| $\Delta y_{nacelle} \cdot \Delta y_{nacelle}$ | ▬ | ▬ | ▬ | |
| **Total Terms** | 7 | 24 | 58 | 73 |

X Terms that are significant to the drag prediction
▬ Terms containing variables that are not active

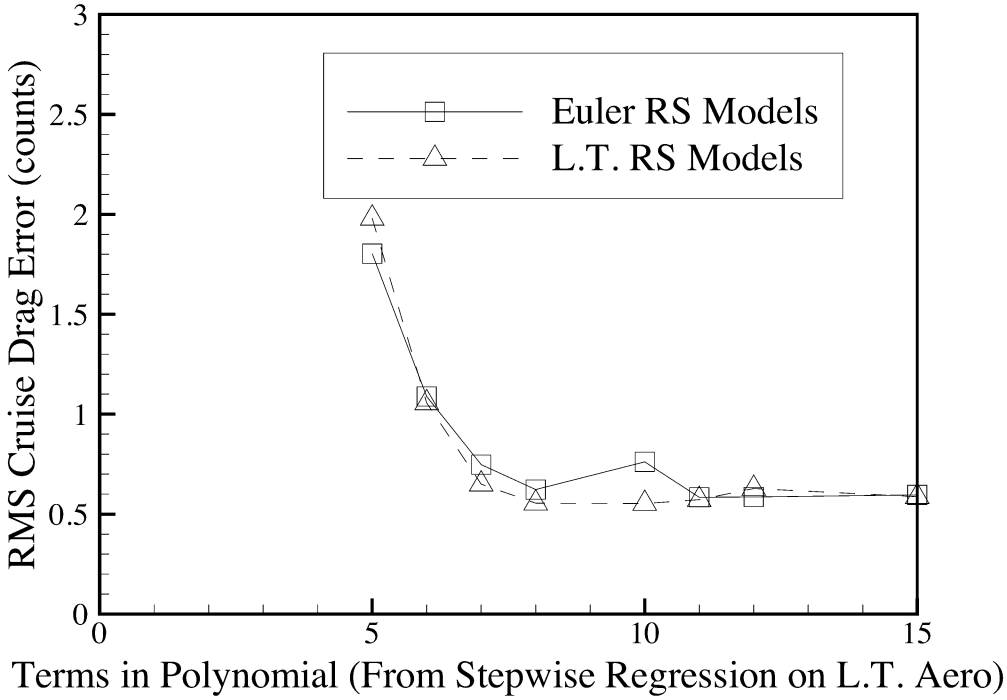


**Figure 9.1:** Stepwise Regression Analysis (5 Variable HSCT Design).

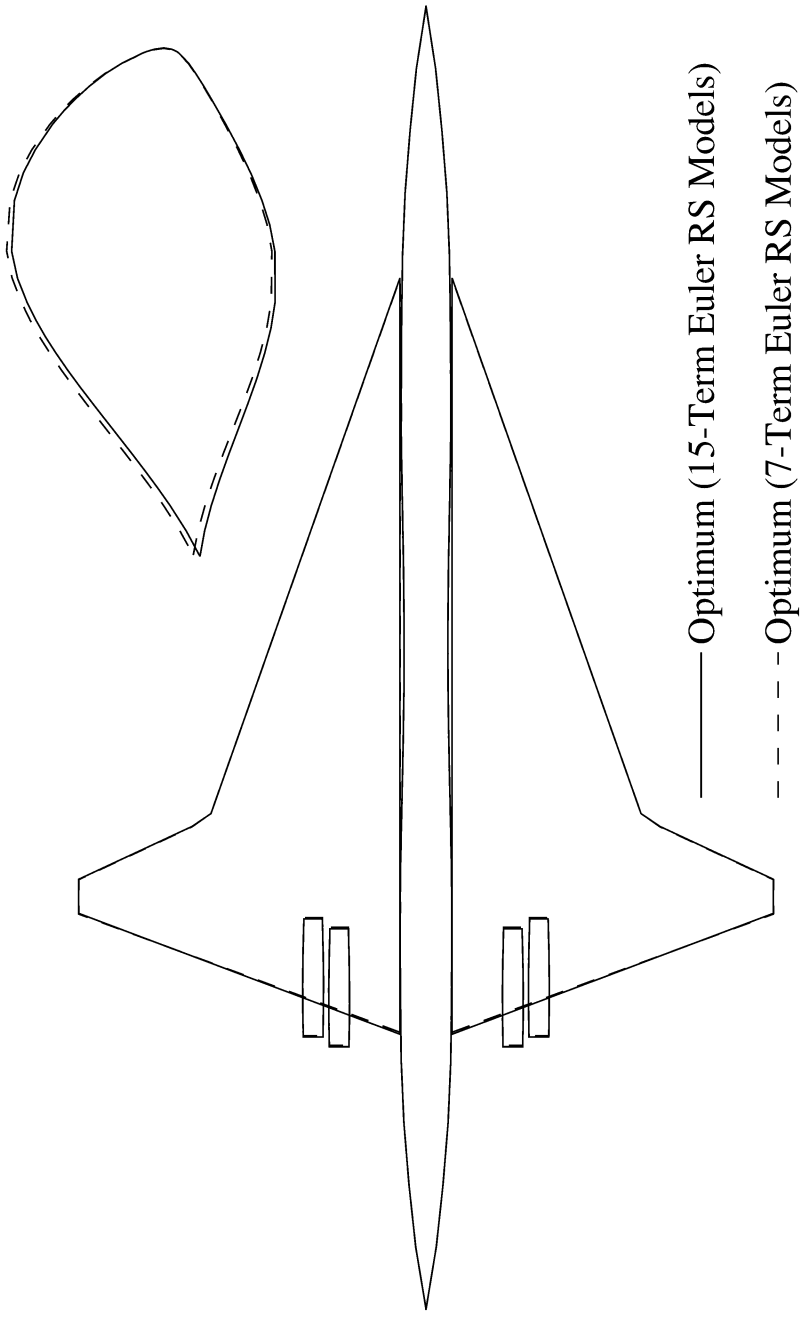


**Figure 9.2:** Optimal Designs from Reduced Term and Full Term Euler RS Models.

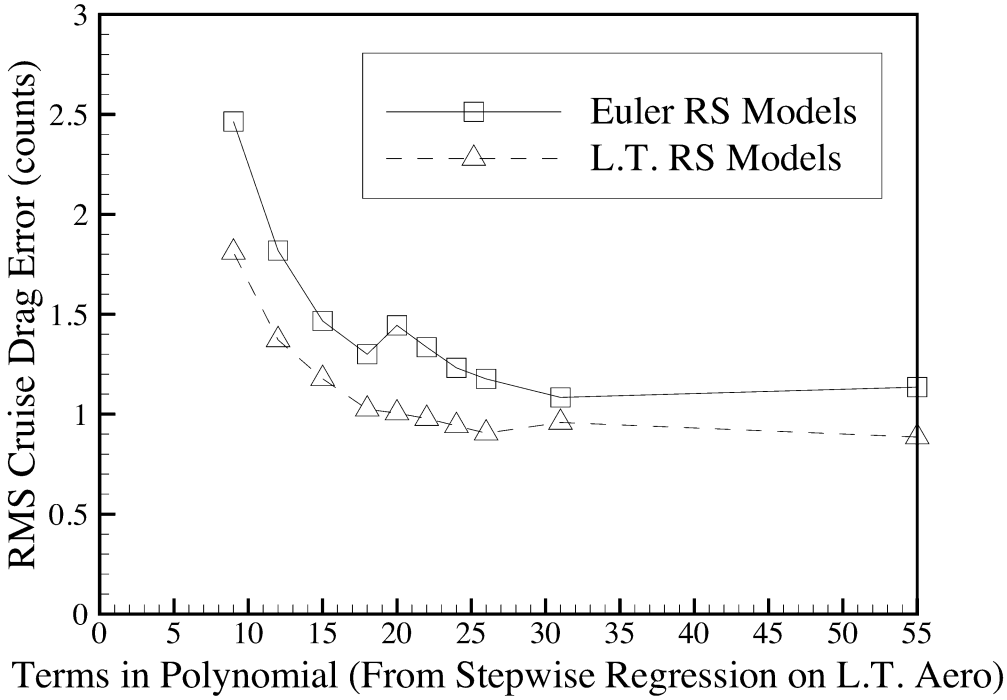


**Figure 9.3:** Stepwise Regression Analysis (10 Variable HSCT Design).

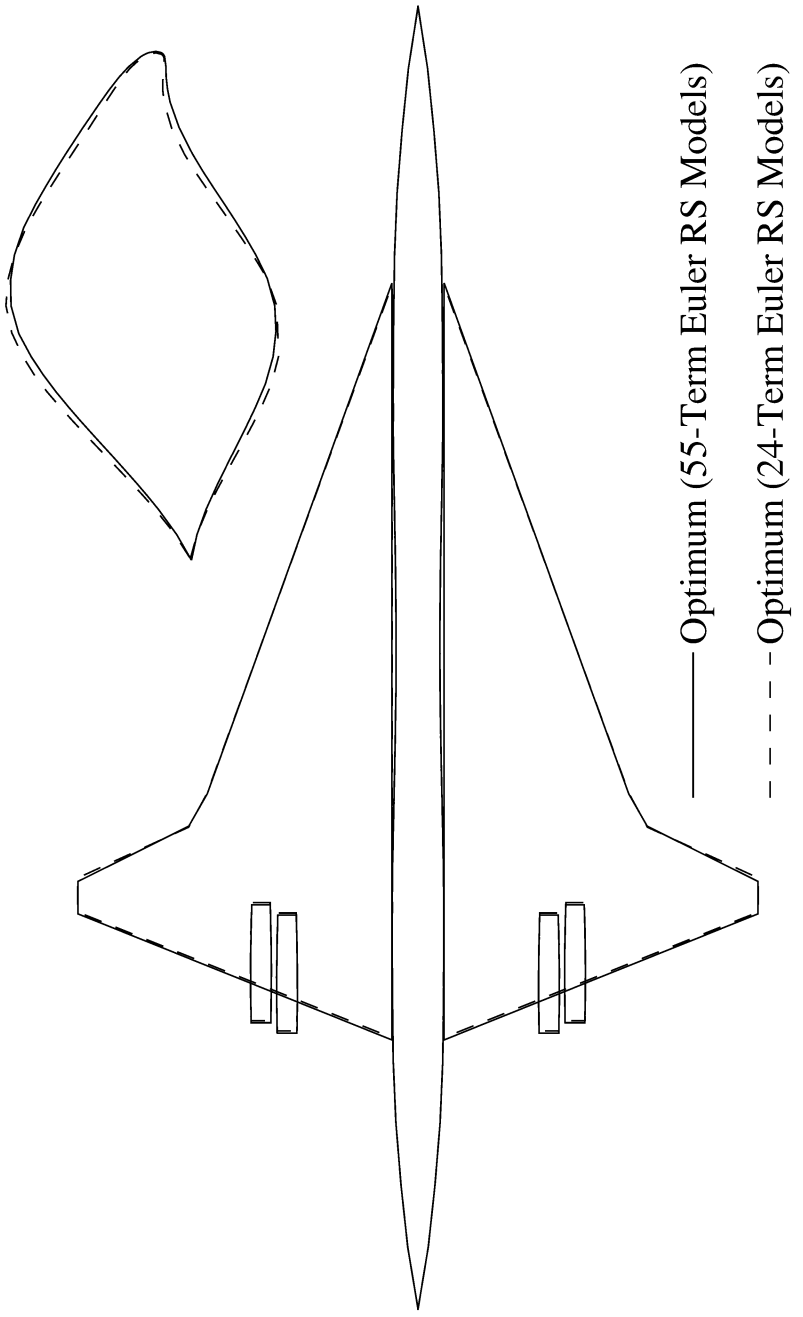


**Figure 9.4:** Optimal Designs from Reduced Term and Full Term Euler RS Models.

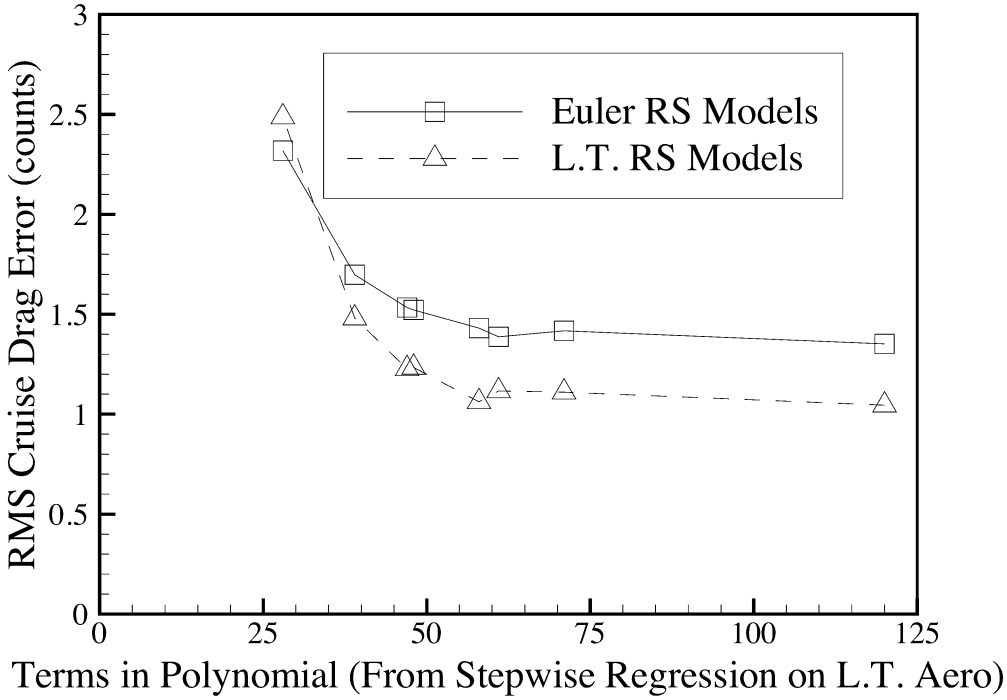


**Figure 9.5:** Stepwise Regression Analysis (15 Variable HSCT Design).

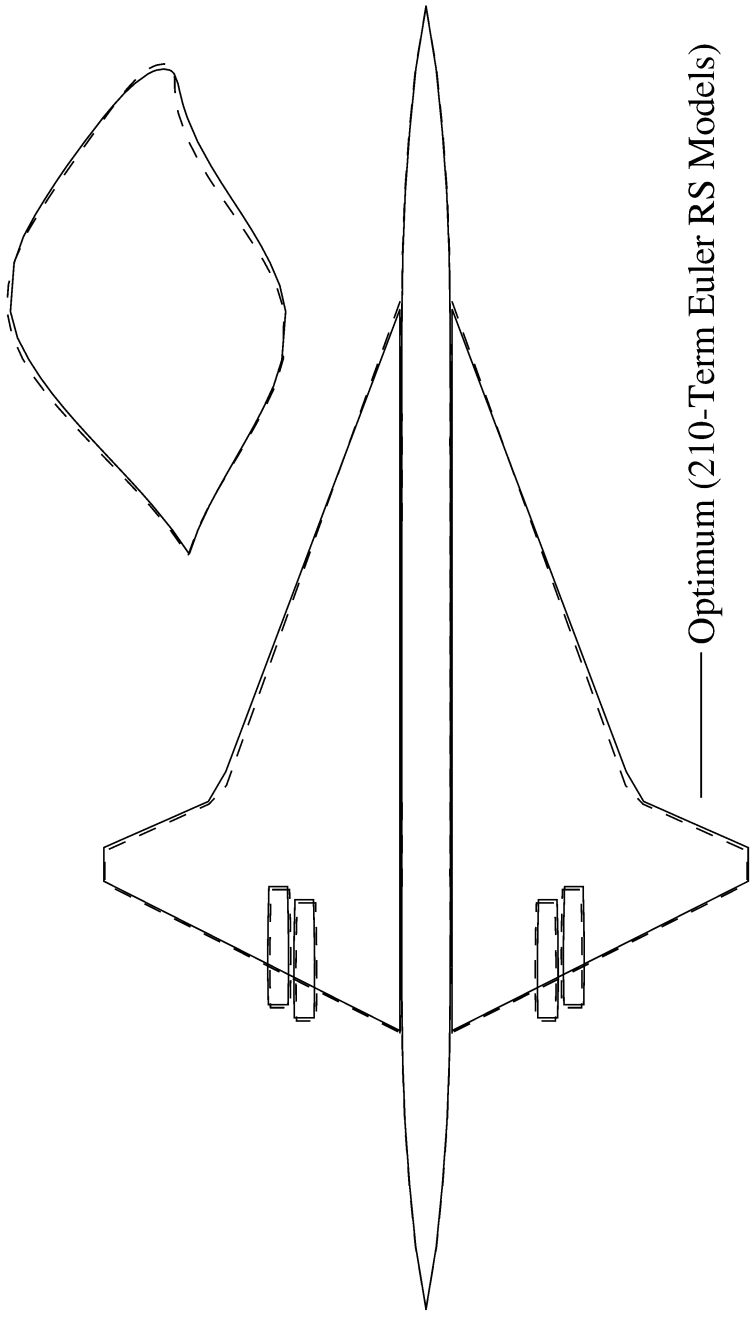


**Figure 9.6:** Optimal Designs from Reduced Term and Full Term Euler RS Models.

# Chapter 10

# Optimization: Incremental RS Models

## 10.1 Five Variable HSCT Design

The regression analysis for the five variable problem (Fig. 10.1) shows improved behavior in the errors for the incremental RS models as the number of terms is reduced. Recall that the incremental RS models are created by adding a reduced term correction RS models for the difference between the Euler and linear theory RS model predictions to the full term linear theory RS models. The RMS error in the incremental RS models is represents the differences between the incremental RS model prediction of the cruise drag and the actual Euler value. These errors are computed at the same randomly selected design points that are used in Section 8.1. The RMS error in the cruise drag for the incremental RS models does not show the abrupt increase below seven terms that is present in the linear theory and reduced term Euler RS models. The five term incremental RS model requires only 5.3 hours to create, as opposed to 16 hours required for the full term model. The optimal design obtained from the incremental RS models compares well (Fig. 10.2) to the full term Euler RS model. Even more importantly, Euler analysis on the optimal design reveals that the RS model cruise drag prediction is less than 1/10 count higher than the Euler value. Table 10.1 shows that the corrected TOGW is only 700 $lb$ higher than that for the full term Euler optimum. The incremental RS models require fewer terms and result

in more accurate drag predictions than the reduced term Euler models.

## 10.2 Ten Variable HSCT Design

Regression analysis for the ten variable problem (Fig. 10.3) exhibits similar improvement in the behavior of the incremental RS models as the number of terms is reduced. The optimal configuration is compared to the full term Euler RS models in Fig. 10.4, and the design variables are presented in Table 10.2. The RS model prediction of the cruise drag is 0.64 counts higher than the Euler value, leading to the 5542 $n.mi.$ actual range. Removing the extra fuel results in a design with no constraint violations that is 4000 $lb$ lighter than the full term Euler optimum.

## 10.3 Fifteen Variable HSCT Design

Stepwise regression analysis for the fifteen variable design is presented in Fig. 10.5. Optimization is performed with the 48 term incremental RS models. The optimal designs from the full term Euler and reduced term incremental RS models (Fig. 10.6) are barely distinguishable from each other. Table 10.3 show the very close agreement in the design variables. In this region of the design space, both the Euler and incremental RS models are extremely accurate. This is evident in the fact that there is only a five mile discrepancy between the range estimates from the RS models and those from Euler evaluations. When the fuel weight is altered to counter the range variations, the TOGW for the Euler and incremental RS models are only 200 $lb$ different. The incremental RS models greatly outperform the reduced term Euler RS models for this case.

## 10.4 Twenty Variable HSCT Design

Due to computational expense, the full quadratic Euler RS models are not available for the twenty variable design. Regression analysis on the linear theory data (Fig. 10.7) shows that the RMS cruise drag error remains nearly constant until about 73 terms (Table 9.4) remain in the RS models. A sufficient number of Euler evaluations were

performed to create the 100 term RS models. Since the full term Euler RS models are not present, this provides a model with which to evaluate the errors in the 73 term RS models. It is seen that there is no major difference in the cruise drag errors of the 100 term and 73 term incremental RS models.

The optimal designs from the incremental and linear theory RS models are shown in Figure 10.8, and the optimal design variable values are presented in Table 10.4. The nacelle separation distance is introduced in the twenty variable design problem, but stepwise regression analysis has removed all terms related to this variable. Even the linear term $\Delta y_{nacelle}$ is found to be insignificant in the prediction of the drag. The large variation in $\Delta y_{nacelle}$ seen in the optimal designs is a direct result of this insensitivity. The cruise drag prediction for the optimal design from the incremental RS models is 0.8 counts lower than the actual Euler value, which is much lower than the RMS error of the RS models. Compensating for the range deficiency gives a corrected TOGW of $588,000\,lb$. Although the error in the RS models is larger, this Euler optimum is $3000\,lb$ lighter than the 15 variable optimum.

Using the reduced term incremental RS models has provided a means to create RS models for high dimensional problems, where computing the coefficients of the full quadratic RS models is not viable. Figure 10.9 shows how the present method extrapolates to 25 and 30 design variables. The trends indicate that a reduced term response surface model in 25 design variables can be created using the same number of terms as a full quadratic model in 15 design variables.

The optimal designs obtained from the reduced term incremental RS models have consistently more accurate drag estimates than do those from the reduced term Euler RS models. This is unusual since the RMS cruise drag error estimates for the two methods are similar for the number of terms chosen. To investigate this phenomenon, plots of the variation in $C_{D_0}$ and $K$ (Fig. 10.10) between two opposite vertices of the design bounding box are created. These vertices are not used in the creation of the RS models. All design variables are linearly varied from their values at one vertex to their values at the other vertex. The plot shows that the reduced term incremental RS models compare much better to the actual Euler results for $C_{D_0}$ than do the reduced term Euler models. However, the comparisons near the vertices are not substantially different. This is important because the points used to evaluate the RS model errors lie on the vertices of the design box. This suggests that the method used to estimate

the RMS errors may not be a sufficiently accurate representation of the RS model fit. Studies which include points on the interior of the design bounding box to check the RS model errors are being performed.

**Table 10.1:** Optimal Design Variables (5 Variable HSCT Optimization).

| | **5 Term Incremental RS** | **15 Term Euler RS** |
|---|---|---|
| $c_{root}$ | $178.0\,ft$ | $174.2\,ft$ |
| $c_{tip}$ | $7.4\,ft$ | $7.8\,ft$ |
| $\Lambda_{LE_I}$ | $71.1°$ | $70.6°$ |
| $t/c$ | $1.81\%$ | $1.81\%$ |
| $W_{fuel}$ | $309,800\,lb$ | $313,200\,lb$ |
| $W_{wing}$ | $103,900\,lb$ | $103,900\,lb$ |
| $W_{TOGW}$ | $622,800\,lb$ | $626,300\,lb$ |
| Range: (Euler) | $5503\,n.mi.$ | $5544\,n.mi.$ |
| $\Delta W_{fuel}$ | $-320\,lb$ | $-4010\,lb$ |
| $W_{C-TOGW}$ | $622,500\,lb$ | $621,800\,lb$ |

**Table 10.2:** Optimal Design Variables (10 Variable HSCT Optimization).

| | **20 Term Incremental RS** | **55 Term Euler RS** |
|---|---|---|
| $c_{root}$ | $170.4\,ft$ | $174.3\,ft$ |
| $c_{tip}$ | $9.0\,ft$ | $7.5\,ft$ |
| $b/2$ | $72.1\,ft$ | $72.3\,ft$ |
| $\Lambda_{LE_I}$ | $70.0°$ | $70.1°$ |
| $\Lambda_{LE_O}$ | $18.7°$ | $26.5°$ |
| $(x/c)_{max\text{-}t}$ | 50.2% | 50.1% |
| $R_{LE}$ | 2.1 | 2.1 |
| $t/c$ | 1.91% | 1.82% |
| $y_{nacelle}$ | $30.0\,ft$ | $30.2\,ft$ |
| $W_{fuel}$ | $306,000\,lb$ | $301,000\,lb$ |
| $W_{wing}$ | $96,100\,lb$ | $99,200\,lb$ |
| $W_{TOGW}$ | $610,400\,lb$ | $608,900\,lb$ |
| Range: (Euler) | $5542\,n.mi.$ | $5485\,n.mi.$ |
| $\Delta W_{fuel}$ | $-3715\,lb$ | $1300\,lb$ |
| $W_{C-TOGW}$ | $606,300\,lb$ | $610,300\,lb$ |

**Table 10.3:** Optimal Design Variables (15 Variable HSCT Optimization).

| | **48 Term Incremental RS** | **120 Term Euler RS** |
|---|---|---|
| $c_{root}$ | $166.2\,ft$ | $166.2\,ft$ |
| $c_{tip}$ | $7.7\,ft$ | $7.7\,ft$ |
| $b/2$ | $68.1^\circ$ | $68.2^\circ$ |
| $s_{LE_I}$ | $120.4\,ft$ | $120.3\,ft$ |
| $\Lambda_{LE_I}$ | $69.4^\circ$ | $69.4^\circ$ |
| $\Lambda_{LE_O}$ | $24.2^\circ$ | $23.8^\circ$ |
| $(x/c)_{max\text{-}t}$ | 49.8% | 49.7% |
| $R_{LE}$ | 2.1 | 2.1 |
| $t/c$ | 1.99% | 1.99% |
| $r_{fus_1}$ | $5.2\,ft$ | $5.1\,ft$ |
| $r_{fus_2}$ | $5.6\,ft$ | $5.6\,ft$ |
| $r_{fus_3}$ | $5.6\,ft$ | $5.6\,ft$ |
| $r_{fus_4}$ | $5.2\,ft$ | $5.2\,ft$ |
| $y_{nacelle}$ | $28.1\,ft$ | $28.0\,ft$ |
| $W_{fuel}$ | $299,614\,lb$ | $300,100\,lb$ |
| $W_{wing}$ | $87,800\,lb$ | $87,900\,lb$ |
| $W_{TOGW}$ | $590,700\,lb$ | $591,500\,lb$ |
| Range: (Euler) | $5495\,n.mi.$ | $5505\,n.mi.$ |
| $\Delta W_{fuel}$ | $450\,lb$ | $-440\,lb$ |
| $W_{C-TOGW}$ | $\star 591,200\,lb$ | $591,000\,lb$ |

**Table 10.4:** Optimal Design Variables (20 Variable HSCT Optimization).

| | **73 Term Incremental RS** | **210 Term Linear Theory RS** |
|---|---|---|
| $c_{root}$ | $169.5\,ft$ | $167.1\,ft$ |
| $c_{tip}$ | $7.8\,ft$ | $8.5\,ft$ |
| $b/2$ | $67.4\,ft$ | $68.1\,ft$ |
| $s_{LE_I}$ | $124.8\,ft$ | $125.8\,ft$ |
| $\Lambda_{LE_I}$ | $70.5°$ | $70.9°$ |
| $\Lambda_{LE_O}$ | $30.4°$ | $29.1°$ |
| $s_{TE_I}$ | $27.4\,ft$ | $16.3\,ft$ |
| $\Lambda_{TE_I}$ | $-29.0°$ | $-24.8°$ |
| $(x/c)_{max\text{-}t}$ | 51.1% | 50.6% |
| $R_{LE}$ | 2.1 | 3.3 |
| $(t/c)_{root}$ | 1.99% | 2.01% |
| $(t/c)_{break}$ | 1.91% | 1.59% |
| $(t/c)_{tip}$ | 1.94% | 1.79% |
| $r_{fus_1}$ | $5.2\,ft$ | $5.0\,ft$ |
| $r_{fus_2}$ | $5.6\,ft$ | $5.8\,ft$ |
| $r_{fus_3}$ | $5.6\,ft$ | $5.8\,ft$ |
| $r_{fus_4}$ | $5.2\,ft$ | $4.7\,ft$ |
| $y_{nacelle}$ | $27.7\,ft$ | $18.6\,ft$ |
| $\Delta y_{nacelle}$ | $6.0\,ft$ | $13.0\,ft$ |
| $W_{fuel}$ | $293,000\,lb$ | $289,200\,lb$ |
| $W_{wing}$ | $86,900\,lb$ | $89,700\,lb$ |
| $W_{TOGW}$ | $583,200\,lb$ | $584,900\,lb$ |
| Range: (Euler) | $5449\,n.mi.$ | $5380\,n.mi.$ |
| $\Delta W_{fuel}$ | $4430\,lb$ | $10,490\,lb$ |
| $W_{C-TOGW}$ | $\star 588,000\,lb$ | $\star 596,500\,lb$ |

$\star$ Adding fuel results in constraint violation

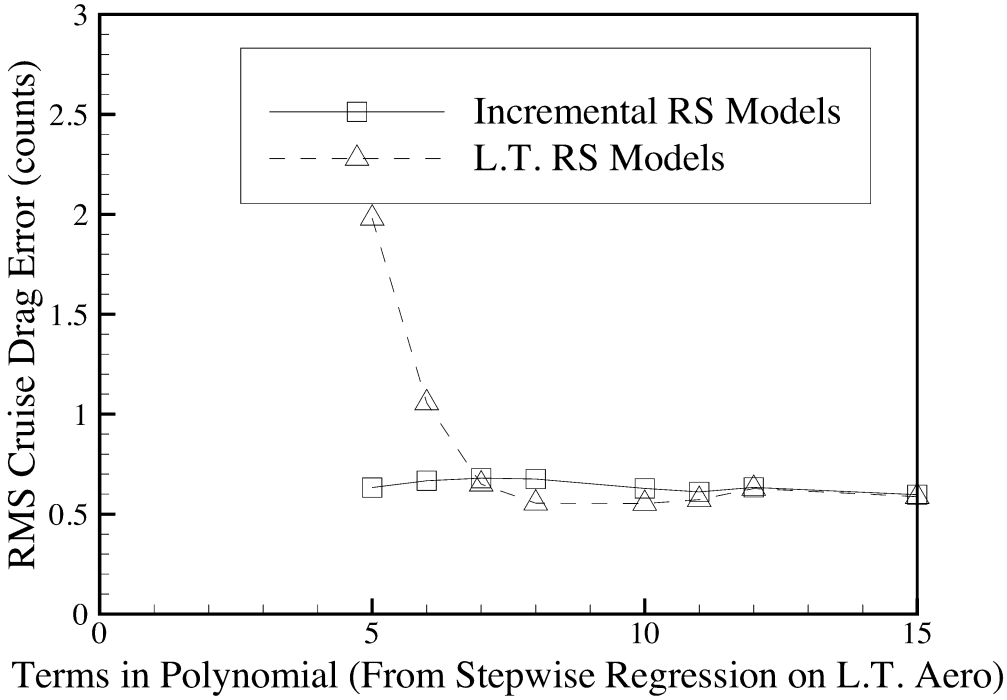


**Figure 10.1:** Stepwise Regression Analysis (5 Variable HSCT Design).

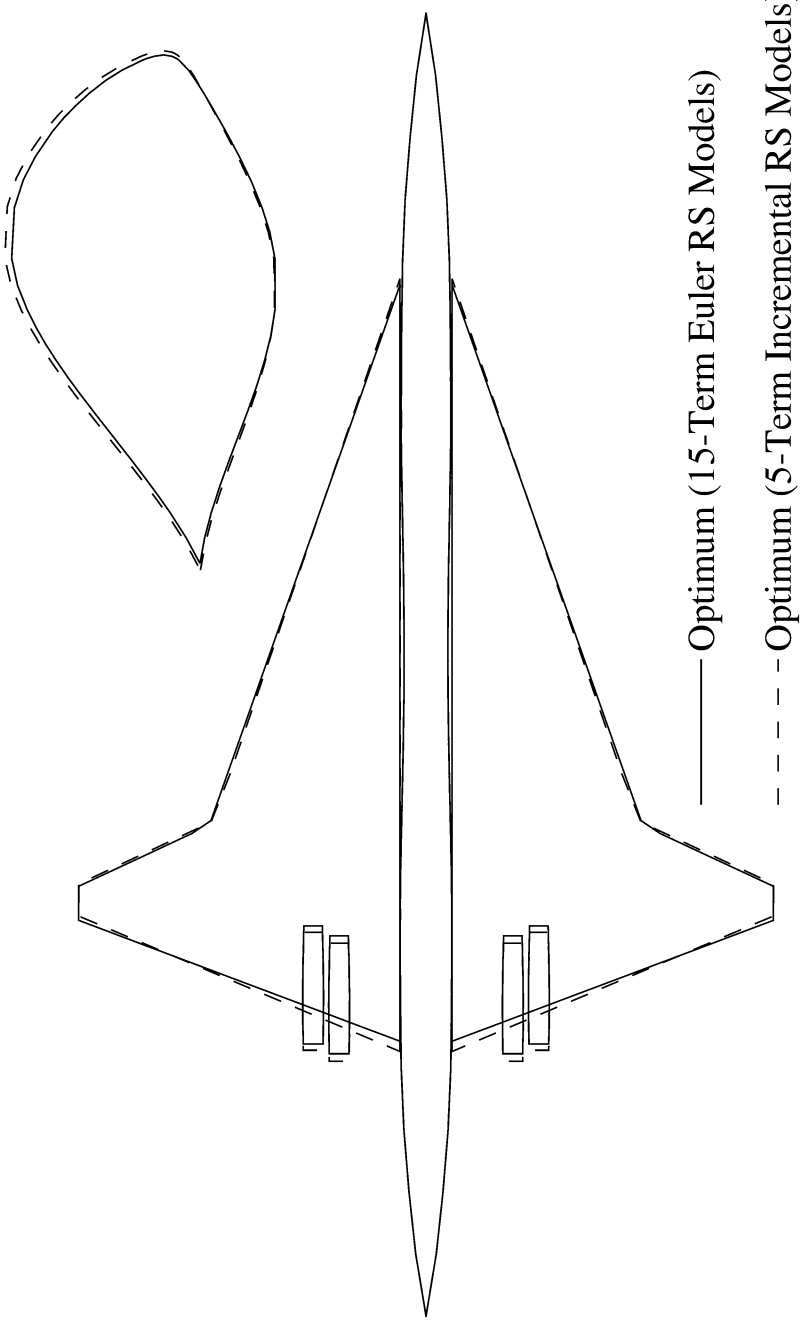


**Figure 10.2:** Optimal Designs from Reduced Term Incremental and Full Term Euler RS Models.

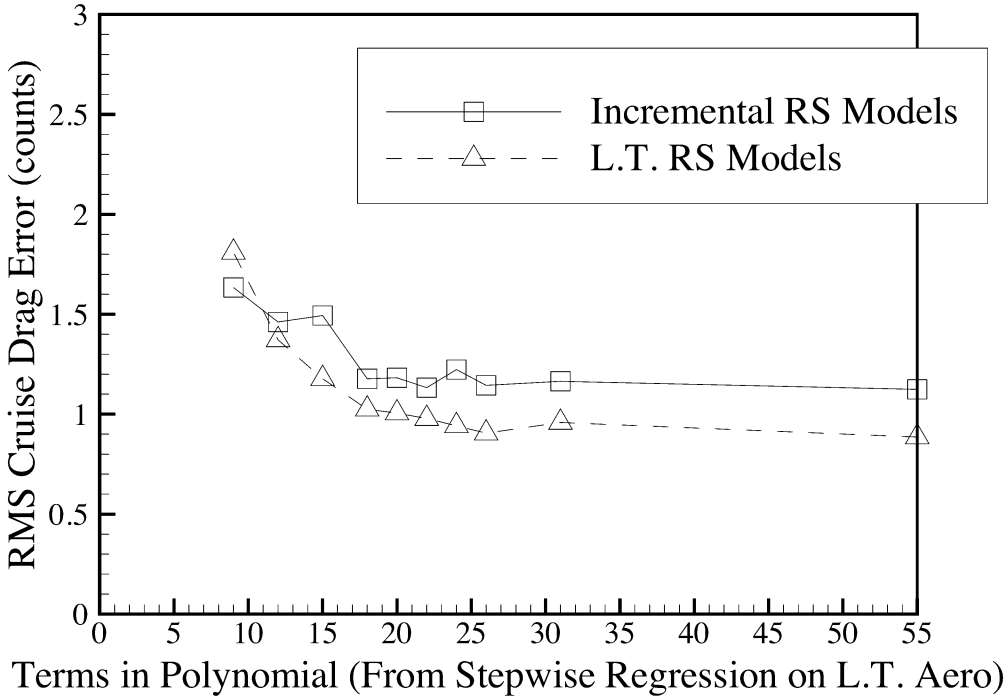


**Figure 10.3:** Stepwise Regression Analysis (10 Variable HSCT Design).

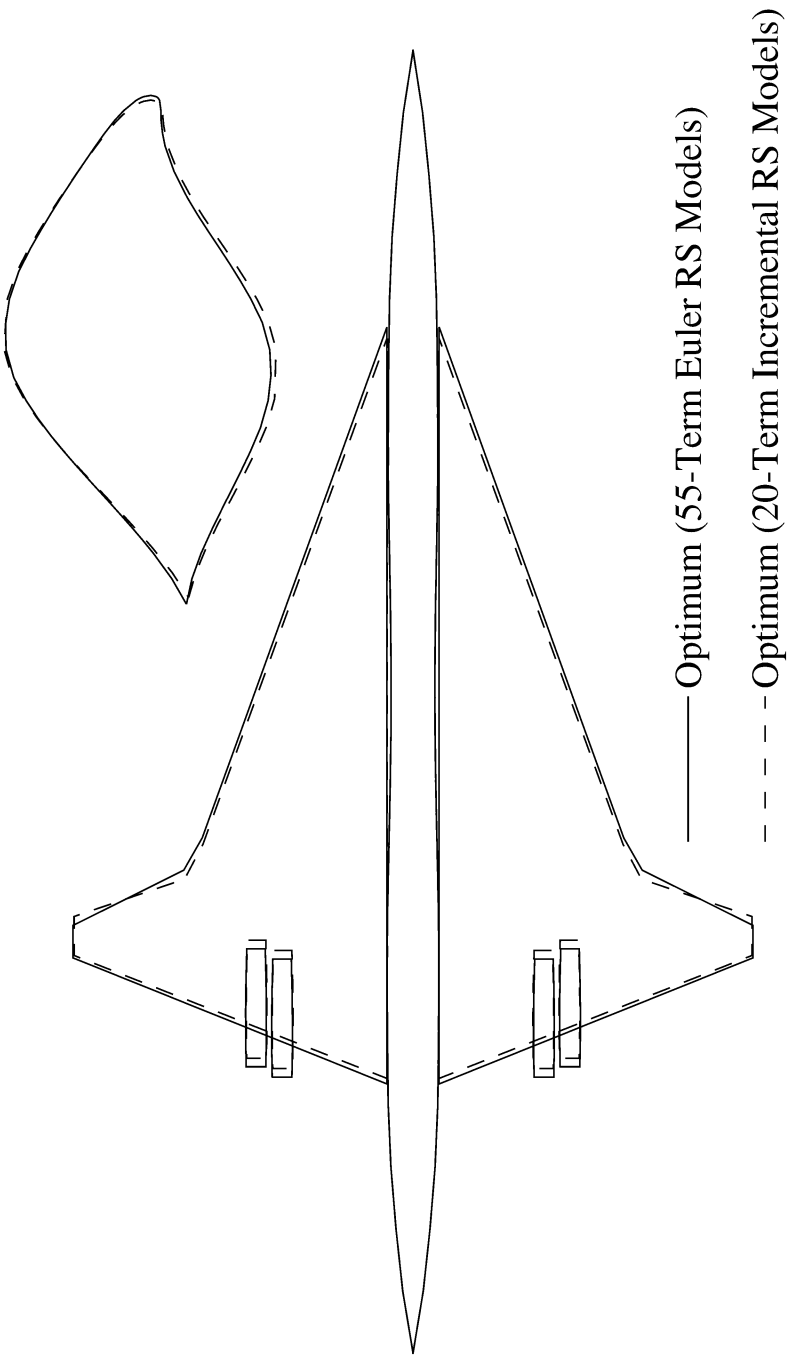


**Figure 10.4:** Optimal Designs from Reduced Term Incremental and Full Term Euler RS Models.

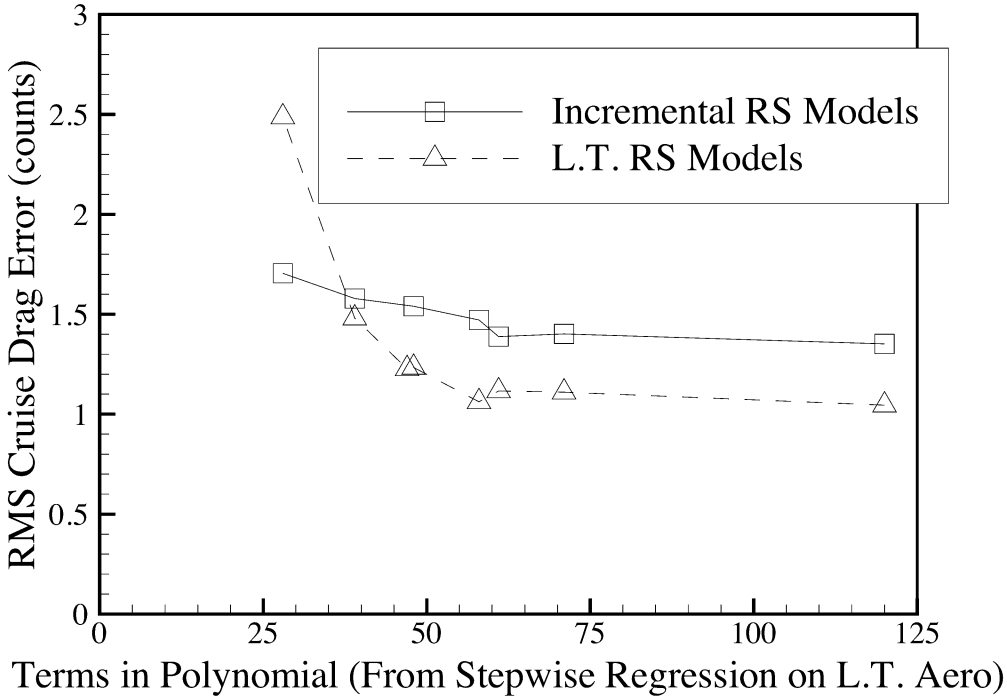


**Figure 10.5:** Stepwise Regression Analysis (15 Variable HSCT Design).

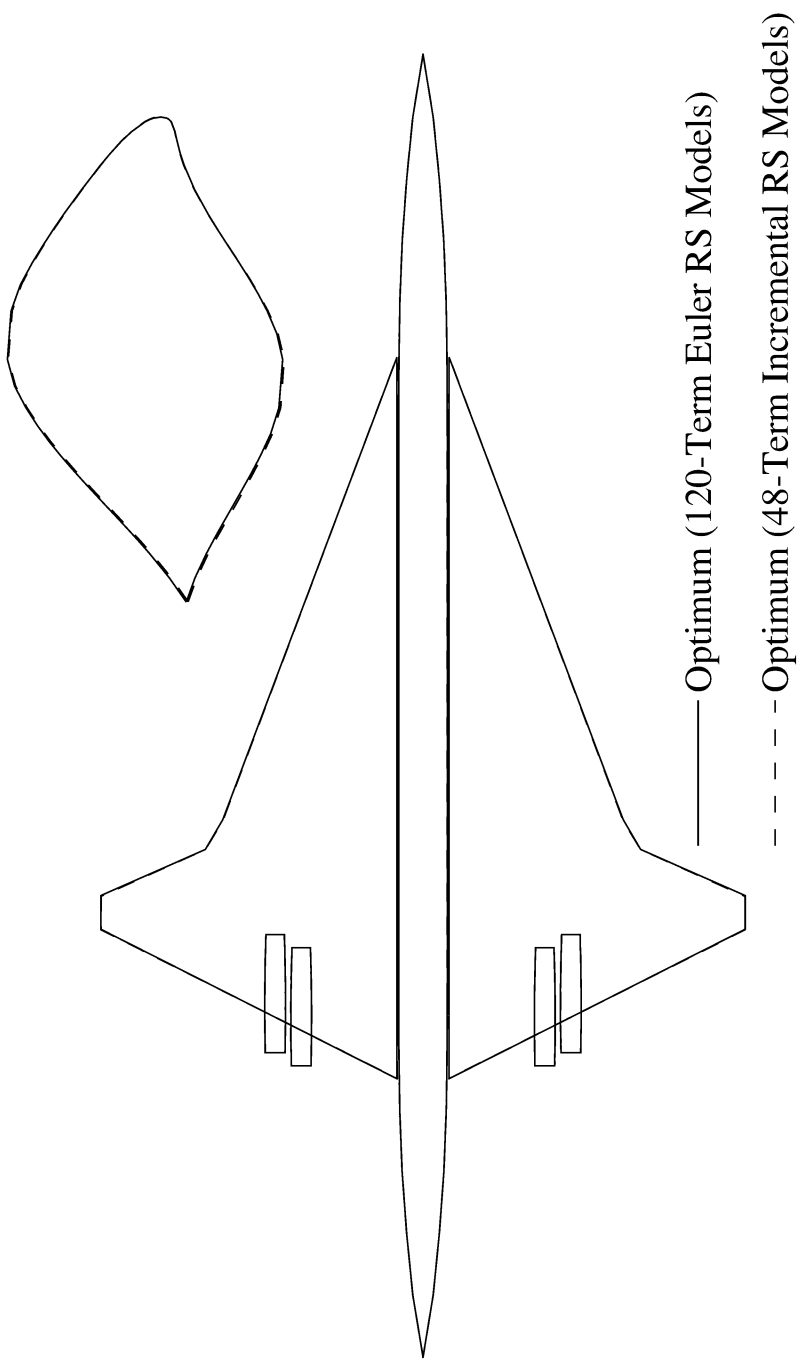


**Figure 10.6:** Optimal Designs from Reduced Term Incremental and Full Term Euler RS Models.

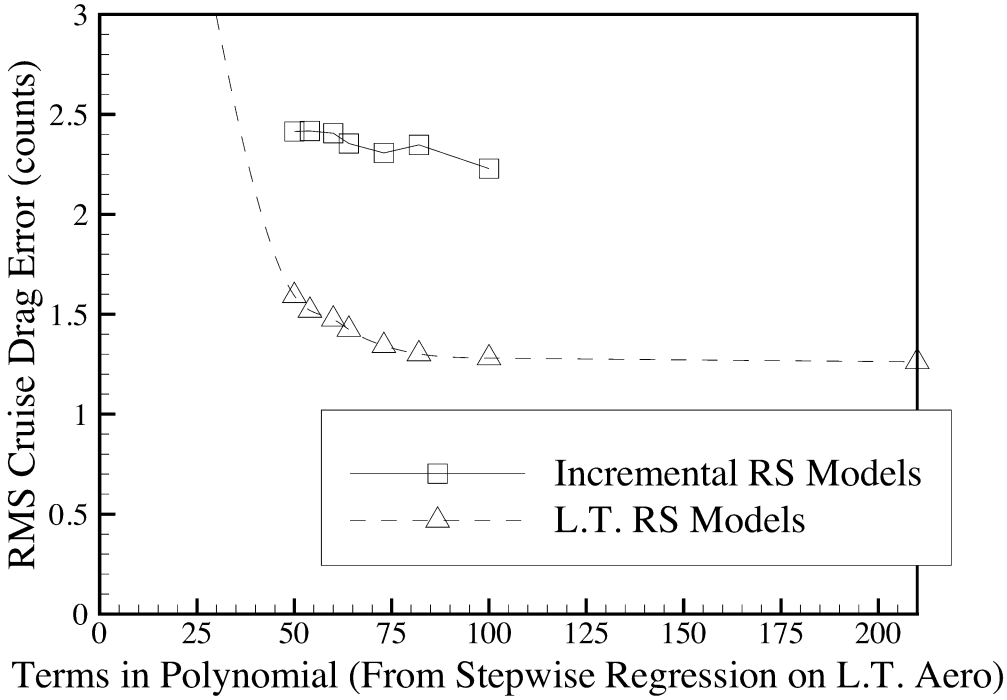


**Figure 10.7:** Stepwise Regression Analysis (20 Variable HSCT Design).

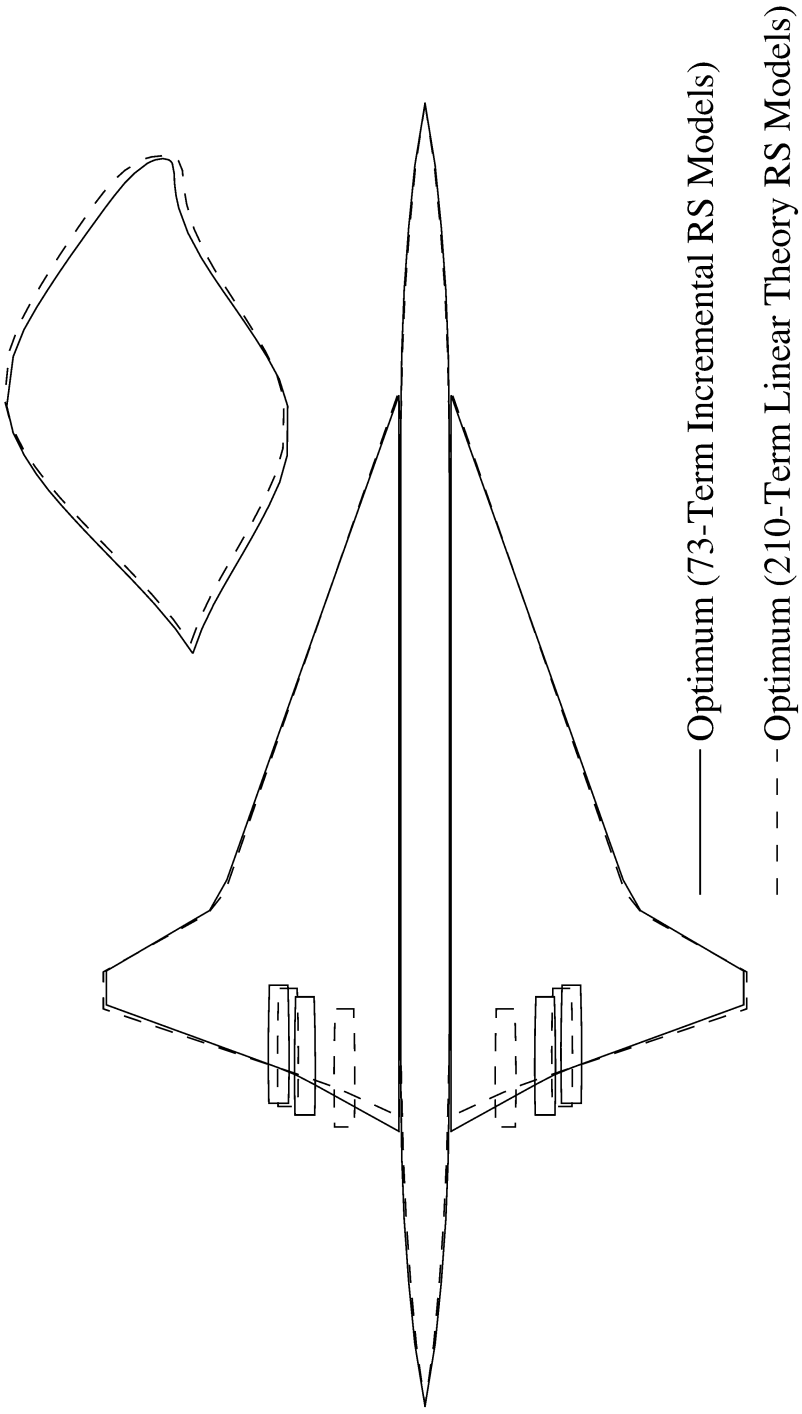


**Figure 10.8:** Optimal Designs from Reduced Term Incremental and Full Term Linear Theory RS Models.

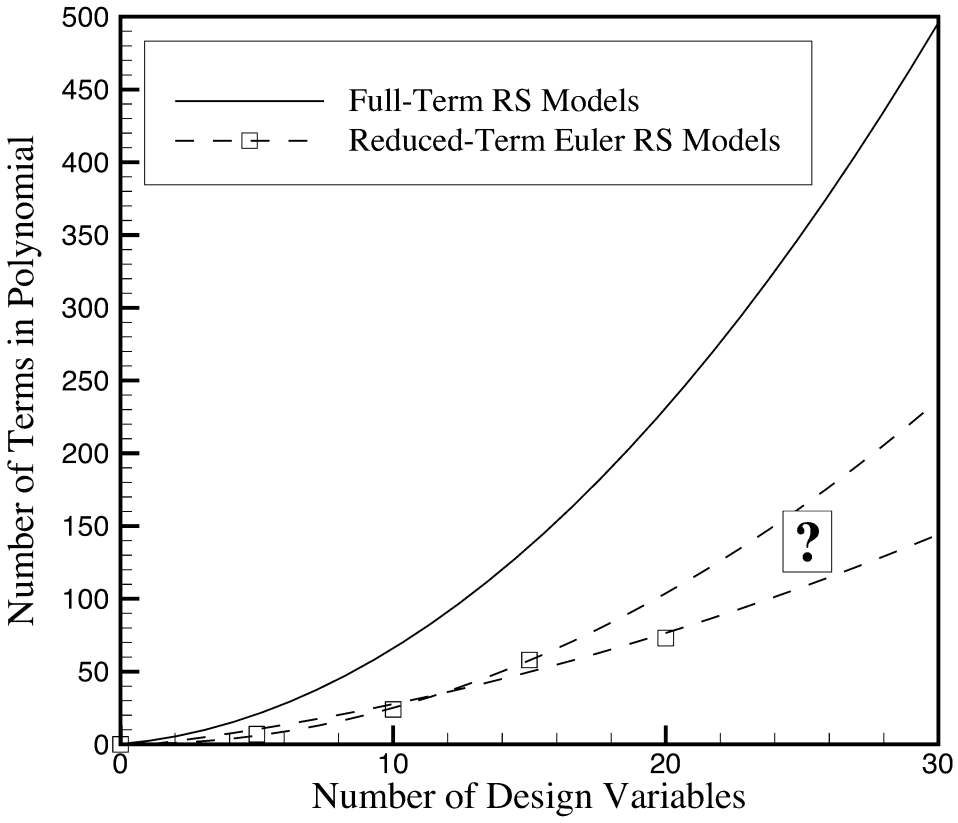


**Figure 10.9:** Terms in RS Models.

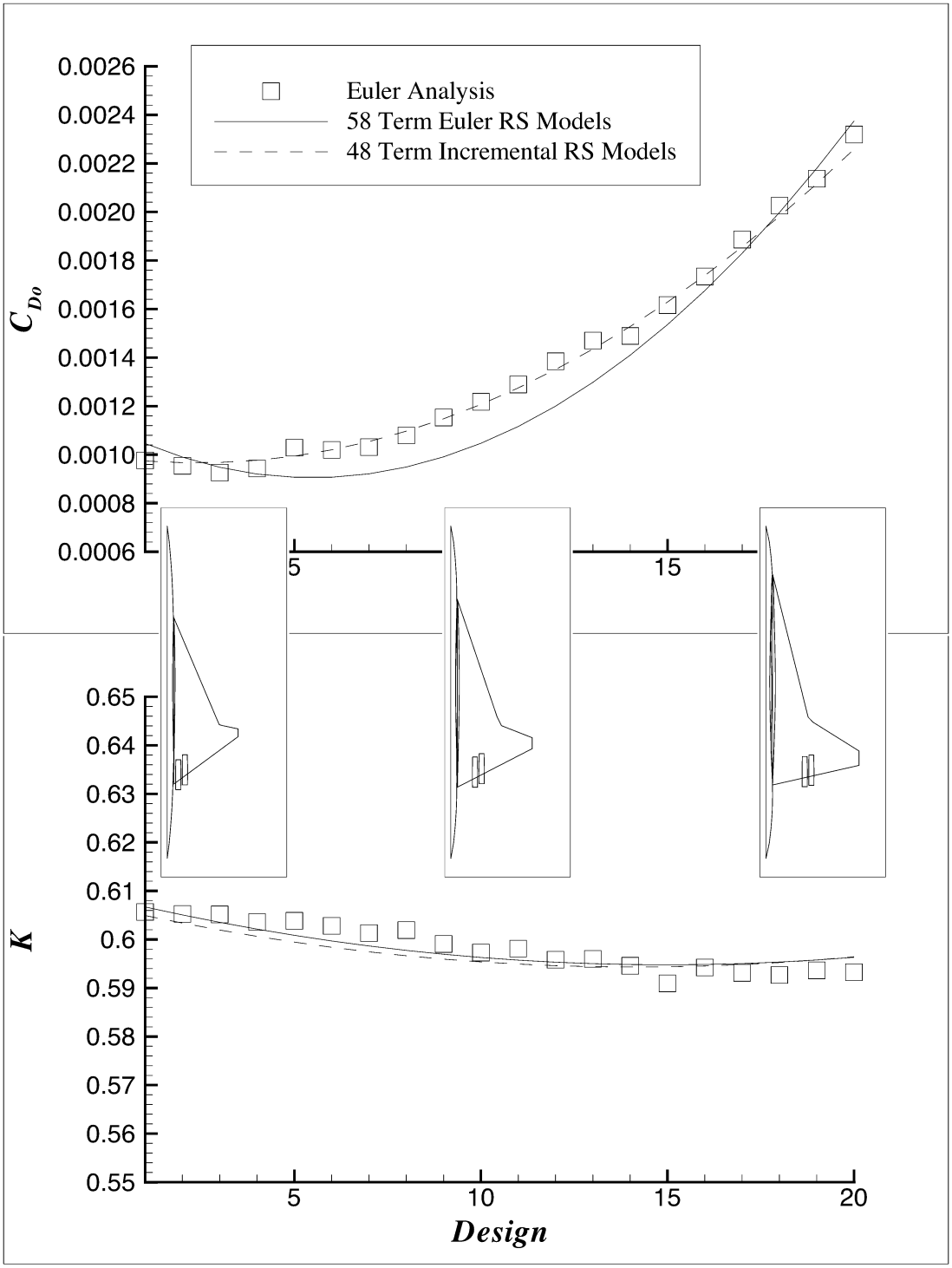


**Figure 10.10:** Comparison of RS Model Fits across the Design Box.

# Chapter 11

# Parallel Computing

Over one thousand CFD drag solutions are required to create the RS models and evaluate the errors for the 15 variable and 20 variable designs. Performing these calculations on a single processor of the SGI *Power Challenge* R8000 machine takes nearly two weeks of wall clock time. This time can be reduced significantly by taking advantage of parallel computing.

A coarse-grained parallelization of the CFD analyses has been implemented on the 119 node, distributed memory Intel *Paragon* XP/S at Virginia Tech. While fine-grained parallelization offers potentially better performance, especially for large numbers of nodes, coarse-grained parallelization is easier to implement and does not require in-depth knowledge of or modifications to the complex codes used. The parallel computations are organized in a "master-slave" paradigm, where one processor creates the directory structure and input files, distributes the jobs, and checks for their completion. Each individual CFD calculation is performed entirely by a single "slave" node. Details about the parallel organization and coding are presented in Appendix A.

Two measures of parallel performance are presented: the parallel speedup and efficiency. Speedup represents the ratio of the serial calculation time to the parallel computation time on $n_p$ nodes. The parallel efficiency is the speedup divided by the number of nodes. Ideally, the speedup equals the number of nodes, bringing the efficiency to 1.0; however, this ideal behavior is not realized. One reason for this is the "master-slave" approach to parallelization. Since the master node is only

an administrative node and performs no calculations, the best obtainable speedup is $(n_p - 1)$ and the highest efficiency possible is $(n_p - 1)/n_p$. This still indicates that, as $n_p$ increases, the efficiency approaches 1.0. File I/O, which is inherently serial, increases with $n_p$ and prevents the user from approaching ideal speedup and efficiency for large numbers of nodes. Reading and writing of input files, CFD grid files, and CFD solution files are examples of the file I/O present in the procedure.

In spite of these detractors, good performance is achieved when implementing the CFD calculations in parallel. Figure 11.1 shows the parallel speedup and efficiency obtained from performing 1080 CFD calculations for 360 HSCT configurations used in the 15 variable design. When using 27 nodes, a speedup of 24.3 (0.90 efficiency) is realized. When using 53 nodes, a speedup of 45.4 (0.86 efficiency) is achieved. Even though a single processor of the Intel *Paragon* is about ten times slower than a single processor of the SGI *Power Challenge*, significant improvements in the turn-around time are achieved when using a large number of nodes. On 53 nodes, the 1080 Euler calculations require only 2.8 days to complete.

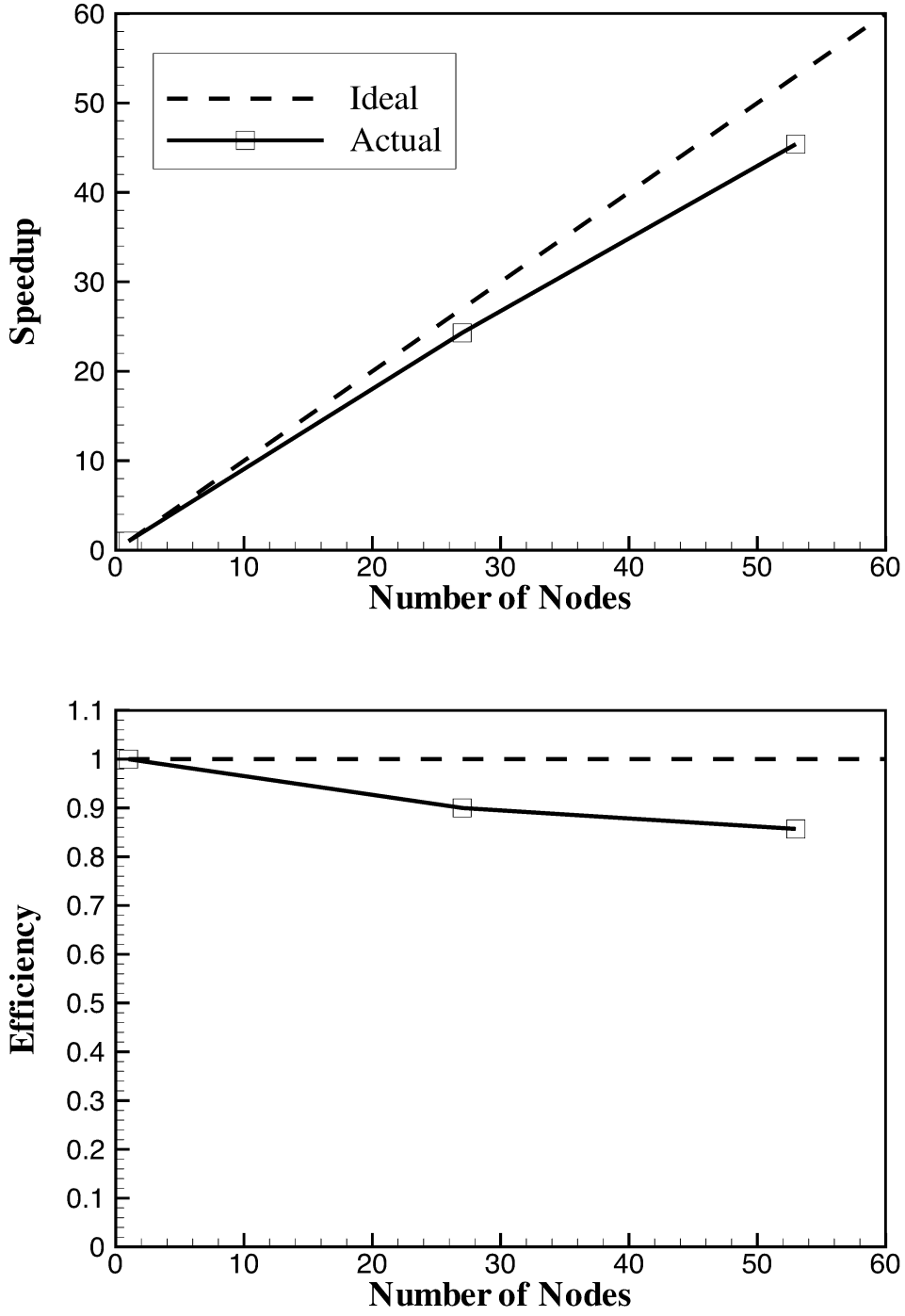


**Figure 11.1:** Parallel Speedup and Efficiency

# Chapter 12

# Design Trade-offs and Sensitivities

Parametric studies are invaluable to a designer. These studies provide information on trade-offs between various disciplines and influences, sensitivities to variations in design variables, and effects of perturbations to a chosen design. To perform a single parametric study, 25–50 analyses may be required. To completely examine a design, many of these parametric studies would be desired. The computational burden involved in performing these numerous studies is greatly reduced by using results from RS models instead of data from a large number of CFD calculations since the expense lies only in the evaluation of the simple quadratic polynomials. In this section, we examine variations in selected design variables to gain insight into the behavior and relative importance of these parameters.

The optimal designs predicted from linear theory and Euler RS models for the five, ten, and fifteen variable design problems show the effects of the higher drag predictions typical of the supersonic Euler solutions. The thickness-to-chord ratio, $t/c$, is a direct trade-off (Fig. 12.1) between aerodynamics and structures. Aerodynamics dictates that the wing should be as thin as possible to reduce the drag and therefore the fuel weight. Structural optimization, on the other hand, would attempt to increase the thickness of wing to reduce the wing weight. A compromise is met between the fuel weight and wing weight to obtain the minimum TOGW. The effects of replacing the linear theory aerodynamics with Euler solutions is apparent in the fuel weight. The higher drag from Euler analysis translates to higher fuel weights and a design in which the aerodynamic aspects are more dominant. The optimal design is obtained at a

lower $t/c$ value to counter the effects of the higher drag at the expense of the wing weight.

The linear theory curve for the fuel weight variation with $t/c$ has a nearly zero slope at $t/c = 1.5\%$. This occurs because the fuel weight required to meet the range constraint is not influenced only by the aerodynamics. As the wing gets thinner and the wing weight increases, there is a point where the fuel weight penalty associated with the increasing weight of the aircraft becomes as important as the fuel weight benefit from the reduced the drag. This point occurs near $t/c = 1.5\%$ when using linear theory analysis. When using Euler analysis, the fuel weight is still dominated by the aerodynamic benefits over the range of $t/c$ investigated.

The decreased inboard leading-edge sweep in the optimal design from Euler aerodynamics is an interesting occurrence. This is not a result of aerodynamic–structural trade-offs, but rather it is due mainly to a compromise between aerodynamic influences. With the semispan, $b/2$, and inboard LE length, $s_{LE_I}$, fixed, there is an increase in the size of the outboard section implicit with any increase in $\Lambda_{LE_I}$. The aerodynamic trade-off (Fig. 12.2) is between the high inboard sweep desired for improved supersonic performance and the size of the outboard section, which has poor supersonic performance. The nonlinear aerodynamic predictions have a relatively larger fuel weight penalty associated with the outboard section than do the linear theory results. This naturally shifts the optimal $\Lambda_{LE_I}$ to a lower value.

The wing weight plot in Fig. 12.2 shows a $\Lambda_{LE_I}$ compromise between structural effects as well. At the lowest wing sweep, the planform takes on a structurally sound shape. However, the large planform area results in extra weight. At the other extreme, the planform area is reduced, but the design is not as sound structurally. Extra weight is required to strengthen the structure. The best design is a trade-off between these two influences. Incidentally, when using Euler aerodynamics the optimum $\Lambda_{LE_I}$ for minimum fuel weight is very close to the optimum for minimum wing weight.

The final design variable whose behavior deserves some discussion is the root chord. The effects of $c_{root}$ on the various components of the aircraft weight (Fig. 12.3) are small in comparison with those of $t/c$ and $\Lambda_{LE_I}$. This information could be very important to a designer when considering other aspects of design such as control surface placement and effectiveness, since varying only the root chord has the effect of changing the TE sweep.

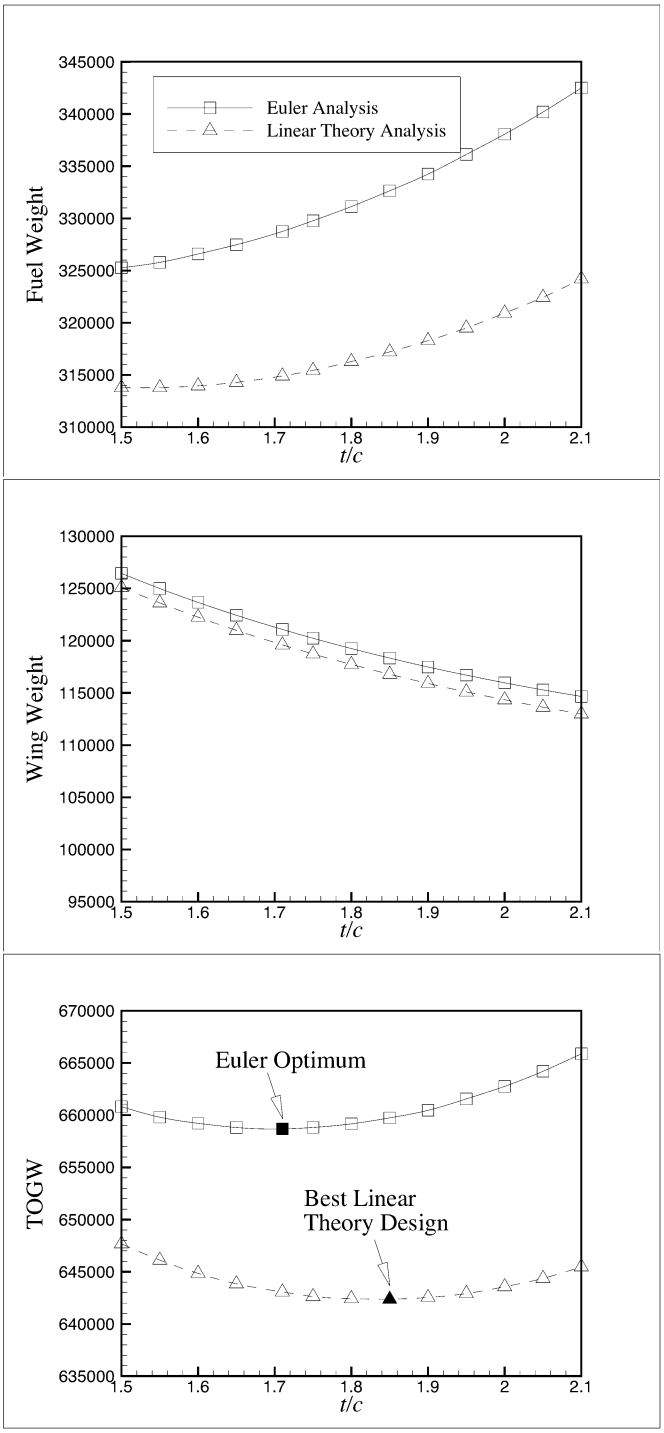


**Figure 12.1:** Aerodynamic–Structural Trade-Off for $t/c$.

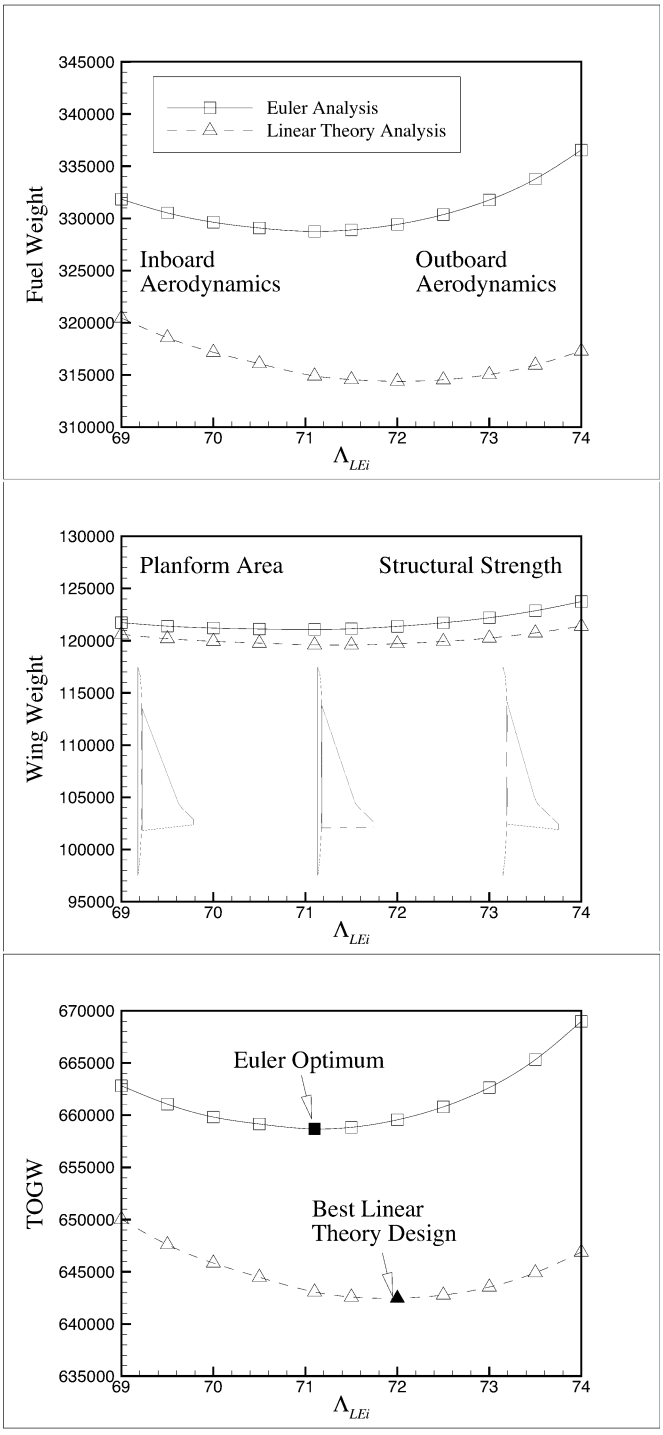


**Figure 12.2:** Aerodynamic and Structural Trade-Offs for $\Lambda_{LE_I}$.

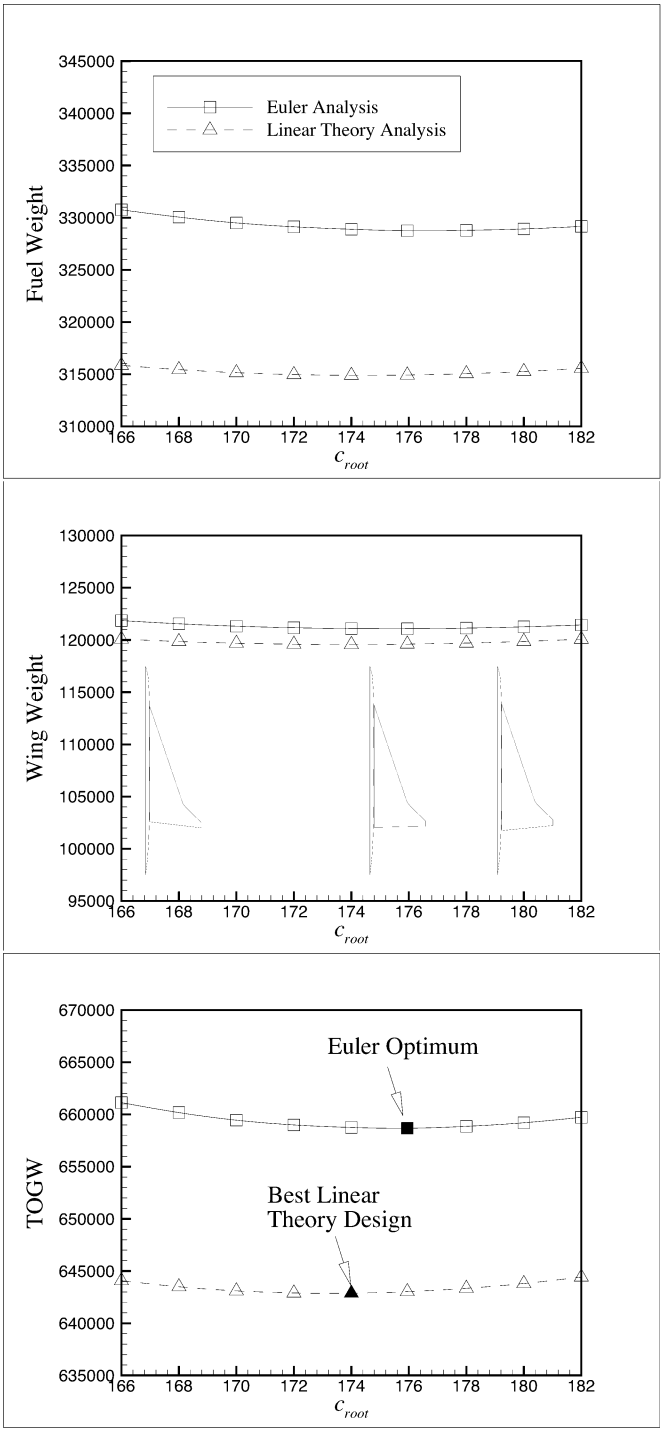


**Figure 12.3:** Effects of $c_{root}$ on Aircraft Weight.

# Chapter 13

# Design Space Visualization

Designers need insight into the shape of the design spaces in which they work. Knowledge of the constraint boundaries and objective function variation can allow more informed selection of an optimal design. A novel and effective approach to visualizing highly constrained, and even nonconvex, design spaces arose during this work. This approach takes advantage of RS models to evaluate a large number of aircraft configurations with minimal computational effort.

A previous ten variable wing design provides a good opportunity to exercise this approach. For certain starting conditions, the optimizer converged to Optimum 1 which is approximately 2000 $lb$ heavier than Optimum 2. To provide an explanation for this behavior, a plane in the ten dimensional design space (Fig. 13.1) is created using Optimum 1, Optimum 2, and another suboptimal feasible point. The remaining points are created by linearly varying the design variables between all three points. This can be thought of as a multidimensional extension of the $\alpha$-plot described in Section 12. Without RS models, Euler solutions would be required for all of the individual design points, but with RS models all the information can be obtained simply by evaluating the quadratic polynomials. The design points represented by the open circles are feasible points, while those represented by the filled circles have violated some constraints. The plot clearly shows the nonconvexity of the design space caused by the aerodynamic constraints. If the optimizer drives the design near Optimum 1, it cannot cross the boundary created by the range constraint to arrive at Optimum 2. While RS modeling of the aerodynamic analyses has removed local

optima caused by noise in the responses, there are still local minima that result from the nonconvex constraint boundaries. The complexity of the constraint boundaries is displayed in Fig. 13.2 which represents a different cut through the design space, created with the same two local optima and a different suboptimal point. In both plots it is apparent that the optimal designs do not reside in a region of minimum weight, but rather they lie next to constraint boundaries which prohibit any further movement.

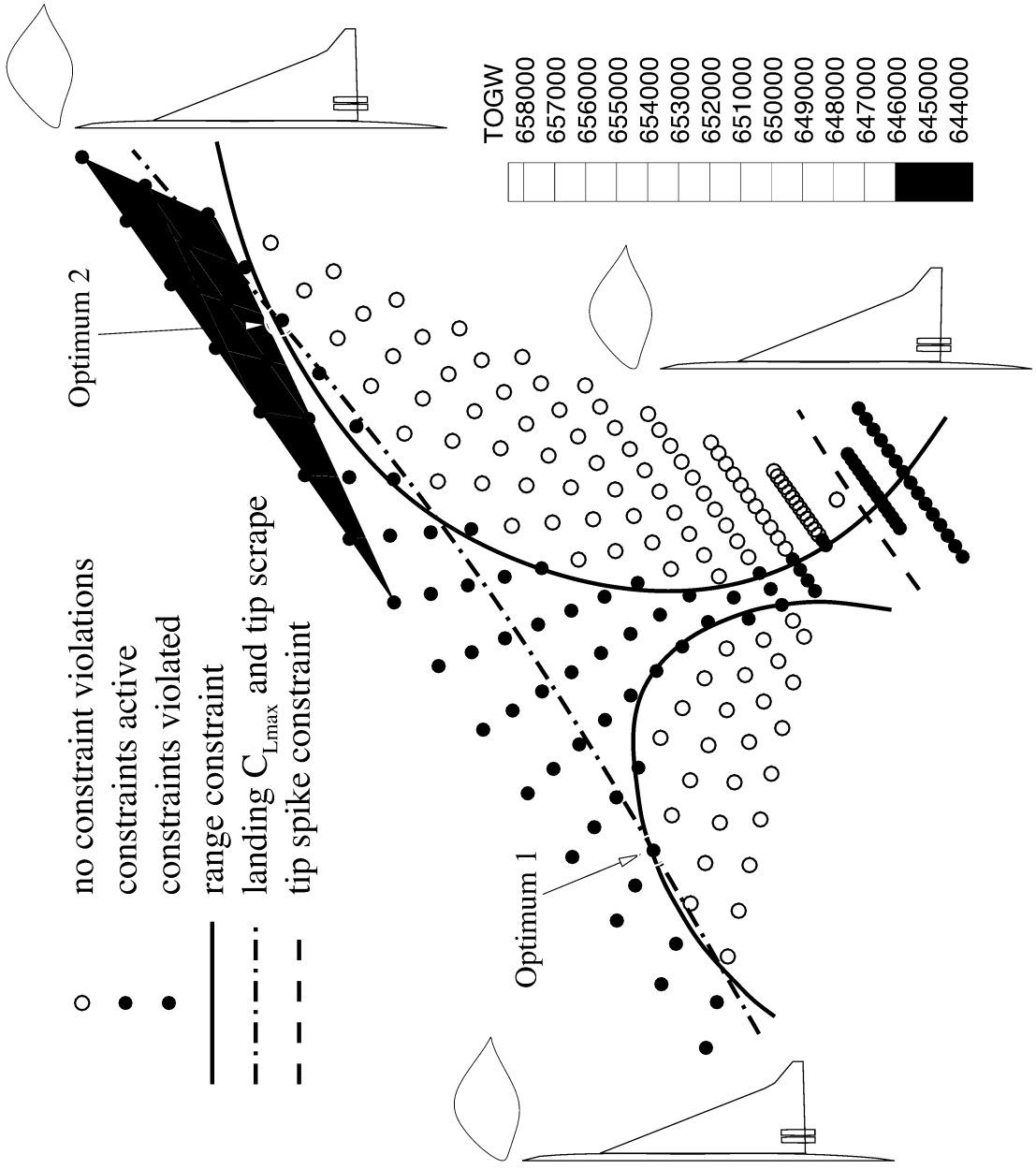


**Figure 13.1:** Nonconvex Design Space in Ten Variable Problem.

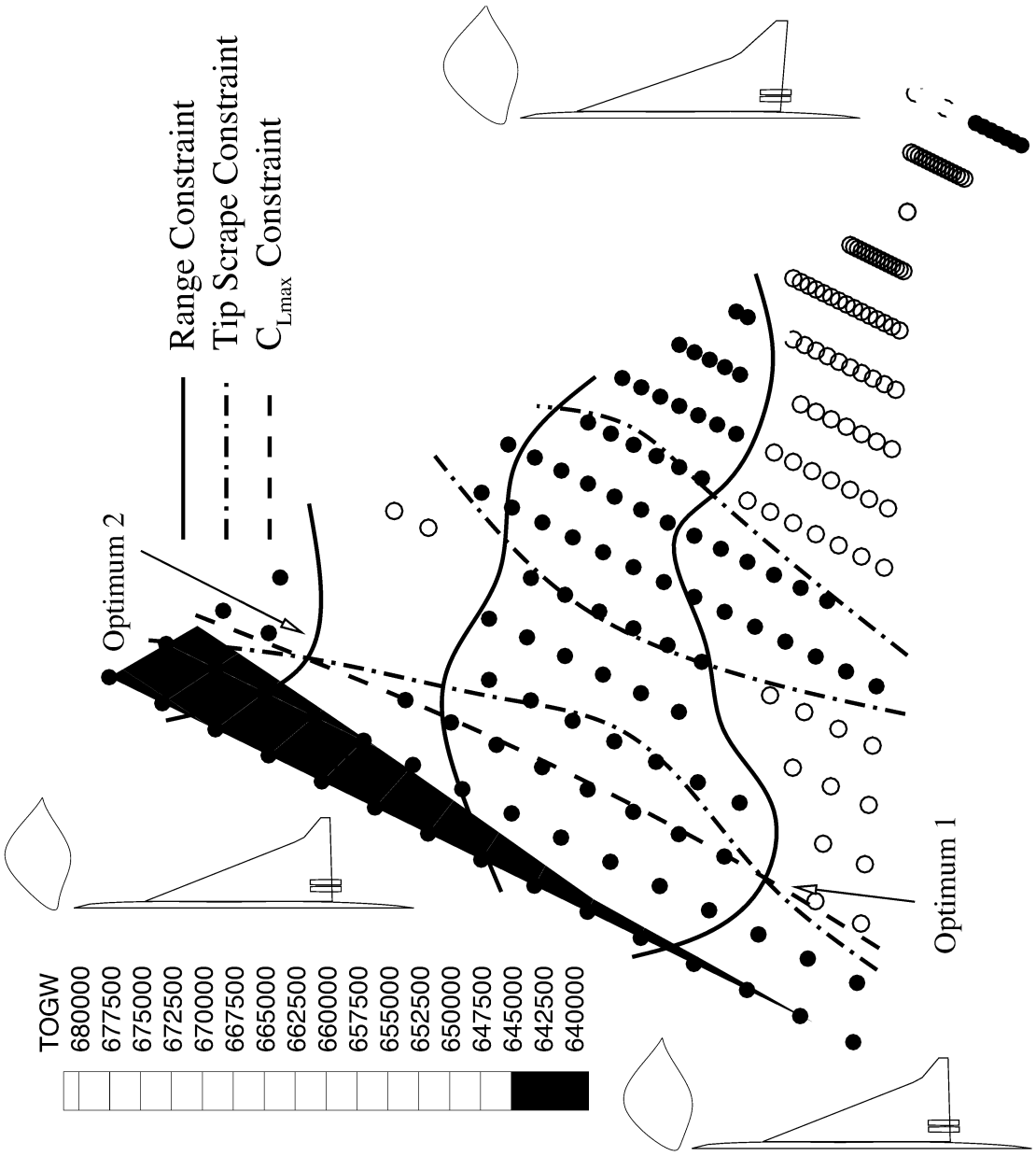


**Figure 13.2:** Nonconvex Design Space in Ten Variable Problem.

# Chapter 14

# Methods for Improving Accuracy

Errors in the linear theory and Euler RS models steadily increase from satisfactory levels in the 5 variable to unacceptable levels in the 20 variable problem. A cursory examination of three ways to improve the accuracy of the RS models is presented in the following sections. These preliminary studies are performed using mainly linear theory results, and are intended to provide insights into the most promising method for use with the more expensive Euler analyses.

The first two methods deal with the nonquadratic nature of the responses, but in a different manner. For small variations in a low number of design variables, the behavior of the response in the design space can be adequately modeled by a quadratic function. As the number of design variables grows, this assumed quadratic form of the response becomes less accurate. One method of dealing with this is by reducing the limits on the design variables as the number of design variables is increased, based on the optimal values of earlier optimizations. This procedure is known as "zooming".

Another way to deal with this problem is to keep the same bounds on the design variables, but include cubic terms in the response surface model. Adding cubic terms will require a much larger experimental design, but one may still apply the *reduced term* model procedure to minimize the number of expensive Euler evaluations required.

The final technique to reduce the RS model error involves using a more accurate physical model to provide the functional form for the response. In the previous studies an uncambered form of the drag polar was used to model the drag variation with the

lift. With an additional CFD evaluation per design, a more accurate cambered form of the drag polar can be evaluated. While not addressing the nonquadratic behavior of the response, this approach should still lead to reduced errors in the RS models.

## 14.1 Reducing Volume of Design Bounding Box

Assuming a quadratic variation in the response will be more valid when the range of the design variables, defined by the difference between the values at the upper and lower bounds, is "small". An alternate 15 variable design provides support for this statement. This design was found prior to those presented in Chapters 8-10, and therefore does not represent an attempt to "zoom in" on the optimal design, but it does show decrease in errors with tighter bounds on the design variables. A comparison of the limits on the design variables is available from Table 14.1. The most significant differences are in $b/2$, $s_{LE_I}$, $\Lambda_{LE_O}$, and $y_{nacelle}$. The alternate design problem has tighter bounds on all active design variables except for the fuselage radii, which have the same limits, and $(x/c)_{max\text{-}t}$.

The RS model fit for the alternate design is evaluated using a randomly selected set of 360 configurations from the central-composite experimental design used to screen the reduced design bounding box. The RMS errors in the full term linear theory and Euler RS models are 0.66 counts and 0.59 counts, respectively. This is a noticeable improvement from the 1.05 and 1.35 count errors in the baseline linear theory and Euler RS models.

Since the design bounding box for the alternate design problem is not contained within that for the baseline problem, there is some question as to whether the differences in the response surface model fit are due entirely to the reduction in the box volume. The response for the alternate design problem may also have more quadratic behavior over its bounding box; however, this cursory study does imply that shrinking the size of the design bounding box can have a beneficial effect on the RS model fit.

## 14.2 Cubic RS Models

The second approach to dealing with the nonquadratic behavior of the response is to include cubic terms in the response surface model. This requires more effort than simply shrinking the design space, but it does allow one to maintain the original bounds on the design variables. To assess the improvement in accuracy, a cubic RS model of the linear theory drag shape parameters is created for the 10 variable problem.

A cubic RS model has the form

$$y = c_0 + \sum_{1 \le j \le m} c_j \, x_j + \sum_{1 \le j \le k \le m} c_{jk} \, x_j \, x_k + \sum_{1 \le j \le k \le l \le m} c_{jkl} \, x_j \, x_k \, x_l, \tag{14.1}$$

where $y$ is the response, the $x_j$ are the design variables, and $c_0$, $c_j$, $c_{jk}$, and $c_{jkl}$ are the polynomial coefficients. There are $(m+1)(m+2)(m+3)/6$ coefficients for a cubic response surface model in $m$ variables. This equates to 220 coefficients for the 10 variable problem, since only nine of the design variables are needed for the RS models.

In order to evaluate the coefficients for the cubic response surface, a new experimental design must be constructed. For this work, the original D-optimal experimental design is supplemented with points from an orthogonal array generator developed by Dr. Art Owen. The orthogonal array is created using a method by Addelman[77] and Kempthorne. This method provides $2 \cdot 9^2 = 162$ designs. Combining these computational experiments with those from the original D-optimal experimental design provides 393 experiments with which to evaluate the 220 terms in the cubic RS model. Including the cubic terms results in a reduction in the RMS error for the linear theory RS models from 0.89 to 0.62 counts.

## 14.3 Improved Drag Polar Representations

The last attempt to increase the accuracy of the RS models involves the use of a more accurate drag polar representation. One of the key themes in this work is using information from simpler methods and knowledge of the problem physics to more accurately create RS models for aerodynamic quantities. While the uncambered form of the drag polar provides good results over the desired range of lift coefficients, using

a more accurate functional form should improve the RS model fit. The cambered form of the drag polar is as follows:

$$\begin{aligned} C_D &= C_{D_m} + K\left(C_L - C_{L_m}\right)^2, \qquad (14.2) \\ \text{where} \quad C_{D_m} &= C_{D_m}(\mathbf{x}), \\ C_{L_m} &= C_{L_m}(\mathbf{x}), \quad \text{and} \\ K &= K(\mathbf{x}) \end{aligned}$$

Quadratic response surface models are created for the shape parameters $C_{D_m}$, $C_{L_m}$, and $K$ in the same manner as they were for $C_{D_0}$ and $K$, using linear theory analyses for the 20 variable design problem. The RMS error in cruise drag coefficient prediction dropped from 1.26 counts to 0.96 counts when using the more accurate functional form of the drag polar. This is approximately the same magnitude change in RMS error as is seen when using the cubic terms in the response surface model in the previous section, but this method required far fewer additional calculations for a given number of design variables.

All three methods showed improvement in the RS model prediction errors. Shrinking the bounds on the design variables, while perhaps the least interesting approach, appears to provide the largest improvement. The RMS error in linear theory results for the alternate 15 variable problem is 0.4 counts lower than for the original problem with larger bounds on the design variables. An even larger improvement of 0.75 counts is seen in the RS models for the Euler aerodynamics. Including cubic terms in the 10 variable problem and using the more accurate functional form for the drag polar in the 20 variable problem both reduced the RMS error in the RS models by about 0.3 counts. Using the cambered form of the drag polar only requires one additional CFD solution per experimental design, while using cubic RS models will require an substantially larger number of solutions since the number of terms grows as $m^3$. The most advantageous and practical approach to improving the accuracy of the RS models appears to be a combination of using the more accurate form of the drag polar along with some type of "zooming" technique. A more in-depth and careful study of these methods is required to reach a conclusive verdict.

**Table 14.1:** Design Variable Limits in the Simplified Optimization Problems.

| Design Variable | 15 Variable | Alternate 15 Variable |
|---|---|---|
| ***Planform Variables*** | | |
| $c_{root}$ | $150\,ft - 190\,ft$ | $150\,ft - 180\,ft$ |
| $c_{tip}$ | $7\,ft - 13\,ft$ | $8\,ft - 12\,ft$ |
| $b/2$ | $58\,ft - 78\,ft$ | $68\,ft - 80\,ft$ |
| $s_{LE_I}$ | $105\,ft - 135\,ft$ | $142\,ft - 158\,ft$ |
| $\Lambda_{LE_I}$ | $67° - 76°$ | $68° - 74°$ |
| $\Lambda_{LE_O}$ | $12° - 32°$ | $38° - 46°$ |
| $s_{TE_I}$ | (straight trailing edge) | |
| $\Lambda_{TE_I}$ | (straight trailing edge) | |
| ***Airfoil Variables*** | | |
| $(x/c)_{max\text{-}t}$ | $38\% - 52\%$ | $35\% - 50\%$ |
| $R_{LE}$ | $2.1 - 4.1$ | $2.0 - 2.8$ |
| $(t/c)_{root}$ | $1.5\% - 2.7\%$ | $1.8\% - 2.6\%$ |
| $(t/c)_{break}$ | ($t/c$ constant across span) | |
| $(t/c)_{tip}$ | ($t/c$ constant across span) | |
| ***Fuselage Variables*** | | |
| $r_{fus_1}$ | $4.5\,ft - 6.0\,ft$ | |
| $r_{fus_2}$ | $4.5\,ft - 6.0\,ft$ | |
| $r_{fus_3}$ | $4.5\,ft - 6.0\,ft$ | |
| $r_{fus_4}$ | $4.5\,ft - 6.0\,ft$ | |
| ***Nacelle and Mission Variables*** | | |
| $y_{nacelle}$ | $10\,ft - 35\,ft$ | $15\,ft - 25\,ft$ |
| $\Delta y_{nacelle}$ | $[6\,ft]$ | |
| $W_{fuel}$ | No Limits | |

$[\,\cdot\,]$ indicates value of a variable when it is not active in the design

# Chapter 15

# Conclusions

Preliminary investigations into the aerodynamic modeling requirements for HSCT design indicate that significant improvements in the aircraft performance estimates can be achieved by replacing linear theory aerodynamic predictions with those from CFD. Differences in the cruise drag coefficient computed from PNS and linear theory of less than 3% occur for the wing and wing-fuselage configurations presented. However, these small discrepancies in the predicted drag lead to large variations in the aircraft range. Discrepancies of up to 126 $n.mi.$ for an aircraft with a nominal range of 5500 $n.mi.$ indicate that linear theory predictions are not sufficient for HSCT range calculations. These studies also show that, for supersonic cruise conditions, adding algebraic skin friction estimates to Euler drag predictions produced accurate results when compared to PNS predictions.

A method for efficiently implementing supersonic Euler analyses in a combined aerodynamic–structural optimization of an HSCT configuration has been tested on five, ten, fifteen, and twenty variable HSCT design problems. This method makes use of RS models for the aerodynamic quantities to avoid problems with numerical noise. Key to the success of this method is making use of information gained from less expensive, lower fidelity aerodynamic models. Conceptual level aerodynamic models provide the functional form of the drag polar. Calculating the drag as $C_D = C_{D_0}(\mathbf{x}) + K(\mathbf{x})\ {C_L}^2$ offers a number of advantages. The intervening functions $C_{D_0}(\mathbf{x})$ and $K(\mathbf{x})$ are functions of only the geometric design variables. Removing the fuel weight dependency reduces the number of terms in the RS models. The intervening

functions also provide more useful information to the designer. Finally, experience has indicated that more accurate results are obtained by building the response from RS models for its components.

Through regression analysis and ANOVA techniques, response surface models created using relatively inexpensive linear theory aerodynamics provide information on the terms which do not play a significant role in the evaluation of the drag. Since the Mach 2.4 cruise flight regime is predominantly linear, these terms can also be removed from the RS models for the Euler aerodynamics. Computational time is saved since fewer Euler analyses are required to evaluate the coefficients of the reduced term polynomials.

For the 5 variable problem, only 7 of the 15 RS terms are significant for the linear theory RS models. For the 10 variable problem, only 24 of the 55 RS terms are significant. For the 15 variable problem, only 58 of the 120 RS terms are significant. For the 20 variable problem, only 73 of the 210 RS terms are significant. A complete listing of the significant terms in the response surface models for the 5 variable, 10 variable, and 15 variable designs is presented in Table 9.4. Using the reduced term RS models instead of the full term RS models for the 5, 10, 15, and 20 variable problems results in computational savings of 8.5, 42, 99, and 255 hours, respectively, on a single 75 MHz IP21 processor of an SGI *Power Challenge* R8000.

The most promising approach to including Euler drag solutions uses response surface models for the difference between the Euler and linear theory RS values of the intervening functions $\Delta C_{D_0}$ and $\Delta K$. The errors in the incremental RS cruise drag prediction for the optimal designs range from less than 0.1 count to 0.8 count for the 20 variable optimum.

The RMS errors in the RS models steadily increase from the five through the twenty variable problems. The inability to perform calculations at all vertices of the design bounding box and the nonquadratic behavior of the response are contributing factors. These errors can be reduced by using the more accurate functional form of the drag polar. However, other methods are necessary to bring the RS model errors in the twenty variable case to acceptable levels. Using a "zooming" technique to reduce the size of the design box appears to be a promising approach. Further research is required to investigate the use of these procedures in the multidisciplinary HSCT design problem.

Important practical design information can be easily obtained from RS models. Information on design trade-offs and sensitivities are readily available from the RS models with little computational effort. Visualization of the design space is also readily available to provide insight into the complex constraint boundaries present in complicated optimization problems. These constraint boundaries give rise to a nonconvex design space and local minima. This information can be easily obtained with the evaluation of simple quadratic polynomials.

# Bibliography


[1] J. P. Geising, S. Agrawal, and B. K. Bharadvaj. "The Role of Computational Fluid Dynamics in Multidisciplinary Design Optimization of Transport Aircraft," *Proceedings of the* $6^{th}$ *International Symposium on Computational Fluid Dynamics, Technology, and Operations Congress*, Lake Tahoe, CA, September 4–7, 1995.

[2] L. M. Nicolai. *Fundamentals of Aircraft Design*, E.P. Domicone Printing Services, Fairborne, OH, pp. 2423 – 2425, 1975.

[3] D. M. Hollenback and G. A. Blom. "Application of a Parabolized Navier-Stokes Code to an HSCT Configuration and Comparison to Wind Tunnel Test Data," AIAA Paper No. 93–3537, August 1993.

[4] J. L. Pittman, D. L. Bonhaus, M. J. Siclari, and S. M. Dollyhigh. "Euler Analysis of a High-Speed Civil Transport Concept at Mach 3," *Journal of Aircraft*, 28, No. 4: 239–245, April 1991.

[5] P. Covell, G. Hernandez, J. Flamm, and O. Rose. "Supersonic Aerodynamic Characteristics of a Mach 3 High-Speed Civil Transport Configuration," AIAA Paper No. 90–3210, September 1990.

[6] M. G. Hutchison, E. R. Unger, W. H. Mason, B. Grossman, and R. T. Haftka. "Variable-Complexity Aerodynamic Optimization of a High-Speed Civil Transport Wing," *Journal of Aircraft*, 31, No. 1: 110–116, 1994.

[7] A. A. Giunta, V. Balabanov, D. Haim, B. Grossman, W. H. Mason, L. T. Watson, and R. T. Haftka. "Wing Design for a High-Speed Civil Transport Using a Design

of Experiments Methodology," *Proceedings of the* $6^{th}$ *AIAA/NASA/ISSMO Symposium on Multidisciplinary Analysis and Optimization,* AIAA Paper No. 96–4001, pp. 168–183, Bellevue, WA, September 1996.

[8] P. J. Röhl, D. N. Mavris, and D. P. Schrage. "Combined Aerodynamic and Structural Optimization of a High-Speed Civil Transport," $36^th$ *AIAA Structures, Dynamics, and Materials Conference,* AIAA Paper No. 95-1222, New Orleans, LA, April 1995.

[9] I. Kroo, S. Altus, R. Braun, P. Cage, and I. Sobieski. "Multidisciplinary Methods for Aircraft Preliminary Design," *Proceedings of the* $5^{th}$ *AIAA/USAF/NASA/ISSMO Symposium on Multidisciplinary Analysis and Optimization,* AIAA Paper No. 94-4325, pp. 697–707, Panama City, FL, September 1994.

[10] R. S. Sellar, S. M. Batill, and J. E. Renaud. "Response Surface Based, Concurrent Subspace Optimization for Multidisciplinary System Design," $34^{th}$ *Aerospace Sciences Meeting and Exhibit,* AIAA Paper No. 96–0714, 1996.

[11] S. Jayaram, A. Myklebust, and P. Gelhausen. "ACSYNT—A Standards-Based System for Parametric Computer Aided Conceptual Design of Aircraft," AIAA Paper No. 92-1268, 1992.

[12] L. A. McCullers. "Aircraft Configuration Optimization Including Optimized Flight Profiles," *Proceedings of Symposium on Recent Experiences in Multidisciplineary Analysis and Optimization,* J. Sobieski, compiler, NASA CP–2327, pp. 396–412, April 1984.

[13] J. Reuther, A. Jameson, J. J. Alonso, M. J. Rimlinger, and D. Saunders. "Constrained Multipoint Aerodynamic Shape Optimization Using an Adjoing Formulation and Parallel Computers," $35^{th}$ *Aerospace Sciences Meeting and Exhibit,* AIAA Paper No. 97–0103, Reno, NV, January 1997.

[14] A. Jameson and N. A. Pierce. "Optimum Aerodynamic Design Using Navier-Stokes Equations," $35^{th}$ *Aerospace Sciences Meeting and Exhibit,* AIAA Paper No. 97–0101, Reno, NV, January 1997.

[15] R. Braun, P. Gage, I. Kroo, and I. Sobieski. "Implementation and Performance Issues in Collaborative Optimization," *Proceedings of the* $6^{th}$ *AIAA/NASA/ISSMO Symposium on Multidisciplinary Analysis and Optimization,* AIAA Paper No. 96–4017, pp. 295–305, Bellevue, WA, September 1996.

[16] R. D. Braun. *Collaborative Optimization: An Architecture for Large-Scale Distributed Design*, Ph.D. thesis, Stanford University, 1996.

[17] C. J. Borland, J. R. Benton, P. D. Frank, T. J. Kao, R. A. Mastro, and J. M. Barthelemy. "Multidisciplinary Design Optimization of a Commercial Aircraft Wing—An Exploratory Study," *Proceedings of the* $5^{th}$ *AIAA/NASA/USAF/ISSMO Symposium on Multidisciplinary Analysis and Optimization, Vol. 1,* AIAA Paper No. 94–4305, pp. 505–519, Panama City, FL, September 1994.

[18] M. Baker and J. Geising. "A Practical Approach to MDO and its Application to an HSCT Aircraft," $1^{st}$ *AIAA Aircraft Engineering, Technology, and Operations Congress,* AIAA Paper No. 95–3885, Los Angeles, CA, September 19–21, 1995.

[19] G. Venter, R. T. Haftka, and J. H. Starnes. "Construction of Response Surfaces for Design Optimization Applications," *Proceedings of the* $6^{th}$ *AIAA/NASA/ISSMO Symposium on Multidisciplinary Analysis and Optimization,* AIAA Paper No. 96–4040, pp. 548–564, Bellevue, WA, September 1996.

[20] A. A. Giunta, R. Narducci, S. Burgee, B. Grossman, W. H. Mason, L. T. Watson, and R. T. Haftka. "Variable-Complexity Response Surface Aerodynamic Design of an HSCT Wing," *Proceedings of the* $13^{th}$ *AIAA Applied Aerodynamics Conference,*AIAA Paper No. 95–1886, pp. 994–1002, San Diego, CA, June 1995.

[21] V. Balabanov, M. Kaufman, D. L. Knill, D. Haim, O. Golovidov, A. A. Giunta, R. T. Haftka, B. Grossman, W. H. Mason, and L. T. Watson. "Dependence of Optimal Structural Weight on Aerodynamic Shape for a High-Speed Civil Transport," *Proceedings of the* $6^{th}$ *AIAA/NASA/ISSMO Symposium on Multidisciplinary Analysis and Optimization,* AIAA Paper No. 96–4046, pp. 599–612, Bellevue, WA, September 1996.

[22] V. O. Balabanov. *Development of Approximations for HSCT Wing Bending Material Weight Using Response Surface Methodology*, Ph.D. thesis, Virginia Polytechnic Institute and State University, 1997.

[23] S. Burgee. *A Coarse Grained Variable-Complexity MDO Paradigm for HSCT Design*, Master's thesis, Virginia Polytechnic Institute and State University, 1995.

[24] S. Burgee, A. A. Giunta, V. Balabanov, , B. Grossman, W. H. Mason, R. Narducci, R. T. Haftka, and L. T. Watson. "A Coarse Grained Parallel Variable-Complexity Multidisciplinary Optimization Paradigm," *International Journal of Supercomputing Applications and High Performance Computing*, 10, No. 4: 269–299, Bellevue, WA, September 1996.

[25] R. H. Myers and D. C. Montgomery. *Response Surface Methodology: Process and Product Optimization Using Designed Experiments*, John Wiley & Sons, Inc., New York, NY, pp. 1–67, 134–174, 297–357, 640–655, 1995.

[26] S. A. Powers. "Drag Minimization Using Exact Methods," *AIAA Journal*, 2: 941–943, 1964, May 1964.

[27] A. A. Giunta. *Aircraft Multidisciplinary Design Optimization Using Design of Experiments Theory and Response Surface Modeling Methods*, Ph.D. thesis, Virginia Polytechnic Institute and State University, 1997.

[28] V. V. Toropov. "Simulation Approach to Structural Optimization," *Structural Optimization*, 1: 37–46, 1989.

[29] V. V. Toropov, A. A. Filatov, and A. A. Polynkin. "Multiparameter Structural Optimization Using FEM and Multipoint Explicit Approximations," *Structural Optimization*, 6: 7–14, 1993.

[30] V. Toropov, F. van Keulen, V. Markine, and H. de Boer. "Refinements in the Multi-Point Approximation Method to Reduce the Effects of Noisy Structural Responses," *Proceedings of the* $6^{th}$ *AIAA/NASA/ISSMO Symposium on Multidisciplinary Analysis and Optimization,* AIAA Paper No. 96–4087, pp. 941–951, Bellevue, WA, September 1996.

[31] R. P. Narducci. *Selected Optimization Procedures for CFD-Based Shape Design Involving Shock Waves or Computational Noise*, Ph.D. thesis, Virginia Polytechnic Institute and State University, 1995.

[32] M. G. Hutchison, E. R. Unger, W. H. Mason, B. Grossman, and R. T. Haftka. "Aerodynamic Optimization of an HSCT Configuration Using Variable-Complexity Modeling," AIAA Paper No. 93–0101, January 1993.

[33] J. Dudley, X. Huang, R. T. Haftka, B. Grossman, and W. H. Mason. "Variable-Complexity Interlacing of Weight Equation and Structural Optimization of the High-Speed Civil Transport," AIAA Paper No. 94–4377, September 1994.

[34] J. Dudley, X. Huang, P. E. MacMillin, B. Grossman, R. T. Haftka, and W. H. Mason. "Multidisciplinary Optimization of the High-Speed Civil Transport," AIAA Paper No. 95–0124, January 1995.

[35] M. Kaufman, V. Balabanov, S. L. Burgee, A. A. Giunta, B. Grossman, W. H. Mason, L. T. Watson, and R. T. Haftka. "Variable-Complexity Response Surface Approximations for Wing Structural Weight in HSCT Design," AIAA Paper No. 96–0089, January 1996.

[36] M. D. Kaufman. *Variable-Complexity Response Surface Approximations for Wing Structural Weight in HSCT Design*, Master's thesis, Virginia Polytechnic Institute and State University, 1996.

[37] O. B. Golovidov. *Variable-Complexity Response Surface Approximations for Aerodynamic Parameters in HSCT Design*, Master's thesis, Virginia Polytechnic Institute and State University, 1997.

[38] J. Sobieszczanski-Sobieski and R. T. Haftka. "Multidisciplinary Aerospace Design Optimization: Survey of Recent Developments," $34^{th}$ *Aerospace Sciences Meeting and Exhibit,* AIAA Paper No. 96–0711, Reno, NV, January 15–18, 1996.

[39] E. Eminton. "On the Minimization and Numerical Evaluation of Wave Drag," *Royal Aircraft Establishment Report AERO.2564*, November 1955.

[40] R. V. Harris, Jr. "An Analysis and Correlation of Aircraft Wave Drag," NASA TM X–947, 1964.

[41] H. W. Carlson and D. S. Miller. "Numerical Methods for the Design and Analysis of Wings at Supersonic Speeds," NASA TN D–7713, 1974.

[42] H. W. Carlson and R. J. Mack. "Estimation of Leading-Edge Thrust for Supersonic Wings of Arbitrary Planforms," NASA TP–1270, 1978.

[43] E. J. Hopkins and M. Inouye. "An Evaluation of Theories Predicting Turbulent Skin Friction and Heat Transfer on Flat Plates at Supersonic and Hypersonic Mach Numbers," *AIAA Journal*, 9, No. 6: 993–1003, June 1971.

[44] H. W. Carlson and K. B. Walkley. "Numerical Methods and a Computer Program for Subsonic and Supersonic Aerodynamic Design and Analysis of Wings with Attainable Thrust Corrections," NASA CR–3808, 1984.

[45] W. D. McGrory, D. C. Slack, M. P. Applebaum, and R. W. Walters. *GASP Version 2.2 Users Manual*, Aerosoft, Inc., Blacksburg, VA, 1993.

[46] R. L. Barger, M. S. Adams, and R. R. Krishnan. "Automatic Computation of Euler-Marching and Subsonic Grids for Wing-Fuselage Configurations," NASA TM 4573, July 1994.

[47] C. B. Craidon. "Description of a Digital Computer Program for Airplane Configuration Plots," NASA TM X–2074, 1970.

[48] R. L. Barger and M. S. Adams. "Automatic Computation of Wing-Fuselage Intersection Lines and Fillet Inserts with Fixed-Area Constraint," NASA TM 4406, March 1993.

[49] X. Huang, R. T. Haftka, B. Grossman, and W. H. Mason. "Comparison of Statistical Weight Equations with Structural Optimization for Supersonic Transport Wings," AIAA Paper No. 94–4379, September 1994.

[50] Vanderplaats, Miura and Associates, Inc., 5960 Mandarin Avenue, Suite F, Goleta, CA 93117. *GENESIS User Manual, Version 1.3*, 1993.

[51] Vanderplaats Research & Development, Inc. *DOT Users Manual, Version 4.20*, Colorado Springs, CO, 1995.

[52] P. J. Bobbitt. "The Pros and Cons of Code Validation," AIAA Paper No. 88–2535, June 1988.

[53] P. W. Sacher, R. G. Bradley, Jr., and W. Schmidt. "Technical Evaluation Report on the Fluid Dynamics Symposium on Validation of CFD [CP-437]," AGARD AR-257, May 1989.

[54] D. P. Aeschliman, W. L. Oberkampf, and F. G. Blottner. "A Proposed Methodology for Computational Fluid Dynamics Code Verification, Calibration, and Validation," $16^{th}$ *International Congress on Instrumentation in Aerospace Simulation Facilities (ICIASF)*, Wright-Patterson AFB, OH, July 18–21, 1995.

[55] R. E. Melnik, M. J. Siclari, T. Barber, and A. Verhoff. "A Process for Industry Certification of Physical Simulation Codes," AIAA Paper No. 94–2235, June 1994.

[56] R. E. Melnik, M. J. Siclari, F. Marconi, T. Barber, and A. Verhoff. "An Overview of a Recent Industry Effort at CFD Code Certification," AIAA Paper No. 95–2229, June 1995.

[57] F. Marconi, M. Siclari, G. Carpenter, and R. Chow. "Comparison of TLNS3D Computations with Test Data for a Transport Wing/Simple Body Configuration," AIAA Paper No. 94–2237, June 1994.

[58] D. L. Knill, V. Balabanov, O. Golovidov, B. Grossman, W. H. Mason, R. T. Haftka, and L. T. Watson. "Accuracy of Aerodynamic Predictions and Its Effects on Supersonic Transport Design," *MAD Center Report 96–12–01*, Multidisciplinary Analysis and Design Center for Advanced Vehicles, Virginia Tech, Blacksburg, VA, December 1996.

[59] R. V. Harris, Jr. and E. J. Landrum. "Drag Characteristics of a series of a Series of Low-Drag Bodies of Revolution at Mach Numbers From 0.6 to 4.0," NASA TN-D 3163, December 1965.

[60] W. H. Mason and J. Lee. "Aerodynamically Blunt and Sharp Bodies," *Journal of Spacecraft and Rockets*, 31, No. 3: 406–413, May-June 1994.

[61] P. J. Roache. "Perspective: A Method for Uniform Reporting of Grid Refinement Studies," *Journal of Fluids Engineering*, 116: 405–413, September 1994.

[62] J. Weber and C. King. "Analysis of the Zero-Lift Wave Drag Measured on Delta Wings," *Aeronautical Research Counsel Reports and Memoranda No. 3818*, 1978.

[63] M. J. Siclari. "The NCOREL Computer Program for 3D Nonlinear Supersonic Potential Flow Computations," NASA CR–3694, 1983.

[64] W. H. Mason, M. J. Siclari, D. S. Miller, and J. L. Pittman. "A Supersonic Maneuver Wing Designed for Nonlinear Attached Flow," AIAA Paper No. 83–0425, January 1983.

[65] M. Siclari, M. Visich, A. Cenko, B. Rosen, and W. Mason. "An Evaluation of NCOREL, PAN AIR, and W12SC3 for Supersonic Wing Pressures," *Journal of Aircraft*, 21, No. 10: 816–822, October 1984.

[66] J. L. Pittman, D. S. Miller, and W. H. Mason. "Supersonic, Nonlinear, Attached-Flow Wing Design for High Lift With Experimental Validation," NASA TP–2336, August 1984.

[67] S. C. Somer and B. J. Short. "Free-Flight Measurements of Turbulent-Boundary-Layer Skin Friction in the Presence of Severe Aerodynamic Heating at Mach Numbers from 2.8 to 7.0," NASA TN 3391, 1955.

[68] R. T. Jones and D. Cohen. *High Speed Wing Theory*, Princeton University Press, 1960.

[69] P. E. MacMillin, O. Golovidov, W. H. Mason, B. Grossman, and R. T. Haftka. "Trim, Control, and Performance Effects in Variable-Complexity High-Speed Civil Transport Design," *MAD Center Report 96–07–01*, Multidisciplinary Analysis and Design Center for Advanced Vehicles, Virginia Tech, Blacksburg, VA, July 1996.

[70] R. S. Sellar, M. A. Stelmack, S. M. Batill, and J. E. Renaud. "Response Surface Approximations for Discipline Coordination in Multidisciplinary Design Optimization," $37^{th}$ *AIAA/ASME/ASCE/AHS/ASC Sructures, Structural Dynamics, and Materials Conference,* AIAA Paper No. 96–1383, Salt Lake City, UT, April 1996.

[71] W. Chen, J. K. Allen, D. P. Schrage, and F. Mistree. "Statistical Experimentation Methods for Achieving Affordable Concurrent Systems Design," *AIAA Journal*, 35, No. 5, May 1997.

[72] R. Mead. *The Design of Experiments*, Cambridge University Press, New York, NY, pp. 542–548, 1988.

[73] M. J. Box and N. R. Draper. "Factorial Designs, the $|\ \mathbf{X}^T\mathbf{X}\ |$ Criterion, and Some Related Matters," *Technometrics*, 13, No. 4, pp. 731–742, 1971.

[74] SAS Institute, Inc. *JMP Users Guide, Version 3.1*, Cary, NC, 1995.

[75] T. J. Mitchell. "An Algorithm for the Construction of D-Optimal Experimental Designs," *Technometrics*, 16, No. 2, pp. 203–210, 1974.

[76] A. A. Giunta, J. M. Dudley, R. Narducci, B. Grossman, R. T. Haftka, W. H. Mason, and L. T. Watson. "Noisy Aerodynamic Response and Smooth Approximations in HSCT Design," *Proceedings of the* $5^{th}$ *AIAA/USAF/NASA/ISSMO Symposium on Multidisciplinary Analysis and Optimization,* AIAA Paper No. 94-4376, pp. 1117–1128, Panama City, FL, September 1994.

[77] S. Addelman and O. Kempthorne, *Annals of Mathematical Statistics*, 32, pp. 1167–1176, 1961.

# Appendix A

# Parallel Computing Code

The coarse-grained parallel computation of the CFD results are implemented in the file `parcomp.f`. This program uses the Message Passing Interface (MPI) protocol to send and receive information from the various nodes. The file contains five subroutines: `intochar()`, `makedir()`, `gridprep()`, `rungasp()`, and `cleanup()`. Subroutine `intochar()` converts an integer into a character representation of that number for use in naming files and directories. Subroutine `makedir()` set up a directory for each slave node, where all the pertinent information for that node in contained. A schematic of the directory structure is given in Fig. A.1. Subroutine `gridprep()` runs the grid generation code and places the output files in the appropriate directory. Subroutine `rungasp()` executes the CFD calculations for a given node. Subroutine `cleanup()` removes the directory for a particular node after it has completed its task.

## A.1 Source Code

```
#include "mpif.h"
c
c Compiling statement:
c if77 -Mdclchk -O4 -o parcomp parcomp.F
c      -L/usr/local/mpi/lib/paragon/ch_nx -lmpi -nx
c
c VARIABLE DESCRIPTION:
c
c Integer Variables:
c des    - if des > 0 : current design number
```

```
c             des < 0 : termination flag for slave node
c it1    - (MPI) tag for sending tasks from master node
c it2    - (MPI) tag for sending replys from slave nodes
c inides - initial starting design number
c maxdes - total number of designs to be evaluated
c maxnod - (parameter) maximum allowable number of nodes on which to run
c nr,nd  - do loop variables for node and design numbers
c nod    - current node number
c req()  - (MPI array) array of requests for nonblocking communication
c size   - total number of nodes used
c stat() - (MPI array) array of status flags for communication
c
c Double Precision Variables:
c tbeg   - starting clock time
c tend   - ending clock time
c tinc   - accuracy of time measurements
c
c Character Variables:
c desnum - 3-digit design number (used in file I/O)
c nodnum - 3-digit node number (used in file I/O)
c
      integer maxnod
      parameter(maxnod=60)
      integer ierr,size,nod,nr,nd
      integer stat(MPI_STATUS_SIZE),req(maxnod)
      integer des,maxdes,inides
      integer it1,it2
      integer nd,nr
      real*8 tbeg, tend, tinc
      character*3 desnum,nodnum
c
      it1=10
      it2=30
      inides=1
      maxdes=350
c
      call mpi_init(ierr)
      tbeg=mpi_wtime()
      call mpi_comm_rank(MPI_COMM_WORLD,nod,ierr)
      call mpi_comm_size(MPI_COMM_WORLD,size,ierr)
c
c--------------------
c Single node calculations
c--------------------
c
      if(size.eq.1)then
        call intochar(nod,nodnum)
```

```
c Create new directory
        call makedir(nodnum)
        do 60 des=inides,maxdes
          call intochar(des,desnum)
c Setup and run GASP
          call gridprep(nodnum,desnum)
          call rungasp(nodnum,desnum)
   60   continue
        tend=mpi_wtime()
        write(*,*) 'Total time=',tend-tbeg
        call cleanup(nodnum)
        call MPI_FINALIZE(ierr)
        stop
      endif
c
c Dimensioning error checks
c
      if(maxnod.lt.size)then
        write(*,*) '!!! Need to adjust maxnod parameter'
        call MPI_FINALIZE(ierr)
        stop
      endif
      if(maxdes-inides+1.lt.size-1)then
        write(*,*) '!!! Number of Designs smaller than number of nodes'
        call MPI_FINALIZE(ierr)
        stop
      endif
c
c--------------------
c Slave Nodes
c--------------------
c
      if(nod.ne.0)then
        call intochar(nod,nodnum)
c Read des from master node
  500   call mpi_recv(des,1,MPI_INTEGER,0,it1,MPI_COMM_WORLD,stat,ierr)
        if(des.gt.0)then
          call intochar(des,desnum)
c         write(*,1000)'Running design',des,'on node',nod
c Setup and run GASP
          call gridprep(nodnum,desnum)
          call rungasp(nodnum,desnum)
c Send completion flag to master
          call mpi_send(nod,1,MPI_INTEGER,0,it2,MPI_COMM_WORLD,ierr)
        else
c         write(*,*)'Slave',nod,' received "stop" from master'
c Remove created directory
```

```
          call cleanup(nodnum)
          call MPI_FINALIZE(ierr)
          stop
        endif
        goto 500
      else
c
c--------------------
c Master Node
c--------------------
c
c Send initial set of tasks
        do 10 nr=1,size-1
          nd=inides+nr-1
          call intochar(nr,nodnum)
          call makedir(nodnum)
          call mpi_send(nd,1,MPI_INTEGER,nr,it1,MPI_COMM_WORLD,ierr)
   10   continue
c Continue sending tasks
        do 20 nd=inides+size-1,maxdes
          call mpi_recv
     <    (nr,1,MPI_INTEGER,MPI_ANY_SOURCE,it2,MPI_COMM_WORLD,stat,ierr)
c         write(*,*)'Master received "done" from node',nr
          call mpi_send(nd,1,MPI_INTEGER,nr,it1,MPI_COMM_WORLD,ierr)
   20   continue
c Wait for slave nodes to complete task and send termination flag
        do 30 nd=1,size-1
          call mpi_recv
     <    (nr,1,MPI_INTEGER,MPI_ANY_SOURCE,it2,MPI_COMM_WORLD,stat,ierr)
          call mpi_send(-1,1,MPI_INTEGER,nr,it1,MPI_COMM_WORLD,ierr)
   30   continue
c Check clock time
        tend=mpi_wtime()
        write(*,*) 'Total time=',tend-tbeg
        tinc=mpi_wtick()
        write(*,*) 'Precision=',tinc
      endif
c
      call MPI_FINALIZE(ierr)
c
 1000 format(a,1x,i4,1x,a,i3)
c
      stop
      end
c
c--------------------------------------------------------------------c
c
```

```
      subroutine intochar(num,chr)
c
c Convert an integer to a character string of length 3
c
      integer num
      integer hun,ten,one
      character*3 chr
c
      hun=num/100
      ten=(num-hun*100)/10
      one=num-hun*100-ten*10
      chr=char(hun+48)//char(ten+48)//char(one+48)
c
      return
      end
c
c-----------------------------------------------------------------------c
c
      subroutine makedir(nodnum)
c
c Create the appropriate files and directories for each node
c
      character*3 nodnum
c
      call system('mkdir Node'//nodnum//
     <            '; cp resid rest01 Node'//nodnum//'/')
c
      return
      end
c
c-----------------------------------------------------------------------c
c
      subroutine gridprep(nodnum,desnum)
c
c Copy appropriate Craidon file into grid directory and run grid generator
c
      character*3 desnum,nodnum
c
c 20 Variable Doptimal Points
c
      call system('cp /home8/knill/20DVOpt/RedDoptPts/wav'//
     <   desnum//'.20dv Node'//nodnum//'/craidon'//
     <   ' ; cd Node'//nodnum//'/ ; ../../MeshGen/grid_exe')

c
      return
      end
```

```
c
c-----------------------------------------------------------------------c
c
      subroutine rungasp(nodnum,desnum)
c
c Run GASP and post-processing utilities for the desired angle of attacks
c
      character*3 desnum,nodnum
c
c Run alpha=2.5 case
c
      call system('cp gasp.z1.25 Node'//nodnum//'/gasp.z1'//
     <            ' ; cd Node'//nodnum//';../run ;'//
     <            ' ../print ; ../delf > ../print'//desnum//'.25')
c
c Run alpha=4.5 case
c
      call system('cp gasp.z1.45 Node'//nodnum//'/gasp.z1'//
     <            ' ; cd Node'//nodnum//';../run ;'//
     <            ' ../print ; ../delf > ../print'//desnum//'.45')
c
      return
      end
c
c-----------------------------------------------------------------------c
c
      subroutine cleanup(nodnum)
c
c Remove the files and directories created for each node
c
      character*3 nodnum
c
      call system('rm -r Node'//nodnum)
c
      return
      end
```

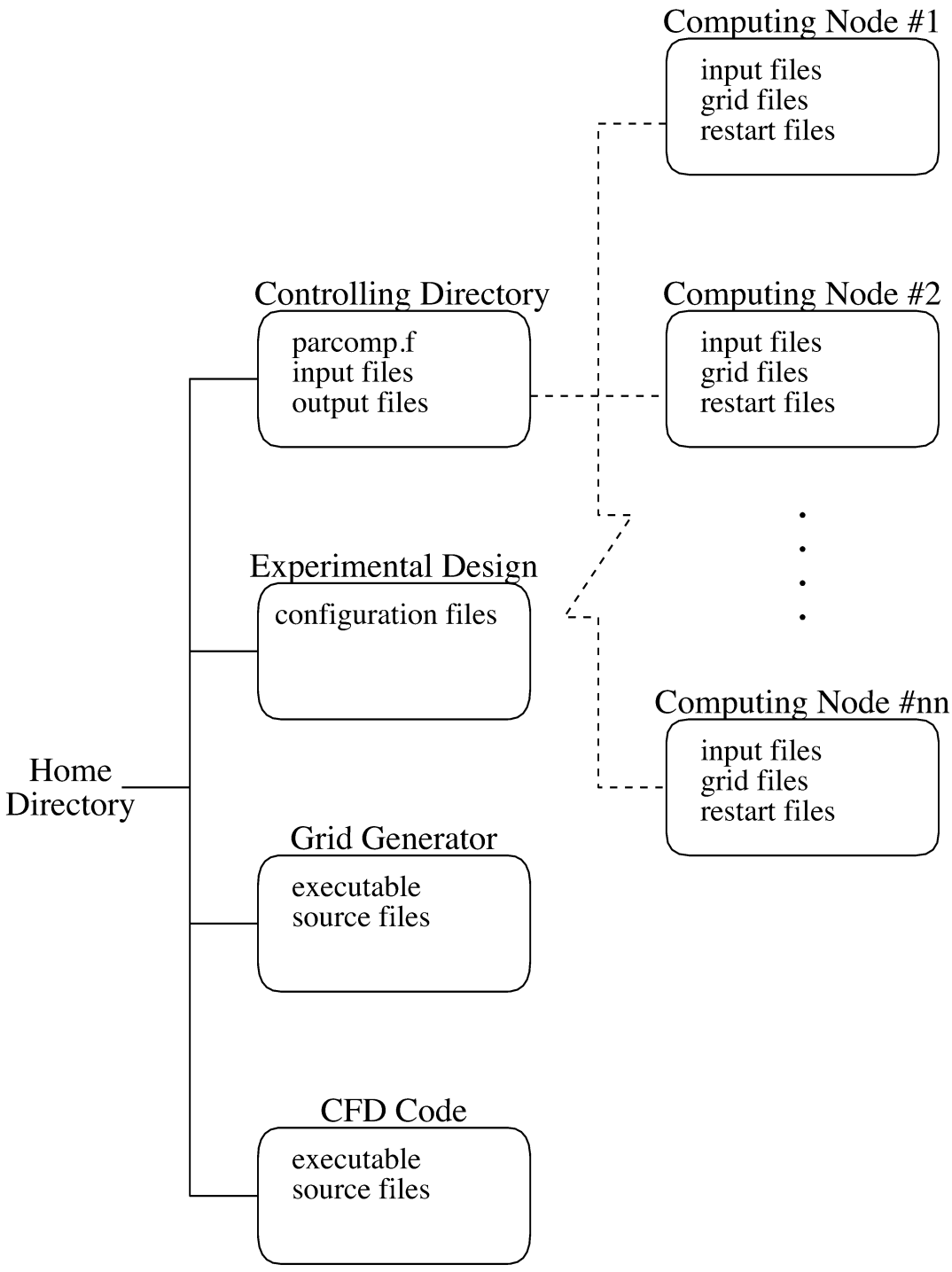


**Figure A.1:** Directory Structure for Parallel Computations.

# Vita

Duane L. Knill was born on February 25, 1972, in Frederick, Maryland. In 1993 he completed the B.S. degree, *magna cum laude*, in aerospace engineering with a minor in mathematics from Virginia Polytechnic Institute and State University in Blacksburg, Virginia. He earned the M.S. degree in 1995 and the Ph.D. degree in aerospace engineering in 1997, both from Virginia Polytechnic Institute and State University. While performing his graduate research, he worked in an internship position with Cessna Aircraft in Wichita, Kansas. He currently holds a post-doctoral position in the Aeronautics and Astronautics Department at the University of Washington in Seattle, Washington.